Graphene Microelectrode Arrays to Combine Electrophysiology with Fluorescence Imaging of Amyloid Proteins

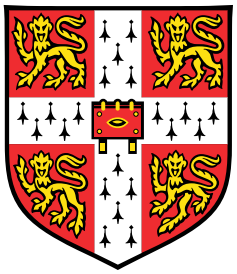

Philippa Jane Hooper

Department of Chemical Engineering and Biotechnology
University of Cambridge

This dissertation is submitted for the degree of
Doctor of Philosophy

Murray Edwards College April 2019

Declaration

I hereby declare that except where specific reference is made to the work of others, the contents of this dissertation are original and have not been submitted in whole or in part for consideration for any other degree or qualification in this, or any other university. This dissertation is my own work and contains nothing which is the outcome of work done in collaboration with others, except as specified in the text and Acknowledgements. This dissertation contains fewer than 65,000 words including appendices, bibliography, footnotes, tables and equations and has fewer than 150 figures.

Philippa Jane Hooper
April 2019

Acknowledgements

The heavens declare the glory of God; the skies proclaim the work of his hands. Day after day they pour forth speech; night after night they reveal knowledge. Psalm 19:1-2 NIV

Thank-you so much to Gabi Kaminski-Schierle for her supervision, for being enthusiastic, encouraging and for seeing the positive side of my work. I really hope the graphene devices can enable experiments to happen in the future. Also, to Antonio Lombardo for supervision, help and insight with the engineering, graphene and fabrication aspects of the work.

In the Cambridge Graphene Centre, many people have helped with the experimental work and provided support. Firstly I would like to thank Domenico de Fazio for patiently guiding me during my first year. Flavia Tomarchio for training on numerous machines. The 2014 graphene CDT cohort especially Tom Albrow-Owen, Tian Carey, David Purdie and Yang Li for countless conversations both about experimental work, data analysis and life. Oliver Burton for growing graphene. Also, Vincenzo Curto for conversations about the MEAs and impedance analysis, and for proofreading. The graphene centre support staff Yury Alaverdyan, Alan Curtis, James McLeod, Rebecca Warner Hodgkin, Anna Mott and Maria without whom nothing would function and the building would be less cheerful. Also, thanks to my fellow MEA student Nathan Jay, and FTIR spectroscopist Jake Leigh Watson.

The Molecular Neuroscience group, Laser Analytics Group and Neuronal Oscillation Group. Specifically to Ole Paulsen for suggestions of electrophysiology experiments. Miranda Robbins for being a 'friendly biologist' brimming with ideas and enthusiasm. Also, to Amberley Stephens, Maria Zacharopoulou, Amanda Haack, Susanna Mierau, Ricado Conchi, Tanja Fuchsberger and Talia Shmool for doing the biological work for these projects as well as for friendship. Timothy Sit and Prez Jarebowski for their matlab code, Jalique Fojas for making3D printing a MEA holder and Chetan Poudel for helping with the imaging. At NMI Reutlingen thanks to Pranoti Kshirsagar and Claus Burkhardt for hosting me and teaching me so much about MEAs.

Thank-you so much to my dear friends, there are far to many people to name so this is a very incomplete list you keep me sain and love me. My Cambridge housemates for being like a family Jhalique Fojas, Funmi Ladejobi, Antonia Reinke. Dominika Boneberg and

Bjoern Soergel with whom I've share many though-provoking conversations over brunch. To the roomies Jeffy Henderson, Maggie McNerney, Heather Martin, Sarah Sigsworth, Emily Thiede. My Church family, and especially my housegroup for challenging me to deepen my faith and for upholding me in your prayers. To my one-to-one's Lynn Pang and Pauline Godart for teaching me so much about God. The iCafe team who show me how to serve other people sacrificially. The Friends International team, Sofia Crump, Jenny Hunter, Josh Bell, Sofia Demler and Huan Chen, for bearing with me patiently and praying during the final writing process.

Finally, thank-you so much to my family. To Mum, Dad, Ollie and George for supporting and loving me through all the highs and lows of a PhD. To my wonderful fiance Ben Woodhams. And an especial mention to Patrick Hodson for being interested in my work and asking thought-provoking questions that have helped me understand its context.

Most importantly I would like to thank God, through Jesus Christ, for creating this beautiful and intricate world and for the time, resources and ability to study it.

Abstract

Alzheimer's disease (AD) and Parkinson's diseases (PD) are neurodegenerative diseases that affect $\sim$60 million people worldwide. Both diseases are linked to the misfolding of proteins from their native conformational state into β-sheeted amyloid fibrils. In AD the implicated proteins are amyloid-β and tau, and for PD the implicated protein is α-synuclein (aSyn). The motivation for this work is to develop and use physical techniques to better understand the role of amyloid proteins in neurodegenerative diseases. Two techniques used in amyloid research are fluorescence microscopy, to map the protein location and aggregation state, and electrophysiology, to examine the effect of the proteins on neurons. To enable these techniques to be combined, a transparent graphene microelectrode array (MEA) was designed, fabricated and characterised. The active electrode site was graphene since it is electrically conductive, optically transparent and biocompatible. The graphene MEA was characterised using Raman spectroscopy to check the graphene quality, and electrochemical impedance spectroscopy (EIS) to probe the electrode-electrolyte interface. The graphene MEAs enabled voltage trace recordings from cultured neurons to be combined with widefield, confocal fluorescence and fluorescence lifetime imaging microscopy (FLIM). Combining fluorescence imaging and electrophysiology will allow amyloid aggregation to be correlated with neuronal firing patterns. Another physical technique used was Fourier transform infrared spectroscopy (FTIR). A script was written to estimate the protein secondary structure content, and used to investigate polymorphism in the monomeric amyloid protein aSyn.

Publications

Published

- Toby P. Call, Tian Carey, Paolo Bombelli, David J. Lea-Smith, **Philippa J. Hooper**, Christopher J. Howe and Felice Torrisi. Platinum-free, graphene based anodes and air cathodes for single chamber microbial fuel cells. *J. Mater. Chem. A*, 45(5):23872-23886, 2017.

Submitted

- Talia A. Shmool, **Philippa J. Hooper**, Gabriele S. Kaminski Schierle, Christopher F. Van der Walle, and J. Axel Zeitler. Terahertz Spectroscopy: An investigation of the Structural Dynamics of Freeze-Dried PLGA Microspheres. *ACS Applied Polymer Materials*.

In preparation

- **Philippa J. Hooper**, Miranda Robbins, Susanna B. Mierau, Tanja Fuchsberger, Timothy Sit, Chetan Poudel, Oliver Burton, Stephan Hoffman, Clemens F. Kaminski, Ole Paulsen, Antonio Lombardo, Gabriele S. Kaminski Schierle. Transparent graphene microelectrode array to combine electrophysiological measurements with fluorescence lifetime imaging.

- Talia A. Shmool, **Philippa J. Hooper**, Markus Leutzsch, Amberley D. Stephens, Mario U. Gaimann, Michael D. Mantle, Gabriele S. Kaminski Schierle, Christoper F. van der Walle, and J. Axel Zeitler. Measurement of Vibrational Confinement in Lyophilised Protein Formulations using Terahertz Spectroscopy.

Table of contents

Nomenclature

Roman Symbols

A Absorbance

a Area

B Background FTIR spectrum

b Resistive nature of constant phase element

C Capacitance

c Concentration

D Raman D peak at $\sim 1350\,\mathrm{cm}^{-1}$

d Neuron-electrode distance

E Energy

e Electron charge, 1.602×10^{-19} C

E_F Fermi energy

f Frequency

G Raman G peak at $\sim 1580\,\mathrm{cm}^{-1}$

g Conductivity

$\hbar$ Reduced Planck constant, $1.054 \times 10^{-34}\,\mathrm{J\,s}^{-1}$

h Plank constant, $6.626 \times 10^{-34}\,\mathrm{m}^2\,\mathrm{kg\,s}^{-1}$

I Intensity

i Current

J Protein FTIR spectrum

j Imaginary number, $\sqrt{-1}$

k_B Boltzmann constant, $1.381\times10^{-23}\,\mathrm{m^2\,kg\,s^{-2}\,K^{-1}}$

l Length

m_e Rest mass of electron, 9.11×10^{-31} kg

N Total number

n Charge carrier concentration

$\tilde{n}$ Refractive index

P Power

p Positive charge doping

Q Constant phase element

q Index

R_g Ideal gas constant, $8.314\,\mathrm{J\,mol^{-1}\,K^{-1}}$

R Resistance

r Radius

S Electronic energy level

T Temperature

t Time

v_F Fermi velocity, $1.1\times10^6\,\mathrm{m\,s^{-1}}$

v_L Speed of light in a vacuum $\sim 299.8\times10^6\,\mathrm{m/s}$

V Voltage

v Velocity

W Warburg element

w Width

x Scaling factor

Z Impedance

z Protein residue

Greek Symbols

α Fine structure constant, $\sim 7.299 \times 10^{-3}$

β Resistance at 1 Hz

δ Coverage coefficient

ε Attenuation coefficient

Γ Full width at half maximum

λ Wavelength

τ Time constant

$\tilde{\nu}$ Wavenumber

π Mathematical constant, $\simeq 3.142$

ρ Resistivity

σ Diffusion coefficient

θ Phase of impedance

ω Angular frequency

χ^2 Chi-squared statistical hypothesis test, sum of the squares of residuals

Acronyms / Abbreviations

2D Overtone of Raman D peak at $\sim 2680\,\mathrm{cm}^{-1}$

2DEG Two-dimensional electron gas

AD Alzheimer's disease

AFM Atomic force microscopy

ALD Atomic layer deposition

aSyn α-synuclein

BAPTA 1,2-bio(o-aminophenoxy)ethane-N,N,N',N'-tetraacetic acid)

BSA Bovine serum albumin

CD Circular dichroism

CPE Constant phase element

Cryo-EM Cryo-electron microscopy

CVD Chemical vapour deposition

DAPI 4',6-diamidino-2-phenylindole

DC Direct current

ECM Equivalent circuit model

EIS Electrochemical impedance spectroscopy

FBS Fetal bovine serum

FET Field effect transistor

FITC Fluorescein isothiocyanate

FLIM Fluorescence lifetime imaging microscopy

FSD Fourier self-deconvolution

FTIR Fourier transform infrared spectroscopy

HEPES 4-(2-hydroxyethyl)-1-piperazineethanesulfonic acid

IPA Isopropyl alcohol

ITO Indium tin oxide

LCM Lumped circuit model

LFP Local field potential

MAD Mean absolute deviation

MAP Microtubule associated protein

MEA Microelectrode array

NAC Non-amyloid component

NMR Nuclear magnetic resonance

OCT Optical coherence tomography

OGB-1 Oregon green BAPTA-1

PBS Phosphate buffered saline

PCA Principle component analysis

PDMS Polydimethylsiloxane

PD Parkinson's disease

PEDOT poly(3,4-ethylenedioxythiophene)-poly(styrenesulfonate)

PEI Poly(ethyleneimine

PET Polyethylene terephthalate

PGMEA Propylene glycol monomethyl ether acetate

PMMA Polymethylmethacrylate

Polysorbate Polyoxyethylene sorbitan monooleate

RMS Root mean square

SG Savitzky-Golay filter

SNR Signal to noise ratio

TCSPC Time correlated single photon counting

TMAH Tetra-methyl ammonium hydroxide

Tris Tris(hydroxymethyl) aminomethane

UV Ultraviolet

UV-vis Ultraviolet-visible

WT Wild type

XRD X-ray diffraction

Chapter 1

Introduction

1.1 Scope and overall aims

Alzheimer's disease (AD) and Parkinson's disease (PD) are neurodegenerative diseases. Implicated in the disease mechanisms of AD and PD, are the misfolding of proteins from their native conformational state into amyloid fibrils. We wanted to address whether the location and aggregation state of amyloid proteins in neurons leads to electrophysiological changes in neurons. This required the development of transparent microelectrode arrays (MEAs) which can combine electrophysiological recordings with advanced fluorescence imaging techniques. In addition to this, we wanted to address how the local environment determines the structural polymorphism of monomeric amyloid proteins. This was performed *in vitro* using Fourier transform infrared (FTIR) spectroscopy.

1.2 Motivation

AD and PD are both neurodegenerative diseases. AD affected $\sim$47.5 million people worldwide in 2015 [1] and PD affected 8–15 million people worldwide in 2017 [2]. Both diseases become more prevalent with age. AD and PD are both linked to the misfolding of proteins from their native conformational state into amyloid fibrils [3]. The formed amyloid fibrils are insoluble in aqueous conditions and have a characteristic β-sheet secondary structure [4]. In AD the implicated misfolded proteins are amyloid-β in the form of senile plaques and tau in the form of neurofibrillary tangles. For PD the implicated misfolded protein is α-synuclein (aSyn) present in Lewy body intracellular inclusions. This thesis focuses on the aggregation of tau and the monomeric polymorphism of aSyn since this relates to previous work performed in the group.

The normal physiological role of tau protein is as axonal microtubule associated protein, which stabilises the microtubules required for structure and transport [5]. Exogenous tau is taken up by neurons and propagated from neuron to neuron [6]. The tau pathology in AD patients starts in the entorhinal cortex and spreads across the brain in a defined pattern which correlates with the cognitive decline observed in clinical AD [7]. The mechanism by which tau is transferred between the brain regions is disputed however, and could be due to secretion [8], trans-synaptic spread [9], tunnelling nanotubes [10] or microglia [11].

The normal physiological role of aSyn is not fully understood. ASyn is expressed in the brain, and exists as a soluble intrinsically disordered monomer [12], in the presynaptic terminal of neurons [13]. The proposed physiological roles for aSyn at the presynapse are to modulate synaptic vesicle release; as a chaperone; to regulate synaptic plasticity and to modulate lipid, dopamine and glucose synthesis [14]. ASyn is implicated in PD because insoluble fibrillary aSyn has been identified in the Lewy body intracellular inclusions associated with the disease [15, 16], and because mutations in the SNCA gene which encodes aSyn correlate with familial PD.

A wide range of physical techniques can be used to better understand the role of amyloid proteins in neurodegenerative diseases. This work presents three techniques used to study these proteins in more detail 1) electrophysiology using MEAs [17, 18], 2) advanced fluorescence imaging [19, 20] and 3) FTIR [21, 22].

MEAs are arrays of electrodes onto which electrogenic cells (neurons or cardiomyocytes) are grown. The MEAs record the external potential generated when the cells fire action potentials [23]. MEAs have been used in studies related to AD, and specifically to see how amyloid-β modulates neuronal firing events [17, 24, 18]; to uncover synaptic changes in transgenic mouse models of AD [25]; for AD drug screening [26]; and as a diagnostic biomarker [27].

In fluorescence microscopy, fluorescent labels are targeted to specific organelles in a biological species, and imaged to create a spatial fluorescence map of the organelle. The use of confocal fluorescence microscopes allows a high resolution of $\sim$300 nm to be achieved, limited only by the diffraction of light. This technique has been used extensively to study amyloid proteins [28]. Fluorescence lifetime imaging microscopy (FLIM) [29] maps the lifetime of the fluorophore across the sample. It has been used in previous studies to map the aggregation state of amyloid proteins *in vitro* and in cell models [30].

Combining fluorescence imaging with electrophysiological recordings, will give the advantages of the high temporal resolution of MEA recordings linked to the high spatial resolution and mapping of the underlying cellular and molecular structures possible with the imaging techniques [31, 32]. This should open up a wealth of possible experiments in the

field of amyloid research. One problem that can be addressed is how the aggregation state of tau affects its propagation between neurons and neuronal electrophysiology. If fluorescently labelled tau is added to a neuronal cell culture, a spatial map of the location and aggregation state of tau can be obtained using FLIM. In combination with this, the effect of tau on neuronal signalling can be measured for 10s of neurons using a MEA. Combining these data will enable the testing of the hypothesis that neuronal stimulation increases the transfer of tau and enhances tau pathology [8, 33], whereas blocking neuronal stimulation decreases the tau transfer [9].

Most MEAs have opaque recording electrodes, so imaging cannot be combined with MEA recordings on an inverted microscope. However, transparent graphene electrodes are ideal for this application as they are electrically conductive, optically transparent, biocompatible and chemically stable [32]. Transparent graphene MEAs that have been previously fabricated were used in combination with widefield, confocal fluorescence and two-photon microscopy [34, 35] however, were not compatible with techniques like FLIM. In addition, the previously fabricated graphene MEAs could not be used on commercially available amplifiers, and therefore had a limited application in electrophysiology labs.

A complimentary understanding of amyloid proteins can be obtained from FTIR. FTIR is a vibrational absorbance spectroscopy used to gain structural information about a sample. It is commonly used to identify the secondary structure composition of proteins by looking at the amide vibrations and is ideal for examining misfolded proteins and amyloids *in vitro*. FTIR can be used to identify the presence of amyloids from their high β-sheet content [4], and can also distinguish between native β-sheet proteins and amyloid proteins [36]. FTIR analysis has been used to study amyloid-β [37, 21], tau [38] and aSyn [22, 39].

The motivation for this work was to develop and use physical techniques to better understand the role of amyloid proteins in neurodegenerative diseases such as AD and PD. The first technique developed was a transparent graphene MEA. This enabled MEA recordings to be combined with advanced imaging modalities which, combines the high temporal resolution of MEA recordings with the high spatial resolution and flexibility of fluorescence imaging. The second technique developed was FTIR spectroscopy, which was used to gain an understanding about the secondary structure of the proteins.

1.3 Main contributions

In this work, physical techniques was developed to better understand the role of amyloid proteins in neurodegenerative diseases. The main contributions from this work are summarised below.

- **Development of a transparent graphene microelectrode array.** Microelectrode arrays were a new technology to the lab and there was little experience of this technique at the start of this project. A graphene MEA was designed, fabricated, characterised and used with neuronal cell cultures. The unique features of this graphene MEA are as follows:
  - The use of a coverslip as the graphene MEA substrate, to enable compatibility with advanced imaging modalities like FLIM.
  - The identification of poly(methyl methacrylate) (PMMA) and Al_2O_3 as suitable encapsulation layers for a graphene MEA. Also, the use of PMMA as an encapsulation layer for recording voltage traces from firing neurons.
  - The design, fabrication and use of a graphene MEA with a commercial amplifier purchasable from Multichannel Systems.
  - Maskless lithographies were used for each patterning step, to enable customisable electrode geometries to be fabricated.
- **Comparison of the equivalent circuit models for graphene MEAs.** A comparison was made between the equivalent circuit models (ECMs) used in previous studies to describe the electrochemical impedance spectra (EIS) of graphene MEAs. Evidence was provided that the model $R1 + C2/(R2 + W)$, where R is a resistor, C a capacitor and W a Warburg element, fits the experimental data and is physically relevant.
- **Comparison of voltage traces between graphene electrodes and TiN electrodes.** The voltage traces recorded by the graphene electrodes were compared for the first time to voltage traces from commercially available TiN electrodes purchased from Multichannel Systems. The graphene electrodes had a similar signal to noise ratio to the TiN electrodes, and as high as similar graphene devices in previous studies.
- **Electrophysiological recordings in combination with advanced imaging.** The graphene MEA inserted in an amplifier could be easily mounted on an inverted microscope. FLIM was shown for the first time to be achievable for cells on a graphene MEA that voltage traces had been recorded from.
- **Fourier transform infrared spectroscopy of α-synuclein.** An analysis of the secondary structure of lyophilised monomeric aSyn at pH 7, pH 4 and with the addition of $CaCl_2$ was performed.

1.4 Thesis structure

In Chapter 2, a background to graphene MEAs is given. First an introduction to measuring neuronal electrophysiology and the available technologies to do this is given. Then MEAs are covered including the coupling between a neuron and an electrode, protocols for processing the recorded voltage traces, and the manufacturing of MEAs. This chapter focuses on the development of transparent MEAs, with graphene MEAs being the most promising technology in this area. Finally, an introduction to the material graphene is given.

Chapter 3 contains the background to each characterisation techniques used in this work. The materials characterisation techniques described are Raman spectroscopy, direct current (DC) testing, ultraviolet-visible (UV-vis) spectroscopy, electrochemical impedance spectroscopy and atomic force microscopy (AFM). The fluorescence microscopy techniques introduced are confocal microscopy and fluorescence lifetime imaging microscopy (FLIM). Finally, the use of FTIR to understand protein secondary structure is presented.

Chapter 4 describes the design and fabrication of a graphene MEA. It contains the constraints for building a MEA capable of combining electrophysiological recordings with advanced fluorescence imaging techniques on an inverted microscope. Each component of the graphene MEA (namely the substrate, electrode, connecting leads and encapsulation layer) is described, along with how they meet the constraints. A final design is proposed along with a fabrication protocol for manufacturing graphene MEAs.

The electrochemical impedance spectra of the fabricated graphene MEA are characterised in detail in Chapter 5. The electrical properties of the leads, encapsulation layer and graphene are first assessed. The experimental impedance spectra of graphene MEAs are presented and discussed. Then the ECMs used in previous graphene MEA studies are compared, and an ECM is chosen that fits the recorded data and makes physical sense. This is then used to identify device breakdown from the EIS spectrum.

After designing, fabricating and characterising the device, Chapter 6 presents the proof of concept for combining voltage trace recordings with advanced fluorescence imaging. Voltage traces are recorded from mouse neuronal cultures on a graphene MEA and compared to voltage traces obtained on a conventional opaque TiN MEA. Spike detection was performed on both devices to identify the neuronal action potentials. Following this, the imaging modalities widefield, confocal fluorescence and FLIM were shown on each material used to fabricate the graphene MEA. Finally, widefield, confocal and FLIM imaging were shown on the graphene MEA voltage traces had been recorded from.

In Chapter 7, the complimentary technique FTIR spectroscopy is used to analyse the secondary structure of monomeric aSyn. A protocol is presented to for how to obtain the secondary structure composition from a protein FTIR spectrum. The protocol is then

applied to understand the structure of monomeric aSyn in physiologically relevant *in vitro* environments.

Chapter 8 sets out the conclusions of this work.

Chapter 2

Background to graphene microelectrode arrays

The misfolding of amyloid proteins to form amyloid fibrils is implicated in Alzheimer's disease (AD) and Parkinson's disease (PD). To address how the location and aggregation state of amyloid proteins in neurons leads to electrophysiological changes in neurons, electrophysiological recordings should be combined with advanced fluorescence imaging. Since fluorescence microscopes are commonly built in an inverted setup this requires the fabrication of transparent microelectrode arrays (MEAs). Graphene MEAs were identified as a suitable technology to enable this.

In this chapter, the background to a graphene MEA is described. Neuronal electrophysiology is introduced with a description of the different technologies for recording and stimulating neurons. The technology developed in this thesis is a transparent graphene MEA. Therefore, MEAs are introduced, with a focus on the coupling between the neuron and electrode, and processing the recorded voltage traces. The different MEA electrode materials are then considered, with a focus on transparent electrodes, the most promising of which is graphene. The previously fabricated graphene MEAs are described and finally, the material graphene is introduced.

2.1 Electrophysiology of neurons

Electrophysiology is the study of cells which can generate and transmit electrical signals (neurons or cardiomyocytes). Electrophysiology can be studied across a range of length scales from single ion channels, to single cell activity, to network dynamics of hundreds of

neurons, to whole organ dynamics. This thesis focuses on the single cell to network level of understanding of neurons.

2.1.1 Neuronal action potentials

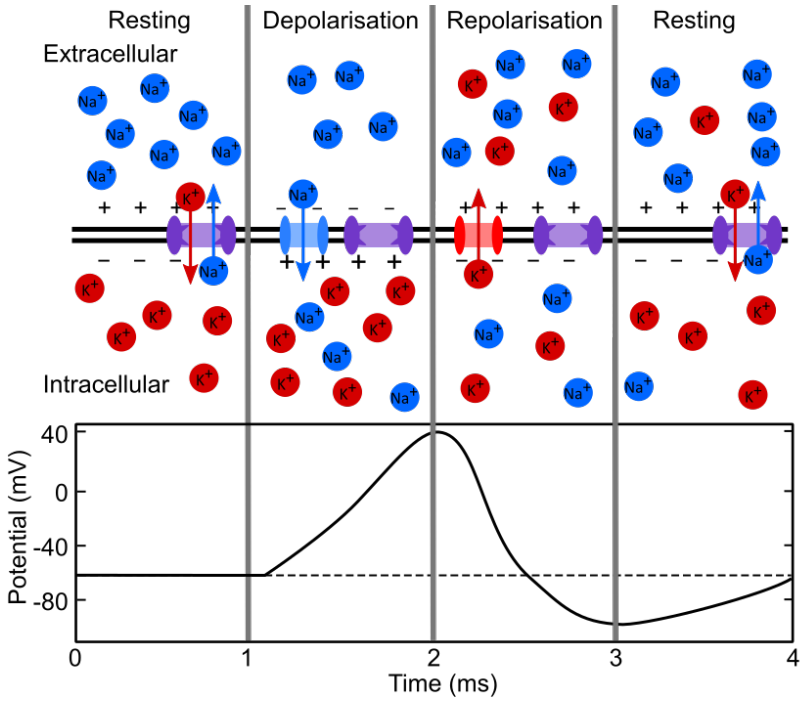

Fig. 2.1 Schematic showing the movement of Na^+ (blue) and K^+ (red) ions in a neuron during an action potential. The sodium-potassium ion pump in the cell membrane maintains its action throughout the action potential. When the action potential fires, selective ion channels open depolarising the cell with an influx of Na^+ ions, followed by an efflux of K^+ ions repolarising the cell.

Neurons are electrochemically excitable cells which transport and process information throughout the nervous system. A human brain has $\sim 10^{11}$ neuronal cells, each cell can have $\sim 10,000$ connections [40]. Each neuron has three major regions: the roughly spherical soma (5–20 µm in diameter); the dendrites (< 2 mm in length) and the axon (1–1000 mm long and 1–20 µm in diameter). These are contained within the cell membrane a (8-10 nm thick) hydrophobic phospholipid bilayer which acts as a barrier between the cytoplasm and the extracellular space [41]. Inside this neuronal membrane are many organelles, and the cytosol which is rich in Na^+, K^+, Ca^{2+} and Cl^- ions [42].

At rest, the intracellular space of a neuron is negatively charged with respect to the extracellular space, with a potential difference of ~ 65 mV. The potential difference is maintained by selective ion pumps in the cell membrane. The most major pump is the

sodium-potassium pump which works against the concentration gradient, pumping K^+ into the cell, and Na^+ and Ca^{2+} out of the cell. This gives a membrane capacitance of $0.9\,\mu F\,cm^{-1}$ [41].

When the neuron is depolarised beyond a threshold of 40–55 mV, an action potential fires (Figure 2.1). The action potential is initiated by opening of sodium channels in the cell membrane for ~ 1 ms. This results in an influx of Na^+ to the cell, reversing the membrane potential. The sodium channels then close and potassium channels open. K^+ flows out of the cell, re-polarising the membrane. After a small undershoot, the resting potential is restored by the sodium-potassium pumps [42].

The action potential is initiated at the axon hillock, where the axon protrudes from the soma. It propagates down the axon because a potential difference is induced between the excited and unexcited axonal regions. The potential difference leads to the generation of small local currents which stimulate unexcited areas further along the axon, causing an action potential to be transmitted. The refractory period of ~ 1 ms at the end of an action potential before the neuron can fire again, ensures the action potential propagates in a single direction. When the action potential reaches the end of the neuron, chemical neurotransmitters are released from vesicles in the axon terminal. The neurotransmitters diffuse across the 10–50 nm synaptic cleft before binding to a receptor at the post synapse. The receiving postsynaptic cell responds to the neurotransmitter by either depolarising or hyperpolarising its cell membrane and thus increasing or decreasing the likelihood of the recipient cell firing. This propagation mechanism ensures that the action potential signal has a fixed size and duration over the entire axon length therefore, information is transmitted between neurons via the frequency and pattern of the received action potentials [42].

2.1.2 Technologies for recording action potentials

A number of technologies exist which can make electrophysiological measurements with single cell resolution. These include intracellular sharp or patch electrodes; extracellular MEAs; optical imaging with fluorescence indicators or genetically encoded molecular probes; or techniques based on magnetism [43].

Intracellular recordings measure the potential difference between the intracellular and extracellular space. This is achieved by either patching to the cell membrane using a thin glass tube containing a wire and filled with saline solution [44, 45], or through inserting sharp electrodes into the cell [46]. The recorded intracellular action potentials show a positive depolarisation period followed by a negative repolarisation period, are 10s mV in amplitude and last <2 ms. Since the electrode has an extremely good coupling with the cell, a very high SNR (signal to noise ratio) can be obtained. The high SNR combined with a high temporal

resolution enables the detection of both action potentials and sub-threshold potentials across the whole dynamic range of the cell [45]. The major drawbacks of intracellular electrodes however, is the cell is perturbed when electrodes are inserted which can change the pattern of firing [47] and limits the lifetime of the recordings to minutes or hours. Additionally, this is a low throughput technique since insertion of electrodes is achieved on a cell-by-cell basis and requires large micromanipulators to insert the electrodes [43].

Extracellular recordings can be made when the cells sit on top of the electrodes and the potential between the extracellular space, and a reference electrode is measured. Many extracellular electrodes can be placed on a single device, creating MEAs which enable the simultaneous recording of large populations of cells. Since the extracellular electrodes do not penetrate the cells, they can be used over long time periods up to months. the extracellular recordings of action potentials are the convolution of signals [48] closer than $\sim 100\,\mu m$ to the electrode [49]. The local field potentials (LFPs, $< 300\,Hz$) recorded are the superposition of the average fluctuations in voltage arising from the extracellular ionic current around the electrode [47]. The fast extracellular action potentials (or spikes, 300–3000 Hz) have a spike amplitude of $10s\,\mu V$ and a low SNR [43]. In addition, the spatial resolution of MEA electrodes is conventionally limited to $\sim 10\,\mu m$ by the size of the recording electrode.

Another technique with single cell resolution is optical electrophysiology, where a reporter molecule translates the electrical potential (or a derivative of this) into to an optical signal which is often a change in fluorescence. The most common optical techniques are voltage sensitive dyes, genetically encoded fluorescent dyes and calcium sensors [50]. The optical techniques have advantages that they do not require physical contact with the cells; can achieve a high spatial resolution; can probe many neurons simultaneously and can target specific cellular and sub-cellular sites by genetic encoding. However, the techniques traditionally suffer from a low photon count, and slow change in fluorescence which cannot capture the fast ~ 1 ms action potentials [31].

Electrophysiology based on magnetism, uses the changes in magnetic field generated by ionic flow to measure electrical activity in cells. Traditional techniques such as functional magnetic resonance imaging, electroencephalography, electrocorticography and magnetoencephalography [43] are used with large neuronal populations and low spatial resolutions of $\sim$mm's, or require bulky detectors [51]. More recently, nitrogen-vacancy quantum defects in diamond has enabled the time-dependent magnetic fields produced by single-neuron action potentials to be measured [52]. Magnetic sensing has the advantages of being noninvasive, label-free, and able to detect neuronal activity through tissue and whole organisms. However, the SNR achieved is much lower than for other electrophysiological techniques [51].

2.1.3 Technologies for stimulating neurons

Spontaneous electrical activity can be recorded from cultured neurons, however it can be challenging to understand the origins of the measured spikes, and the propagation of the signal though the network. Artificial external stimulation of identified cells can provide a way to assess the response of the system. External stimulation can be achieved using chemical, electrical or optical techniques. Whereas for recording techniques, the main consideration is noise reduction, for stimulation the main consideration is to avoid electrode or tissue damage.

Chemical stimulation can be used to depolarise or hyperpolarise the neuron and elicit or prevent an action potential being fired. This is performed by applying salts like KCl [53], or neurotransmitters like glutamate [54]. The applied chemical can either be added through a bath application, affecting the whole cell culture [55], or it can be applied locally to specific areas using puffer pipettes or microfluidics [56].

Electrical stimulation occurs by intra- or extra-cellular charge injection. The charges are delivered from the electrode and cause a buildup of membrane potential and activate voltage sensitive ions under a sufficiently high field. The charges used are typically 0.1-1mC$\,$cm^{-1} in pulses of 0.1-1 ms in length. Individual neurons can be targeted using intracellular electrodes [57], and networks of neurons can be targeted over long time scales using external MEAs [58]. The electrical stimulation techniques however, are not suitable for inhibiting action potentials, and can damage the cells at high stimulation intensities.

Neurons can also be stimulated using optical techniques via optogenetics, or light induced chemical stimulation. Optogenetic techniques use proteins which can modulate neuronal activity upon exposure to light, for example channelrhodopsin, light-gated ionotropic glutamate receptor or halorhodopsin [31]. Alternatively, chemical species can be stored in inert cages and locally released upon exposure to light [59]. The optical techniques have the advantages of being able to stimulate or inhibit with spatial, temporal and genetic specificity.

2.2 Microelectrode arrays

MEAs are an assembly of external electrodes, of a similar size to the cells they are recording from. The first MEAs were developed by Gross in 1979 [23] and Pine in 1980 [60]. They are now in widespread use in neuroscience research, with many companies offering either the hardware or software associated with MEAs including Alpha MED Sciences, Japan; Axion Biosystems, USA; Qwane Biosciences, Switzerland; 3-Brain, Switzerland; Multichannel Systems, Germany; Plexon Inc., USA; Tucker-Davis Technologies, USA [61].

2.2.1 Applications of microelectrode arrays

External electrode arrays can be used in fundamental research *in vivo* as implants [32], *in vitro* with cell cultures [17] and with brain slices [62]. The external electrodes also find regular clinical use today in pacemakers, cochlear implants [40] and to treat epilepsy. They also show promise as deep brain simulators in PD [63] and in prosthetics for paraplegic patients [64]. Some *in vivo* applications include drug discovery [65], toxicity studies [61], brain-computer interfacing [64], understanding neuronal function [66], and understanding neuronal network dynamics [67]. Electrophysiological studies have also been applied to investigate AD, specifically to see how amyloid-β modulates neuronal firing events [17, 24, 18]; to uncover synaptic changes in transgenic mouse models of AD [25]; for AD drug screening [26]; and as a diagnostic biomarker [27].

One system of interest related to the study of amyloids is the propagation of tau protein between neurons. Tau is an axonal microtubule associated protein found in neurons, it stabilises the microtubules required for structure and transport [5]. The progression of clinical AD correlates with the hyperphosphorylation, aggregation and spreading of tau across the brain. Tau pathology in AD patients starts in the entorhinal cortex and spreads across the brain anatomically in a defined pattern which correlates with the cognitive decline observed in clinical AD [68, 7]. The mechanism by which tau is transferred between cells however is disputed, and could be due to secretion [8], trans-synaptic spread [9], tunnelling nanotubes [10] or microglia [11]. Neuronal stimulation leads to an increase in tau spreading and potentially to an increase in aggregation (preliminary data found in our lab). The increase in tau aggregation can be measured using fluorescence lifetime imaging microscopy (FLIM) [6].

2.2.2 Lumped circuit model of the neuron-electrode interface

The neuron adheres to the electrode via electrostatic and chemical interactions. A lumped circuit model (LCM) can be used to describe the neuron-electrode interface using linear electrical components. The interface can be divided into three sections: 1) neuron to electrolyte conduction; 2) volume conduction through the electrolyte, across the cleft and 3) electrolyte to electrode conduction (Figure 2.2). Additionally, the recording electronics are represented in this model by the wire resistance R_{lead}, shunt capacitance C_{shunt} through the encapsulation layer, and the amplifier. The wire resistance, can be broken down into the resistances of each of the materials, plus the contact resistance between each of the materials.

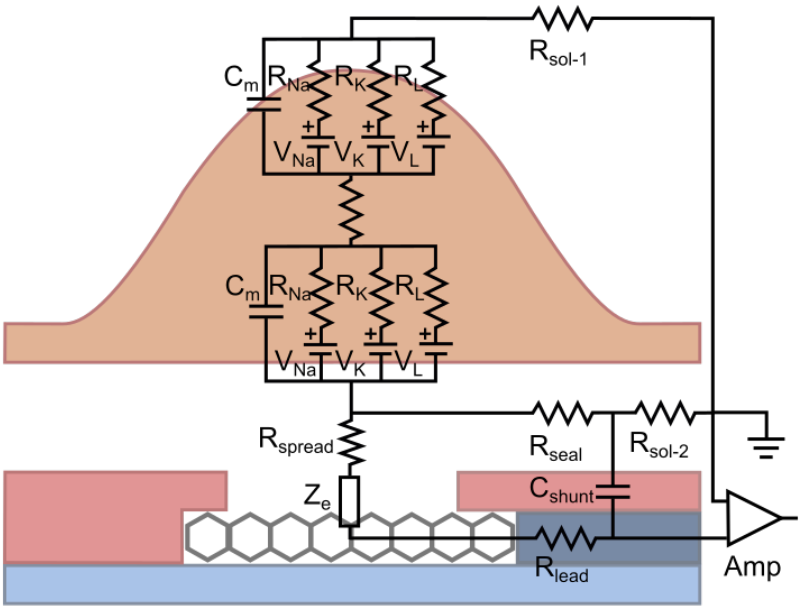

Fig. 2.2 Lumped circuit model using linear circuit elements to describe the electrical properties of a neuron (orange) coupled to a graphene electrode through a saline cleft. The device contains a substrate (light blue), graphene electrode (black hexagon), connecting lead (dark blue) and encapsulation layer (red).

2.2.2.1 Neuron-electrolyte interface

The Hodgkin-Huxley model (Figure 2.3) represents the neuron-electrolyte behaviour by describing the ionic currents with linear electrical components. The cell membrane has a capacitance, C_m, and a current $i_c = C_m(dV_m/dt)$, where V_m is the potential across the cell membrane and t is time. The voltage gated ion channels are dependent on membrane potential, described by variable resistors with conductance $g_q = 1/R_q$, and currents $i_q = g_q V_q$ where q =Na, K. All other ions are collectively described by a leakage conductance g_L, and potential V_L.

The total membrane current is the sum of capacitive and ionic currents, and can be solved for a uniformly behaving axon as:

$$i_m = i_c + i_{Na} + i_K + i_L \tag{2.1}$$

$$i_m = C_m(dV_m/dt) + g_{Na}(V_m - V_{Na}) + g_K(V_m - V_K) + g_L(V_m - V_L) \tag{2.2}$$

where V_q are the equilibrium potentials for the ions and V_L is the potential that gives zero leakage current [69]. This model can be applied to an action potential as follows. At rest, $g_k >> g_{Na}$ so the potential lies near V_K. When the membrane is depolarised, g_{Na} greatly increases, leading the potential towards V_{Na}, which drops again when the ion channels close

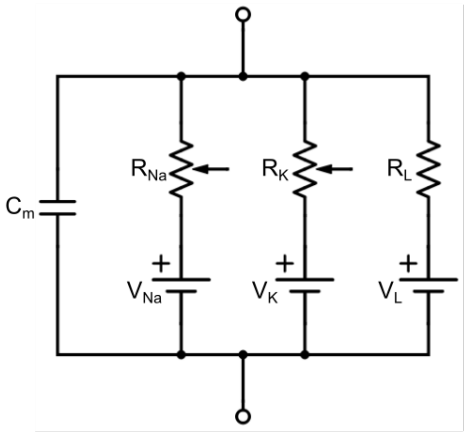

Fig. 2.3 The Hodgkin-Huxley model describing the neuronal cell membrane potential using linear electrical elements. C_m is the cell membrane capacitance, R_n and E_n are the ion channels with $n = \mathrm{Na}, \mathrm{K}$ for the voltage gated channels and $n =$L describing all other ions.

and g_{Na} decreases again. When the sodium ion channels close, potassium channels open, g_K greatly increases, leading the potential back to near V_K.

2.2.2.2 Conduction through the electrolyte

The neuron-electrode cleft is 20–100 nm across [40, 70], and filled with electrolyte. The diffusion of ions across the cleft gap is described by the spreading resistance R_{spread}, solution resistance R_{sol}, seal resistance R_{seal} and Helmholtz-diffuse capacitance C_{hd} [71].

The spreading resistance is caused by the high current density close to the small electrode surface [72], described for a circular electrode as:

$$R_{spread} = \frac{\rho_s}{4r} \tag{2.3}$$

where ρ_s is the resistivity of the solution, and r is the radius of the electrode [73]. The spreading resistance decreases with decreased electrolyte resistivity, and increased electrode size. An electrode with a diameter of 30 µm in phosphate buffered saline solution, has a spreading resistance of 4.7–5.9 kΩ, which is assumed to be negligible compared to the electrode-electrolyte resistance [72].

The sealing resistance describes the ionic current that leaks out of the neuron-electrode cleft. The SNR can be increased by a high sealing resistance which gives a low leakage current [47]. The simplest mathematical description of the sealing resistance is

$$R_{seal} = \frac{\rho_s}{l}.\delta \tag{2.4}$$

where ρ_s is the solution resistivity, l is the neuron-electrode distance and δ is a coefficient describing the proportion of the electrode area covered by the cell. Sealing resistance increases with a decreased neuron-electrode distance, and an increased coverage of the electrode by the neuron. A maximum SNR occurs when the neuron covers and binds tightly to the electrode [72]. Adhesion promoting proteins such as laminin, fibronectin, L1Ig6 and poly-L-lysine are used to increase R_{seal} [40]. By monitoring the changes in R_{seal} over time, changes to the cell adhesion can be monitored [72].

2.2.2.3 Electrolyte to electrode interface

The cleft-electrode interface can be described in isolation from the neuronal effects by the electrode impedance Z_e. A Randles model is often used which combines a resistor R_e in parallel with a capacitor C_e, in series with the spreading resistance R_{spread} [74]. The capacitive charging describes how the ion distribution in the cleft causes electron redistribution in the electrical double layer and the electrode. The resistive component describes the Faradaic electrochemical reactions occurring at the electrode [40]. At low frequencies, the capacitive effects dominate whereas at high frequencies the resistive Faradaic effects dominate [75].

The electrical double layer is described by the Helmholtz-diffuse capacitance formed by the distribution of ions around the interface. At the cell-electrolyte interface, the inner Helmholtz layer or hydration sheath is a monolayer of highly orientated water molecules. This is followed by the outer Helmholtz plane, a layer of ions. The ion concentration decays with distance from the electrode forming the Gouy-Chapman diffuse-charge layer [76]. C_{hd} is the series capacitance of the Helmholtz double layer and the Guoy-Chapman capacitance's.

The simple resistor-capacitor model can guide the choice of material used for the electrode. Ideally polarisable electrodes have an infinite Faradaic resistance, and are modelled by a capacitor, whereas ideally non-polarisable electrodes have zero Faradaic resistance. Ideally, stimulating electrodes are highly polarisable electrodes which can accommodate a large amount of injected charge through the electrical double layer before starting Faradaic reactions. An increased capacitance generally leads to a reduction in noise levels alongside a wider voltage window for safe stimulation [77]. Physical electrode materials behave in either a predominantly Faradaic, or capacitive manner, but will exhibit both behaviours [77]. Examples of predominantly Faradaic materials include gold, platinum, titanium, and iridium, iridium oxide, stainless steel, and semiconductors such as silicon, poly(3,4-ethylenedioxythiophene)-poly(styrenesulfonate) (PEDOT). Predominantly capacitive materials include titanium nitride, tantalum-tantalum oxide and carbon nanotubes [63, 77].

2.2.3 Processing voltage traces

MEAs measure the change in the extracellular electric field caused by ionic flows from the neurons closest to the electrode. The actual sign, magnitude and shape of the detected potential depend strongly on the coupling of the cells through the electrode-neuron interface. Measured voltage traces generally consist of a low frequency background potential with fast spikes superimposed on this. Low frequency LFP (<300 Hz) variations are generated by the synchronised synaptic currents across many neurons and through the formation of dipoles. High frequency ($\sim$ 1 kHz) spikes are assumed to be caused by Na^+ and K^+ transients from action potentials. The measured spikes have an amplitude of 10–100s µV, last $<$ 2 ms and vary in morphology [49].

2.2.3.1 Electronic noise

Obtaining information from a MEA voltage trace requires separating the spikes from the background LFP and noise. The background noise can come from many sources: the biological environment, which includes the action potentials of distant cells, subthreshold events and synaptic activity; noise contributions from the amplifier; and also the electronic noise.

The electronic noise in an MEA arises from the electrode resistance and the electrode-electrolyte interface. The electrode resistance, R (or real impedance, $Re(Z)$) of the electrode and leads creates the Johnson, or white noise, which has a flat spectrum. For a system with a resistance, R, and bandwidth, Δf, the root mean square (RMS) resistive component of the Johnson noise V_{nJ} is:

$$V_{nJ} = \sqrt{4k_B T R \Delta f} \tag{2.5}$$

where k_B is the Boltzmann constant and T is temperature. Plot 2.4 shows how the RMS square of the resistive noise varies with the device resistance and the bandwidth of the recording, eg. a device with 100 kΩ resistance and a bandwidth of 10 kHz has a noise of 4.0 µV. Although the simple relationship between decreased electrode impedance and increased SNR does not necessarily hold quantitatively [78], having a low electrode resistance is important to minimise the thermal noise.

Other types of electrical noise include the shot noise, $1/f$ noise and 50 Hz noise. The shot noise, i_{ns}, occurs because current is the quantised flow of individual electrons and is equal to $i_{ns} = \sqrt{2ei_{dc}\Delta f}$ where e is the electron charge and i_{dc} is the dc current. The $1/f$ noise, or flicker noise has a number of origins, normally related to the current (for a MEA the electrode-electrolyte interface at <10 Hz). Interference noise at 50 Hz comes from the hum associated with alternating current at the frequency of the mains electricity. The different

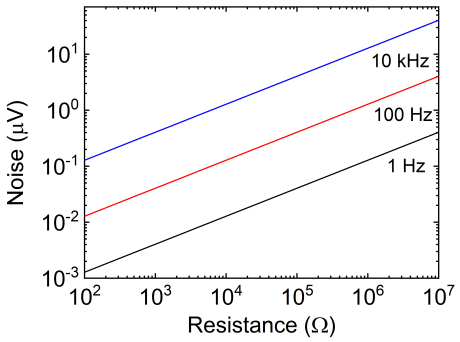

Fig. 2.4 Plot showing how the root mean square of the resistive noise varies with the device resistance and the bandwidth of the recording.

noise components add to give a total noise in the recorded voltage of $V_{nT} = \sqrt{V_{n1}^2 + V_{n2}^2}$, where V_{n1} and V_{n2} are different noise components [79].

2.2.3.2 Signal to noise ratio

If both the amplitude of the signal and the noise are known, the SNR can be calculated as:

$$SNR = \left(\frac{V_s}{V_n}\right) \tag{2.6}$$

where V_s is the signal, V_n is the noise, or in dB as:

$$SNR(dB) = 10\log_{10}\left(\frac{P_s}{P_n}\right) = 20\log_{10}\left(\frac{V_s}{V_n}\right) \tag{2.7}$$

where P_s and P_n are the power of the signal and noise, respectively.

In MEAs the signal is the peak-to-peak voltage V_{p-p}, and the noise can be calculated as the RMS noise V_{rms}, [80], $2 \times V_{rms}$ [32] (to account for the positive and negative amplitudes), or the mean absolute deviation (MAD), V_{MAD} [81]. The RMS can be calculated as:

$$V_{rms} = \sqrt{\frac{1}{N}\sum_{q=1}^{N}|V_q|^2} \tag{2.8}$$

where N is the number of measurements, q is an index and V_q is the voltage amplitude. The MAD can be calculated as:

$$V_{MAD} = \frac{1}{N}\sum_{q=1}^{N}|V_q - \bar{V}| \tag{2.9}$$

where $\bar{V}$ is the mean voltage.

2.2.3.3 Processing voltage traces

MEA recordings contain a combination of LFPs (< 300 Hz) and action potentials (300–3000 Hz). To a first approximation, the LFPs can be considered as biological noise, and just the spikes are considered. Spike analysis is performed in three steps: filtering the raw data, detecting spikes and sorting the spikes. Firstly, the raw data is band pass filtered at 300–3000 Hz to remove the low frequency LFP and noise. Secondly, spike detection is performed by amplitude thresholding, two-point procedures or template matching. With amplitude thresholding, the most common detection method, a firing event is identified when the measured potential is greater than a set threshold value, the threshold is set to a multiple (often $5\times$) of the baseline noise level (calculated from the standard deviation) [82, 83]. Finally, the spikes can be classified and grouped by shape using principal component analysis, or wavelet transformation. Ideally, this will allow the identification of distinct neurons, which have identifiably different spike shapes [84].

2.2.4 Transparent microelectrode arrays

2.2.4.1 Conventional electrode materials

Many materials have been used as the electrodes in a MEA. The external electrodes were initially fabricated from metals like tungsten and stainless steel which achieved low SNRs, and limited biocompatibility [40]. Through a combination of materials engineering, and an improved understanding of the neuron-electrode coupling the electrodes have been improved. The most implemented improvement is to coat a conventional planar electrode with TiN, electroplated platinum [85] or carbon nanotubes [86] which reduce the electrode impedance, increase the SNR, and provide rougher surface for cell adhesion. More recent work has shown the benefits of conductive polymers like PEDOT which is soft, flexible and combines both electronic and ionic conductivity [87]. Also, nanostructuring of the electrodes into penetrating wires [88], nanowires [89], kinked wires [46], or mushrooms [43] can increase the SNR by increasing the area in contact with the cells. In addition to the underlying material, adhesion promoting molecules are commonly coated on the electrodes, increase the neuron-electrode adhesion which increases the SNR by increasing R_{seal}. Adhesion promoting polymers include poly-lysine, poly(ethyleneimine) (PEI), poly(N-isopropylacrylamide) [77], polyornithine, laminin molecules and nitrocellulose.

In parallel to improving the SNR by materials engineering, work has been undertaken to increase the spatial resolution obtainable from the MEAs and to provide on-chip amplification

of the signal. High density MEAs can have 10,000s of electrodes *in vitro* enabling a sub-neuron resolution to be achieved [90]. On-chip amplification of the signal can be achieved using field effect transistors (FET). In a FET, the conductivity between the source and drain is modulated by the electric field experienced by the gate, which can be modulated by ionic current from the neuron [91]. FETs have the advantage that they can be scaled down to 10 nm [89] without losing band width, no material is exchanged with the cell, and they do not depend on the interface impedance [46]. However, two leads per electrode are needed to measure from a FET.

2.2.4.2 Transparent microelectrode arrays

The advantages of MEAs over other recording techniques is their high temporal resolution and the ability to record from multiple sites in a neuronal network simultaneously. This makes MEAs ideal for: studying the LFP at different locations in the same sample concurrently to probe the spatio-temporal dynamics of a network; reducing the time required for an experiment by recording simultaneously at multiple sites; providing a statistical description of the system; and monitoring changes in activity over long time periods up to months [65]. In contrast, optical imaging techniques allow high spatial resolution across a large area to be achieved, and can enable the targeting and imaging of sub-cellular components. The advantages of MEAs can be combined with the advantages of optical techniques by developing transparent MEAs. This enables the electrophysiological function of the nervous system to be linked to its underlying cellular and molecular structures [31] and enables the high temporal resolution of MEA recordings to be combined with the high spatial resolution of the imaging techniques.

To fabricate a transparent MEA, the substrate, electrodes and encapsulation layer must all be transparent. Transparent substrates have been regularly used like glass [92] or polymers like SU-8 [80], polyimide [32] , parylene C [34] or polyethylene terephthalate (PET) [93]. The use of optically transparent insulating layers such as Si_3N_4 [92], SU-8 [92], Parylene C [34], polyimide [94] is also routine. However, finding suitable transparent conductors to interface with the neurons is more challenging.

The most common transparent conductor indium tin oxide (ITO) has been used in MEAs since 1985 [95], and has been combined with fluorescence imaging [85]. ITO is 87–90% transparent in the visible range and is conductive in its fully reduced state. The electrodes are stable under warm saline solution for at least 8 months [96], and can record action potentials for at least 25 days [97]. However, under repeated stimulation trains, oxidation of the electrodes occurs which results in a loss of transparency and an increased impedance (Figure 2.5a,b) [96]. The ITO electrodes are therefore typically coated with an opaque layer

of gold [96], platinum black [98] or TiN [92]. This ensures that the connecting leads and therefore the majority of the devices is transparent, however the crucial recording electrodes are opaque.

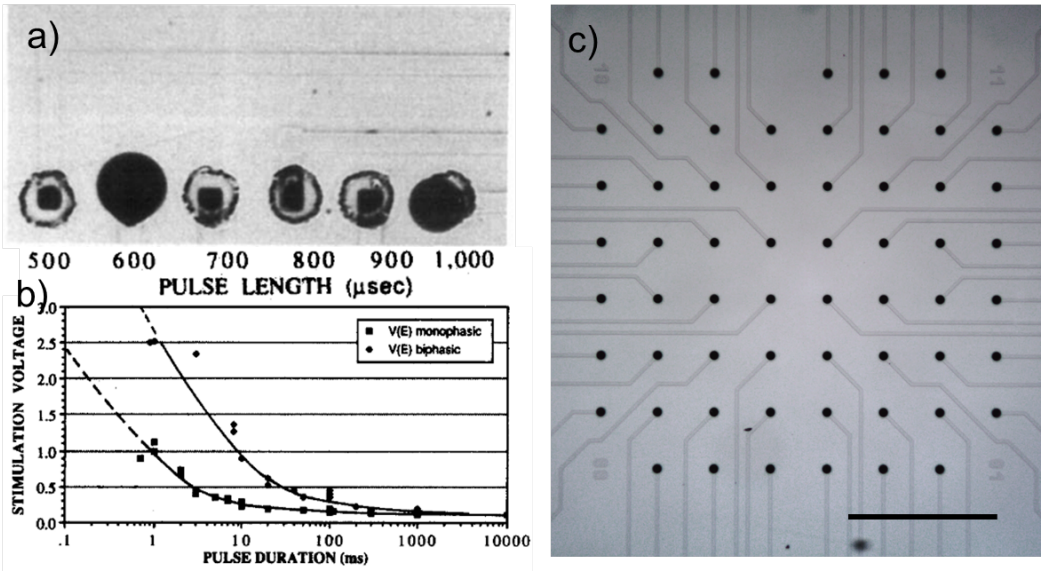

Fig. 2.5 Repeated stimulation using an ITO electrode in saline solution leads to oxidation of the material resulting in a loss in transparency and decrease in conductivity. a) A reduction in transparency revealing the electrode oxidation under biphasic stimulation of 3 V, 200 Hz for 60s. b) The breakdown voltage for monophasic and biphasic voltage pulses. Plot reproduced from [96]. c) An ITO MEA purchased from Multichannel Systems showing the opaque TiN coating used on the recording electrodes, scale bar 500 µm.

A number of other transparent conductors have been used in MEAs to stimulate or record neuronal signals. These include pillars of the wide-bandgap semiconductor ZnO, deinsulated at the top and coated with ITO [99], which will break down if used to stimulate. Stimulation, but not recording can be achieved using layered SnO_2 and hydrogenated amorphous silicon [100]. Recordings have been made with 40 % transparent carbon nanotube planar electrodes [101]. Also, FETs with transparent channels made from silicon nanowires [102], N,N'-ditridecylperylene-3,4,9,10-tetracarboxylic diimide [103] and 6,13-bis(triisopropylsilylethynyl)pentacene [104] have been used, however in these cases, opaque source and drain contacts are used, making much of the field of view opaque. By far, however the most successful transparent electrode is graphene [32, 34, 80, 81, 93, 94, 105].

2.2.4.3 Graphene microelectrode arrays

The successful recording of action potentials using arrays of passive graphene electrodes was first shown in 2013 [80]. Graphene is a transparent conductor made of sp^2 hybridised

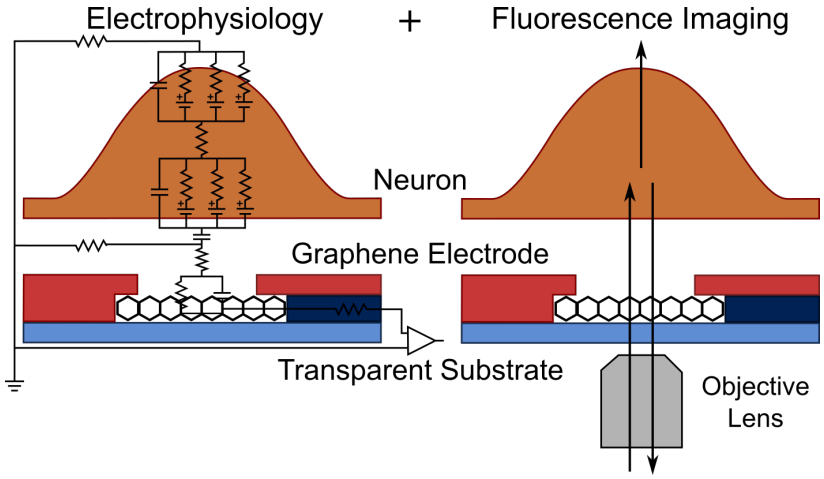

Fig. 2.6 A schematic showing how transparent external graphene electrodes enable the concurrent measurement of electrophysiological recordings and fluorescence microscopy on an inverted microscope. The neuron is shown in orange, the encapsulation layer in red, the graphene electrode with black hexagons, the connecting layers in dark blue and substrate in light blue.

two-dimensional carbon. If fabricated on a transparent substrate such as polyimide [32] or parylene C [34], graphene has a transmission of 80–90%, with each graphene monolayer reducing the transmission by 2.3% over a broad spectral range of 400–750 nm [106]. The material graphene is more fully introduced later in Section 2.3.

Graphene has been used to record neuronal action potentials in two main device architectures, as FETs and as passive electrodes. As active devices, FETs provide onsite amplification of the neuronal signal, however suffer from the necessity of having opaque source and drain contacts [107]. This work therefore focuses on passive graphene electrodes. Table 2.1 gives an overview of the transparent graphene electrodes which have been fabricated and successfully used to measure neuronal action potentials.

The successful recording from external graphene electrodes has been shown for neuronal cell cultures, cardiomyocyte cell cultures [81], rat cortices [32, 34, 94] and mouse cortices [105]. Since the graphene is flexible, the microelectrodes can be fabricated on flexible polymers, which is beneficial for implantation into the brain. The graphene electrodes have a highly capacitive nature, with changes in the local dielectric environment modulate the capacitance and the graphene carrier density. The high interfacial capacitance reduces the noise from resistive charge transfer, giving an overall low noise which is dominated by the 1/f and 60 Hz noise [32]. This has enabled a high SNR of $48 \pm 26\,\mu V$ to be recorded for bursting neurons from embryonic rats, using electrodes with diameters of 20 µm [81]. A number of modifications from single layer-untreated graphene have been proposed to reduce

the electrode impedance and enhance the SNR. Modifications to the graphene include steam plasma [80], doping with nitric acid [32], four graphene layers [34], structuring the films to increase the surface area [108] and enhanced cleaning methods [105]. It is however, unclear which of these techniques increase the SNR due to the wide range of fabrication techniques and biological systems that have been tested.

Stimulating neurons using monolayer graphene electrodes has proved difficult. Porous carbon electrodes fabricated by the pyrolysis of polyimide have been shown to successfully stimulate the motor cortex of a rat [109]. Additionally, four layer graphene electrodes have successfully stimulated the somatosensory cortex of a mouse in combination with fluorescence microscopy [110]. It is suggested by some that monolayer graphene electrodes show some promise for electrical stimulation with $0.31\,\mathrm{mm}^2$ electrodes having a charge injection capacity of $0.8\,\mathrm{mC\,cm}^{-2}$ [111]. However, monolayer graphene electrodes have not yet been used for electrical stimulation, which is likely due to their high quantum capacitance. The graphene electrodes have however, enabled optogenetic stimulation through the recording electrode. Thy1::ChR2 mice express channel rhodopsin which make the neurons susceptible to excitation with 460–470 nm light. The Thy1::ChR2 mouse neurons have been successfully excited through both monolayer [112, 93] and four-layer graphene electrodes [34].

2.2.4.4 Imaging with microelectrode array recordings

The transparency of the graphene electrode has enabled multiple fluorescence imaging modalities to be combined with the electrophysiological readout (Figure 2.6). Cells have been visualised through the electrode using bright field [32], wide field fluorescence [34, 81], confocal imaging [32], two photon microscopy [32, 105] and optical coherence tomography (OCT) [32, 105]. Some dyes that have been used to image through graphene include β III tubulin as a cytoskeletal marker and 4',6-diamidino-2-phenylindole (DAPI) as a nuclear marker [113, 114]; fluorescein isothiocyanate (FITC) as a vasculature marker [34, 112]; Microtubule-associated protein-2 (MAP-2) as a microtubule marker; SMI 321 as an axonal marker and propidium iodide to reveal cell death. For more information about the imaging techniques see section 3.2. The external electrode measurements have also been combined with intracellular fluorescent calcium imaging, enabling the high temporal resolution of the graphene electrodes to capture the high-frequency bursting activity, and the high spatial resolution of the calcium imaging to capture sub-cellular information [32].

Optical electrophysiology using calcium imaging has also been combined with voltage trace recordings using transparent graphene MEAs in hippocampal slices [32] and a live mouse dorsal cortex [115]. Electrical recordings were made using a $50 \times 50\,\mu\mathrm{m}^2$ graphene electrode, and calcium imaging was performed using the fluorescence intensity of oregon

green BAPTA-1 (OGB-1, BAPTA is 1,2-bio(o-aminophenoxy) ethane-N,N,N',N'-tetraacetic acid) on a confocal and a two-photon microscope [32, 105]. The techniques are complimentary, with both techniques simultaneously probing multiple neurons with single (or few neuron) resolution. The electrical recordings give a high temporal resolution of ~ 1 ms, and the optical methods giving a high spatial resolution of ~ 200 nm.

In conventional metal MEAs, light shone on the metal electrode elicits an additional peak in the voltage trace which can interfere with spike recordings. The peak is caused by the Becquerel (or photovoltaic) effect, which occurs when light is shone on electrically conductive materials in ionic solutions [116]. The artefact can vary in size depending on the frequency and duration of the light stimulus. It is agreed that the graphene electrodes elicit a smaller artifact than metal electrodes, and some devices do not show the artefact at all [34, 32, 93]. These differences are likely due to the cleanliness of the graphene, with a four step cleaning process being sufficient to remove the artefact for light pulses with powers up to 60 mW [105].

Table 2.1 Transparent graphene passive electrodes for sensing neuronal action potentials.

	Substrate	Graphene treatment	Encapsulation layer	Number of electrodes	Electrode size (μm^2)	Biological system	RMS noise (μV)	SNR*	Fluorescence imaging techniques
Chen *et al.* 2013 [80]	SU8	-	PDMS	1	13500	Crayfish abdominal nerve cord	-	5.2 ± 0.7	-
Chen *et al.* 2013 [80]	SU8	-	PDMS	1	13500	Zebrafish heart	7.64	4.7 ± 0.5	-
Chen *et al.* 2013 [80]	SU8	Steam plasma	PDMS	1	13500	Crayfish abdominal nerve cord	3.3	12.3 ± 0.4	-
Chen *et al.* 2013 [80]	SU8	Steam plasma	PDMS	1	13500	Zebrafish heart	4.2	12.2 ± 0.5	-
Kuzum *et al.* 2014 [32]	Polyimide	Nitric acid doping	SU8	8	2500	Implant rat cortex	31.0 ± 1.2	40.8	Confocal, two photon
Park *et al.* 2014 [34]	Parylene C	Four layer graphene	Parylene C	16	49087	Implant rat cortex	-	-	Wide field
Du *et al.* 2015 [94]	Quartz	-	Polyimide	60	314	Embryonic rat cortex	15 ± 5	5.2 ± 0.6	-
Kireev *et al.* 2017 [81]	SiO_2	-	Polyimide	64	79	HL-1 cardiomyocyte	10 ± 5**	45 ± 22	-
Kireev *et al.* 2017 [81]	SiO_2	-	Polyimide	64	314	HL-1 cardiomyocyte	11 ± 7**	35 ± 12	Wide field
Kireev *et al.* 2017 [81]	SiO_2	-	Polyimide	64	314	Embryonic rat neuron	11 ± 7**	16 ± 6	Wide field
Kireev *et al.* 2017 [81]	SiO_2	-	Polyimide	64	314	Embryonic rat neuron, bursting	11 ± 7**	48 ± 26	-
Liu *et al.* 2017 [93]	PET	-	SU8	16	10000	Hippocampal slice	-	-	Wide field
Thunemann *et al.* 2018 [105]	PET	Four step cleaning	SU8	16	10000	Implant mouse cortex	10	-	Wide field, two photon

* Signal to noise ratio calculated as $V_{p-p}/(2 \times V_{rms})$ where V_{p-p} is the peak-to-peak spike voltage and V_{rms} is the root mean square of the recorded signal.

**Noise calculated as the mean absolute deviation (MAD). PDMS (Polydimethylsiloxane), PET (polyethylene terephthalate)

2.3 Graphene

As a very promising material for fabricating transparent MEAs, graphene is described in more detail. Graphene was first isolated in 2004 [117] and is a single layer of carbon atoms, arranged in a honeycomb lattice, with each atom attached via sp^2 hybridised bonds to the neighbouring carbon atoms. Graphene has many unique materials properties and is likely to find technological applications when these properties are combined resulting in both improvements to existing products and the creation of new products. Some fields where graphene shows promise are electronic devices, spintronics, photonics, optoelectronics, sensors, flexible electronics, energy storage and energy conversion. Graphene also has potential biomedical applications in bioelectronics, biosensors, imaging, diagnosis, targeted drug delivery and gene transfection [118].

2.3.1 Production and transfer of graphene

Graphene can be produced by a number of methods including micromechanical exfoliation, chemical vapour deposition (CVD), anodic bonding, laser ablation, photoexfoliation, liquid phase exfoliation, growth on SiC, growth on metals by precipitation, molecular beam epitaxy, atomic layer epitaxy, heat driven conversion of carbon or chemical synthesis [118].

2.3.1.1 Micromechanical exfoliation

Graphene was first produced by micromechanical exfoliation. For this method, scotch tape is used to peel away individual graphitic layers in graphene, by breaking the weak inter-plane van der Waals bonds [117]. This simple method produces very pure, defect-free graphene flakes with sizes of 20–100 µm. Micromechanical exfoliation is ideal therefore for making proof of concept devices and for investigating physical principles, however the small size of the flakes limits its potential in large scale applications [119].

2.3.1.2 Chemical vapour deposition

CVD is a promising candidate for commercialised graphene since it allows routine polycrystalline graphene production on the order of meters, with single crystallites tens of centimetres in diameter [120]. Some factors affecting the growth quality in CVD include the catalyst, carbon feedstock, temperature, pressure, dilutent and etchant. Graphene was originally grown under ultrahigh vacuum conditions on single crystal transition metals substrates [121]. Today, it is much more commonly grown at ambient pressure conditions on nickel or copper catalytic films at temperatures of 900–1100°C [122]. In the CVD reaction, hydrogen is often

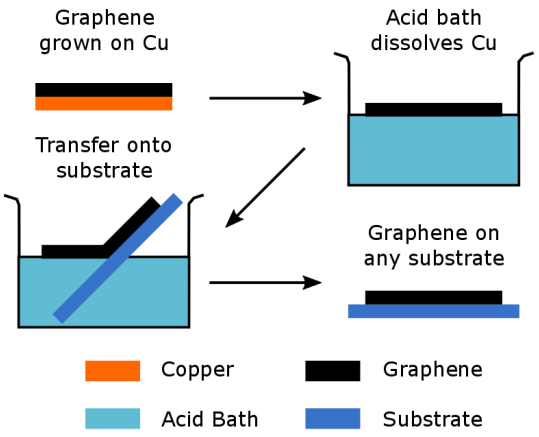

Fig. 2.7 Schematic showing how graphene grown on copper can be transferred into an arbitrary substrate using a polymer assisted transfer.

used to activate carbon binding to the metal surface and to etch multilayer domains which have relatively weak carbon-carbon bonds [123].

CVD graphene can be grown on various substrates including metals like Cu [124], Ni [125], and insulators like SiO_2 [126] and glass [127]. However, it cannot be grown on all materials. It is most commonly grown on copper and transferred to the target substrate (Figure 2.7). Many methods exist to transfer graphene and are generally categorised as with or without a support layer. The support layers contact the graphene and provide support whilst the substrate is removed via chemical etching or is physically separated from the graphene. Often polymers like polymethylmethacrylate (PMMA) [125] or polydimethylsiloxane (PDMS) [128] are used which are flexible, enabling a good contact between the polymer and graphene and are strong enough to prevent the fragmentation of the graphene during the etching process. The disadvantage of the polymers is that after the transfer they cannot be fully removed from the graphene without introducing defects into the film [129]. Non-polymer approaches give cleaner transfers. These include metal assisted transfer [130] which is more expensive than the polymer assisted methods, or the use of small molecules like napthalene which can induce cracking of the graphene as they are less flexible than polymers [129]. Support free transfer is also possible if surface tension of the etching solution is reduced so it does not damage the graphene [131].

2.3.2 Material properties of graphene

Pristine graphene has a hexagonal atomic arrangement, and a gapless electronic band structure which appears like two cones touching at their points (Figure 2.8) [132]. Graphene can

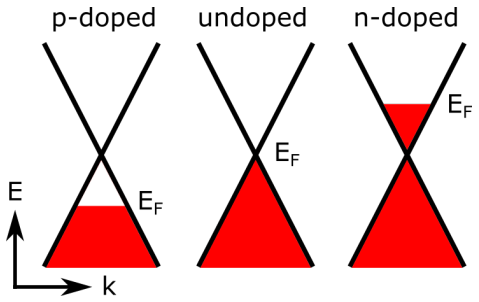

Fig. 2.8 Monolayer graphene has a conical shaped band structure at low energies up to 1 eV. The charge carrier concentration can be tuned continuously between holes and electrons, resulting in p or n-type doping.

therefore be described as either a zero-bandgap semiconductor or a zero-overlap semimetal. The charge carriers can be continuously tuned between electrons and holes by doping. In the limit of zero doping, the Fermi energy, E_F, sits at the charge neutrality point. At the charge neutrality point, there are no charge carriers and the conductivity decreases to the conductivity quantum $\frac{e^2}{h}$ per carrier type where e is the charge on an electron and h is the Planck constant.

In pristine monolayer graphene, electrons interact with the honeycomb lattice and create quasiparticles known as Dirac fermions. The Dirac fermions are described by the Dirac equation rather than the Schrödinger equation, and behave like a massless electron or a charged neutrino. The Dirac fermions undergo ballistic transport through pristine graphene with effective speeds of $10^6\,\mathrm{m^{-1}\,s^{-1}}$ [119]. This means pristine graphene has an extremely high mobility of at least $6\times10^6\,\mathrm{cm\,V^{-1}\,s^{-1}}$ at 4 K and $1.8\times10^5\,\mathrm{cm^2\,V^{-1}\,s^{-1}}$ at room temperature [133].

Other interesting material properties of graphene include its optical transmittance, where the absorbance of a single graphitic layer is defined only by fundamental constants which do not depend on physical parameters. Namely, an individual graphitic layer absorbs:

$$\frac{\pi e^2}{\hbar v_L} = \pi\alpha \approx 2.3\% \tag{2.10}$$

where e is the charge on an electron, $\hbar = 1.054\times10^{-34}\,\mathrm{J\,s^{-1}}$ is the reduced Planck constant, v_L is the velocity of light and α is the fine structure constant [106]. Graphene also has a Young's modulus of 1 TPa, an intrinsic strength of 130 GPa [134] and a thermal conductivity of $\sim 2000-5300\,\mathrm{W\,m^{-1}\,K^{-1}}$ [135].

The properties of graphene change with the number of layers, doping levels, and defects in the material. As the number of graphitic layers increases, the electronic band structure changes, reaching the limit of bulk graphite at ~ 10 layers [136]. Graphene can be doped

electrically using backgating or chemically using molecules like NO_2 [137]. Defects in graphene come from the material edges, functional groups and structural disorders. A major mechanism that reduces the mobility in graphene is scattering off defects [138].

2.3.2.1 Graphene quantum capacitance

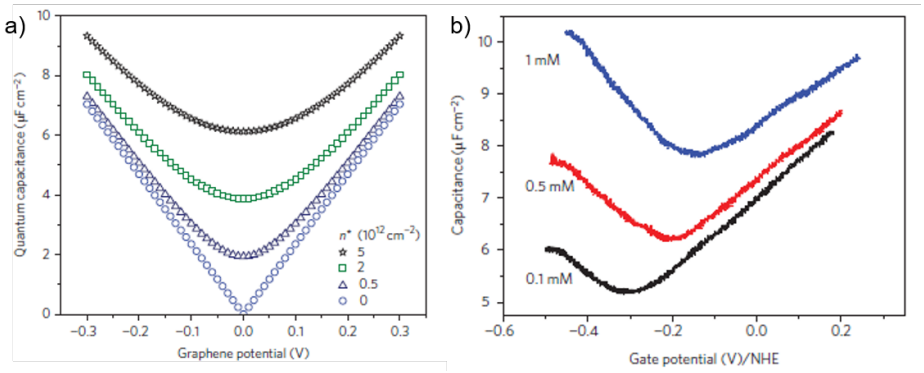

Fig. 2.9 From Xia *et al.* a) Simulated quantum capacitance of undoped graphene against gate potential for different levels of charged impurities. b) Experimental measurements showing the capacitance of graphene in aqueous NaF. The potential is quoted with respect to the normal hydrogen electrode. Plots reproduced from [139].

The phenomenon of quantum capacitance as been observed in graphene. Conventional capacitance exists when a potential is applied across a dielectric sandwiched between two conducting plates, and results in the build up of charge. Quantum capacitance exists when a potential is applied perpendicular to a two-dimensional electron gas (2DEG). The 2DEG cannot completely screen the electric field, giving a capacitance, C_Q, of

$$C_Q = \frac{m_e e^2}{\pi \hbar^2} \tag{2.11}$$

where m_e is the effective electron mass incident on the 2DEG, e is the electron charge and $\hbar$ is the reduced Planck constant [140].

Since graphene behaves as a 2DEG, it shows a quantum capacitance [141, 142]. The quantum capacitance of graphene varies with the applied gate voltage, doping levels, the level of charged defects and the ionic concentration. When the doping in graphene is varied by applying a gate voltage, the quantum capacitance has a symmetric V-shape with a minimum at the Dirac point where there are the minimum number of charge carriers (Figure 2.9). The

quantum capacitance for graphene can be calculated as:

$$C_Q = \frac{2e^2}{\hbar v_F \sqrt{\pi}} \sqrt{|n_d| + |n_D|} \tag{2.12}$$

where $v_F \approx c/300$ is the Fermi velocity of the Dirac electrons, n_d is the charge carrier concentration from doping and n_D is the carrier concentration from defects [139].

2.3.2.2 Biocompatibility of neurons on graphene

Graphene has many potential biomedical applications, it is therefore important to asses its biocompatibility. Biocompatibility is a complex issue with each material, and biological application potentially having a unique biological response. For example, different carbon based materials have different biological responses [143, 144], and the effect of graphene is different if present in the cell medium, and if cells are plated directly onto a graphene substrate [145]. Here, we will focus on the biocompatibility of neurons grown on CVD graphene substrates for bioelectronics and biosensing applications.

When neurons are plated on a CVD graphene coated substrate and compared to glass, the graphene does not increase the cytotoxicity [146], increase the stress in the cells, affect the mitochondrial membrane potential [147] or change the neuronal activity [148]. There is a difference between high an low quality graphene. High quality graphene enhances neuronal adhesion between neurons and graphene [149] with increased neurite sprouting and outgrowth [150, 99]. Whereas, low crystal quality graphene, can reduce the neuronal adhesion [151].

Chapter 3

Background to the microscopy and spectroscopy techniques used

In Chapter 2 the background to graphene microelectrode arrays (MEAs) is presented. Physical techniques were used during the fabrication and characterisation these devices in Chapters 4 and 5. The graphene MEA is then combined with fluorescence microscopy in Chapter 6 to enable studies related to the impact amyloid proteins on neuronal electrophysiology. One specific amyloid protein is examined in more detail using Fourier transform infrared spectroscopy (FTIR) in Chapter 7.

In this chapter, the background to each spectroscopic and microscopic techniques used in this work is introduced, along with any data analysis required to interpret the data. The techniques are introduced in the order they appear in the main body of the work. It is recommended that this chapter is used as reference for the background to individual microscopy or spectroscopy techniques rather than read as a whole. The techniques used to characterise the fabricated devices are Raman spectroscopy, direct current (DC) testing, ultraviolet visible (UV-vis) spectroscopy, electrochemical impedance spectroscopy (EIS) and atomic force microscopy (AFM). The fluorescence microscopy techniques introduced to image sub-cellular components are confocal microscopy, fluorescence lifetime imaging microscopy (FLIM). Finally, the use of FTIR to understand protein secondary structure is presented.

3.1 Materials characterisation

3.1.1 Raman spectroscopy

In this work, Raman spectroscopy was used to identify and characterised graphene in the MEA, therefore an introduction to Raman spectroscopy is given, with a focus on the Raman spectrum of graphene.

Raman spectroscopy is a vibrational technique used to gain structural information about a sample. In Raman spectroscopy, a monochromatic laser is shone on a sample, exciting electrons to virtual states between the electronic energy levels (Figure 3.1). When the electrons return to the ground state they can occupy different vibrational (or rotational) energy levels. If the electron returns to its original vibrational state, the elastic (Rayleigh) scattering gives no information about the system. If the electron occupies a higher vibrational state, the emitted photon has a lower energy (Stokes process), and if the electron returns to a lower vibrational state the emitted photon has a higher energy (Anti-Stokes process). Raman scattering is a fundamentally inefficient process with only 1 in 10^7 incident photons being inelastically scattered [152, 153]. One method to overcome this is resonant Raman spectroscopy where electrons are excited to real electronic states instead of virtual ones. Each peak in a Raman spectrum can be characterised by its Raman shift in cm^{-1}, $\tilde{\nu}$, area, a, intensity, I, and full width at half maximum Γ.

3.1.1.1 Raman spectroscopy of graphene

Since graphene has no bandgap, every Raman excitation excites an electron to a real electronic state, so all graphene Raman spectroscopy is resonant [154]. The Raman spectrum of pristine graphene has the following peaks: the G ($\sim 1580\,\mathrm{cm}^{-1}$) peak occurs from a one phonon processes; the 2D ($\sim 2680\,\mathrm{cm}^{-1}$) and 2D' ($\sim 3200\,\mathrm{cm}^{-1}$) peaks from two phonon processes [155]; the D+D' ($\sim 2450\,\mathrm{cm}^{-1}$) and D+D" ($\sim 2680\,\mathrm{cm}^{-1}$) are the combination bands. In addition to these, the presence of defects within the graphene gives rise to D ($\sim 1350\,\mathrm{cm}^{-1}$) and D' ($\sim 1600\,\mathrm{cm}^{-1}$) peaks [156]. Careful analysis of these Raman peaks reveals a wealth of information about the graphene and can be used to identify, amongst other things, the number of graphitic layers [155], the doping levels [157], the disorder [154], and the strain on the graphene [158].

The number of graphitic layers in few-layer graphene changes its bandstructure and therefore Raman spectrum. This can be characterised by the shape of the 2D peak (Figure 3.2). Monolayer graphene has a conical band structure giving a sharp, symmetrical, single-Lorentzian 2D peak. Due to its more complex band structure, the bilayer graphene is

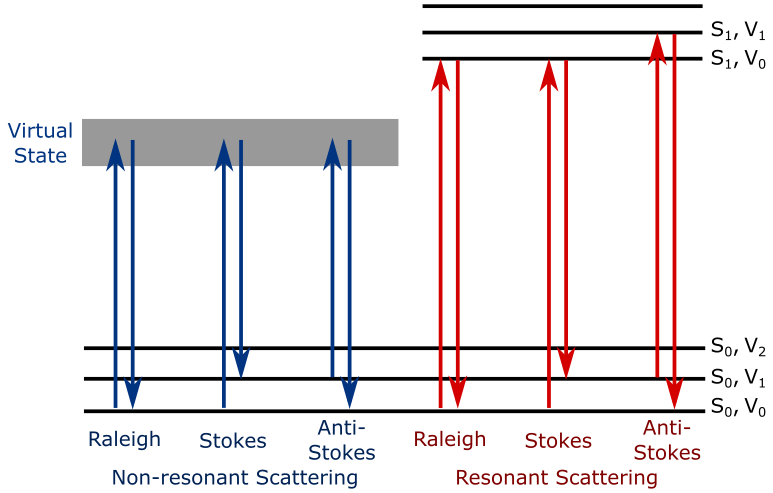

Fig. 3.1 Schematic showing the basic principle behind resonant and non-resonant Raman spectroscopy. In non-resonant Raman spectroscopy, light excites electrons to virtual energy states, whereas for resonant Raman spectroscopy, the electrons are excited to real electronic, S_n, and vibrational, V_n energy states.

a superposition of four Lorentzian peaks. Multilayer graphene has a significantly more complex band structure and shows a clear shoulder at a lower wavenumber than the main peak. Finally, the 2D peak of bulk graphite has a broad shoulder below the main peak and a sharper shoulder at a higher wavenumber [155].

Defects in the sample can be clearly seen by the presence a D peak at $\sim$1350 cm^{-1} [156]. If the mean distance between defects is > 10 nm, the concentration of defects in undoped graphene is calculated from the ratio of $I(D) : I(G)$ (Figure 3.3a) as follows [159]:

$$n_D(\mathrm{cm}^{-1}) = \frac{1.8 \times 10^{22}}{\lambda_L^4} \left(\frac{\mathrm{I(D)}}{\mathrm{I(G)}} \right) \tag{3.1}$$

where λ_L is the light wavelength. The mean distance between defects is therefore

$$L_D^2(\mathrm{nm}^2) = 1.8 \times 10^{-9} \lambda_L^4 \left(\frac{\mathrm{I(D)}}{\mathrm{I(G)}} \right)^{-1} \tag{3.2}$$

This can be modified to find the defect concentration for doped samples [160]. The absence of a measurable D peak suggests that mean distance between defects is > 25 nm [159].

The graphene doping levels can also be obtained from the Raman spectrum. Low doping levels should give a high $I(2D) : I(G)$ and a sharp G peak. P- and n-type doping can be distinguished by the downshifting or upshifting respectively of the 2D peak [157]. By using information about $\tilde{\nu}$(G), $\Gamma(G)$ (Figure 3.3b), $\tilde{\nu}(2D)$, $I(2D)/I(G)$ [157] or $a(2D)/a(G)$ [158],

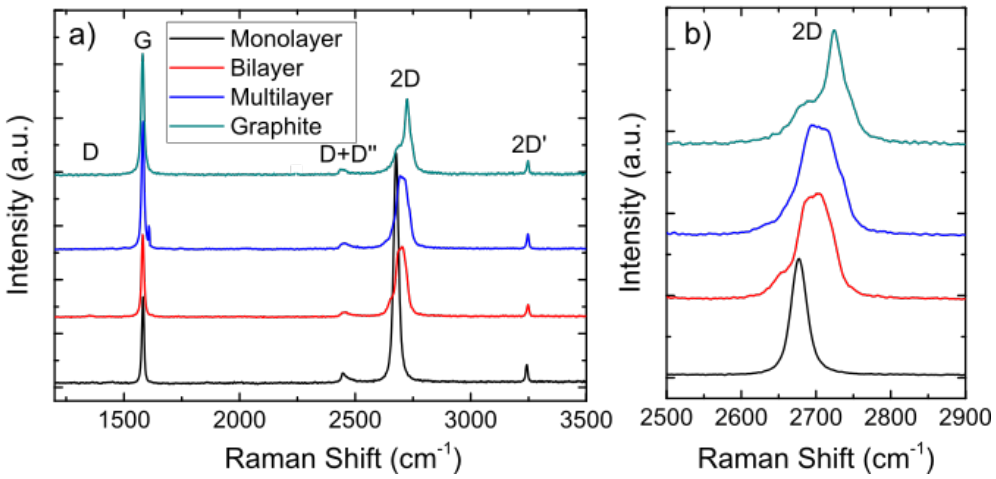

Fig. 3.2 a) 514 nm Raman spectra of defect free single layer graphene, bilayer graphene, multilayer graphene and graphite produced by micromechanical exfoliation. The spectra show the following peaks: G at $\sim 1580\,\mathrm{cm}^{-1}$, 2D at $\sim 2680\,\mathrm{cm}^{-1}$, 2D' at $\sim 3200\,\mathrm{cm}^{-1}$ and D+D" at $\sim 2680\,\mathrm{cm}^{-1}$. b) The shape of the 2D peak changes with the number of graphitic layers. Spectra taken by Silvia Milana.

it is possible to find the Fermi energy and charge carrier concentration in the sample. The Fermi energy, E_F, and charge carrier concentration from doping, n_d, are related as follows:

$$E_F(n) = \hbar|v_F|\sqrt{\pi n_d} \tag{3.3}$$

where $v_F = 1.1 \times 10^6\,\mathrm{m\,s}^{-1}$ is the Fermi velocity and $\hbar = 1.054 \times 10^{-34}\,\mathrm{J\,s}^{-1}$ is the reduced Planck constant.

Strain on the graphene sample causes shifts in $\tilde{\nu}(G)$ and $\tilde{\nu}(2D)$ [161, 162]. Therefore, unless it is confidently known that the sample is unstrained, the graphene doping levels should be assessed by $\Gamma(G)$, $I(2D)/I(G)$ or $a(2D)/a(G)$, which do not give information about whether the sample is p- or n-doped. This information can instead be found from measuring the resistance of a graphene strip whilst changing the doping levels of the graphene by backgating, and the observed minimum in conductivity corresponds to the charge neutrality point.

3.1.2 Direct current testing

It is important to understand the direct current (DC) electrical properties of each material in the graphene MEA. Resistance, R, is the ability of a material to oppose the flow of charge carriers. For a thin film of uniform thickness, the resistance measured in a two-probe

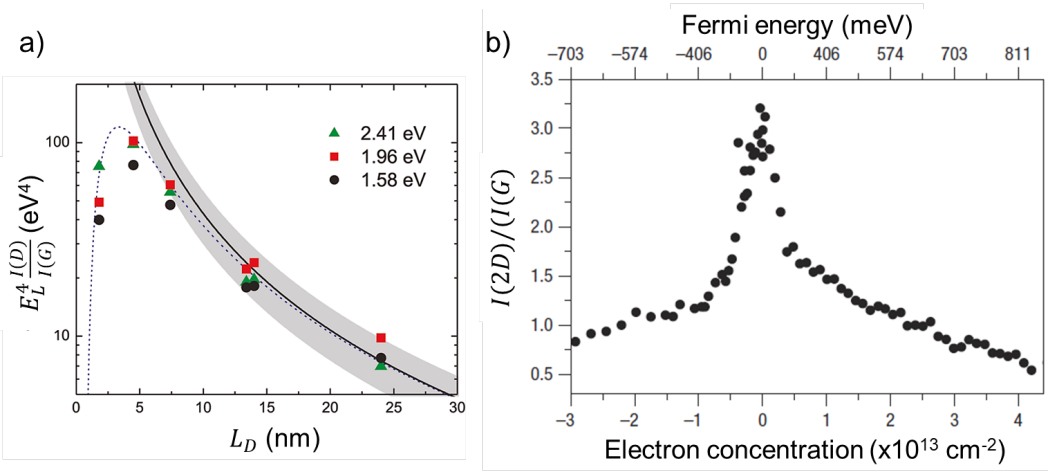

Fig. 3.3 a) The mean distance between defects in graphene, L_D, correlates with the intensity ratio of the D to G peak in the Raman spectrum at different excitation energies. b) The doping levels of graphene relate to ratio of the 2D to G peak in the Raman spectrum $\Gamma(2D)$. Figures reproduced from [159] and [157].

arrangement will contain components from the sheet resistance, R_S, (characterising the material resistance), and the contact resistance, R_C, (characterising the resistance between the probe and material). The sheet and contact resistance can be distinguished using a transmission line method where a device is fabricated with channels of a known width, and varying length. The sheet resistance can be calculated from the slope of the graph of sheet resistance against channel length using the equation

$$R_T = \frac{R_S}{w} \cdot l + R_C = slope \cdot l + R_C \tag{3.4}$$

where R_T is the measured total resistance, R_S is the sheet resistance, R_C is the contact resistance, w and l are the width and length of the transmission line pattern [163].

3.1.3 Ultraviolet-visible spectroscopy

Ultraviolet-visible (UV-vis) spectroscopy was used in this work to measure the transmission of light through each material used in the graphene MEA. UV-vis is an absorption spectroscopy in the ultraviolet (200–400 nm), visible (400–765 nm) and near infrared (765–3200 nm) range. Photons across these wavelengths are absorbed by the sample when electrons are excited from their ground to excited electronic states.

The absorbance is logarithmically related to the ratio of the beam intensity that passes through the sample, I, to the initial beam, I_0, as:

$$A = \log_{10}(I_0/I) \tag{3.5}$$

From the absorbance data, the concentration c of the constituent molecules can be found using the Beer-Lambert law as:

$$A = \varepsilon l c \tag{3.6}$$

where l is the effective path length of the light through the sample matrix. The attenuation coefficient ε describes the probability of an excitation [164]. If the refractive index is the same at different thicknesses, UV-vis spectrometry can be used to determine the thickness of thin films [165, 166].

3.1.4 Electrochemical impedance spectroscopy

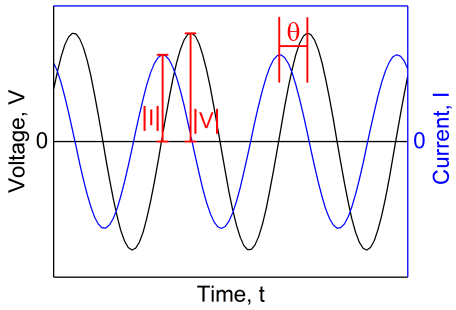

Fig. 3.4 The magnitude and phase of the impedance can be calculated from the current response to an applied sinusoidal potential.

Electrochemical impedance spectroscopy (EIS) is used to gain information about an electrochemical system, in this work this is the electrode-electrolyte interface between the graphene electrode and saline solution. This is achieved by recording the non-linear resistive, and capacitive properties of the electrochemical circuit, and fitting this to an equivalent circuit model (ECM). Since Chapter 5 of this thesis is devoted to understanding the graphene electrolyte interface using EIS, a larger background to this technique is included.

During EIS, a sinusoidal potential is applied between the working electrode and a reference electrode which is located in the bulk electrolyte. The applied potential $V(t)$, has the form:

$$V(t) = \bar{V} + |V|\cos(\omega t) \tag{3.7}$$

where $\bar{V}$ is an offset potential, $|V|$ is the magnitude of the applied oscillation or perturbing potential, ω is the angular frequency and t is the time. The resultant sinusoidal current, $i(t)$, is measured (Figure 3.4) and has the form:

$$i(t) = \bar{i} + |i|\cos(\omega t + \theta) \tag{3.8}$$

where $\bar{i}$ is the offset current, $|i|$ is the magnitude of the sinusoidal current, and θ is the phase. From this, the complex impedance at a given time can be obtained using:

$$Z = \frac{\Delta V}{\Delta i} \tag{3.9}$$

The complex impedance can be expressed either by its real, $Re(Z)$, and imaginary, $Im(Z)$, components or its amplitude, $|Z|$, and phase, θ [167]. These representations can be interconverted as:

$$|Z| = \sqrt{Re(Z)^2 + Im(Z)^2} \tag{3.10}$$

$$\theta = \tan^{-1}\left(\frac{Im(Z)}{Re(Z)}\right) \tag{3.11}$$

An EIS spectrum is obtained by varying the frequency of the applied voltage. The resultant impedance and frequency data are represented as a Nyquist or Bode plot. A Nyquist plot shows presents $Im(Z)$ against $Re(Z)$, with each point corresponding to a measurement at a single frequency. Nyquist plots have the advantage that the shape of the plot can give details about the mechanism involved. A Bode plot shows the $|Z|$ and θ against frequency, $f = 2\pi/\omega$. This has the advantage of showing the frequency dependence explicitly [168].

3.1.4.1 Electrochemical charge transfer

EIS is measured between two electrodes in an electrolyte. An EIS spectrum gives information about the bulk conductivity through the electrolyte, the electrode-electrolyte interface at both electrodes and the connecting wires. Charge transfer at an electrochemical interface between an electrode-electrolyte interface can show capacitive and/or resistive properties [168]. The interface behaves like a capacitor when charge is transferred by charging and discharging the electrical double layer (which combines the inner and outer Helmholtz planes and the Gouy-Chapman diffuse-charge layer) [76].

The interface behaves like a resistor during Faradaic reactions when ions are oxidised or reduced at the electrodes. In this case, the reaction rate is limited by either the reaction kinetics or by diffusion. Kinetic controlled reactions are limited by the electrochemical reaction rate, which gives negligible local concentration gradients of the reactive species.

Diffusive controlled reactions are limited by mass transport of the reactive species entering or leaving the electrode surface [169].

3.1.4.2 Equivalent circuit elements

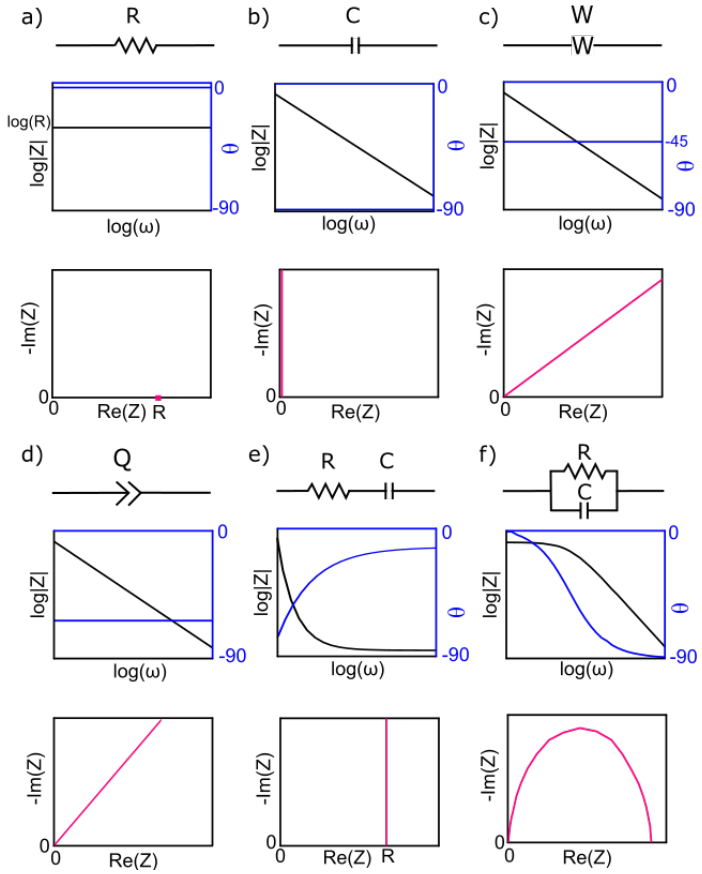

Fig. 3.5 EIS spectra can be modelled using a combination of circuit elements a) capacitors, b) resistors, c) Warburg elements and d) constant phase elements. Combinations of these elements can be added in e) series or f) parallel. An example Bode and Nyquist plot is given for each combination of circuit elements.

ECMs can be fitted to EIS spectra to understand the underlying phenomena in a device. The choice of a good ECM can also enable the characteristics of each region to be found. The ECM can contain the following elements: resistors, capacitors, inductors, Warburg elements and constant circuit elements which each have a distinct frequency response and can be combined to describe more complex phenomena (Figure 3.5).

A pure resistor has a constant phase of $\theta = 0°$ and a fixed magnitude of $|Z| = R$ [170]. Resistors are used in the ECM to describe the resistance of conductive leads, the solution resistance, or a Faradaic reaction.

In a pure capacitor, C, current flows by the attraction and repulsion of electrons to the charged plates. A capacitor has a phase response of $\theta = -90°$, and the impedance magnitude decreases with increased frequency as $|Z| = 1/\omega C$ [170]. Capacitors are used in the ECM to describe dielectric materials or the charge redistribution at interfaces like the electric double layer [168].

Warburg elements, W, have a constant phase of $\theta = -45°$, and the impedance magnitude decreases with increased frequency. They are used with diffusion (or mass transport) limited Faradaic reactions to describe the frequency dependence of the ion transport to the electrode [171]. The Warburg resistance is low at high frequencies because diffusing reactants are near the electrode, but is high at low frequencies where reactants must travel further to reach the electrode [172]. For semi-infinite diffusion to a planar surface the Warburg impedance is

$$Z_W = \frac{\sqrt{2}\sigma}{\sqrt{j\omega}} \tag{3.12}$$

where σ characterises the diffusion coefficients of the reactive species, electrode area and kinetic orders of the reaction [167].

The Warburg element can be modified to describe a finite diffusion length in an external homogeneous solution, by the convective Warburg element, W_d, as:

$$Z_{W_d} = \frac{R}{\sqrt{\tau j\omega}} \tanh(\sqrt{\tau j\omega}) \tag{3.13}$$

where τ characterises the amount of time the reactant takes to diffuse across the layer [173]. For systems with a finite length which have an impermeable barrier, the restricted diffusion element W_o is [174]:

$$Z_{W_o} = \frac{R}{\sqrt{\tau j\omega}} \coth(\sqrt{\tau j\omega}) \tag{3.14}$$

For electrodes with a diameter $< 100\,\mu$m, hemispherical diffusion of species to the electrode occurs, as previously described by the spreading resistance. The Nyquist plot of this impedance takes the form of a flattened hemispherical disk [175–177].

The constant phase element (CPE), Q, has a constant phase between 90° and −90° [178]. The impedance of a CPE is:

$$Z_Q = \frac{1}{\beta(j\omega)^b} \tag{3.15}$$

where β has the numerical value of resistance at 1 Hz, and b can take any value between 1 and 0. For $b = 1$, the CPE behaves as an ideal capacitor with $C = Q$ and has the unit F. For $b = 0$, the CPE behaves as an ideal resistor with $R = 1/Q$ and has the unit Ω^{-1}. For $b = 1$, the CPE behaves as an ideal inductor. For $1 > b > 0$, the CPE has units s^b/Ω. By looking at the phase

angle, the CPE can also be used to characterise the resistive-like or capacitive-like nature of an electrode [32]. CPEs model systems where each reaction or physical phenomenon has multiple time constants or interacts with a non-uniformly active electrode surface [168]. The physical origin of the time constant distribution can be attributed to distributed surface reactivity, surface inhomogeneity, grain boundaries, roughness, fractal geometry, electrode porosity, current distributions, or potential distributions across the electrode [179].

3.1.4.3 Equivalent circuit models

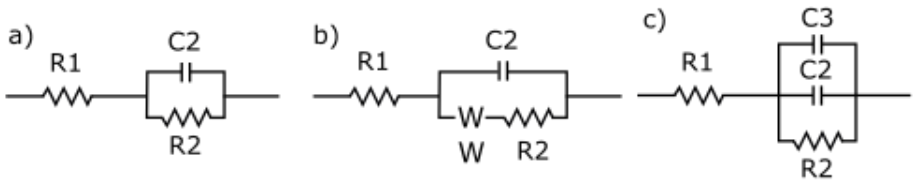

Fig. 3.6 EIS spectra can be modelled using linear circuit elements. a) A single electrochemical reaction is modelled by a series resistance $R1$, double layer capacitance $C2$ and charge transfer resistance $R2$. b) A single electrochemical reaction controlled by both the potential and mass transfer, where mass transfer is modelled by a Warburg element, W. c) An electrode partially blocked by a dielectric with capacitance $C3$.

In a real EIS spectra, $|Z|$ can take any positive value, and θ is 0–90°. This can be modelled by combining linear elements. The elements are combined in series when the same current flows through each element and in parallel when the potential across the elements is the same [168]. For a simple resistor and capacitor in series, at low frequencies the impedance is limited by the flow of charge through charging and discharging the capacitor and thus shows a capacitive like behaviour with $\theta \approx 90$. At high frequencies the impedance is limited by the resistor, with $\theta \approx 0$ and $|Z| \approx R$ (Figure 3.5e). The opposite is true of a resistor and capacitor in parallel, where the current can flow through either element. At low frequencies, current flows through the resistor, but at high frequencies the current flows by charging and discharging the capacitor (Figure 3.5f) [170].

Systems that are only dependent on a single electrochemical reaction, and not by mass transport can be described by the Randles circuit $R1 + R2/C2$ (Figure 3.6a). $R1$ is the series resistance which combines the electrolyte resistance, intrinsic substrate resistance and contact resistance; $C2$ describes the double layer capacitance; and $R2$ describes the charge transfer resistance of the Faradaic reaction [74].

For systems where mass transport to the electrode is also important, the Warburg element, W, is included in series with the charge transfer resistance $R1 + (R2 + W)/C2$ (Figure 3.6b).

The exact nature of the Warburg element depends on the mass transport limits of the system being studied.

An additional feature that can be described in the model is the partial coverage of the electrode by a dielectric. Electrically, the dielectric behaves like an additional capacitor $C3$ in parallel to the electrode model (Figure 3.6c).

3.1.4.4 Electrochemical impedance spectroscopy to study microelectrode arrays

EIS is used in MEAs to characterise the electrode-electrolyte interface, and can be used in two or three electrode setup. The electrolyte chosen to mimic the cell medium is generally phosphate buffered saline (PBS) [80, 32, 94, 81], a water based solution at pH 7.4 containing the salts KH_2PO_4, NaCl, $Na_2HPO_4-7H_2O$ and KCl. PBS is non-toxic to cells and is commonly used in cell culture for washing cells before dissociation, transporting cells, diluting cells for counting, and preparing reagents. If the voltage applied across the microelectrodes is sufficiently small, EIS is a non-destructive method to probe the device electrochemistry [63]. In addition to this, cells can be plated onto the MEA and EIS is used to track biological phenomena [180].

The simplest EIS bench marking performed for MEAs is measuring the real impedance at 1 kHz [75], a physiologically relevant frequency similar to a typical firing event with $\sim$1 ms [181]. For recording electrodes, the 1 kHz impedance varies from approximately 30 kΩ to 1 MΩ [63], with signal attenuation becoming problematic above 5 MΩ [23]. The 30 µm Multichannel Systems TiN electrodes have a 1 kHz impedance of $30-50$ kΩ [92].

A more thorough analysis of MEA electrodes is performed by measuring the complex impedance over a frequency range. The data is plotted as a Bode [32] or Nyquist [80] plot, and interpreted by fitted to a physically relevant ECM.

3.1.4.5 Equivalent circuits for graphene microelectrodes

EIS on graphene MEAs has been performed, and an ECM fitted to interpret the data. Each ECM used in the literature is based on the Randles model $R1+R2/C2$ [74]. The Randles model has been modified to fit the system better by introducing a CPE [111, 80, 32, 81, 94], a Warburg element [80, 94], a bounded Warburg element [32] and/or a second resistor and capacitor in series [81, 94] (Table 3.1).

Every paper that fits to the EIS of a graphene MEA replaces the capacitor $C2$ with a CPE $Q2$ [111, 80, 32, 81, 94] to fit the data better. The Warburg element [80, 94] or bounded Warburg element [32] can be placed in series with the charge transfer resistance. There is however, a debate whether a Warburg element is physically relevant for the small

microelectrodes given the materials and frequency ranges of interest in electrophysiological experiments [76]. For example, 20 µm diameter graphene electrodes are deemed too small to be described by linear diffusion [81].

It has been suggested that including an additional resistor $R3$ and capacitor $C3$ can describe the graphene quantum capacitance and its associated leakage resistance [81, 94]. The quantum capacitance arises because graphene is a two-dimensional electron gas. It varies with the graphene doping, the presence of charged impurities and the ionic solution (Section 2.3.2.1) [139].

Each paper that fitted an ECM to the EIS of a graphene microelectrode used a different ECM (Table 3.1), and the electrodes vary in size from 12 mm^2 to 314 μm^2. Some general observations, however, can be made. Increased electrode area, increases the electrode capacitance and reduces the electrode resistance. The phase of the CPE is closer to 1 than 0, showing that the graphene electrodes have a more capacitive than resistive behaviour [80, 32]. The high capacitance of monolayer graphene arises from the quantum capacitance of the graphene, and also from correlations between ions in the electrolyte and π-band electrons in the graphene, where attractive interactions occur between the ions and the graphene image charges decrease the separation distance of the double layer [182]. The capacitive nature of the electrodes shows that charge is predominantly transferred by the redistribution of electrodes at the electrode/electrolyte interface rather than by a Faradaic reaction.

Table 3.1 The equivalent circuit models used to fit the electrochemical impedance spectra of graphene microelectrodes in phosphate buffered saline solution.

		Electrode area	R1	Q2	a2	R2	W*	Q3	a3	R3
		mm^2	Ω	$nF \cdot s^{a2-1}$		$M\Omega$	$\Omega \cdot s^{-0.5}$	$nF \cdot s^{a3-1}$		$M\Omega$
[111]	$R1 + \frac{Q2}{R2}$	0.31	156	1248	0.5	0.3				
[113, 80]	$Rs + \frac{Q2}{R2+W2}$	0.0135	246	-	0.94	6.63	-			
[32]	$Rs + \frac{Q2}{R2+W_o2}$	0.0025	-	5.6	0.67	84.9	57.4×10^{6}			
[81]	$R1 + \frac{Q2}{R2} + \frac{Q3}{R2}$	0.00031	800	5	0.68	5.8×10^{-3}		7.36×10^{9}	0.78	140
[94]	$R1 + \frac{Q2}{R2+W2} + \frac{Q3}{R3}$	12	100	985	0.67	1.95×10^{-3}	8.62×10^{3}	9.52×10^{-7}	0.91	13.7

* [32] uses the bounded Warburg element to describe the graphene electrode, whereas [94] uses the porous bounded Warburg element.

3.1.5 Atomic force microscopy

Atomic force microscopy (AFM) maps the topology of a surface. In this work, it is used to determine the thickness of the materials used in the graphene MEA. AFM is a scanning probe microscopy where a sharp tip on the end of a cantilever is scanned across the surface of the sample [183]. The cantilever is bent by the force between the tip and the surface. Bending is measured by reflecting a laser beam off the end of the cantilever and measuring its deflection using a photodiode. The topography of the sample is measured by plotting the cantilever deflection against the position on the sample, or by moving the height of the cantilever with respect to the surface to maintain a constant force. The height resolution of an AFM can be down to 0.01 nm [184], the lateral resolution however is larger and is determined by the curvature of the tip and the sensitivity of the system to cantilever deflection [185].

The most common AFM scanning modes are contact, tapping and non-contact mode. In contact mode, the tip is dragged across the surface and physically moved up and down to ensure a constant force is felt on the cantilever, thus mapping the surface topology. Contact mode has the highest scan speeds, but can damage fragile samples [185]. Tapping mode is more suitable for fragile samples, the tip oscillates up and down at its resonance frequency "tapping" the surface at the bottom of each oscillation, and measuring the surface topology. The AFM measures any quantity that affects the tip-surface force [186]. Non-contact mode minimises both the lateral and normal forces on the sample. It uses a cantilever oscillating with a small amplitude above the surface of the sample. The sample is detected by the change of oscillating frequency and amplitude of the tip by van der Waals attraction or other long range forces [187]. PeakForce tapping mode is an innovation by Bruker Corporation enabling automated peak force tapping. In this mode, the cantilever oscillation is well below its resonance frequency. This enables force-distance curves to be obtained for each "tap", and speeds up the acquisition time. The peak force constant can be as low as 10 pN, smaller than with conventional methods [188].

3.2 Fluorescence microscopy

The transparent graphene MEAs were designed and fabricated to enable voltage trace recordings to be combined with the fluorescence imaging of amyloid proteins. Therefore, a background to fluorescence microscopy is included, with a specific focus on the imaging modalities used in this work.

Fluorescence occurs when a fluorescent substance (fluorophore) absorbs a photon and emits a different wavelength of light. The absorbed photon has energy $E = hf_1 = hv_L/\lambda_1$ where h is Plank constant, v_L is the speed of light and f and λ are the frequency and

wavelength of the photon. This excites a ground state electron into a higher electronic energy level. Thermal relaxation then occurs, and the electron drops down internal energy levels to its ground vibrational and rotational energy state. Finally, the fluorophore relaxes to the ground electronic state either by emitting a photon with energy $E = hf_2 = hv_L/\lambda_2$, or by non-radiative decay where the energy is dissipated as heat to the solvent. Due to thermal relaxation, the emitted photon always has a lower energy, and higher wavelength than the absorbed photon (Figure 3.7) [153]. A fluorophore can be described by its emission spectrum, absorbance spectrum, quantum yield, fluorescence lifetime, τ, and extinction coefficient at the maximum of absorption.

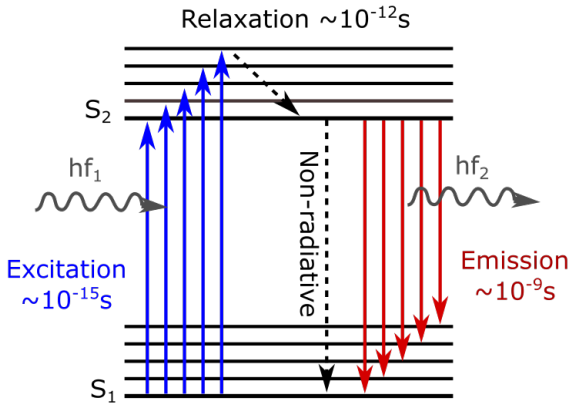

Fig. 3.7 Schematic showing the process of fluorescence. Incident light with energy $E = hf_1$ excites electrons from their ground energy level, S_1, to an excited energy electronic level, S_2. After thermal relaxation, they return to the ground electronic state emitting light with energy hf_2.

3.2.1 Fluorescent dyes and staining

Fluorescent labels can be added to biological structures of interest in order to image them. The fluorescent dye can be applied generally to the system, or targeted to specific organelles via covalent bonding or immunostaining. This enables the spatial mapping of biomolecules and organelles within biological samples.

One example of a fluorescent dye used to quantitatively determine the local calcium content is Oregon Green BAPTA-1 (OGB-1, where BAPTA is 1,2-bus(o-aminophenoxy)ethane-N,N,N',N'-tetraacetic acid). OGB-1 is excited at 488 nm (or 840 nm in two photon microscopy) and emits at 500–600 nm with a peak at 520 nm [32]. OGB-1 is normally added to the extracellular space. The dye shows changes in fluorescence intensity and lifetime with different calcium concentrations. Fluoresence lifetime measurements are advantageous as the

absolute calcium concentration can be determined independent of the dye concentration. The lifetime of calcium-free OGB-1 was first measured as ~ 346 ps and later revised to ~ 650 ps, whereas the calcium-bound dye has a longer lifetime of ~ 3700 ps (Figure 3.8) [189, 190]. OGB-1 is normally added to the extracellular space.

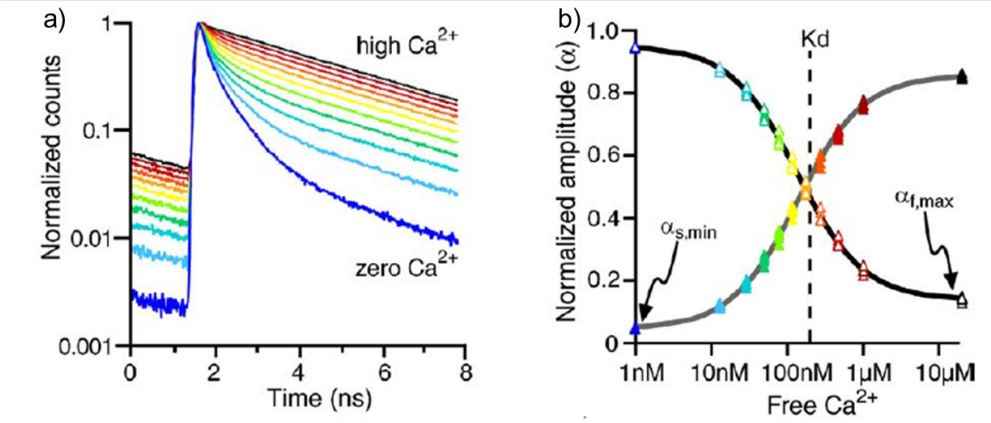

Fig. 3.8 a) Fluorescence lifetime curve of OGB-1 at different calcium concentration, the colour code corresponds calcium concentrations shown in b. b) Normalised amplitude (α) of the fast (calcium-free, lifetime 346 ps) and slow (calcium-bound, lifetime 3630 ps) dyes. The solid line indicates the fit of the data. Plot reproduced from [189].

3.2.2 Confocal microscopy

In conventional wide field fluorescence microscopy, monochromatic light is focused on the sample using a condenser lens, and excites the fluorophores present. Emitted fluorescent light then passes through an objective lens, reaches a photomultiplier which measures the brightness incident on it, and an image is formed. The majority of fluorescence microscopes are built in an epifluorescent arrangement, where a single lens is used as the condenser and objective. The lens is generally placed under the sample, in an inverted configuration. In an epifluorescence microscope, a dichroic mirror is needed to maximises the transmission of long wavelength emitted fluorescent light whilst minimising the transmission of incident light [191]. The resultant image includes light from the entire depth of field of the objective lens (0.5–1 µm) and is therefore a 2D projection of a volume, resulting in blurring of the image.

In confocal fluorescence microscopy, a pinhole is inserted into the light path eliminating fluorescence from out of focus planes [192]. Laser light is passed through a pinhole, focused by an objective lens and scanned across the sample illuminating it sequentially. In-focus emitted light passes through a second aperture which is confocal to (has the same focus as)

the first aperture. The second aperture removes any light contributing to the background haze that comes from above, below or beside the point of focus. This enables a confocal microscope to have a resolution of $\sim 300\,\text{nm}$, limited by the diffraction of light [193]. The drawbacks of the confocal technique are a slow image acquisition speed since the data are acquired on a pixel-by-pixel basis, and the inclusion of a pinhole reduces the amount of light hitting the detector.

3.2.3 Fluorescence lifetime imaging microscopy

Conventional fluorescence microscopy techniques map the fluorescence intensity across a sample. Fluorescence lifetime imaging microscopy (FLIM), maps the fluorescence lifetime across the sample. Individual fluorophores emit light stochasticly, however when a population of fluorophores is excited, a characteristic fluorescence intensity-time distribution can be seen. The fluorescence intensity, I, shows an exponential decay, with a characteristic lifetime τ as:

$$I(t) = I_o e^{-t/\tau} \tag{3.16}$$

where I_0 is the initial intensity and t is time. The fluorescence lifetime (generally a few nanoseconds) can be defined further as:

$$\tau = \frac{1}{1/\tau_r + 1/\tau_{nr}} \tag{3.17}$$

where τ_r is the radiative decay constant, and τ_{nr} is the non-radiative decay rate [29, 194].

Time resolved fluorescence measurements can be acquired using gated or modulated image intensifiers, or using photon counting techniques. The photon counting approach is known as time correlated single photon counting (TCSPC). In this method, the arrival times of large numbers of photons (thousands to millions) are collected, and a histogram of photon arrival times is built. The TCSPC method can be combined with a confocal microscope to create high resolution lifetime maps. The disadvantage of this technique however, is that each image has a long acquisition time $\sim$minutes, due to the pixel-by-pixel image acquisition [195].

FLIM is advantageous for inhomogeneous samples, as fluorescence lifetime (unlike fluorescence intensity) is insensitive to fluorophore concentration or laser power, and less sensitive to photobleaching. The fluorescence lifetime depends on the local environment, so amongst other things, it can be used to probe the concentration of ions, presence of oxygen, pH and protein binding to the fluorophore.

3.3 Fourier transform infrared spectroscopy of proteins

Another method to study the pathological function of misfolding proteins in neurodegenerative diseases is looking at their structure *in vitro*. In this work a data analysis script was written to gain information about the secondary structure of a protein from Fourier transform infrared spectroscopy (FTIR) data. Therefore, a large background to the analysis of FTIR spectra and the effect of protein structure on FTIR spectra are included.

FTIR is a vibrational spectroscopy used to gain structural information about a sample. In vibrational spectroscopies, the constituent molecules are described as a collection of atoms connected by internal coordinates, which can collectively vibrate at given fundamental frequencies, or normal modes. A non-linear molecule with N atoms, will have $3N-6$ normal modes. During FTIR measurements, the frequency and intensity of light absorbed by the normal modes in a sample is measured. The frequency of the normal mode increases with increased electron density between the atoms and decreases with increased atomic mass. The first order vibrational modes of the species are captured in the mid infrared region of 2.5–25 µm (4000–400 cm^{-1}) [196, 164].

3.3.1 Protein secondary structure

Since proteins have 10,000s atoms, more vibrational modes are present in an FTIR spectrum than can be assigned. Therefore, known spectroscopic regions of the FTIR spectrum are examined to obtain specific information [196]. Most commonly, vibrations in the peptide backbone are used in FTIR to analyse the protein secondary structure content.

The structure of proteins can be characterised on different length scales by their primary (amino acid sequence), secondary (local structure) and tertiary (overall three-dimensional shape) structures. The most common types of secondary structures are helices, sheets, turns, and random coils (Table 3.2). The secondary structures can be described by the hydrogen bonds they form between the CO and NH_3 groups on different residues. A turn occurs when a hydrogen bond between the zth and the $z+q$th residual where $q=3,4,5$, which creates a change in the backbone direction of at least 70°. Helicies are repeated turn structures, with the most abundant α-helix having $q=4$, the 3_{10}-helix having $q=3$ and the rare π-helix having $q=5$. Bridge structures have hydrogen bonds between different regions of the protein residual z_1 to residual z_2. Repeated bridge structures which connect to the same region of the protein create strands, which can bond to each other to form β-sheets. β-sheets can take a parallel or antiparallel arrangement [197]. Random coils are non-ordered conformations that do not fit into these categories.

Table 3.2 The main types of secondary structures with the characteristic hydrogen bonding pattern between the CO group on residue z and the NH_3 group on another residual. The abundance shows the percentages of amino acid residues that occupy the secondary structures. The amide I band shows the characteristic absorbance wavenumber for the secondary structure types.

Type	Hydrogen bond [197]	Abundance % [198–200]	Amide I band cm^{-1} [201, 202]
α-helix	Repeated z to $z+4$	34–39	1654–1658
3_{10}-helix	Repeated z to $z+3$	5	1660–1666
π-helix	Repeated z to $z+5$	Rare	–
Parallel β-sheet	Repeated z_1-1 to z_2 and z_2 to z_1+1	12-15	Multiple 1623–1643 and 1689–1698
Antiparallel β-sheet	Repeated z_1 to z_2 and z_2 to z_1	11	Multiple 1623–1643 and 1689–1698
Turn	z to $z+q$, $q=3,4,5$	20–22	Multiple 1666–1687
Random coil	Other	15–20	1646–1650

3.3.2 The effect of protein secondary structure on the amide I band

All proteins show amide vibrations since they are chains of amino acids bonded together by peptide bonds (-R-CO-NH-R'-). The infrared active vibrations of the amide group are amide A, B and I-VII. The amide I region at 1600-1700 cm^{-1} is 70–80% attributed to the C=O stretch, with contributions from the out-of-phase CN stretch, CCN deformation, and NH in-plane bend [203].

The amide I band is not affected by the side chains, yet is sensitive to secondary structure conformations which have different protein backbone configurations [203]. The main mechanism causing the secondary structure dependent splitting of the amide I region, is the transition dipole coupling. This is a resonance interaction between oscillating dipoles on neighbouring amide groups and depends on the distance between, and the relative orientations of the dipoles. A smaller, but also significant effect is the hydrogen bonding between the amide groups [196].

3.3.3 Resolution enhancement

The amide I band contains many component bands representing the different secondary structure types found in the protein. The peaks are broadened by radiation damping, the

Doppler effect, collision broadening and instrument effects and overlap resulting in the width of the component bands being larger than the interband spacing. They therefore appears as a broad essentially featureless asymmetric band [202]. To resolve the underlying secondary structure domains, resolution enhancing (or band-narrowing) techniques are used which do not increase the instrument resolution, but allow overlapping bands to be resolved [204]. The most common resolution enhancement techniques are the Fourier self-deconvolution (FSD) or second derivative methods.

FSD considers each peak as the convolution of a delta function which has position but no width, with a Gaussian or Lorentzian peak which has a finite width [204]. The broadening effects can therefore be removed by deconvolving the measured spectrum with a function describing the line broadening effects [205]. In reality, the delta functions cannot be recovered, and attempting to reduce the band width too far can result in side lobes appearing, however the band widths of the overlapping bands can be decreased. To perform FSD, the full-width at half maximum and a resolution enhancing factor must be chosen to maximise band narrowing, and to minimise the increase in noise and appearance of side lobes [206].

Resolution enhancement using the second derivative does not require the operator to choose any parameters. The simplest method to calculate the derivative is using the finite differences where the first derivative is the difference between two subsequent points in the spectra, and the second derivative is the difference between the first derivative points. The finite differences method is extremely simple but greatly increases the noise of the spectrum. A Savitsky-Golay (SG) derivative is more commonly used since it is more robust to noise. In a SG derivative, a polynomial of a given order is fitted to a symmetric region around the point of interest, and the derivative of this is calculated at each point.

3.3.4 Protein secondary structure determination from the amide I band

Three methods can be used to relate the absorbance of the amide I peak to the secondary structure content of the proteins, these are principal component analysis (PCA), fitting peaks to the absorbance spectrum, and fitting peaks to the resolution enhanced spectrum.

PCA is used in this application by comparison to a training set of FTIR spectra from proteins with a known secondary structure content from x-ray diffraction (XRD). From the training set, pure-structure spectra (or principal components) are defined which account for each secondary structure type. The measured proteins are then broken into these principal components to give an estimate of the secondary structure content [207]. In order to recognise all the structural features in the protein using PCA, they must all be included in the calibration set [208].

Alternatively, peak fitting works by dividing the amide I band into sub-bands which are assigned to particular secondary structure types based on their characteristic wavenumbers. The peak positions are assigned using knowledge from computational modelling and structures solved by XRD. A frequency range is given in the band assignments, since local environmental effects can cause similar structures to absorb at different wavenumbers [209]. The characteristic wavenumber for each secondary structure type are as follows (Table 3.2): α-helix at 1654–1658 cm^{-1}; 3_{10}-helix at 1660–1666 cm^{-1}, β-sheet with multiple peaks at 1623–1643 and 1689–1698 cm^{-1}; turn structures at 1666–1687 cm^{-1} and the random coil structure at 1646–1650 cm^{-1} [201, 202]. Some tables discriminate between the parallel and antiparallel β-sheet structures because a peak at 1689–1698 cm^{-1} is predicted for infinite antiparallel β-sheets but not for infinite parallel β-sheet. This peak however, is predicted for finite β-sheets structures, which makes it difficult to distinguish between parallel and antiparallel β-sheets using FTIR [196].

The Beer-Lambert law shows that the concentration of the molecules responsible for a vibration, c, is proportional to absorbance $A(\tilde{\nu})$ as:

$$A(\tilde{\nu}) = \varepsilon(\tilde{\nu})lc \tag{3.18}$$

where $\tilde{\nu}$ is the wavenumber, l is the effective path of the light through the sample matrix and $\varepsilon(\tilde{\nu})$ is the attenuation coefficient which is proportional to the change in transition dipole moment occurring during the vibration. Therefore, the concentration of the constituent molecules responsible for a vibration is proportional to the absorbance at the wavenumber of its normal mode. In practice, peak broadening occurs, so the area under the absorbance peak is used instead of the peak height to calculate the concentration of the molecule with an observed vibration. Fitting secondary structure peaks to the amide I absorbance band is difficult since the amide I region is broad and featureless. Therefore, the peak positions are obtained from a resolution enhanced spectrum, then fitted to the absorbance data [206].

The resolution enhanced, second derivative of the Beer-Lambert law is:

$$\frac{d^2A(\tilde{\nu})}{d\tilde{\nu}^2} = \frac{d^2\varepsilon(\tilde{\nu})}{d\tilde{\nu}^2}lc \tag{3.19}$$

Since l and c are not affected by the differentiation, quantitative information can be obtained also from the second derivative spectra [210]. Predicting the percentage secondary structure composition from the second derivative spectrum is accurate to within 4–10% of the XRD determined structures. The predictions however, are less accurate for structures with an α-helical content >60%, where the β-sheet content is commonly overestimated and the presence of β-sheets can be predicted where there are none [211].

There are a number of issues inherent to fitting FTIR data using the methods which are described below. Both the PCA and fitting techniques assume that the structure measured in XRD or modelled computationally is the same as the structure as the aqueous or dried protein measured in the FTIR studies. The amino acid side chains of tyrosine, phenylalanine, glutamine, arginine, and lysine can contribute 10–30% of the absorption in the amide I region, yet it is difficult to distinguish and subtract out these vibrations from the secondary structure vibrations [204]. Peak fitting methods assume that each structure type has the same molar absorptivity regardless of their local environment, so the percentage of each component is proportional to the peak intensity (or area). Peak fitting methods also rely on the correct number of fitted bands and assignment of each band to a secondary structure. Band assignment can be difficult for some features, for example the α-helix band is commonly assigned between 1666–1687 cm^{-1}, yet can absorb in the entire amide I range overlapping with the turn and random structure bands [196]. Some structures will absorb outside their specified range due to the distortion of structural elements or strong solvent-protein interactions [204]. Peak fittings also assume that the chosen band shape describes the system under investigation. A Lorentzian shape is used for simple molecules, whereas it is less clear for more complex structures, and is unclear if every secondary structure type will give the same band shape [204].

Chapter 4

Design and fabrication of transparent graphene microelectrode arrays

Oliver Burton (OB) grew monolayer graphene on a copper substrate. Miranda Robbins (MR) prepared, maintained and imaged the cultured rat neurons. All other experiments and analysis were performed by the author.

4.1 Introduction

Misfolded amyloid proteins are implicated in neurodegenerative diseases such as Alzheimer's disease (AD) and Parkinson's disease (PD). To address how the location and aggregation state of amyloid proteins in neurons leads to electrophysiological changes in neurons, electrophysiological recordings should be combined with advanced fluorescence imaging. Since fluorescence microscopes are commonly built in an inverted setup this requires the fabrication of transparent microelectrode arrays (MEAs). In this work, a transparent graphene MEA was designed, fabricated and characterised to enable this.

In this chapter, the constraints for building a MEA capable of concurrent electrophysiological recordings with advanced fluorescence imaging techniques on an inverted microscope are laid out. Each component of the graphene MEA is described, along with how it was designed subject to the imposed constraints. Finally, a fabrication protocol for manufacturing fully transparent graphene MEAs is proposed.

The background information about MEAs, and specifically transparent graphene MEAs can be found in Chapter 2. The background information about the characterisation techniques used here are given in Chapter 3. The devices described here are further characterised and used for electrophysiology and imaging experiments in later chapters of this thesis.

4.2 Design constraints

The requirement of a graphene MEAs to enable concurrent electrophysiological recordings and super-resolution imaging imposed a number of constraints on the design. The constraints are listed below:

1. Material processability: Each layer must be deposited and patterned using conventional microfabrication techniques and without damaging other deposited layers.

2. Biocompatibility: Every material in contact with the cells must be biocompatible with primary hippocampal neurons. The cells must adhere to the surface, grow neurites, form an interconnected network of active neurons and survive for at least 28 days.

3. Transparency: Each material must be optically transparent and compatible with advanced microscopy techniques such as widefield, confocal fluorescence and fluorescence lifetime imaging microscopy (FLIM) on inverted microscopes.

4. Device geometry: The Multichannel System MEA-2100 Mini amplifier can fit on most standard microscope stages. The MEA device must fit in this amplifier stage which accommodates a $4.9 \times 4.9\,\mathrm{mm}^2$ MEA with a height of 1 mm. The amplifier records from 60 electrodes (including the reference). The amplifier lid contains contact pins spaced by 2.4 mm, which are pressed into the planar contact pads when the lid is closed.

5. Electrode impedance: The electrode impedance must be low enough to reduce the Johnson noise described by equation 2.5 to lower than the 2.5 µV noise from the voltage trace recordings.

6. Electrode geometry: The electrode spacing must be optimised to reduce crosstalk between electrodes, yet record from synaptically connected neurons. Additionally, the electrode size must be small enough to selectively record from a few neurons, yet large enough to maintain a low impedance.

7. Encapsulation layer: An encapsulation layer must be coated over the whole surface of the device except the electrode sites. The encapsulation layer must have a high impedance >30 MΩ to prevent electrode crosstalk.

8. Stimulation: It must be possible to stimulate the neurons at the location of the recording electrode. The most common ways to stimulate are electrically using the recording electrode, or optogenetically through the electrode.

4.3 Graphene microelectrode array fabrication

In light of these constraints, a graphene MEA was designed and fabricated. The main MEA components are the substrate, electrodes, connecting leads and encapsulation layer (Figure 2.6). Each component is considered independently in light of the imposed constraints, and an appropriate lithographic patterning technique is chosen.

4.3.1 Substrate

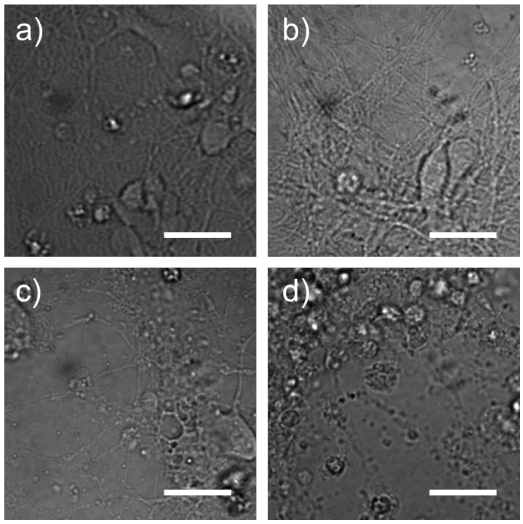

Fig. 4.1 Images of primary embryonic day 14-17 rat neurons on a) a coverslip, b) CVD graphene transferred on a coverslip, c) ITO and d) gold. Scale bar is 20 µm. Each material is biocompatible shown by the attachment of the neurons to the substrate and the sprouting of neurites. Rat neuronal cultures were prepared, plated and imaged by MR.

The first component considered is the substrate. The graphene MEA is fabricated on an underlying substrate to provide support for the device, and allow it to be handled. In previous studies, graphene MEAs have been fabricated on optically transparent substrates such as glass [92] or polymers like SU-8 [80], polyimide [32], parylene C [34] or polyethylene terephthalate (PET) [93]. However, in general these are not compatible with the high numerical aperture objectives used in high resolution fluorescence imaging which are aberration corrected for #1.5 coverslips (Constraint 3) [212].

In this device, the graphene MEAs were fabricated on #1.5 coverslips made of borosilicate glass with a thickness of 160–190 µm. Coverslips are compatible with conventional microfabrication techniques such as photolithography, thermal evaporation and lift-off in acetone (Constraint 1). The substrate is also biocompatible with rat neurons (Figure 4.1a,

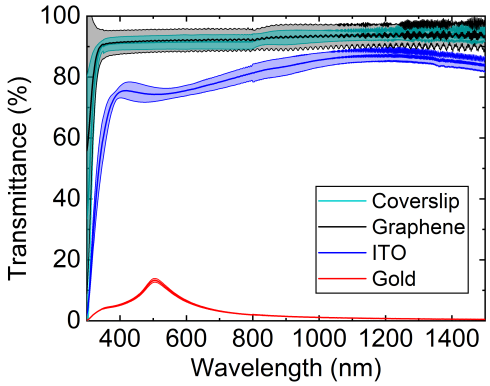

Fig. 4.2 Transmittance of light through the different conducting materials, measured using UV-vis spectrometry. The materials under investigation are a coverslip, a coverslip with monolayer CVD graphene, a coverslip with 100 nm sputter coated ITO and a coverslip with 5 nm chromium plus 50 nm gold. The coverslip, graphene on coverslip and ITO on coverslip are sufficiently transparent to allow imaging on an inverted setup, with a transmittance >91 $\pm$ 3% for the coverslip and graphene across 400–1400 nm, and >74 $\pm$ 2% for ITO across 400–1400 nm. The gold layer however is opaque with a transmittance <13 $\pm$ 1% across 400–1400 nm.

Constraint 2) shown by the attachment of the neurons to the substrate and the sprouting of neurites. The majority of objectives used in advanced fluorescence imaging are aberration corrected for these coverslips, which have a transmittance of >85% across 400–1400 nm (Figure 4.2, Constraint 3). The coverslips were cut to 4.8 $\times$ 4.8 mm to fit in the Multichannel Systems MEA-2100 Mini headstage (Constraint 4).

4.3.2 Graphene electrodes

The most critical material in the MEAs are the transparent recording electrodes. Historically, indium tin oxide (ITO) was the most common transparent conductor used in MEAs. However under repeated stimulation trains, ITO oxidises, looses transparency and increases in impedance, therefore is not suitable as an electrode material in a MEA [96]. Other possible transparent conductors used in MEAs are pillars of ZnO [99]; SnO_2 and hydrogenated amorphous silicon [100] and 40% transparent carbon nanotubes [101]. By far, the most successful transparent MEA material however is graphene [80, 32, 34, 94, 81, 93, 105], which is used in this work.

Monolayer graphene can be grown, transferred and patterned using conventional microfabrication techniques (Constraint 1). Chemical vapour deposited (CVD) graphene is ideal for this application as monolayer polycrystalline graphene can be grown on $\sim$m size scales [120]. CVD graphene was grown by Oliver Burton at ambient pressure, a temperature of

1070°C on a copper foil [122]. Methane gas was used as the carbon feedstock, argon as a dilutant and hydrogen to activate carbon binding to the metal surface and to etch multilayer domains which have relatively weak carbon-carbon bonds [123]. This gave a sample with >97% monolayer coverage, and a grain size >100 µm.

To transfer the graphene onto the coverslip, a poly(methyl methacrylate) (PMMA) supporting layer was coated over the graphene grown on copper. The PMMA layer is flexible enabling a good contact between the polymer and graphene and strong enough to prevent the fragmentation of the graphene during the etching process [125]. The disadvantage of using PMMA, is it cannot be fully removed from the graphene after the transfer without introducing additional defects to the film [213]. To pattern the transferred graphene, a mask was photolithographically defined, and the exposed graphene was etched with an O_2 plasma.

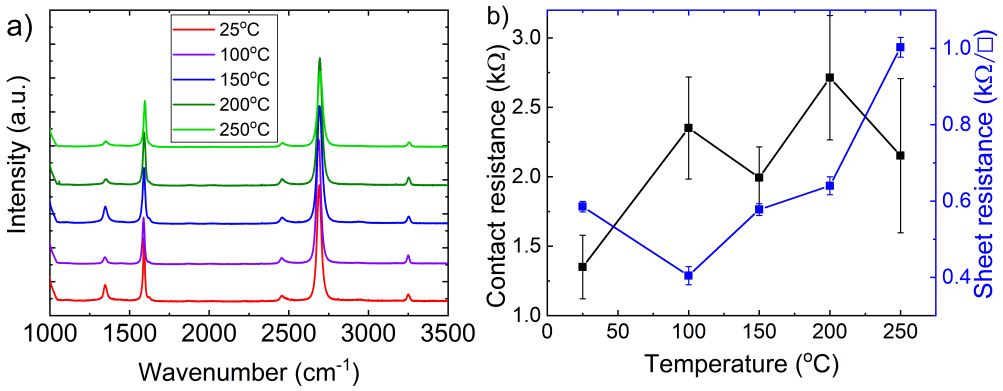

Fig. 4.3 Graphene is heated from room temperature to 250°C on a hotplate after the transfer. a) Raman spectra of graphene after each heating step. The presence of monolayer graphene through the transfer and heating steps is confirmed by the single Lorentzian shape of the 2D peak at $\sim 2680\,\mathrm{cm}^{-1}$. b) The sheet resistance and contact resistance were found using a transmission line, and the graph of sheet resistance versus channel length. The sheet resistance increased from $584 \pm 13\,\Omega\square^{-1}$ at room temperature, to $1000 \pm 20\,\Omega\square^{-1}$ at 250°C, and the contact resistance between the graphene and gold wires increased from $1.3 \pm 0.2\,\mathrm{k}\Omega$ at room temperature, to $2.1 \pm 0.5\,\mathrm{k}\Omega$ at 250°C. Graphene was grown by OB.

It was investigated whether a post transfer heating step would alter the quality of the graphene, and increase its conductivity. Thermal annealing was performed on a hotplate in air, the transferred graphene was heated sequentially for 5 min on a hotplate at increasing temperatures up to 250°C (Figure 4.3). Monolayer graphene was present on the substrate after each heating step, evidenced by the single Lorentzian shape of the 2D peak at $\sim 2680\,\mathrm{cm}^{-1}$ in the Raman spectrum. The sheet resistance and contact resistance were calculated using a transmission line measurement. The sheet resistance increased from $584 \pm 13\,\Omega\square^{-1}$ at room temperature, to $1000 \pm 20\,\Omega\square^{-1}$ at 250°C, and the contact resistance between the graphene

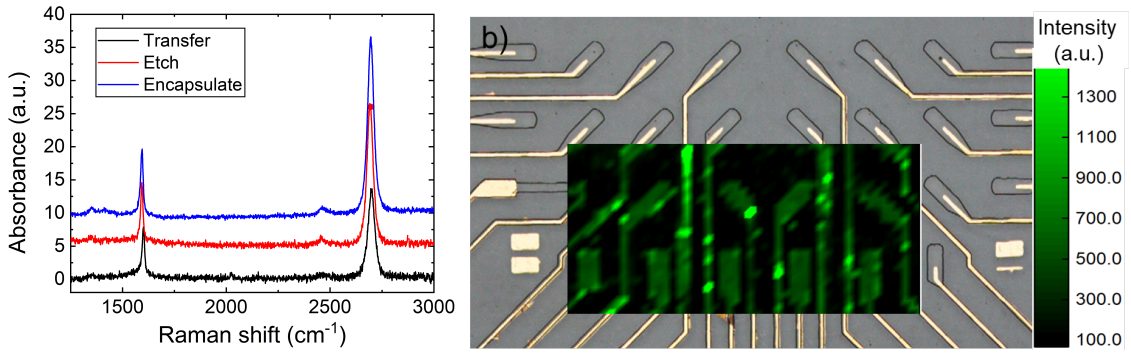

Fig. 4.4 a) Raman spectra of the graphene MEA taken at 514 nm, with a linear subtraction of the coverslip background. Spectra are taken after transferring the graphene onto glass, etching the graphene into wires, and coating and patterning a PMMA encapsulation layer over the device. The presence of monolayer graphene at each step is confirmed by the single Lorentzian shape of the 2D peak at $\sim 2680\,\mathrm{cm}^{-1}$. b) Map of the Raman intensity of the 2D peak at $2694\,\mathrm{cm}^{-1}$ overlayed on an image of the electrodes. A photolithographically defined AZ5214E mask defines the regions of graphene that has been successfully etched by O_2 plasma. Graphene was grown by OB.

and gold wires increased from $1.3 \pm 0.2\,\mathrm{k\Omega}$ at room temperature, to $2.1 \pm 0.5\,\mathrm{k\Omega}$ at 250°C. This contrasts with the thermal annealing of graphene in a vacuum [214, 215] and is likely due to oxidation of the graphene in air. Based on these results, no post transfer heating step was implemented.

Since the optical contrast of graphene on a coverslip is extremely low, Raman spectroscopy was used to identify and characterise the graphene at each fabrication stage (Figure 4.4). After transfer, a mask was photolithographically defined, and the exposed graphene was etched using O_2 plasma. The successful patterning of the graphene was confirmed by Raman mapping the 2D peak at $2694\,\mathrm{cm}^{-1}$.

To characterise the graphene using the Raman spectra, a single Lorentzian peak was fitted under each of the D ($\sim 1350\,\mathrm{cm}^{-1}$), G ($\sim 1580\,\mathrm{cm}^{-1}$) and 2D ($\sim 2680\,\mathrm{cm}^{-1}$) Raman peaks (Table 4.1). The good fit of a single Lorentzian to the 2D peak confirms the transferred material was monolayer graphene [155]. Mean defect density can be calculated from the intensity ratio of the D to the G peak which was ($I(D)/I(G) < 0.2$). The low defect concentration renders Equation 3.2 inaccurate, so it was concluded that the mean defect density was $n_D < 2 \times 10^{10}\,\mathrm{cm}^{-2}$ giving a mean interdefect distance of $L_D > 30\,\mathrm{nm}$ [159]. Charge carrier concentration from doping can be determined from the position of the G or 2D peak ($\tilde{\nu}(G)$, $\tilde{\nu}(2D)$), the full width at half maximum of the G peak ($\Gamma(G)$), the intensity ratio of the 2D to G peak $I(2D)/I(G)$, or the area ratio of the 2D to G peak $a(2D)/a(G)$ [158]. $I(2D)/I(G)$ is not affected by strain, so was used to calculate the charge carrier concentration

Table 4.1 Fit of the Raman spectra of graphene at each stage of fabricating a graphene MEA, giving the Raman shift, $\tilde{\nu}$, width, Γ and intensity I, of each peak. The parameters are given from a single Lorentz fit of the Raman D peak at $\sim 1350\,\mathrm{cm}^{-1}$, G peak at $\sim 1580\,\mathrm{cm}^{-1}$ and 2D peak at $\sim 2690\,\mathrm{cm}^{-1}$ at each processing step. Additionally, the defect and doping levels as calculated from these peak fittings. The concentration of defects, n_D, was calculated from $I(D)/I(G)$, and the concentration of holes from doping, n_h, as calculated from $I(2D)/I(G)$. Graphene was grown by OB.

Peak	Transfer	Etch	Encapsulate
D peak			
$\tilde{\nu}$ (cm^{-1})	1350 ± 8	1350 ± 8	1360 ± 9
Γ (cm^{-1})	32 ± 18	27 ± 16	40 ± 30
I (a.u.)	0.6 ± 0.6	1.2 ± 1.6	0.5 ± 0.6
G peak			
$\tilde{\nu}$ (cm^{-1})	1591 ± 6	1593 ± 6	1592 ± 4
Γ (cm^{-1})	23 ± 6	23 ± 6	20 ± 7
I (a.u.)	3.3 ± 1.3	3.3 ± 1.2	3.8 ± 1.7
2D peak			
$\tilde{\nu}$ (cm^{-1})	2693 ± 6	2695 ± 4	2696 ± 4
Γ (cm^{-1})	40 ± 7	39 ± 6	37 ± 6
I (a.u.)	8.4 ± 3	7 ± 2	7 ± 2
Doping & defects			
n_D ($\times 10^{12}\,\mathrm{cm}^{-1}$)	< 0.02	< 0.02	< 0.02
n_h ($\times 10^{12}\,\mathrm{cm}^{-1}$)	3 ± 3	3 ± 4	3 ± 3

from doping as $n_h = 3 \times 10^{12}\,\mathrm{cm}^{-2}$. Generally, the graphene grown on copper is n-doped [216], but becomes p-doped after PMMA assisted transfer with ammonium persulphate etching [217].

The biocompatibility of the graphene (Constraint 2) was investigated by imaging embryonic day 18 rat neurons on graphene and glass substrates (Figure 4.1a,b). The criteria for neuronal viability was the neurons had survived on the substrate to this age without clustering, rounding up or dying, and in addition grew axonal and dendtritic extentions. This was true for both the graphene and glass substrates, so they were deemed sufficiently biocompatible for this context in agreement with Rastogi *et al.* [147].

The transparency of the graphene is important for constraint 3. The transparency of graphene transferred onto a coverslip measured using UV-vis spectroscopy had a high transmittance of $>91 \pm 3\%$ of light from 400–1500 nm (Figure 4.2). This makes sense since a single graphene layer absorbs 2.3% of light from 400–750 nm [106].

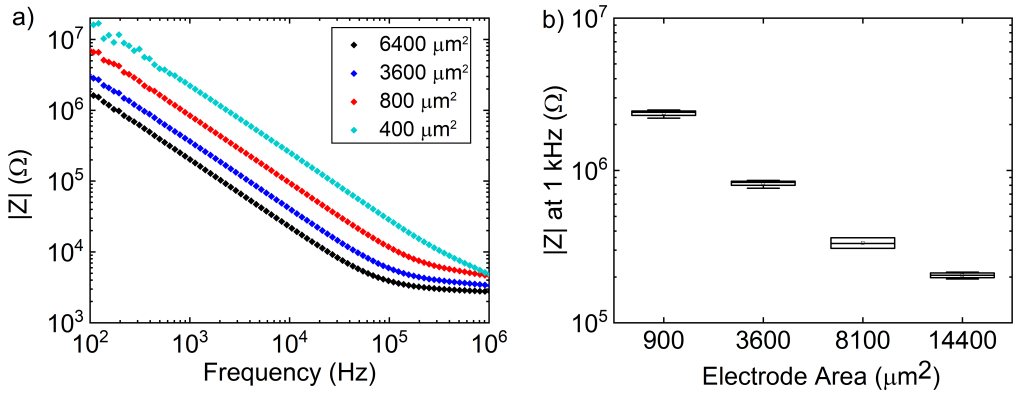

Fig. 4.5 a) Electrochemical impedance spectra and b) Box plot showing the dependence of 1 kHz impedance magnitude on area for gold electrodes in phosphate buffered saline. The box shows the mean, upper and lower quartile, and the whiskers represent 1.5× the inter quartile range. The data shows the decrease in electrochemical impedance magnitude when the electrode area is changed from $2.378 \pm 0.012\,\text{M}\Omega$ for a $14400\,\mu\text{m}^2$ electrode to $205 \pm 9\,\text{k}\Omega$ for a $900\,\mu\text{m}^2$ electrode.

The finished device was used in a Multichannel System MEA-2100 Mini amplifier. This amplifier can record from 60 electrodes, therefore the device was fabricated with 60 working electrodes (Constraint 4). To ensure crosstalk between the electrodes does not need to be considered in the data analysis (Constraint 6), the electrodes should be spaced by at least 100 µm [47]. Devices with a lower electrode spacing, and therefore a higher density of electrodes are able to record sub-cellular features, but can experience the effects of cross talk especially for high impedance electrodes [66, 218]. To ensure recording from a synaptically connected network of neurons, the electrode spacing should be smaller than the length of neuronal axons *in vivo* which is up to 500 mm in rats [219]. In this graphene MEA, the electrodes were spaced by 200 µm, allowing an area of $1.6\,\text{mm}^2$ to be mapped by electrodes.

In general the larger the recording electrode area, the smaller the electrode impedance and subsequently the Johnson noise (Figure 4.5). However, smaller electrodes have a greater specificity since they record from fewer neurons. For the gold electrodes in phosphate buffered saline (PBS), the impedance magnitude decreases from $2.378 \pm 0.012\,\text{M}\Omega$ for a $14400\,\mu\text{m}^2$ electrode to $205 \pm 9\,\text{k}\Omega$ for a $900\,\mu\text{m}^2$ electrode. The fabricated electrodes had a diameter of 30 µm larger than the size of a neuronal soma (5–20 µm in diameter) [42]. The measured voltage trace will be the superposition of signals from 10s of neurons, including the neurons in contact with the electrode and signal from a broader surrounding area up to 100 µm away. Assuming each firing neuron has a distinct spike shape, individual neurons should be identifiable from the ensemble voltage trace measurement by grouping the spikes

by shape [84]. The planar internal reference electrode was made of gold with an area of 26.3 mm^2.

Each MEA included two features to check the resistance of the transferred graphene. Firstly, two electrodes were short circuited by a graphene bridge, to measure the resistance of the connecting wires plus the 50×200 µm graphene strip. The second was a transmission line outside the recording area which allowed the graphene sheet resistance to be calculated using equation 3.4 to be $500 \pm 200\,\Omega$.

Having worked through each constraint related to the graphene electrodes, the final graphene MEA design used transparent graphene electrodes, grown by CVD on a copper catalyst and transferred onto the substrate using a PMMA supporting layer. There were sixty electrodes with a diameter of 30 µm and a pitch of 200 µm. This geometry allows for the direct comparison with devices purchased from Multichannel Systems. From characterising the graphene, we found $n_D < 2 \times 10^{10}\,cm^{-2}$, $n_h = 3 \times 10^{12}\,cm^{-2}$ and the graphene sheet resistance is $500 \pm 200\,\Omega$.

4.3.3 Connecting leads

The lid of the Multichannel Systems MEA2100-60 headstage contains 60 pins spaced by 2.4 mm. When the lid is closed, the pins press against the 2.2 mm^2 contact pads on the MEA to connect the amplifier and the MEA. Connecting leads interface between the external contact pads and the internal electrodes. Since graphene would delaminate when contacted by the pins and has a high sheet resistance, the connecting leads were fabricated from Au or ITO. Three designs for the connecting wires were considered, pure gold wires, pure ITO wires and a 5 mm^2 central ITO region with external gold leads (Figure 4.6) [220, 97]. In addition, with each wire has a short 15 µm graphene length bridging to the graphene electrode.

The pattern for the connecting leads was defined by photolithography and lift-off. The Au and ITO were deposited by thermal evaporation and sputter deposition respectively (Constraint 1).

The ITO on coverslip is sufficiently transparent to allow imaging on an inverted setup (Constraint 3), with a transmittance $>74 \pm 2\%$ across 400–1400 nm. The gold layer however is opaque with a transmittance $< 13 \pm 1\%$ across 400–1400 nm (Figure 4.2). The Au-ITO and pure ITO lead configurations give transparent central regions.

Complete devices were fabricated using the different lead materials, with a short circuit between two central electrodes to enable the resistance of the leads to be measured (Constraint 5). The resistance of the Au, Au-ITO and ITO leads were 0.70 ± 0.03, 8 ± 3 and $23 \pm 7\,k\Omega$ respectively, with a Johnson noise of 0.32 ± 0.06, 1.1 ± 0.7 and $1.9 \pm 1.0\,\mu V$ respectively given a bandwidth of 10 kHz. The mean noise measured in the voltage trace recordings was

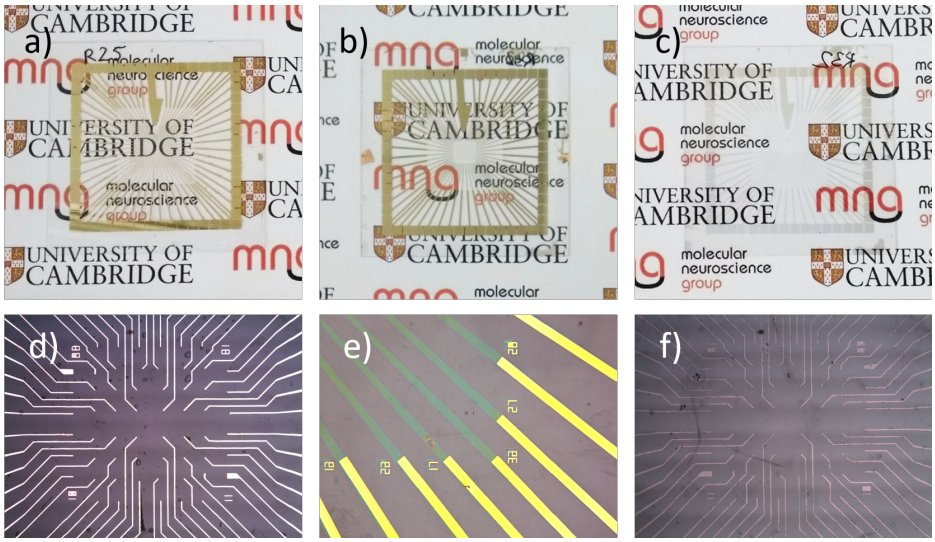

Fig. 4.6 Images of a MEA with a) gold connecting leads b) transparent ITO central region with gold connections and c) transparent ITO connecting leads. Images of the connecting leads showing d) gold connecting leads, e) the gold-ITO junction and f) ITO connecting leads.

2.5 µV, which is similar to the lead contribution for the pure ITO leads. Therefore, the Au or Au-ITO wire configurations were deemed to have a sufficiently low resistance for this application.

Table 4.2 Resistance of the connecting leads for the graphene MEA, with the corresponding Johnson noise from the leads. The Au-ITO arrangement was chosen as the most suitable since it combines a relatively low lead resistance and resultant Johnson noise of 1.1 ± 0.7 with a high transmittance at 550 nm of $74.6 \pm 1.7\%$.

Lead material	Resistance (kΩ)	Noise* (µV)	Transmittance at 550 nm (%)
Au	0.70 ± 0.03	0.32 ± 0.06	10.0 ± 0.4
Au-ITO	8 ± 3	1.1 ± 0.7	74.6 ± 1.7
ITO	23 ± 7	1.9 ± 1.0	74.6 ± 1.7

*Johnson noise with 10 kHz bandwidth, calculated from Equation 2.5

The Au-ITO connecting leads were chosen to bridge between the graphene electrode and amplifier. This ensures transparent connecting leads in the central region where cells are cultured. In addition, it means the lead resistance has a minimal effect on the recorded noise (Table 4.2).

4.3.4 Encapsulation layer

An encapsulation layer covered the entire device, with etched holes to allow the neurons to contact the electrodes. This ensured the recorded signal only came from the electrode site and not from contact with the neurons at different places along the leads or from crosstalk between the leads.

The materials used as the encapsulation layer in past transparent graphene MEAs, are PDMS [80], parylene C [34], polyimide-8820 [94] and SU-8 [32]. Regarding the processability (Constraint 1), PDMS and parylene C are typically patterned using an O_2 plasma which also etches graphene [221] and therefore requires an additional protective layer that must be etched separately; and Polyimide-8820 is a photodefinable polymer which is cured upon heating to 350°C, which would greatly increase the resistance of the graphene if heated in air (Figure 4.3), however could possibly be used if cured under vacuum. The materials investigated which could be deposited and etched without the need for additional protective layers or damaging the graphene were the Multichannel Systems standard Si_3N_4 which can be etched with phosphoric acid [222]); the photoresists SU-8 and AZ5214E; the electron beam resist PMMA; and Al_2O_3 which can be etched with TMAH (tetra-methyl ammonium hydroxide). A summary of the deposition and etching methods for each proposed encapsulation layer can be seen in Table 4.3.

Table 4.3 Deposition and etching methods for different possible encapsulation layers that can be used in an MEA. The chemical TMAH is tetra-methyl ammonium hydroxide, PGMEA is propylene glycol methyl ether acetate, IPA is isopropyl alcohol, ALD is atomic layer deposition.

Material	Deposition method	Etching method
Parylene C	CVD	O_2 plasma
Polyimide-8820	Spincoat	Photolithography, develop TMAH
SU-8	Spincoat	Photolithography, develop PGMEA
Si_3N_4	CVD	Phosphoric acid
AZ5214E	Spincoat	Photolithography, develop TMAH
PMMA	Spincoat	Electron beam lithography, develop water/IPA
Al_2O_3	ALD	TMAH

The majority of the cultured cells will be in contact with the encapsulation layer (Constraint 2). The biocompatibility of each encapsulation material was tested by culturing rat neurons on coverslips coated with each material (Figure 4.7) and looking at the cell viability. From visual inspection, it can be seen that the coverslip, Si_3N_4, PMMA and Al_2O_3 were biocompatible, with the neurons adhering to the coverslip and sprouting many neurites.

AZ5214E and SU-8 were deemed not to be biocompatible since isolated dead spherical cells are observed with no neurites [223].

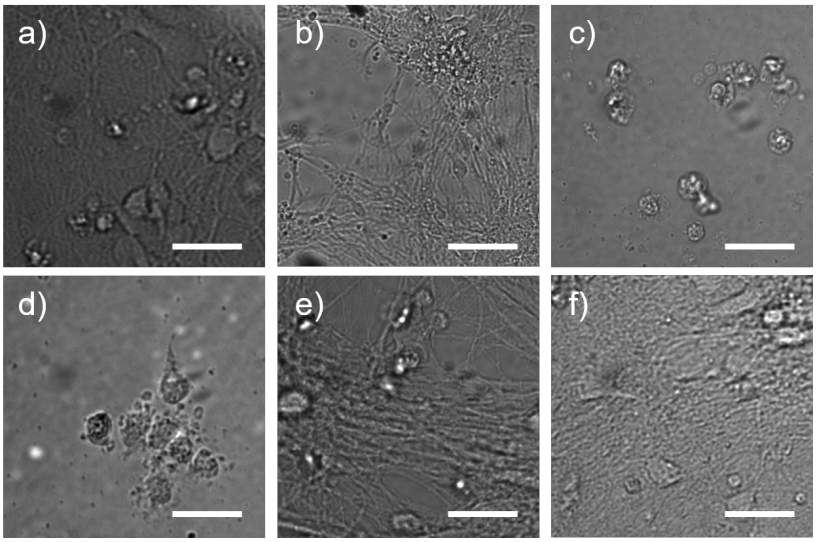

Fig. 4.7 Images of primary embryonic day 14-17 rat neurons on a) a) coverslip b) Si_3N_4, c) SU-8, d) AZ5214E, e) PMMA and f) Al_2O_3 to test cell viability. Scale bar is 20 µm. For the biocompatible materials the coverslip, Si_3N_4, PMMA and Al_2O_3, the neurons adhered to the substrate and sprouted neurites. For AZ5214E and SU-8, isolated dead spherical cell bodies can be observed with no neurites. Neurons were prepared, maintained and imaged by MR.

To test constraint 3, UV-vis spectroscopy was performed for each encapsulation material deposited on a coverslip (Figure 4.8). Each encapsulation material tested had a high transparency at >$87 \pm 3\%$ for SU-8, PMMA and Al_2O_3 from 400–1500 nm, and for AZ5214E from 440–1500 nm.

A high (>30 MΩ [23]) impedance across the encapsulation layer reduces the crosstalk between electrodes and the leakage current (Constraint 7). The Si_3N_4 layer on the standard Multichannel Systems MEAs had a shunt impedance at 1 kHz of 900 ± 200 kΩ. The impedance magnitude of the other materials are 1.9 ± 0.6, 1.9 ± 0.7, 0.4 ± 0.2 and 1.2 ± 0.5 MΩ for SU-8, AZ5214E, PMMA and Al_2O_3 respectively (Figure 4.9). Each trialled material has an impedance lower than that suggested by Gross *et al.* but higher than the Multichannel Systems Si_3N_4 standard. The PMMA impedance magnitude is lower than that of the other trialled materials, and similar to the magnitude of graphene, which could be problematic as an encapsulation layer. To behave as a purely capacitive blocking layer, the impedance phase should be $-90°$, like for the inorganic materials Si_3N_4 and Al_2O_3 which have phases of -89.4 ± 1.2 and $-89.6 \pm 0.5°$ respectively. The impedance phase for PMMA is low at $-65 \pm 5°$, possibly due to a low stability of PMMA in water.

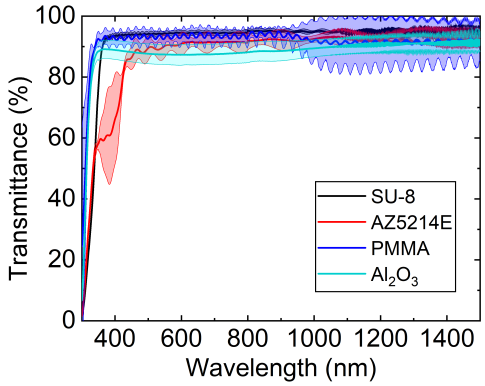

Fig. 4.8 Ultraviolet-visible spectrum showing the transmittance through different encapsulation layers coated on a coverslip. The transmittance was high for each material, being >87 ± 3% for SU-8, PMMA and Al_2O_3 from 400–1500 nm, and for AZ5214E from 440–1500 nm.

Both PMMA and Al_2O_3 passed every constraint applied to the encapsulation layer (Table 4.4). Both materials can be deposited and patterned, are biocompatible, transparent and have a high shunt impedance. A 500 nm PMMA encapsulation layer was used in the final devices. This was simpler to deposit and pattern than Al_2O_3, as it could be deposited and etched by spin coating and pattern using electron beam lithography, whereas Al_2O_3 was deposited by atomic layer deposition (ALD) and patterned using a PMMA mask, electron beam lithography and TMAH wet etching. The impedance magnitude of PMMA however is near that for graphene, and could potentially show water leakage.

Table 4.4 Suitability of different encapsulation layers for a MEA. PMMA and Al_2O_3 passed every constraint applied to the encapsulation layer. Both materials can both be deposited and patterned, are biocompatible, transparent and have a high impedance.

Material	Thickness (nm)	Transmittance at 550 nm (%)	|Z| at 1 kHz (MΩ)	Biocompatible
Si_3N_4*	500	-	1.0 ± 0.3	Yes
SU-8	5000	93.9	19 ± 6	No
AZ5214E	1400	92.1	19 ± 7	No
PMMA	500	93.0	2 ± 2	Yes
Al_2O_3	100	91.7	12 ± 5	Yes

*Si_3N_4 from Multichannel Systems 60ThinMEA200/30iR-ITO

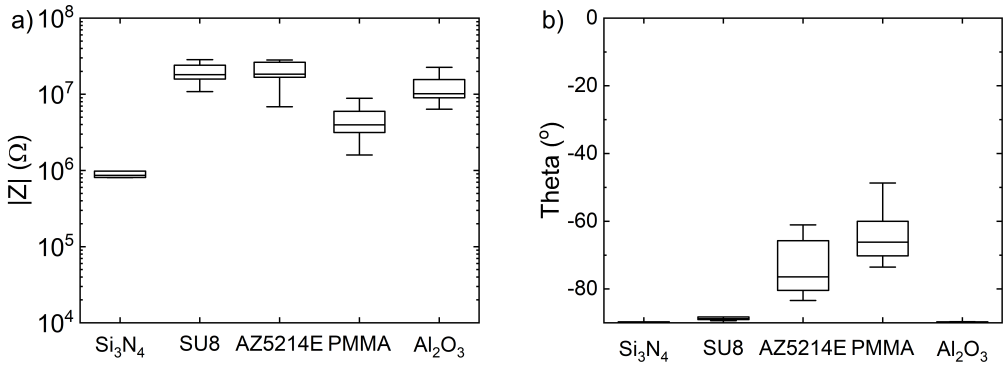

Fig. 4.9 Box plot showing the a) magnitude and b) phase of the 1 kHz impedance measured between a gold wire and reference electrode under different possible encapsulation layers, in a PBS saline solution. The box shows the mean, upper and lower quartile, and the whiskers represent 1.5× the inter quartile range. The Si_3N_4 provides a comparison to the Multichannel Systems commercial standard. Each investigated material has a shunt resistance higher than the Multichannel Systems standard. The inorganic materials Si_3N_4 and Al_2O_3 show the most capacitive-like blocking behaviour with a phase closest to $-90°$

4.3.5 Preparation for cell culture

MEA devices bought from Multichannel Systems have a glass culture ring glued onto the device. To mirror this, a glass ring with an inner diameter of 19 mm and an outer diameter of 24 mm was attached using a multipurpose silicone sealant [224]. The sealant formed a liquid-impermeable seal, and did not induce cell death in the cultured neurons as evidenced by the successful culture of neurons within the wells. A removable semi-permeable fluorinated ethylene-propylene membrane was used to reduce evaporation from the wells during the cell culture.

A number of sterilisation techniques were investigated to clean the MEAs before plating cells, these include O_2 plasma, autoclaving, soaking in ethanol, and UV (ultraviolet) exposure. O_2 plasma treatment was unsuitable for use with graphene MEAs as it etches graphene from the electrodes. Autoclaving had the potential to damage the devices with the applied heat. Using only an ethanol soaking step did not prevent infections. The sterilisation technique chosen was therefore a combination of UV exposure and soaking in ethanol, which prevented infections during the cell culture. To assess the stability of the graphene after sterilisation, and especially UV exposure which could oxidise the graphene, Raman spectroscopy or impedance measurements should be performed after sterilisation.

4.3.6 Lithography

The graphene MEA fabrication requires material deposition, patterning and aligning with a minimum feature size of 12 µm precision on a coverslip (Constraint 1). During the lithographic patterning, a polymer resist was coated over the partially fabricated device. Specified areas of the resist were exposed to photons or electrons, changing the local resist solubility. The more soluble areas were preferentially dissolved to create a mask for further processing steps like etching or deposition. The lithographic techniques used were a direct laser writer with the image reversal photoresist AZ5214E, and electron beam lithography with PMMA. Both technologies are maskless lithographies which directly implement a pattern drawn in AutoCAD (Figure 4.10) [225, 226]. This is ideal for prototyping devices in a research laboratory.

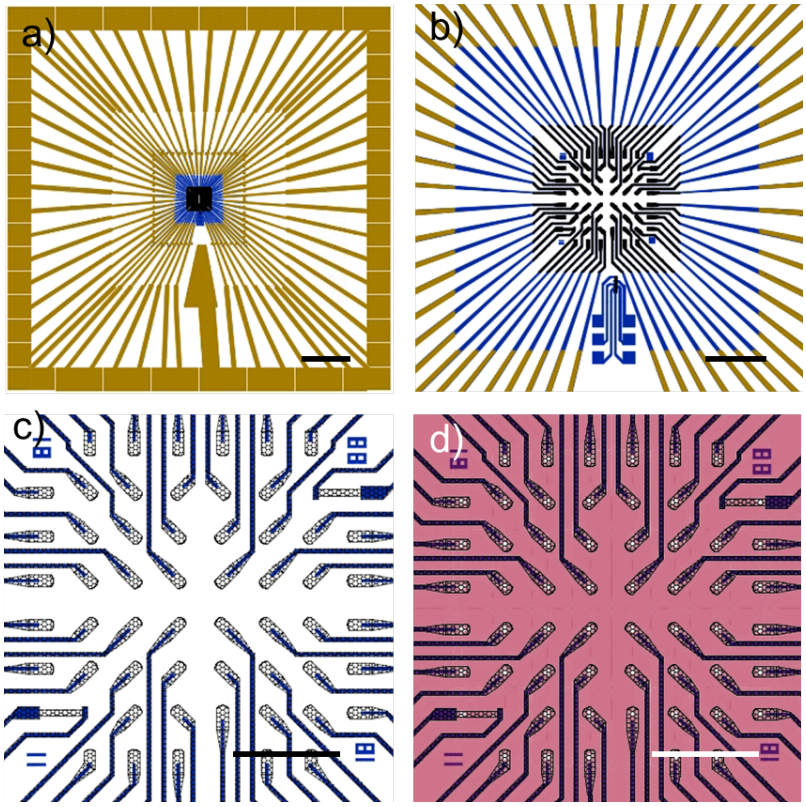

Fig. 4.10 CAD design showing the layers used when fabricating a graphene MEA. Dark yellow is gold, blue is ITO, black patterned is graphene and red is the insulating layer. a), b), c) Gold to ITO connecting leads with graphene electrodes, the scale bars are 5, 1 and 0.5 mm respectively. d) The encapsulation layer is shown in pink covering the structure with holes etched at the electrode sites. The scale bars are 5 mm, 1 mm, 0.5 mm and 0.5 mm respectively.

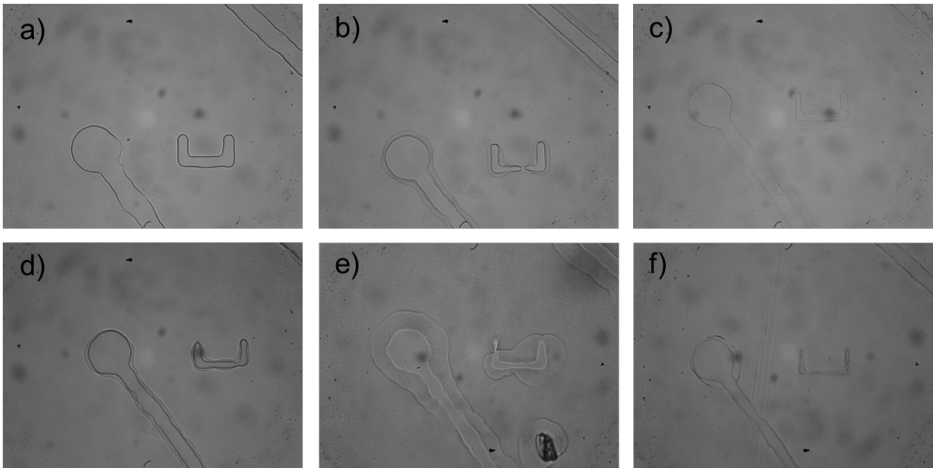

Fig. 4.11 Optimisation of image reversal photoresist AZ5214E on a coverslip. The AZ5214E is spin coated at 500 rpm 5 s, then 4000 rpm 40 s and baked at 105°C followed by 405 nm patterned exposure with different doses. The resist is then baked at different temperatures and has a flood exposure of 260 mJcm^{-2}. In this work, a pre-bake dose of 55 mJcm^{-2} was chosen with a baking temperature of 100°C.

Firstly, the direct laser writer with the image reversal photoresist AZ5214E was optimised for use with the coverslips. With a direct laser writer, light is scanned across the photoresist, exposing areas in a predefined pattern. The image reversal photoresist AZ5214E includes a crosslinking agent which is active above 110°C in exposed areas. After flood exposure and development, the non-crosslinked regions remain giving a negative image of the mask pattern, and a negative wall profile ideal for lift-off techniques. The laser writer process was optimised for the coverslips with an objective lens capable of writing features >8 µm. The most critical parameters are the image reversal temperature and the initial exposure dose (Figure 4.11). For a low pre-bake dose or high temperature, the pattern will not fully develop (Figure 4.11c,e,f). For a high pre-bake dose or low temperature, the pattern will overdevelop (Figure 4.11a). In this work, a pre-bake dose of 55 mJcm^{-2} was chosen with a baking temperature of 100°C.

Electron beam lithography was used to pattern PMMA. A beam of electrons was scanned across the resist, exposing areas according to a predefined pattern. Due to the insulating nature of the PMMA and the glass coverslip substrate, charge builds up during the patterning distorting the features [227], to prevent this a charge dissipation layer is needed [228]. In this work the charge dissipation layer was 15 nm gold deposited by thermal evaporation over the PMMA layer and removed after the lithography.

4.3.7 Summary of graphene microelectrode array design

A graphene MEA was designed within the constraints described in Section 4.2. The graphene MEA was fabricated on a 170 µm glass coverslip. The recording electrode sites were fabricated from CVD graphene grown on copper and transferred to the substrate. There were 60 circular electrodes, 30 µm in diameter, with a spacing of 200 µm. Connecting leads were fabricated from ITO and gold, providing external contact pads for the amplifier. An encapsulation material made of PMMA was deposited over the device, with holes patterned by electron beam lithography at the recording electrode sites.

4.4 Graphene microelectrode array fabrication protocol

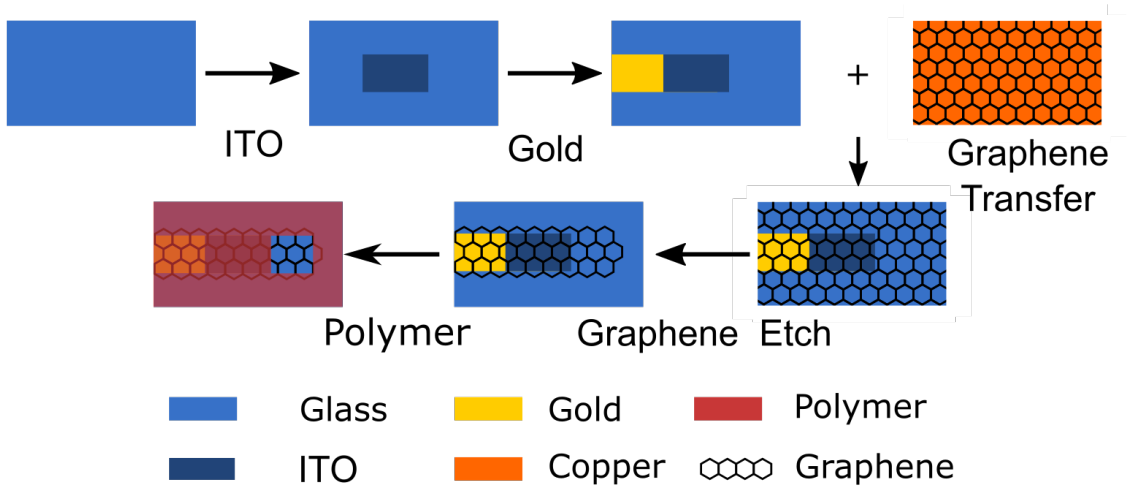

Fig. 4.12 Schematic showing the fabrication of a graphene MEA with ITO and gold connecting leads and a polymer encapsulation layer.

Based on the design specified from the constraints, an optimised fabrication protocol was developed for making graphene MEAs. The graphene MEAs were fabricated following the schematic in Figure 4.12. Images at each fabrication stage are shown in Figure 4.13. The substrates were $48 \times 48\,\text{mm}^2$ #1.5 borosilicate glass coverslips purchased from Soham Scientific. To remove glass dust remaining from the cutting process, the substrates were cleaned by ultrasonication in 1:10 deacon 90 soap:water, rinsed in water to remove the soap, ultrasonicated in acetone to remove organic residues and rinsed in isopropyl alcohol (IPA) to remove acetone residues.

Photolithography was performed using image reversal process with AZ5214E photoresist and a direct laser writer to create a negative wall profile for the lift-off process. ITO (100 nm)

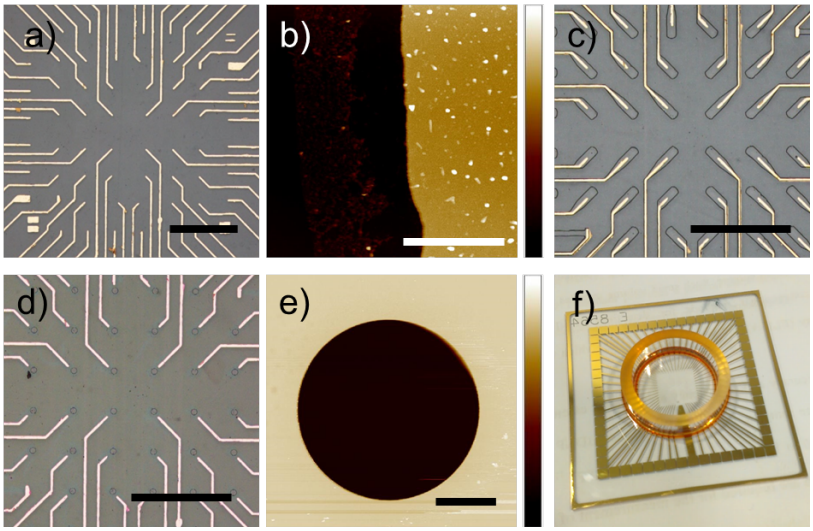

Fig. 4.13 a) Optical image of connecting leads with 500 µm scale bar. b) AFM of gold leads with 2 µm scale bar, and 100 nm height range. c) Optical image of connecting leads with pattern for graphene etching defined by photolithography with 500 µm scale bar. d) Connecting leads with graphene electrodes exposed by etching holes in the encapsulation layer with 500 µm scale bar. e) AFM of hole in PMMA encapsulation layer with 10 µm scale bar, and 600 nm height range. f) Finished MEA with glass culture ring attached.

was sputter deposited using Ar ions at 50 W, to form the patterned wires (blue in Figure 4.10). For the gold deposition, a second photolithography was performed using identical conditions (yellow in Figure 4.10). The layers were aligned by matching points on the deposited ITO pattern to the CAD design. Chromium/ gold (5 nm/50 nm) was deposited using thermal evaporation (Figure 4.13b). Chromium provided an adhesion layer between the glass and gold.

Monolayer graphene was grown on copper foil by Oliver Burton, at ambient pressure, a temperature of 1070°C on a copper foil [122], with methane, argon and hydrogen gasses. This gave a sample with >97% monolayer coverage, and a grain size >100 µm.

Graphene was transferred on top of the connecting leads using a wet transfer method. PMMA was spin coated on the copper/graphene and the copper was etched using an ammonium persulphate solution. The remaining graphene/PMMA was washed in water and transferred over the wires. PMMA was removed by soaking in acetone. The pattern for graphene etching was made using AZ5214E as a positive photoresist with a direct laser writer, (black hatched in Figure 4.10). The results of the photolithography can be seen in Figure 4.13c. Exposed graphene was etched using an O_2 reactive ion etcher, and the AZ5214E resist was removed in acetone leaving the bare graphene wires.

To form the encapsulation layer, PMMA was spin coated over the device and patterned using electron beam lithography. A 15 nm conductive gold layer was coated over the device as a discharge layer to enable charge dissipation of the incident electrons. 30 µm holes were opened in the PMMA layer (red in Figure 4.10d, and 4.13d,e) to create an array of sixty electrodes with a pitch of 200 µm. The PMMA was removed from the external contact pads using a selective acetone bath.

To form a well for cell culture, a glass ring (inner diameter 19 mm, outer diameter 24 mm, purchased from Soham Scientific) was attached using multipurpose silicone-elastomer based sealant (Dow Corning® 732, Figure 4.13f). A removable semipermiable fluorinated ethylene-propylene membrane was used to reduce evaporation from the wells during the cell culture.

4.5 Conclusion

A transparent graphene MEA was designed and fabricated to combine electrophysiology from MEA recordings and advanced fluorescence imaging. The application imposed design constraints based on the material processability, biocompatibility, transparency, device geometry, electrode impedance, electrode geometry, encapsulation layer and the need to stimulate the neurons.

The substrate was a #1.5 coverslip, since the high numerical aperture objectives used in advanced fluorescence microscopy are aberration corrected for these coverslips. The transparent electrode was graphene since it can be grown, transferred and patterned using conventional microfabrication processes, is biocompatible with primary neurons, and is transparent. The graphene electrodes were 30 µm in diameter, with a spacing of 200 µm which mirrors commercial devices that can be purchased from Multichannel Systems. Connecting leads bridged between the graphene electrodes and the amplifier pins. The leads had a transparent ITO central region, and gold external leads which have a low resistivity. Finally, Al_2O_3 and PMMA were identified as possible encapsulation layers which can be deposited over the device, with holes etched at the electrodes. Both materials were patternable without damaging the graphene, were biocompatible with the neurons, had a high impedance, were transparent and had a high blocking impedance. The devices were fabricated using maskless lithography techniques which give the maximum flexibility in the device design.

Chapter 5

Electrochemical impedance spectroscopy of graphene microelectrode arrays

5.1 Introduction

The graphene microelectrode array (MEA) has different materials for the leads, encapsulation layer and working graphene electrodes. The electrical or electrochemical properties of each layer affects the device operation. Electrochemical impedance spectroscopy (EIS) is a nondestructive technique used to study the electrical and electrochemical properties of MEAs. The EIS spectra give information about the reproducibility of the manufacturing process and breaks in the device. By fitting physically relevant equivalent circuit models (ECMs) to the EIS data, the electrochemical properties of the electrode-electrolyte interface can be decoupled from the other EIS contributions. The electrochemical properties of the electrode-electrolyte interface describe about how the biological action potentials to are converted to electrical voltage traces.

In this chapter, the electrical and electrochemical properties of a graphene MEA are characterised using EIS. Firstly the electrical properties of each component in the graphene MEA are probed independently. Following this, EIS spectra are obtained by measuring the impedance between the graphene electrode and a large reference electrode in a saline solution. To interpret these data, the ECMs used in previous studies of graphene MEAs are compared, and an ECM is identified which fits the data well and is physically relevant. Knowledge obtained from the fitting is used to gain information about the reproducibility of the manufacturing, breakages in the device and the electrode-electrolyte interface.

The protocol for designing and fabricating the graphene MEA used here is found in Chapter 4. Background information about the Raman spectroscopy of graphene can be found

in Section 3.1.1. Background information about EIS, fitting ECMs and the application of this to MEAs can be found in Section 3.1.4. Background information about neuron-electrode coupling can be found in Section 2.2.2.

5.2 Electrical characterisation of graphene microelectrode arrays

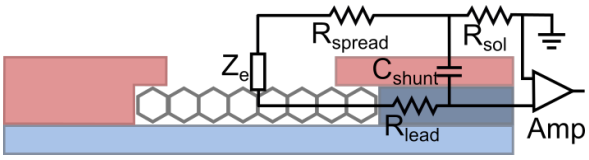

Fig. 5.1 A graphene MEA has four main components the substrate (light blue), connecting leads (dark blue), encapsulation layer (red) and recording graphene electrode (black hexagons). Overlayed is the lumped circuit model (LCM) describing the electrical properties of the electrode-electrolyte interface without cells. The LCM contains the spreading resistance R_{spread}, solution resistance R_{sol}, electrode-electrolyte impedance Z_e, shunt capacitance across the encapsulation layer C_{shunt} and lead resistance R_{lead}.

A graphene MEA contains different components which have distinct electrical or electrochemical properties and affect the device operation. The graphene MEA has four major components (Figure 5.1): the glass coverslip substrate; the gold connecting leads which bridge between the working electrode and the amplifier; the poly(methyl methacrylate) (PMMA) encapsulation layer which insulates the leads; and finally the working graphene electrodes which act as transducers converting the neuronal action potentials to electrical voltage traces.

Each component has a distinct electrical or electrochemical response, and will be considered individually in this section. The coverslip behaves as a dielectric. The connecting leads behave as a resistor, R_{lead}. The an ideal encapsulation layer behaves as a capacitor, C_{shunt}. The saline solution has a solution resistance, R_{sol}. The graphene electrodes show a complex electrochemical impedance, Z_e where charge is transferred resistively through Faradaic reactions or capacitively though charging and discharging the electrical double layer.

5.2.1 Resistance of the leads

Gold leads (with a 50 µm graphene bridge) connect the graphene electrodes to the amplifier. They have a purely resistive electrical properties. The resistance of the gold leads

(21 mm×12 µm×50 nm) was measured by joining two neighbouring leads. The gold lead resistance was 351±14 Ω. The resistance of the gold leads plus the 50 µm graphene bridge to the electrode site was $R_{lead} = 2.4 \pm 0.4\,\text{k}\Omega$.

5.2.2 Capacitance of the encapsulation layer

A PMMA encapsulation layer covers the entire device. Holes are etched through the encapsulation to enable cells to contact the electrode. The PMMA thickness was confirmed by atomic force microscopy (AFM) to be 500 nm. The EIS spectrum between an encapsulated working electrode and the reference electrode coated with PMMA and covered with phosphate buffered saline (PBS) was measured (Figure 5.2). Electrically, the dielectric PMMA encapsulation layer is highly capacitive properties above 5 kHz, however at lower frequencies than this leakage of electrolyte through the PMMA layer becomes significant. By fitting a resistor and capacitor in parallel to this spectrum, a shunt resistance of $60 \pm 50\,\text{M}\Omega$ and shunt capacitance of $C_{shunt} = 8 \pm 3\,\text{pF}$ was found.

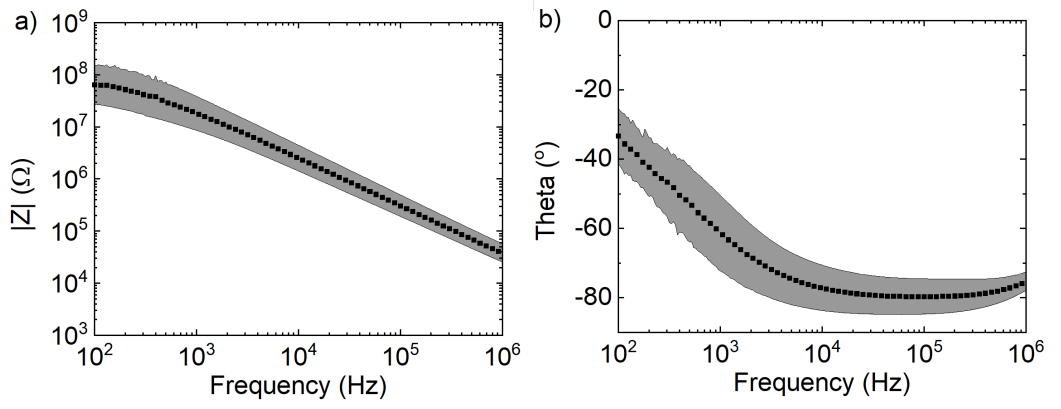

Fig. 5.2 Representative plots of the a) magnitude and b) phase of the electrochemical impedance spectrum between a 26.3 mm^2 gold reference electrode and a 706 µm^2 graphene working electrode with a 500 nm with a PMMA coating and covered with PBS.

5.2.3 Quantum capacitance of graphene

The graphene working electrode acts as a transducer between the neuronal action potential and electrical voltage trace. For a conventional electrode, the transduction mechanism combines the charging and discharging of the electrical double layer, and the Faradaic reactions at the electrode surface. For graphene, in addition to these properties, a quantum capacitance is induced if an electric field is applied perpendicular to the material. The graphene quantum

capacitance varies with the charge carrier concentration from doping and charged defects in the graphene, and the ionic concentration of the electrolyte [139].

Raman spectroscopy showed that the charge carrier concentration from doping was $n_d = 3 \times 10^{12}\,\mathrm{cm}^{-2}$ [158], and the charged defect density was $n_D < 2 \times 10^{10}\,\mathrm{cm}^{-2}$ [159] (Section 4.3.2). The quantum capacitance, with no applied voltage, C_Q was calculated as:

$$C_Q = \frac{2e^2}{\hbar v_F \sqrt{\pi}} \sqrt{|n_d| + |n_D|} = 5\,\mu\mathrm{Fcm}^{-2} \tag{5.1}$$

where e is the charge on the electron, $\hbar$ is the reduced Plank constant, v_F is the Fermi velocity of the Dirac electrons. This will change with applied voltage, by up to mbox2 $\mu\mathrm{Fcm}^{-2}$ for a 10 mV perturbation in the EIS experiment.

5.2.4 Summary of the electrical properties of a graphene microelectrode array

The electrical properties of the graphene MEA were probed independently of the EIS measurements to decouple the device characteristics from the electrode-saline interface. The connecting leads were found to have a resistance of $R_{lead} = 2.4 \pm 0.4\,\mathrm{k}\Omega$. The encapsulation layer behaved like a non-ideal capacitor with a capacitance of $C_{shunt} = 8 \pm 3$ pF. The graphene quantum capacitance was estimated from Raman spectroscopy data to be $C_Q = 5\mu\mathrm{Fcm}^{-2}$. This understanding of the independently measured electrical properties of the graphene MEA will be used to help interpret the physical relevance of the EIS spectra recorded in this chapter.

5.3 Graphene microelectrode electrochemical impedance spectra

EIS is a non-destructive method which can be used to characterise the electrical and electrochemical properties of a graphene MEA. EIS spectra were obtained by applying a sinusoidal potential between a working graphene microelectrode and a planar gold reference electrode through a saline solution. The data obtained combines information about the electrical and electrochemical properties of each component of the MEA. In this section, considerations for the experimental protocol are laid out, following an analysis of the 1 kHz impedance and the full EIS spectrum. Information about the reproducibility of the manufacturing process and

suggestions about the charge-transfer mechanism between the saline solution and electrode are given.

5.3.1 Considerations for experimental protocol

To obtain accurate EIS spectra, a number of experimental factors must be considered. This includes the choice of electrolyte, the reference electrode, the perturbing potential and the frequency range recorded over.

The electrolyte chosen to mimic the cell medium was PBS [80, 32, 94, 81], a water based solution at pH 7.4 containing the salts KH_2PO_4, NaCl and $Na_2HPO_4-7H_2O$, with a resistivity of 56–71 Ω cm [229]. PBS is non-toxic to cells and is used commonly for washing cells before dissociation, transporting cells, counting cells, and preparing reagents.

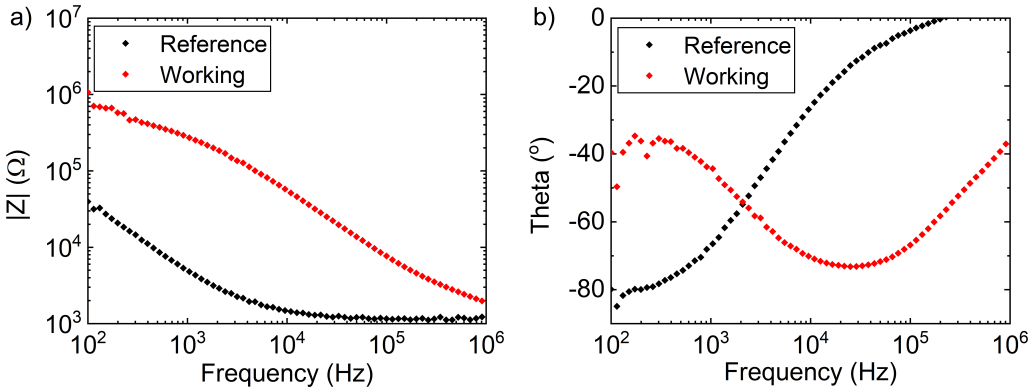

Fig. 5.3 Representative plots of the a) magnitude and b) phase of the electrochemical impedance spectrum of a 26.3 mm^2 gold reference electrode and a 706 μm^2 graphene working electrode measured against a Tungsten probe in PBS. The impedance magnitude of the working electrode is $> 3\times$ greater than that of the reference electrode across the full frequency range, and below 6×10^5 Hz is more than an order of magnitude greater than the reference electrode impedance magnitude.

Impedance spectra can be measured in a two electrode [81] or three electrode arrangement [80, 32]. In this work, a two electrode arrangement was used with a 706 μm^2 working graphene electrode and a 26.3 mm^2 planar gold reference electrode. In a two electrode setup the measured impedance, Z_{cell}, is the difference between the impedance across the working electrode, and reference electrode as:

$$Z_{cell} = \frac{V_{WE} - V_{Ref}}{i} \tag{5.2}$$

where V_{WE} and V_{ref} are the potentials applied across the working and reference electrodes respectively, and i is the measured current [168]. The two probe arrangement is only appropriate if the impedance magnitude of the working electrode is much greater than that of the reference electrode. In this experiment, the impedance magnitude of the working electrode is $> 3\times$ greater than that of the reference electrode across the full frequency range, and is more than an order of magnitude greater than the reference electrode impedance magnitude below 6×10^5 Hz (Figure 5.3). This was deemed suitable for a two electrode arrangement, and additionally mirrors the device geometry used to record voltage traces.

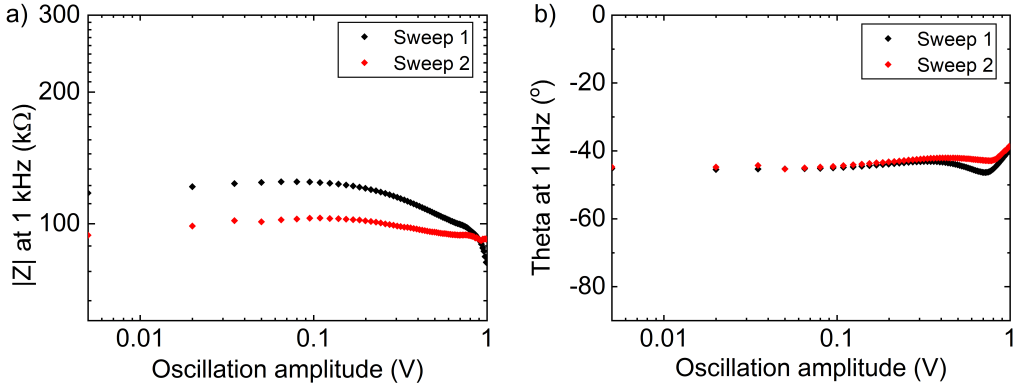

Fig. 5.4 Representative plots of the a) magnitude and b) phase of the 1 kHz impedance, when the oscillation amplitude was swept twice from 5 mV to 1 V. The impedance magnitude is approximately constant up to 100 mV, when it decreases slowly, followed by a rapid decrease at $\sim$ 700 mV. Irreversible reactions occurred in the first voltage sweep, shown by the lower impedance magnitude of the second voltage sweep.

The amplitude of the applied sinusoidal potential is known as the perturbing potential. A high-amplitude perturbation reduces the noise, whereas a low-amplitude perturbation keeps the system within its linear limits (preventing irreversible electrochemical reactions) [168, 230]. An appropriate perturbation amplitude for the graphene electrodes was found by varying the amplitude from 5 mV to 1 V at 1 kHz (Figure 5.4) and measuring the impedance . The impedance magnitude was approximately constant up to 100 mV, when it decreased slowly, followed by a rapid decrease at $\sim$ 700 mV. The reduction in impedance between 100–700 mV is likely due to increased porosity of the PMMA encapsulation layer. Irreversible reactions occurred in the first voltage sweep, shown by the lower impedance magnitude of the second voltage sweep. It is likely that by 1 V this includes the splitting of water [231, 232]. The phase data from the recordings is around $-40°$ at 1 kHz, which is high compared to other graphene electrodes recorded and is likely due to damage to the PMMA encapsulation layer. In this work, a low-amplitude perturbation of 10 mV was chosen which is well within the linear electrochemical limit [80, 32, 233, 81].

The applied frequency range should include frequencies high and low enough to reach the asymtopic limits of the system behaviour [168]. In this work, the frequency range of 100 Hz to 1 mHz was dictated by the range of the Agilent 4294A precision impedance analyser. Within this frequency range, 100 points with a logarithmic spacing were recorded [168].

5.3.2 1 kHz electrochemical impedance

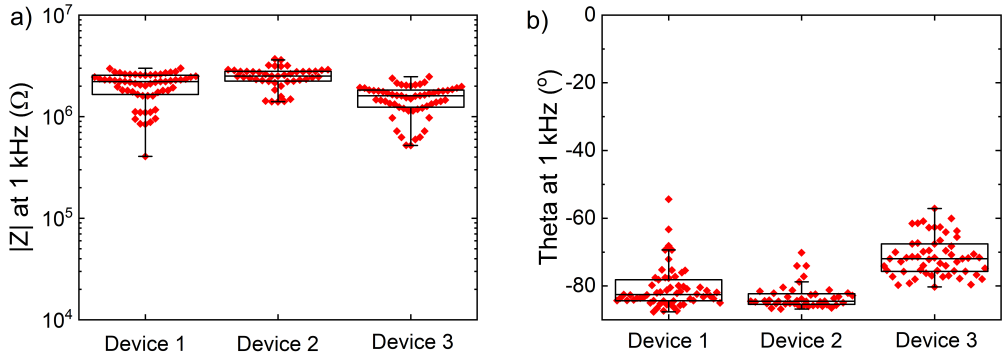

Fig. 5.5 Box and whisker plots showing the a) magnitude and b) phase of the 1 kHz impedance for three graphene MEAs. Each point is an individual electrode on the device measured, the box shows the mean, upper and lower quartile, and the whiskers represent 1.5× the inter quartile range. The average impedance magnitude was $2.0 \pm 0.6\,\text{M}\Omega$. The mean 1 kHz phase across the devices was $-78 \pm 7°$ suggesting a predominantly capacitive behaviour. The fabrication process was fairly reproducible with the variation of the mean impedance between the three devices having a magnitude of 0.97 MΩ, and a phase of 12°.

The 1 kHz impedance magnitude is a single diagnostic number which can be used to describe the impedance characteristics of a MEA and to screen many devices quickly. The 1 kHz impedance was measured for each of the 60 graphene microelectrodes, across three devices to assess the reproducibility of the fabrication protocol (Figure 5.5) [234]. The average 1 kHz impedance magnitude was $2.0 \pm 0.6\,\text{M}\Omega$. Although this impedance magnitude is much higher than for the Multichannel Systems TiN electrodes ($40 \pm 10\,\text{k}\Omega$ [92]), it is lower than the 5 MΩ limit suggested as the cutoff for serious attenuation to the recorded signal [23] and is similar to measurements on 20 µm graphene electrodes (0.17 MΩ [94] and 4 MΩ [81]).

The 1 kHz analysis can be continued to look at the phase. The mean 1 kHz phase across the devices was $-78 \pm 7°$ suggesting the electrode-saline interface has a predominantly capacitive behaviour.

Under the assumption of an entirely capacitive interface, the capacitance at the electrode can be calculated as $Z = 1/\omega C$. For a 1 kHz impedance of 2.0 ± 0.6 MΩ, this gives a predicted electrode capacitance of 80 ± 20 pF. This is significantly larger than expected for graphene electrodes which have a commonly show a capacitance of 2 μF cm^{-2}, which for 30 μm electrodes would give a capacitance of 25-30 pF. It is likely that his difference is due to a larger electrode area due to leakage through the PMMA encapsulation layer.

The reproducibility of the fabrication process can be assessed by comparing the 1 kHz impedance of three devices. The variation of the mean impedance between the three devices had a magnitude of 0.97 MΩ, and a phase of 12°. This suggests a broadly reproducible fabrication protocol, although there is scope to improve this.

5.3.3 Experimental electrochemical impedance

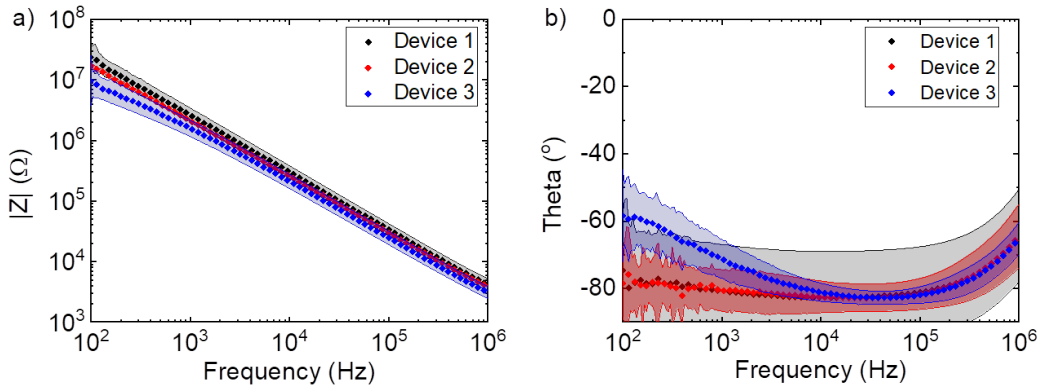

Fig. 5.6 Bode plot of the a) magnitude and b) phase of the impedance. The impedance spectra of three graphene MEAs. For each electrode, a full impedance scan was recorded between the graphene working electrode and a gold reference electrode. The log-log plot of impedance magnitude against frequency shows a straight line from ∼ 10 MΩ at 100 Hz to 4000 Ω at 1 MHz. The charge transfer is predominantly capacitive, shown by the phase of ∼-80° from 1–100 kHz.

Measuring the full electrochemical impedance spectrum gives a better understanding of the MEA than just the 1 kHz impedance data, and is presented as a Bode plot in Figure 5.6. The log-log plot of impedance magnitude against frequency shows a straight line from ∼ 10 MΩ at 100 Hz to ∼ 4 kΩ at 1 MHz for two devices, in agreement with other ∼10s μm graphene electrodes [32, 233, 105].

The phase is ∼-80° from 1–100 kHz. This reveals a predominantly capacitive charge transfer between the saline and the graphene electrode, as suggested in the 1 kHz measurement. The capacitive charge transfer is advantageous since it reduces the likelihood of

toxic Faradaic reactions occurring at the electrode, damaging the cells. As the impedance magnitude becomes constant, the phase increases away from -90°, seen above 100 kHz for each device and below 1 kHz for device 3.

It is notable that the impedance plot from the full graphene device shows similarities to the device coated with PMMA, although the PMMA had a slightly higher impedance across all frequencies. This suggests the PMMA has a large effect on the overall recorded impedance spectrum.

The measured frequency range was limited by the impedance analyser used. At some point above 1 MHz, the impedance magnitude is expected to become constant as the solution and device resistance become the limiting factor. In addition, at lower frequencies (1-100 Hz) the magnitude is expected to become constant as the charge transfer is limited by Faradaic reactions [32, 105]. This is partially seen in device 3 below 1 kHz.

5.4 Interpretation of the impedance spectra using an equivalent circuit model

To interpret EIS spectra and gain information about the electrical and electrochemical properties of an MEA, ECMs were fitted to the data. The most appropriate ECM was chosen on three criteria 1) each component in the ECM should make physical sense 2) the model should fit the data well (quantified by $\chi^2/|Z|$, the sum of the squares of residuals normalised to the impedance magnitude) and 3) the simplest model should be used to avoid overfitting the data. In this work ECMs which are used in previous graphene MEA publications are compared [111, 113, 80, 32, 81, 94]. A discussion is presented of the choice between different ECMs. Either a capacitor or a constant phase element (CPE, Q) can be used to describe the electrode-saline interfacial impedance, in general the physical interpretation of a capacitor is simpler but a CPE fits the data better. In this work the data is fitted by ECMs containing a capacitor first (EC1-6, Figure 5.7), and then ECMs containing a CPE (EQ1–6 Figure 5.8).

5.4.1 Fit electrical double layer with a capacitor

The EIS data were first fitted with ECMs containing capacitors (Figure 5.9, Table 5.2). The simplest model, $EC1 = R1 + C1$, describes a fully capacitive (or blocking) electrode with no Faradaic reactions [235]. This fit is qualitatively similar to the experimental data showing a straight line in the Bode magnitude plot, although the fitted slope is different to that of the

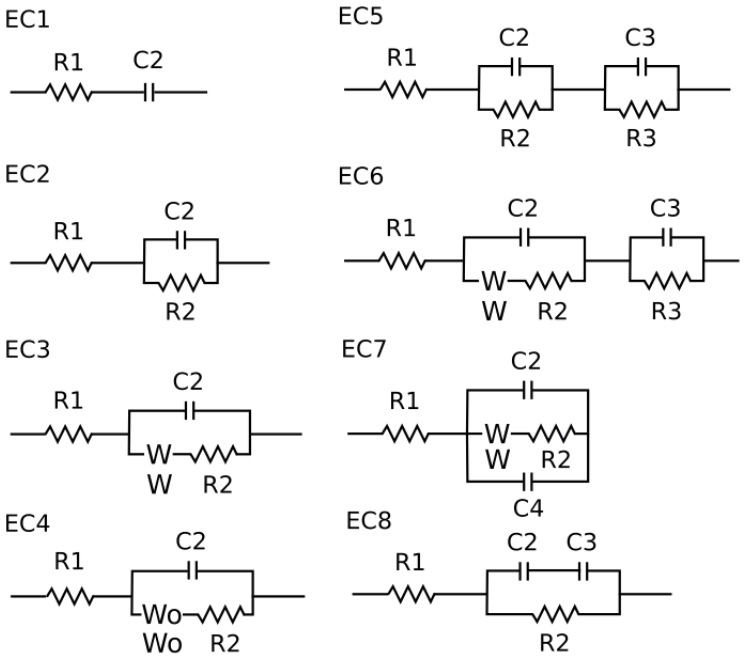

Fig. 5.7 ECMs including a capacitor used to fit the EIS spectrum of a graphene MEA. The models used are $EC1 = R1 + C1$, $EC2 = R1 + C2/R2$, $EC3 = R1 + C2/(R2 + W)$, $EC4 = R1 + C2/(R2 + W_o)$, $EC5 = R1 + C2/R2 + C3/R3$, $EC6 = R1 + C2/(R2 + W) + C3/R3$, $EC7 = R1 + C2/(R2 + W)/C4$ and $EC8 = R1 + (C2 + C3)/R2$.

data. The difference between the fitted and experimental data is shown more clearly by the phase plot, where the fit holds the phase at -90° instead of -80°.

Faradaic reactions are modelled by the inclusion of a charge transfer resistance $R2$ to make the Randles model $EC2 = R1 + C2/R2$. The exact nature of the potential Faradaic reactions at a perturbing potential of 10 mV are unknown. It is unlikely that PBS reacts with graphene at 10 mV, since the splitting of water by carbon electrodes requires the application of 1.23 V [231, 232]. It is more likely that defects in the graphene catalyse the reduction of gaseous oxygen contained in the buffer [236], this theory could be tested by degassing the PBS and repeating the experiments. The Faradaic reactions are modelled in the low frequency regime, seen by the plateau of impedance magnitude at 100 Hz and the phase increase below 1 kHz. This effect is expected to be stronger in the frequency range 1-100 Hz. The better fit of the data is shown as $\chi^2/|Z|$ decreases from 20.8 to 12.7 for the models $EC1$ to $EC2$ respectively. This reveals that even at the small perturbing potential of 10 mV, Faradaic reactions occur.

Including a Warburg, W, or bounded Warburg element, W_o, in series with the charge transfer resistance gives the models $EC3 = R1 + C2/(R2 + W)$ and $EC4 = R1 + C2/(R2 + W_o)$. There is a debate about the validity of using a conventional Warburg element for

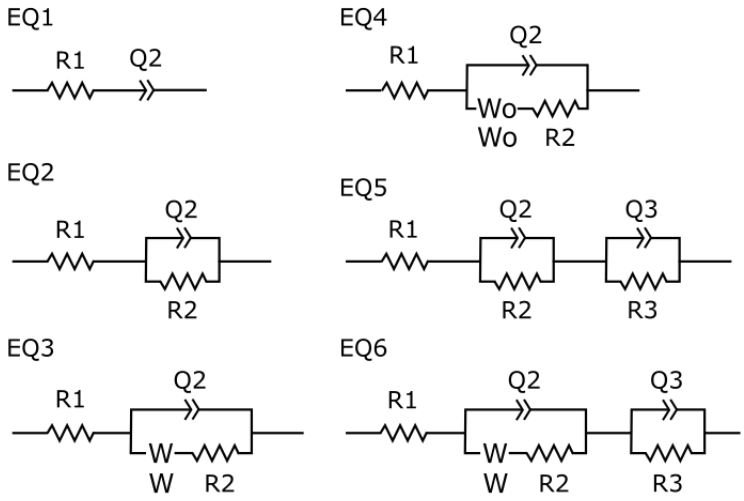

Fig. 5.8 ECMs including a CPE used to fit the EIS spectrum of a graphene MEA. The models used are $EQ1 = R1 + Q1$, $EQ2 = R1 + Q2/R2$, $EQ3 = R1 + Q2/(R2 + W)$, $EQ4 = R1 + Q2/(R2 + W_o)$, $EQ5 = R1 + Q2/R2 + Q3/R3$ and $EQ6 = R1 + Q2/(R2 + W) + Q3/R3$.

microelectrodes. The conventional Warburg element assumes linear diffusion to the electrode, however below a characteristic size (which one study suggests is 100 µm), diffusion to the electrode becomes hemispherical rather than linear. The characteristic size where the diffusion characteristics change for a graphene electrode could be tested by performing EIS on different sized graphene electrode [176, 111]. The goodness of is clear as $\chi^2/|Z|$ decreases from 12.7 to 2.25 and 2.21 for $EC2$, $EC3$ and $EC4$ respectively. This increased goodness of fit corresponds with the good fit of both magnitude and phase data, with the shape of the phase including fitting much closer to $-80°$.

Fits of $EC2$ and $EC3$ to the data suggest different limiting factors for the Faradaic reactions. Fitting with $EC2$, suggests the Faradaic reactions are under kinetic control due to a high $R2 = 25.9\,\mathrm{M\Omega}$. Whereas fitting with $EC3$ suggests the Faradaic reactions are under diffusive control with a high $W = 415\,\mathrm{M\Omega \cdot s^{-0.5}}$, and low $R2 = 0.108\,\Omega$. To understand which situation is correct, further EIS experiments should be performed with a greater frequency range of 1 Hz–10 MHz. This would ensure the region (< 1 kHz) is captured after the impedance magnitude plateaus as the charge transfer becomes limited by the Faradaic reactions rather than the capacitance.

In previous studies, the quantum capacitance of graphene has been included in the model with an additional capacitor, $C3$, and resistor, $R3$, to give $EC5 = R1 + C2/R2 + C3/R3$. This model however, should be modified as the quantum capacitor and double layer capacitor would add in series as $EC8 = R1 + (C2 + C3)/R2$. Despite this, the previously proposed model $EC5$ was fitted to complete the work comparing circuits suggested in other works.

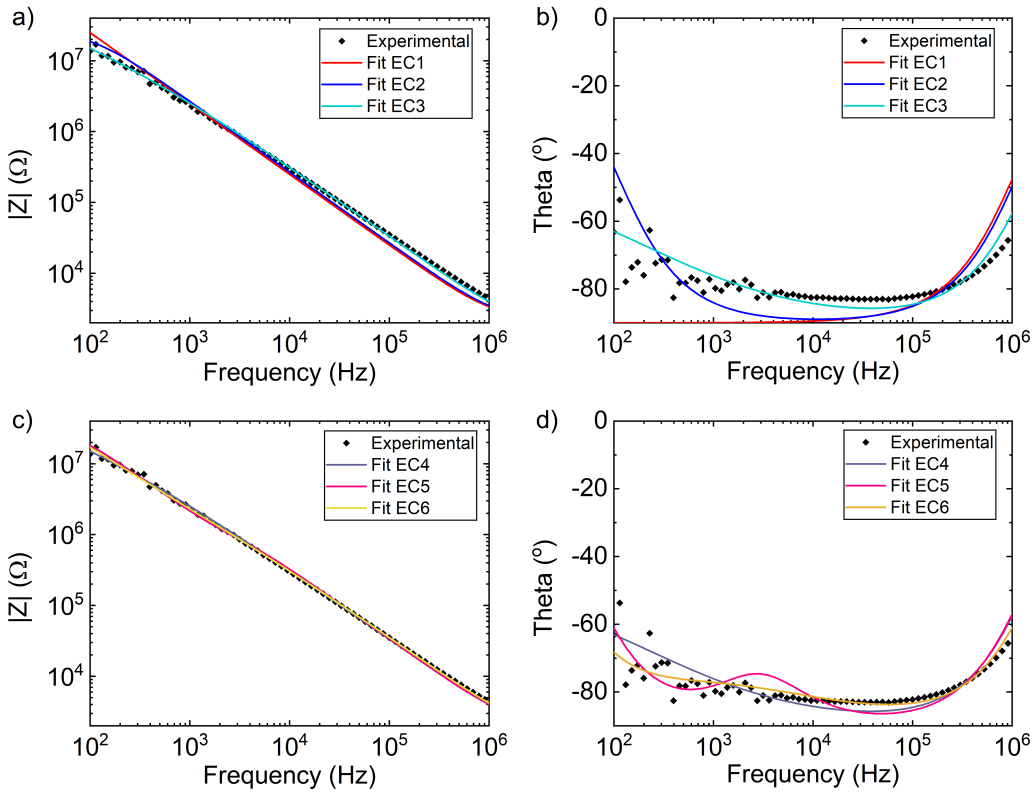

Fig. 5.9 Fitting of the electrochemical impedance spectrum of a graphene microelectrode to different ECMs. The models used are $EC1 = R1 + C1$, $EC2 = R1 + C2/R2$, $EC3 = R1 + C2/(R2 + W)$, $EC4 = R1 + C2/(R2 + W_o)$, $EC5 = R1 + C2/R2 + C3/R3$ and $EC6 = R1 + C2/(R2 + W) + C3/R3$..

The fitted data suggest a quantum capacitance of $C3 = 118\,\text{pF}$, very similar to the fitted double layer capacitance $C2 = 78.2\,\text{pF}$. Additionally, this is much larger than the quantum capacitance was $C_Q = 33\,\text{pF}$ for a 30µm diameter electrode predicted from by the Raman spectra. Including $C3$ and $R3$ improves the fit as $\chi^2/|Z|$ reduces from 12.7 to 2.69 for $EC2$ and $EC5$ respectively. The reduction in $\chi^2/|Z|$ is due to the better fit of the slope of the impedance magnitude. The model does not fit the phase data better however, since the model creates an additional peak at $2 \times 10^3\,\text{Hz}$ which is not present in the experimental data. Interestingly, additional phase peaks are observed at $< 10^2\,\text{Hz}$ in the Bode plots from previous works [93, 32, 105], and it is possible that this feature would also appear in these data at $< 100\,\text{Hz}$. However, this model was therefore deemed to not fit the data well.

A Warburg element can be included in combination with the quantum capacitance to give an ECM of $EC6 = R1 + C2/(R2 + W) + C3/R3$. This model fits the data very well however, has no clear advantage over the simpler model $EC3$.

From fitting the EIS data with an ECM containing a capacitor, it was found that the addition of either a Warburg element, or a second capacitor and resistor to the Randles model greatly reduced $\chi^2/|Z|$. The use of a Warburg element fitted the phase data much better than an extra capacitor and resistor, therefore $EC3$ was deemed the most appropriate to describe the impedance data. To check this conclusion, and make it easier to distinguish between the different models, the fitting of EIS spectra across a greater frequency range of 1 Hz–10 MHz, over different sized graphene electrodes, and using a better encapsulation layer should be performed [235].

5.4.2 Fit electrical double layer with a constant phase element

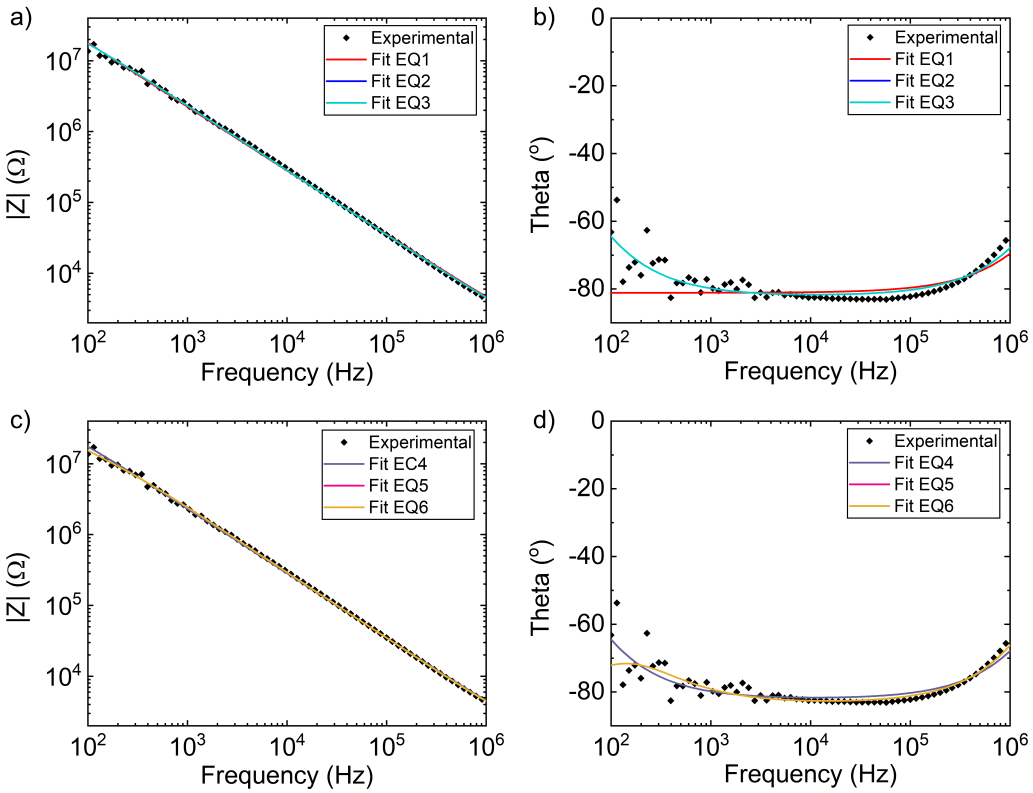

Fig. 5.10 Fitting of the electrochemical impedance spectrum of a graphene microelectrode to equivalent circuit models. The models used are $EQ1 = R1 + Q1$, $EQ2 = R1 + Q2/R2$, $EQ3 = R1 + Q2/(R2 + W)$, $EQ4 = R1 + Q2/(R2 + W_o)$, $EQ5 = R1 + Q2/R2 + Q3/R3$ and $EQ6 = R1 + Q2/(R2 + W) + Q3/R3$. The fit of $EQ2$ and $EQ3$ overlap, as do $EQ5$ and $EQ6$.

Each ECM used in previous publications to fit graphene MEA impedance data used a CPE in the place of a capacitor. The deviation of a CPE from a pure resistor or capacitor can be attributed to a number of physical causes including inhomogeneities in the surface

reactivity, surface inhomogeneity, roughness, fractal geometry, electrode porosity, current distributions, or potential distributions across the electrode [179].

Mirroring the work performed with capacitors, the EIS was fitted to ECMs with CPE (Figure 5.10, Table 5.3). In all cases, the fit was much better than for a capacitor, for example $\chi^2/|Z|$ decreases from 20.8 to 2.58 for $EC1$ and $EQ1$ respectively. The value b can take any value between 1 and 0. For $b = 1$, the CPE behaves as an ideal capacitor, for $b = 0$ the CPE behaves as an ideal resistor and for $1 > b > 0$, the CPE has units s^b/Ω. In this work, $b \sim 0.9$ for each fitted model showing the graphene electrode-electrolyte interface had a highly but not exclusively capacitive behaviour. The fitted value of Q2 was $146 - -181\,\mathrm{pF} \cdot s^{b2-1}$, this is much higher that the predicted value for a 30 µm graphene electrode of 25-30 pF.

The model $EQ2 = R1 + Q2/R2$ fits both the magnitude and phase data very well although, the models which included a CPE greatly overestimated the value of the electrode capacitance.. The addition of extra components such as a Warburg element, or an CPE and resistor did not fit the data significantly better. In order to avoid over fitting the data, this was chosen as the most appropriate best model including a CPE. $EQ2$ has the advantage of being easy to compare to fits from previous studies [111].

5.5 Physical interpretation of electrochemical impedance spectra

The physical significance of each component in the fitted ECM can be understood when compared to a lumped circuit model (LCM) (Table 5.1). The LCM describes the electrical and electrochemical properties of the physical device using linear circuit elements (Section 2.2.2). In the absence of cells, the LCM is simplified from Figure 2.2 to Figure 5.1. The simplified LCM contains a spreading resistance R_{spread}, solution resistance R_{sol}, electrode-electrolyte impedance Z_e, shunt capacitance across the encapsulation layer C_{shunt} and lead resistance R_{lead}. In this section, the fit of $EC3$ is compared to the electrical properties of each component of the MEA as described in Section 5.2.

5.5.1 Physical interpretation of equivalent circuit model

The resistance $R1$, is the sum of the lead resistance and the solution resistance, R_{sol} as:

$$R1 = R_{lead} + R_{sol} \tag{5.3}$$

The independently measured lead resistance was $R_{lead} = 2.4 \pm 0.4\,\text{k}\Omega$. The maximum distance between a reference and working electrode in the MEA design is 5.4 mm across PBS, giving R_{sol} =100–130 Ω. Combined, these give a value of $R1 = 2.5 \pm 0.4\,\text{k}\Omega$, in agreement with the ECM fitted value of $R1 = 2.1\,\text{k}\Omega$ from the ECM.

The main contribution of PMMA to the electronic characteristics as a shunt capacitor parallel with the electrode-electrolyte interface. This can be accounted for by adding a capacitor $C_{shunt} = C4$ to make $EC7 = R1 + C2/(R2 + W)/C4$ [237]. The independently measured shunt capacitance was $C_{shunt} = 8 \pm 3\,\text{pF}$, one order of magnitude lower than the electrode-electrolyte interface capacitance ($C2 = 46\,\text{pF}$), however is close to the expected capacitance for a 30 µm graphene electrode of 25–30 pF. This, along with the similarity between the PMMA and graphene EIS spectra suggests that a leaky PMMA encapsulation layer has a significant effect on the impedance spectrum.

The electrode-electrolyte interface is described in the LCM by the complex impedance, Z_e, and the spreading resistance, R_{spread}. The spreading resistance is caused by the high current density close to the small electrode surface. To a first approximation R_{spread} gives the diffusion resistance caused by the high current density close to the small electrode surface. For an electrode with a radius of 30 µm PBS the spreading resistance was calculated from equation 2.3 to be $R_{spread} \sim 10\,\text{k}\Omega$ [229].

The charge transfer through the electrode-electrolyte interface is described in the ECM as $Z_e = C2/(R2 + W)$, and contains contributions from charging and discharging the double layer capacitor, the quantum capacitance and Faradaic reactions. The value $C2$ contains contributions from the double layer capacitance, C_{dl}, and the quantum capacitance, C_Q, as $1/C2 = 1/C_{dl} + 1/C_Q$. The quantum capacitance derived independently of Raman spectroscopy measurements was $C_Q = 33\,\text{pF}$ with no applied voltage for a 30µm diameter electrode. This is similar in magnitude to the value of $C2 = 46\,\text{pF}$ from the ECM. It is therefore concluded that a major main capacitive contribution to the graphene electrode is its quantum capacitance.

The Faradaic reactions are described by $R2 + W$, with $R2$ representing the kinetically controlled regime and W representing the diffusive controlled regime. Fitting the data with this model suggests the Faradaic reactions are predominantly under diffusive control with a high $W = 415\,\text{M}\Omega \cdot \text{s}^{-0.5}$, and low $R2 = 0.108\,\Omega$. Further experiments including the frequency range 1 Hz–10 MHz are needed to decouple the kinetic and diffusive regimes better.

From the fitting of the EIS data to an ECM, then comparing to a LCM, it can be concluded that the mechanism by which the graphene electrode reports on the neuronal activity is predominantly via capacitive coupling with the electrode through the electrical double

layer and the quantum capacitance. This is advantageous since it reduces the likelihood of toxic Faradaic reactions occurring at the electrode. If the charge transfer mechanism was predominantly Faradaic, the high electrode impedance would result in a large thermal noise for small electrodes [108, 101], however the highly capacitive nature of the electrodes reduces the thermal noise.

Table 5.1 Comparison of the LCM and the ECM $EC7$.

ECM ($EC7$)	LCM
$R1$	$R_{lead}+R_{sol}$
$C4$	C_{shunt}
$C2/(R2+W)$	Z_e
$\frac{1}{C2}$	$\frac{1}{C_{dl}}+\frac{1}{C_Q}$

5.5.2 Non-destructive identification of device breakdown

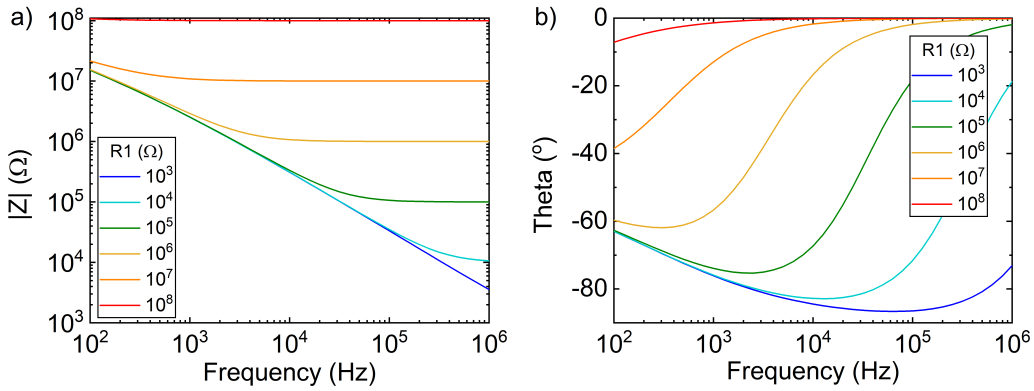

Fig. 5.11 The effect of changing the value of $R1$ on the electrochemical impedance spectrum, from $EC3$ where $C2 = 46.3\,\text{pF}$, $R2 = 0.108\,\Omega$ and $W = 415\,\text{M}\Omega$. As $R1$ is increased, the cutoff frequency for a capacitive limited versus a resistive limited impedance (shown by the plateau in impedance magnitude) decreases, and the impedance in regions with resistive limited impedance increases.

The understanding of the link between the impedance data and the device components can be applied to offer a non-invasive, non-damaging method to identify broken electrodes in the device. Each component of the MEA can fracture. Breaks in the connecting leads and encapsulation layer are specifically considered here. The simplest impedance based method checking for device breakdown is the 1 kHz impedance. For a standard device, an impedance

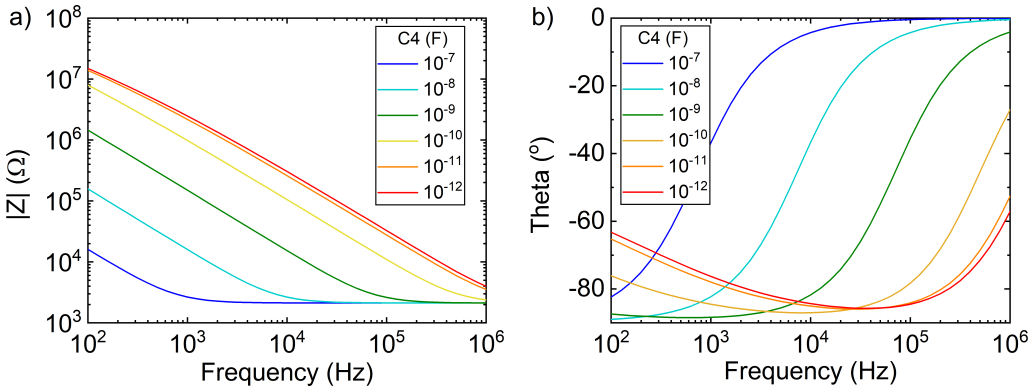

Fig. 5.12 The effect of changing the value of $C4$ on the electrochemical impedance spectrum from $EC3$ where $R1 = 2.12\,\text{k}\Omega$, $C2 = 46.3\,\text{pF}$, $R2 = 0.108\,\Omega$ and $W = 415\,\text{M}\Omega$. As $C4$ is increased, the cutoff frequency for a capacitive limited versus a resistive limited impedance (shown by the plateau in impedance magnitude) decreases. The impedance in regions with capacitively limited impedance decreases with the increased charge leakage through $C4$.

$> 100\,\text{k}\Omega$ suggests a break in the lead, and an impedance $< 10\,\text{k}\Omega$ suggests leaky insulation [238]. However, if the full impedance spectrum is considered, more information about the device damage can be found [110].

To investigate changes to the EIS spectrum from damaged connecting leads $EC3$ was used, and $R1$ was varied from 10^3–$10^8\,\Omega$ (Figure 5.11). Higher values of $R1$ represent increased damage to the leads. As $R1$ is increased, the frequency at which the impedance magnitude plateaus decreased and impedance magnitude of the plateaued regions decreased. This is because the cutoff frequency for a capacitive limited versus a resistive limited impedance decreases as $R1$ becomes the dominant factor. The 1 kHz impedance magnitude is sensitive to this when breaks in the wire give $R1 > 10^6\,\Omega$. The 1 kHz phase, is more sensitive to smaller changes in series resistance, with theta increasing from -80° at $R1 = 10^3\,\Omega$, to 0° at $R1 = 10^8\,\Omega$.

Charge leakage through the insulation layer can described using $EC7$ with $C4$ was varied from 10^{-12}–$10^{-7}\,\text{F}$ (Figure 5.12). As $C4$ increased, the frequency at which the impedance magnitude plateaus decreased and the impedance magnitude of the plateaued regions stays constant. This is again because $R1$ becomes the dominating factor as charge is transferred more easily by charging and discharging $C4$. At 1 kHz, the impedance magnitude is more sensitive than the impedance phase to changes in $C4$. The 1 kHz impedance magnitude changes from $\sim 10^6\,\Omega$ at $C4 = 10^{-12}\,\text{F}$ to $\sim 10^3\,\Omega$ at $C4 = 10^{-7}\,\text{F}$. As $C4$ approaches the value of $C2$, the change in spectrum observed greatly decreases, suggesting that in this device, the PMMA capacitance could be the main factor recorded in the EIS spectrum.

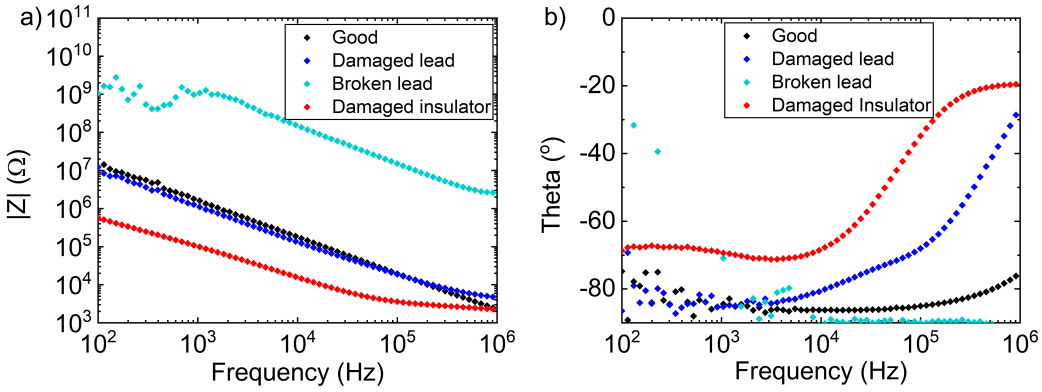

Fig. 5.13 EIS spectra showing experimental spectra from of broken electrodes in a graphene MEA. Damaged leads increased the impedance magnitude and a damaged encapsulation layer decreased the impedance magnitude. A characteristic change in phase is also observed for damage to the leads or encapsulation layer.

The experimentally acquired impedance data from broken graphene microelectrodes (Figure 5.13) are in good agreement with the predicted impedance data. With damaged connecting leads, the impedance becomes resistively limited at a lower frequency. With broken leads, the measured impedance is the capacitance of the encapsulation layer, with a high impedance magnitude and phase of -90°. For a damaged encapsulation layer, the impedance magnitude decreases and the phase tends to -90°. It can be seen that acquiring the full impedance spectrum, gives more information about the nature of damage to the device, than if only the 1 kHz impedance is measured, especially for partially damaged leads.

5.6 Conclusion

The electrical and electrochemical properties of a graphene MEA were probed using EIS. Many ECMs have been used in previous publications to interpret the EIS spectrum. In this work, each previously used ECM was compared. The simplest model which made physical sense and fitted the data was $EC3 = R1 + C2/(R2 + W)$ [80].

The fitted values obtained from this model were then compared with independently obtained measurements describing the electrical and electrochemical characteristics of each component of the MEA. From this it could be seen that $R1$ is the series resistance of the leads and electrolyte, $C2$ combines the double layer and quantum capacitance's at the electrode-electrolyte interface, $R2$ describes the kinetic and W the diffusive limit of the Faradaic charge transfer reactions. This model was then used to predict changes in the EIS spectrum when the device breaks.

The 1 kHz impedance, full Bode plot and ECM all suggest that the graphene electrode reports on the neuronal activity predominantly via capacitive coupling with the electrode through the electrical double layer and graphene quantum capacitance. This is advantageous since it reduces the likelihood of toxic Faradaic reactions occurring at the electrode. The data also suggests that the PMMA encapsulation layer is a limiting feature of the fabricated MEA.

Table 5.2 Fitting of the electrochemical impedance spectrum of a graphene microelectrode to an equivalent circuit model, where R is a resistor, C is a capacitor, W is a Warburg element, and W_o is a bounded Warburg element.

Model	R1	C2	R2	W	t2	C3	R3	$\chi^2/\lvert Z\rvert$
	kΩ	pF	MΩ	$\Omega \cdot s^{-0.5}$	s	pF	MΩ	
$EC1$	2.28	63.8						20.8
$EC2$	2.69	59.3	25.9					12.7
$EC3$	2.12	46.3	0.108×10^{-6}	415×10^{6}				2.25
$EC4$	2.12	46.1	0.0579×10^{-6}	49.8×10^{6}	7.52×10^{-3}			2.21
$EC5$	2.19	78.2	38.3			118	0.358	2.69
$EC6$	1.96	66.0	0.671×10^{-6}	85.1×10^{6}		116	45.6	1.24

Table 5.3 Fitting of the electrochemical impedance spectrum of a graphene microelectrode to an equivalent circuit model, where R is a resistor, Q is a constant phase element, W is a Warburg element, and W_o is a bounded Warburg element.

	Model	R1 kΩ	Q2 $\mathrm{pF}\cdot\mathrm{s}^{\mathrm{b2}-1}$	b2	R2 MΩ	W $\Omega\cdot\mathrm{s}^{-0.5}$	t2 s	Q3 $\mathrm{pF}\cdot\mathrm{s}^{\mathrm{b3}-1}$	b3	R3 MΩ	$\chi^2/\lvert Z\rvert$
–	$EQ1$	0.953	167	0.901							2.58
[111]	$EC2$	1.13	146	0.913	56.7						1.52
[80]	$EQ3$	1.13	146	0.913	56.7	2.32					1.52
[32]	$EQ4$	1.13	146	0.913	56.7	5.77×10^{6}	361				1.52
[81]	$EQ5$	1.32	180	0.943	66700			347	0.907	5.12	1.08
[94]	$EQ6$	1.32	181	0.943	297×10^{9}	14.4×10^{3}		347	0.907	5.13	1.08

Chapter 6

Electrophysiological recordings in combination with fluorescence microscopy

Mouse neuronal cell cultures were prepared and maintained by Susanna Mireau (SM), Timothy Sit (TS) and Ricardo Conci (RC). Rat neuronal cell cultures were prepared and maintained by Miranda Robbins. Voltage traces were recorded by SM, TS and RC. Matlab code for processing the voltage traces was written by TS and Prez Jarzebowski (PJ). All analysis of the voltage traces was performed by the author. An adaptor to fit the graphene MEA in to the amplifier was 3D printed by Jhalique Fojas (JF). The microscopy images were acquired and analysed by Miranda Robbins (MR), Chetan Poudel (CP) and the author. All text is written by the author.

6.1 Introduction

Combining electrophysiological recordings with optical imaging, links the function of the nervous system to its underlying cellular and molecular structures. However, with conventional microelectrode arrays (MEAs) the combination of these two techniques is limited by the opacity of the recording electrode. The use of transparent graphene MEAs has the potential to overcome this limitation. Combining electrophysiological recordings with optical imaging would be useful to understand the role of amyloid proteins in neurodegenerative diseases like Alzheimer's disease (AD) and Parkinson's disease (PD). The effect of these proteins on neuronal firing has been investigated using electrophysiological recordings from MEAs [17, 24, 18]. Separately, the aggregation state of the amyloids has been studied using

advanced imaging techniques like confocal fluorescence, and fluorescence lifetime imaging microscopy (FLIM) [30].

In this chapter, a proof of concept is presented for combining electrophysiological recordings with a graphene MEA with advanced fluorescence microscopy through the device. The custom fabricated transparent graphene MEA had gold leads, graphene electrodes and a poly(methyl methacrylate) (PMMA) encapsulation layer. This was compared to a conventional opaque TiN MEA purchased from Multichannel Systems. Mouse neurons were plated on the graphene and TiN MEAs, voltage traces were recorded, and spike detection performed to identify neuronal action potentials. Following this, the imaging modalities widefield, confocal fluorescence and FLIM were shown on each material used to fabricate the graphene MEA. Finally, widefield, confocal and FLIM imaging were shown on the graphene MEA voltage traces had been recorded from.

The design and fabrication protocol of the graphene MEAs is found in Chapter 4, and its characterisation by impedance spectroscopy in Chapter 5. Background information about processing voltage traces is in Section 2.2.3, and background information about the fluorescence imaging is in Section 3.2.

6.2 Recording voltage traces

Voltage traces were recorded from, and a comparison was made between an opaque conventional MEA and a transparent graphene MEA. The conventional MEA had opaque TiN electrodes and was purchased from Multichannel Systems (60MEA200/30iR-Ti). The second MEA was a custom transparent fabricated graphene MEA. Both devices had 60 circular electrodes with a diameter of 30 µm, a pitch of 200 µm, an 8×8 electrode grid and an internal reference electrode with an area of 26.3 mm^2. The TiN MEA had opaque TiN electrodes, leads and internal reference and a 500 nm SiN encapsulation layer (Figure 6.1a). The graphene MEA had opaque gold leads, an opaque gold internal reference, transparent graphene electrodes and a 500 nm PMMA encapsulation layer (Figure 6.1c). It is a simple step to further modify the graphene device to have transparent indium tin oxide (ITO) leads, and thus be a fully transparent graphene MEA device. Post natal day 1 mouse cortex or hippocampal neurons were cultured on the MEAs, and the voltage trace recorded at days in vitro (DIV) 14 (Figure 6.1).

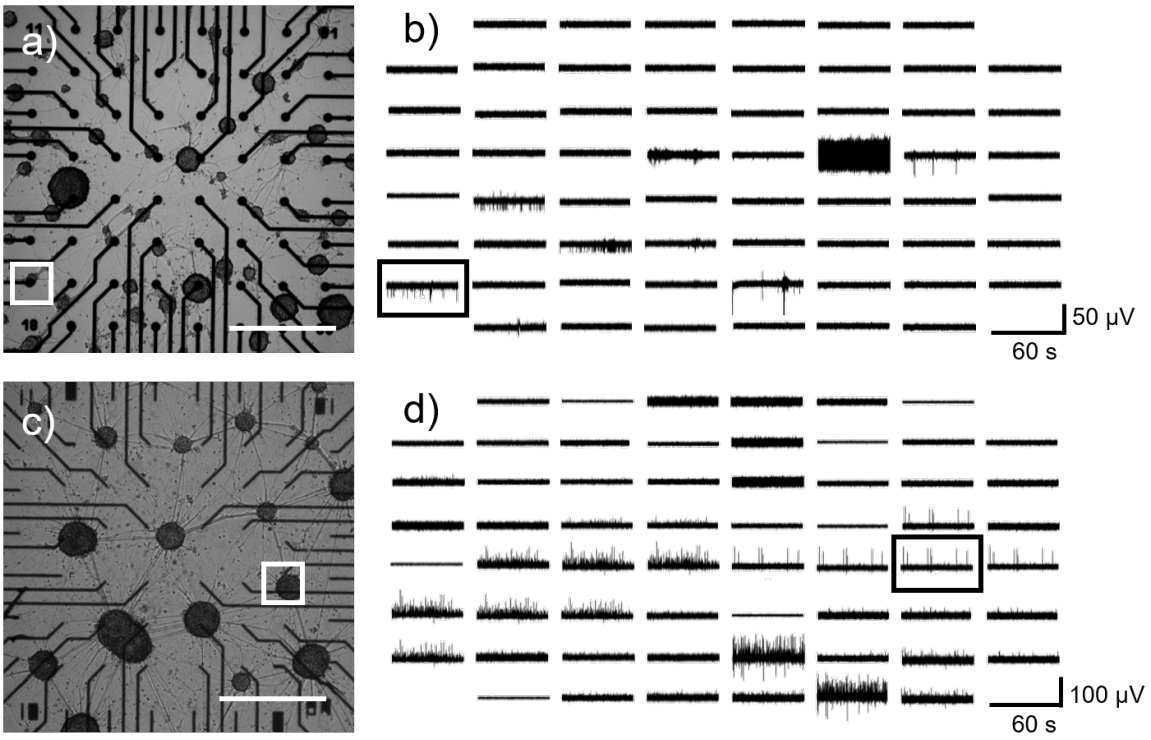

Fig. 6.1 Images of mouse cortex or hippocampal neurons growing and sprouting neurites at DIV 14 on a) TiN MEA and c) graphene MEA. Scale bar 500 µm. The corresponding voltage traces showing the spontaneous activity measured by each electrode using b) TiN electrodes and d) graphene electrodes. The SNR is sufficiently high to distinguish spikes from the noise floor. Mouse neuronal cell cultures were prepared, maintained and voltage traces recorded by SM, TS and RC.

6.2.1 Voltage traces

The cultured mouse neurons grew on both the TiN MEA and graphene MEA, clumping together, and sprouted neurites which extended between the clumps. This shows the cultured neurons can adhere equally well to the graphene [149] and PMMA [239] as they do to the TiN and SiN. However, the clustering issues on both substrates, including the widely used MEA purchased from Multichannel Systems, suggest improvements to the cell culturing protocol are needed to improve this.

On both devices, spikes in the voltage trace were recorded, with 7 electrodes recording spiking activity on the TiN MEA and 22 electrodes on the graphene MEA. The replication of distinct voltage trace patterns seen with the graphene electrodes, suggests there is crosstalk between the electrodes which is likely due to an incomplete etching of deposited graphene between the electrodes. The signal to noise ratio (SNR) across these electrodes was high enough to distinguish spikes from the noise floor. This agrees with work showing that

graphene does not alter the electrophysiological response of cultured neurons [148], and that voltage traces can be recorded from cultured neurons using graphene electrodes [81]. The action potentials recorded from the TiN electrodes generally have a negative deflection, whereas the recordings from the graphene electrodes generally have a positive deflection. The origin of this is possibly because of the difference in standard electrode potentials between the recording and reference electrodes where the TiN recordings were relative to a planar TiN reference electrode whereas the graphene recordings were relative to a planar gold reference electrode. However, the shape of the recorded action potentials is difficult to predict and can even depend on the position of the electrode in relation to the cell. The voltage traces from a single electrode on each device, shown by the squares in Figure 6.1, were further analysed.

6.2.2 Spike detection

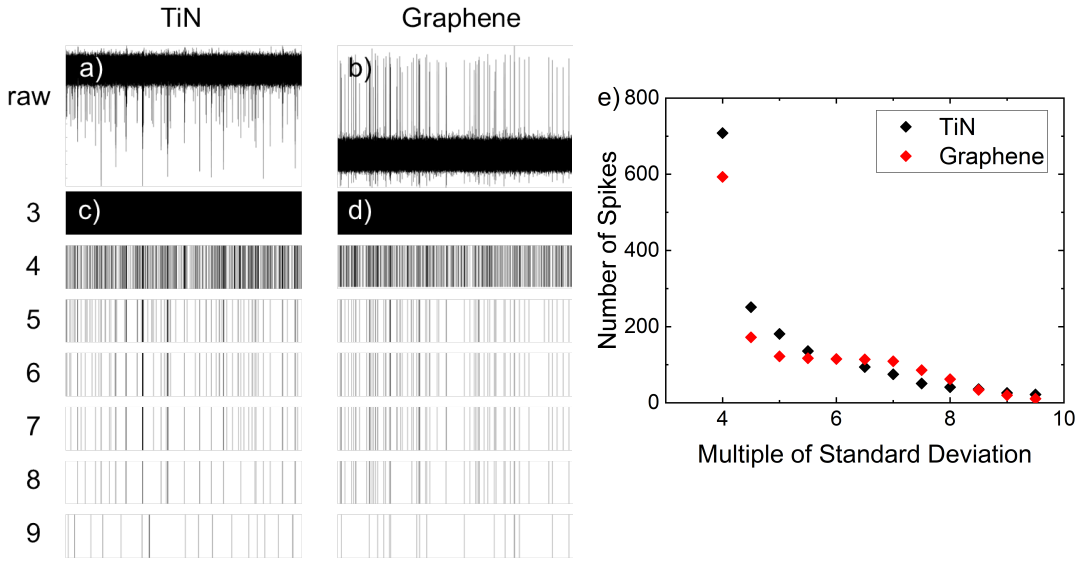

Fig. 6.2 The spontaneous activity of mouse neurons recorded for one minute shown as a), b) raw and c), d) raster plots. Spike detection was performed by amplitude thresholding, with the threshold set to a multiple of the root mean square of the voltage from 3–9. Data were recorded using a), c) opaque TiN electrodes purchased from Multichannel Systems and b), d) transparent graphene electrodes. e) A plot of the number of detected spikes in one minute against the multiplier. Cell cultures were prepared, maintained and voltage traces recorded by SM, TS and RC. Matlab code to process the voltage traces was written by TS and PJ.

Spike detection assumes the only information obtainable from the voltage trace is the timings of the action potentials. Spike detection distinguishes the high frequency (~ 1 kHz) action potentials caused by Na^+ and K^+ transients during action potentials, from the noise

floor and low frequency potentials. The noise arises from a combination of biological sources like the action potentials of distant neurons; low frequency (< 300 Hz) local field potentials arise from by the synchronised synaptic currents and the formation of dipoles [49]; and electronic sources [83].

To perform spike detection, the data was bandpass filtered from 600–8000 Hz to remove low or high frequency noise that is outside the action potential frequency range. The spike detection was performed by amplitude thresholding, where voltage peaks above a given value were deemed to be spikes [240]. The voltage threshold, V_t, was set to the mean voltage, $\bar{V}$, minus the standard deviation V_σ, times a multiplier, x as:

$$V_t = \bar{V} - xV_\sigma \tag{6.1}$$

To choose an appropriate multiplier, different values were applied to the data from 3–9.5 and the number of detected spikes was recorded (Figure 6.2). A multiplier that is too small will detect large noise fluctuations as action potentials, and a multiplier that is too large will miss genuine signals. For these data, a multiplier of 5–7 successfully detects the spikes whilst not detecting noise. A multiplier of 5.5 was chosen for both TiN MEA and graphene MEA, which is near the standard multiplier of 5 [82, 83].

Additionally, a refractory period of 2 ms was set to ensure each spike was only counted once. This time is a compromise between having a long time to reduce the detection of spikes at non-physiological firing frequencies, and a short time to detect high frequency bursts.

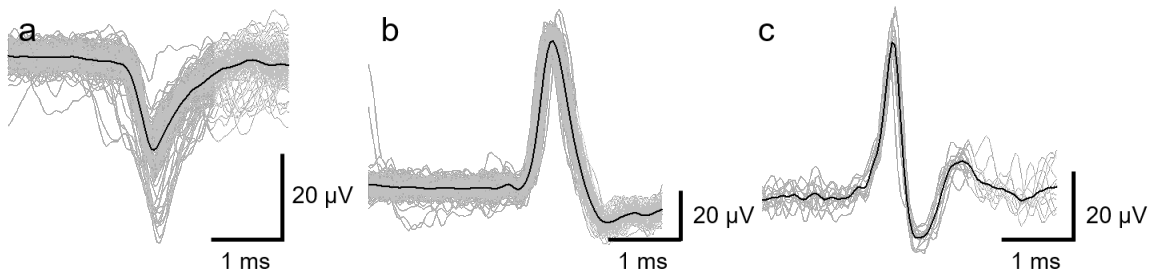

Fig. 6.3 Spikes were detected from the spontaneous activity of mouse neuronal cultures. An overlay of the identified spikes a) recorded from the TiN electrode, b, c) the two spares of spikes recorded from the graphene electrode. Cell cultures were prepared, maintained and voltage traces recorded by SM, TS and RC. Matlab code for processing the voltage traces was written by TS and PJ.

The spikes detected from the electrodes in Figure 6.2 were further analysed by plotting the shape of the peak over a 4 ms time window (Figure 6.3). Each observed spike has an amplitude of 10–100s µV and a duration < 2 ms suggesting they are indeed action potentials

[49]. The biological mechanism for this is as follows, the action potential is initiated by opening of sodium channels in the cell membrane for ~ 1 ms. This results in an influx of Na^+ to the cell, reversing the membrane potential. The sodium channels then close and potassium channels open. K^+ flows out of the cell, re-polarising the membrane. After a small undershoot, the resting potential is restored by the sodium-potassium pumps [42].

The peak-to-peak voltage, V_{p-p}, from the TiN electrode was 11–45 µV, with a single peak shape which has a single dip in potential. V_{p-p} on the graphene electrode was 21–90 µV. It is expected that the graphene V_{p-p} graphene is larger due to enhanced neural adhesion between the neurons and graphene compared to the neurons and TiN [149]. The better the adhesion of the cell to the electrode, quantified by the sealing resistance (R_{seal}), the higher the peak-to-peak voltage, which is why cell adhesion molecules like poly-L-lysine are commonly used in MEA recordings [43].

Two distinct peak shapes were observed from the graphene electrode which were separated out, it is expected that these correspond to two separate neurons positioned near the electrode [84]. Both graphene peak shapes had a sharp increase in potential, followed by a decrease which is more pronounced in the second shape. The morphology of the spike in Figure 6.3b looks very similar to recordings made from intracellular electrodes although the amplitude is much smaller. The differences in morphology observed are expected for external action potentials, since the ionic concentration at the electrode is measured, which strongly depends on the coupling of the cells to the electrode [81].

6.2.3 Noise

The noise on the electrodes was calculated from the root mean square (RMS) voltage, V_{rms}, with the spikes included in the data (Figure 6.4). The noise of the empty amplifier was 4.52 ± 0.04 µV, meaning any broken electrodes would have this noise. The mean noise of the TiN MEA and graphene MEA was 1.1 ± 0.3 µV and 2.5 ± 0.7 µV respectively across the device. This is likely due to the higher impedance on the graphene electrodes compared to the TiN electrodes of 2.0 ± 0.6 MΩ and 40 ± 10 kΩ respectively at 1 kHz (Section 5.3.2). In general the low noise seen on the graphene electrodes arises from a high interfacial capacitance reducing the noise from resistive charge transfer, and instead the noise is dominated by the 1/f and 60 Hz noise. The noise of the graphene MEA in this work was similar to the work of Chen *et al.* who had the lowest noise level of 3.3 µV for 13500 μm^2 steam plasma treated electrodes (with a bandwidth from 0.5 Hz to 10 kHz) [80], and smaller than other non-treated graphene 100s μm^2 electrodes which had a lowest noise of 10 ± 5 µV [81] (Table 2.1). Further analysis of the noise could be performed by looking at the point spread distribution of the voltage to define the more features of the noise and gain.

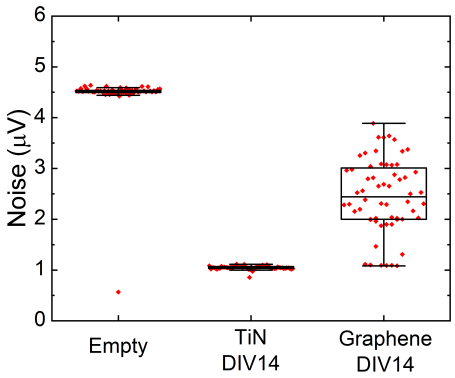

Fig. 6.4 Box plot showing the electrode noise as defined by V_{rms} of the voltage traces recorded from the spontaneous activity of mouse neuronal cultures. Each point is an individual electrode on the device, the box shows the mean, upper and lower quartile, and the whiskers represent 1.5× the inter quartile range. The noise from an empty amplifier is compared to the noise from the TiN MEA and graphene MEA. Cell cultures were prepared, maintained and voltage traces recorded by SM, TS and RC.

The spread in the noise level across the graphene MEA was much larger than for the empty amplifier or TiN MEA due to the custom manufacture of the devices. The high noise on some electrodes arises from breaks in the graphene which give a higher electrochemical impedance and thermal noise. The low noise on some electrodes likely arises from breaks in the PMMA encapsulation layer resulting in a larger area of the electrode in contact with the electrolyte, a lower electrochemical impedance and thermal noise (Section 5.5.2).

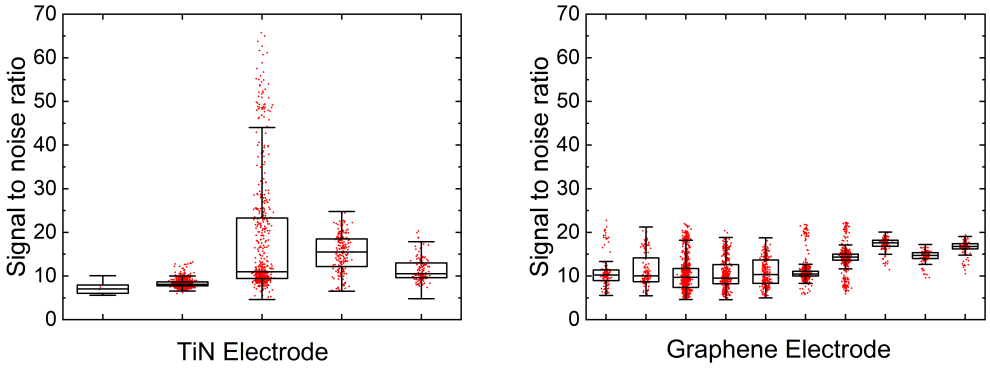

Fig. 6.5 Box plot showing the signal to noise ratio from a) TiN electrodes and b) graphene electrodes. Each point represents the SNR of an individual action potential, the box shows the mean, upper and lower quartile, and the whiskers represent 1.5× the inter quartile range. Cell cultures were prepared, maintained and voltage traces recorded by SM, TS and RC.

The SNR for an individual peak was calculated using:

$$SNR = \left(\frac{V_{p-p}}{2 \times V_{RMS}} \right) \tag{6.2}$$

The SNR for each detected action potential was calculated and the TiN device compared to the graphene device (Figure 6.5). The highest SNR recorded from the TiN MEA was 79 on an isolated electrode, with a maximum SNR of 24 on the next best electrode. The highest SNR from the graphene MEA was 23. This is because the TiN MEA has a lower signal and noise compared to the graphene MEA. The SNR recorded from the graphene MEA is very similar to previous work where a SNR of 16 ± 6 was recorded using 20 µm diameter electrodes and the spontaneous activity of mouse neurons [81].

6.3 Imaging through each material in the graphene microelectrode array

The graphene MEA was fabricated on a glass coverslip with gold connecting leads, graphene electrodes and PMMA encapsulation layer. The suitability of each material for widefield, confocal and FLIM was examined. Widefield imaging was tested by growing and imaging primary neurons on the substrates. The transparency of each material was found using ultraviolet-visible (UV-vis) spectroscopy. The fluorescence lifetime of a dye on each substrate was checked using Rhodamine 6G.

6.3.1 Widefield microscopy

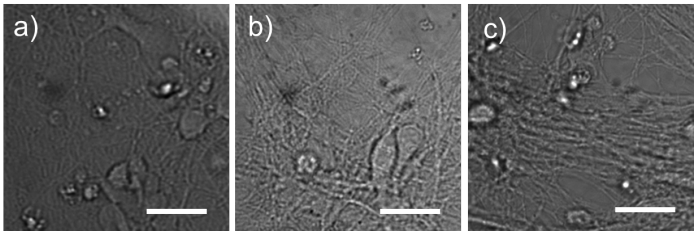

Fig. 6.6 Widefield images showing juvenile rat neurons grown on the different graphene MEA materials. a) Glass coverslip, b) PMMA and c) graphene. Scale bar 20 µm. Neurons were prepared, maintained and imaged by MR.

The simplest imaging modality is widefield brightfield microscopy. In this method, the entire sample is illuminated by light and contrast is caused by attenuation of the transmitted

light. Widefield images were acquired of juvenile rat neurons on a coverslip, graphene and PMMA (Figure 6.6). Each substrate is suitable for widefield imaging, shown as the cells can clearly be seen on each substrate. In addition to this, each substrate was shown to be biocompatible as the neurons attached to the substrate and sprouted neurites.

6.3.2 Confocal fluorescence intensity imaging

Images were taken on a confocal fluorescence microscope capable of taking fluorescence lifetime images [241]. In confocal fluorescence microscopy, a monochromatic light is scanned across the sample exciting a fluorophore, and the emitted fluorescence at a given wavelength is imaged. A confocal setup uses a pinhole inserted into the light path to eliminate fluorescence from out of focus planes, enabling a resolution of ~ 300 nm, limited by the diffraction of light. Most confocal microscopes are built in an epifluorescent arrangement, where a single lens acts as the condenser and objective. The lens is commonly placed under the sample in an inverted setup, thus requiring a transparent substrate for imaging.

The transparency of each material was found using UV-vis spectroscopy (Figure 4.2 and 4.8). 40 nm gold is opaque with a transmittance $<13 \pm 1\%$ across 400–1400 nm, it is therefore not used in the further imaging experiments. Monolayer graphene transferred on a coverslip had a transmittance $>91 \pm 3\%$, and 500 nm PMMA on a coverslip had a transmittance $>87 \pm 3\%$ across 400–1500 nm making these materials suitable for imaging in an inverted setup.

6.3.3 Fluorescence lifetime imaging microscopy

When a population of fluorophores are excited, they emit fluorescent light with a characteristic lifetime. The microscopy technique FLIM maps the fluorescence lifetime of a fluorophore across the sample. High resolution lifetime maps, limited only by light diffraction, can be acquired using the time correlated single photon counting (TCSPC) method. In this method, the arrival times of large numbers of individual photons (thousands to millions) are collected, and a histogram of photon arrival times is built [195].

To investigate if the substrates affected the fluorescence lifetime, the well characterised fluorescent dye Rhodamine 6G was used [242]. The dye was pipetted onto a coverslip, graphene and PMMA and imaged using FLIM. The fluorescence lifetime of Rhodamine 6G was found for each pixel by fitting a mono exponential function to the fluorescence lifetime curves (Figure 6.7). The mean fluorescence lifetime for Rhodamine 6G was 3.98 ± 0.18 ns on graphene and 3.95 ± 0.15 ns on PMMA. This is within the statistical uncertainty of the glass coverslip standard with 4.09 ± 0.14 ns and previous reports in the literature of 4.08 ns

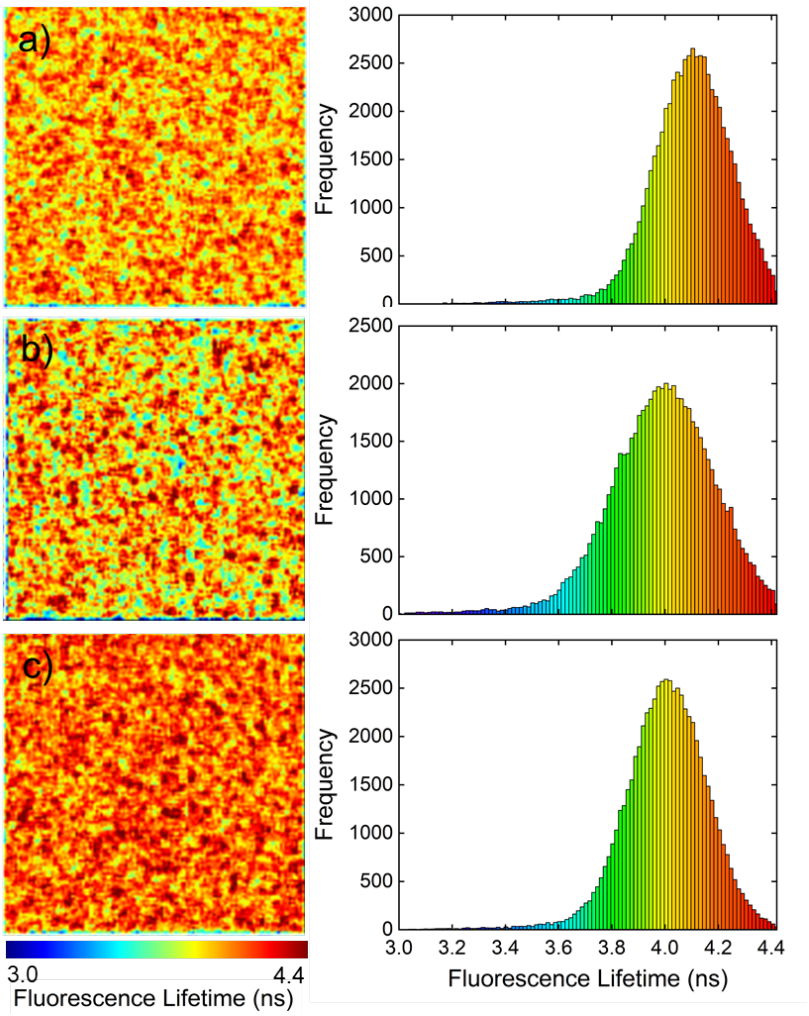

Fig. 6.7 Fluorescence lifetime maps and histograms of Rhodamine 6G on the graphene MEA materials a) glass coverslip, b) PMMA and c) graphene. The mean fluorescence lifetime was not perturbed by graphene or PMMA. Data were acquired and analysed by MR and CP.

[243]. Graphene is well known to have a fluorescence quenching effect close to material surface, and can also lead to changes in fluorescence lifetime within 30 nm of the surface. This should not be significant for measuring fluorophores within cells which are at a greater distance than 30 nm from the graphene surface [244]. It was therefore shown that neither graphene nor PMMA obscured of perturbed the fluorescence lifetime, and were deemed suitable for FLIM imaging as well as widefield and confocal fluorescence intensity imaging.

6.4 Imaging through a graphene microelectrode array

After voltage traces had been recorded on the graphene MEA, as shown earlier in this chapter, images of the neurons on the device were taken using different imaging modalities. In previous studies, the *in vivo* imaging modalities shown to work through transparent graphene electrodes are wide field fluorescence, confocal microscopy [113, 114], optical coherence tomography [34, 112] and two-photon microscopy [105]. In this work, the modalities widefield, confocal are revisited, and the use of FLIM is shown for the first time.

6.4.1 Mounting the microelectrode array on an inverted microscope

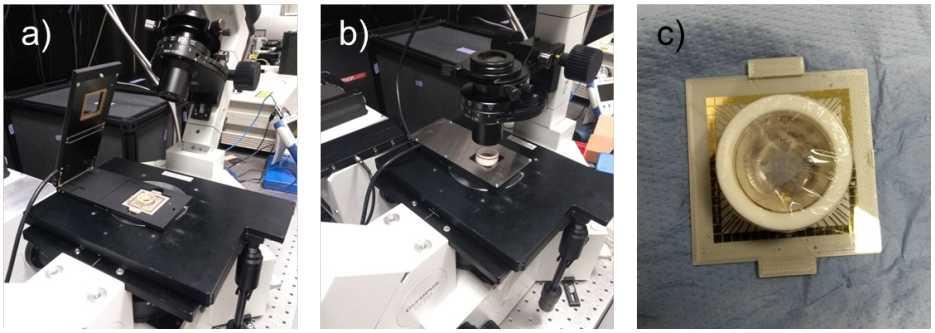

Fig. 6.8 a), b) The MEA-2100 Mini amplifier on an inverted Olympus FV300 microscope stage. c) A 3D printed adaptor was used to fit the graphene MEA, which was manufactured on a coverslip, into the MEA-2100 Mini amplifier. The 3D printed adaptor was fabricated by JF.

To perform live confocal and FLIM imaging, alongside making electrophysiological recordings, the graphene MEA and amplifier were mounted onto an inverted Olympus FV300 microscope stage (Figure 6.8a,b). The amplifier used was a 2100-Mini (Multichannel Systems). The amplifier was designed to record from 60 electrodes simultaneously, had a hole at the base for imaging on inverted setup and has a small size of $250 \times 83 \times 25$ mm enabling it to be mounted on the microscope stage.

An adaptor for the graphene MEA was 3D printed (Figure 6.8c). The adaptor was a 48×48 mm square, the same dimensions as the MEA coverslip. It has a height of 830 µm, making the total height of the adaptor plus coverslip 1 mm. This gave the coverslip plus adaptor the same height as a conventional microscope slide, enabling the MEA-2100 amplifier pins to contact the MEA connecting pads. The adaptor also had a 20 mm diameter hole in the centre, allowing the objective lens from the microscope to contact the coverslip. The graphene MEA slid onto the adaptor which fitted directly into the MEA-2100 amplifier

(Figure 6.8a). A lid was placed over the device to reduce evaporation of the cell media during imaging.

6.4.2 Widefield microscopy

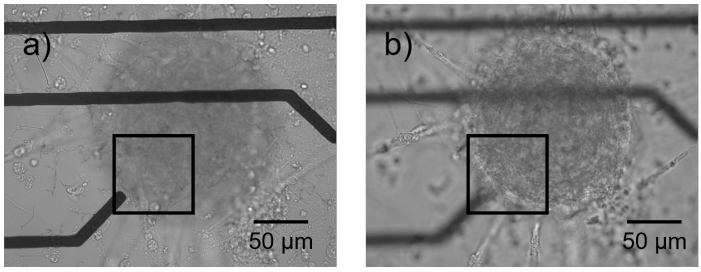

Fig. 6.9 Widefield images a) focused on the gold connecting leads, b) focused on the cells, showing neurons grown on the graphene electrodes (located inside the black squares). The neurons can clearly be seen through the graphene electrodes, whereas the gold leads obscure the view. Neurons were prepared, maintained and imaged by MR.

After voltage traces had been recorded on the graphene MEA, low and high magnification images of the graphene MEA were taken using widefield a microscope (Figure 6.1 and Figure 6.9). The neurons can clearly be imaged through the graphene electrode and PMMA, however are obscured by the opaque gold connecting leads.

6.4.3 Fluorescence intensity imaging

Following widefield imaging, fluorescence intensity images were acquired using the dye Oregon Green 488 BAPTA-1 (OGB-1, where BAPTA is 1,2-bio(o-aminophenoxy)ethane-N,N-N',N'-tetraacetic acid). OGB-1 shows changes in fluorescence intensity and lifetime with different calcium concentrations, it is therefore commonly used to quantitatively determine the local calcium content in cells (Section 3.2.1).

OGB-1 was added to the extracellular space and taken up by the neurons. Fluorescence intensity images were acquired of juvenile neuronal cultures with OGB-1, excited at 485 nm (Figure 6.10). Like in the widefield images, the graphene electrodes do not obscure or alter the image obtained. This makes sense since the transmittance of a coverslip with a monolayer of graphene, plus a 500 nm layer of PMMA was found to transmit be >88% from 400–1500 nm. This also mirrors previous work showing confocal imaging through a working graphene electrode using OGB-1 in brain slices [32, 105].

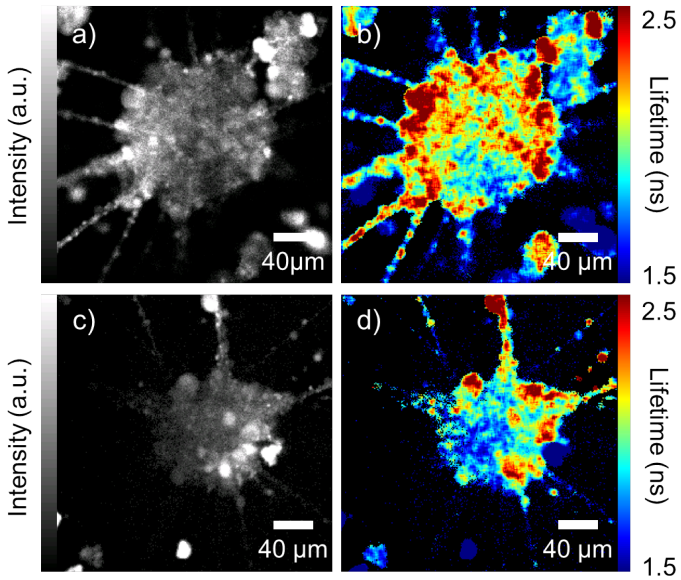

Fig. 6.10 a), c) Confocal fluorescence intensity images and b), d) fluorescence lifetime images of mouse neuronal cultures with calcium sensor OGB-1, on the graphene MEA after voltage traces recordings. The graphene electrodes do not obscure or alter the images obtained. Cell cultures were prepared and maintained by SM, TS, RC and MR. Imaging and data analysis was performed by MR, CP and the author.

6.4.4 Fluorescence lifetime imaging microscopy

Both the fluorescence intensity and lifetime of OGB-1 are sensitive to calcium concentration. The lifetime of calcium-free OGB-1 is ~ 0.6 ns, whereas the calcium-bound dye has a longer fluorescence lifetime of ~ 3.7 ns (Figure 3.8). The calibration of this dye was performed by Wilms *et al.* and Lattarulo *et al.* [189, 190]. The fluorescence lifetime decay curves of juvenile neuronal cultures with OGB-1 were fitted with a double decay function [190] to obtain FLIM maps of the same region as the fluorescence intensity images (Figure 6.10). The graphene electrodes did not obscure or alter the image obtained. The measured fluorescence lifetimes were between 1.5–2.5 ns, within the region expected for the partial binding of calcium. There is a general agreement between the regions of high and low calcium concentration in the imaged cluster of cells, as measured by the fluorescence intensity and lifetime of OGB-1.

In previous works, calcium imaging using the fluorescence intensity of OGB-1 was proven on a confocal microscope [32] and two-photon microscope [105]. This work showed for the first time, that FLIM can be performed on a graphene MEA capable of recording neuronal voltage traces. The advantage of FLIM over these other systems is insensitive to fluorophore concentration or laser power, and less sensitive to photobleaching. This means

fluorescence lifetime measurements are independent of the concentration of dye present, so the absolute calcium concentration can be determined independent of the dye concentration. Another application where FLIM in combination with a graphene MEA could be useful is to enable experiments which correlate the location and aggregation state of amyloid proteins, with the effect of these proteins on neuronal electrophysiology. This would add to work showing the location and aggregation state of a number of amyloid proteins using FLIM including K18 tau *in vitro*, polyQ in fixed cells [245], human full length tau in tissue sections from AD patients [246] and α-synuclein in *in vitro* and in live cells [30].

6.5 Conclusion

A transparent graphene MEA was fabricated with gold leads, graphene electrodes and a PMMA encapsulation layer. Voltage traces of the spontaneous firing of mouse neurons on the graphene MEA were successfully recorded, and spikes were detected from firing neurons. The recorded voltage traces were compared to conventional opaque TiN MEA. The mean noise on the graphene MEA was $2.5 \pm 0.7\,\mu V$, similar to steam plasma treated graphene electrodes [80], but lower than untreated graphene electrodes [81]. The maximum SNR observed on the graphene MEA was 23, similar to the SNR recorded from the TiN MEA and graphene electrodes plated with embryonic rat neurons [81] and high enough to clearly detect spikes.

The graphene MEA was fitted in a commercial amplifier and mounted on an inverted microscope. Each imaging modality widefield, confocal microscopy and FLIM was shown to be compatible with the graphene MEA, which did not perturb the images.

It was shown for the first time that FLIM was compatible with electrophysiological recordings from graphene MEAs. This adds to the range of microscopy techniques compatible with a graphene MEA. FLIM has the advantage over confocal microscopy that the fluorescence lifetime measurements are independent of the concentration of dye present. Therefore, the fluorescence lifetime of OGB-1 could be used to determine the absolute calcium concentration independent of the dye concentration.

Additionally, FLIM could be used with a graphene MEA to correlate the location and aggregation state of amyloid proteins in live cells. This would add to work showing FLIM imaging of amyloid proteins in live cells with α-synuclein [30], and *in vitro* for K18 tau [245] and human full length tau [246]. Some of the challenges for this experiment include combining the expertise of the electrophysiology, FLIM imaging and amyloid protein understanding. It would also be very useful to stimulate the neurons, especially for tau propagation

of tau experiments. However, electrical stimulation using the graphene electrodes is likely to be challenging, so instead optogenetic stimulation of the cells could be used.

Chapter 7

Fourier transform infrared spectroscopy of monomeric α-synuclein

α-synuclein was purified and lyophilised, and buffers prepared by Amberley Stephens (AS) and Maria Zacharopoulou (MZ). Lyophilised bovine serum albumin formulations were prepared by Talia Shmool (TS). All FTIR data were acquired and analysed by the author.

7.1 Introduction

Electrophysiology and fluorescence imaging can be combined to better understand the role of amyloid proteins in neurodegenerative diseases. Complimentary to these techniques is Fourier transform infrared spectroscopy (FTIR), a vibrational absorption spectroscopy used to study the secondary structure of the amyloid proteins. The amyloid protein α-synuclein (aSyn) is implicated in Parkinson's disease (PD). Monomeric aSyn is highly dynamic, existing in many conformations which are dependent on the local environment. The fibrils formed from these different monomeric conformations have different biophysical properties and toxicity in cells [247, 39], and it is possible that the different structural variations of aSyn are responsible for different pathophysiologies [248].

In this chapter, the polymorphism of monomeric aSyn in different environments is examined using FTIR. To achieve this, a protocol is described to batch process protein FTIR spectra, and calculate their secondary structure composition. Pre-processing of the spectra removed water and buffer peaks, flattened the baseline and normalised the spectra. The secondary structure composition is then estimated by curve fitting the second derivative of the amide I region, and relating this to the secondary structure. This protocol is used to understand the monomeric aSyn structure. Firstly, the structural implications of preparing

the lyophilised aSyn are considered. Following this, the secondary structure of monomeric aSyn in a number of physiologically relevant conditions are examined.

Background information about FTIR spectroscopy and the analysis of protein FTIR spectra can be found in Section 3.3.

7.2 Background to α-synuclein

Two main forms of PD exist, early-onset (familial) and late-onset (idiopathic). PD first manifests itself in patients as small cognitive deficits, then develops into motor symptoms including resting tremor in limbs, limb stiffness, slow movement, difficulty initiating movement, gait problems and balance problems [2]. These symptoms are accompanied by the deterioration of midbrain dopaminergic neurons in the substantia nigra pars compacta [249].

Although the mechanism of neuronal death in PD is still not fully understood, a number of observations implicate the protein aSyn in the disease mechanism. Firstly, aSyn has been identified in the Lewy body intracellular inclusions associated with the disease [15, 16]. Additionally, familial PD correlates with six point mutations (A30P, A53T, A53E, E46K, H50K and G51D) in the SNCA gene which encodes aSyn [250].

The normal physiological role of aSyn is not fully understood. ASyn is expressed in the brain and in red blood cells. In the brain, aSyn is primarily found at the presynaptic terminal [13]. The proposed physiological roles for aSyn at the presynapse are to modulate synaptic vesicle release; as a chaperone; to regulate synaptic plasticity and to modulate lipid, dopamine and glucose synthesis [14]. At the presynapse, the aSyn may encounter local environments with different concentrations of ions and pH. The free calcium concentration of the extracellular space and intracellular space is 1.3 mM and 100 nM respectively [248], for lysosomes it is either 0 or 0.5-0.6mM [251]. The pH of the extracellular space, intracellular space and lysosomes is 7.4, 7.2 and 4.6-5 respectively [248].

Monomeric wild type (WT) aSyn contains 140 amino acid residues and under physiological conditions is intrinsically unstructured, highly dynamic and exists in many conformations. ASyn can be separated into a N-terminal region, a non-amyloid-β component (NAC) region and a C-terminal region [252]. The N-terminus is positively charged and forms an α-helical structure when bound to lipid membranes [253]. The NAC region is highly hydrophobic and can aggregate to form insoluble β-sheeted fibres [254]. The C-terminal is negatively charged and intrinsically disordered [255]. Many long range interactions have been identified within aSyn, generally between the N- and C- terminus. The local cellular environment also has an effect on the monomeric aSyn structure, and the fibrils formed from different monomeric conformations have different biophysical properties and different toxicity in cells [247, 39].

It is possible that the different structural variations of aSyn are responsible for different pathophysiologies [248].

7.3 Batch processing Fourier transform infrared spectra

Many physical techniques can be used to understand the structural polymorphism of a protein like aSyn. X-ray diffraction (XRD) gives the full 3D atomic structure of proteins that can crystallised. Nuclear magnetic resonance (NMR) gives the full atomic structure of solid and liquid state proteins with molecular weights less than (40–50 kDa) [256]. For large proteins that cannot be crystallised, the full atomic structure cannot be obtained, however some structural information can be obtained by circular dichroism (CD) [257], FTIR, Raman spectroscopy [196] or cryo-electron microscopy (cryo-EM) [258]. FTIR was used in this work and has the advantages that: a small quantity of protein can be used ($\sim 1\,\mathrm{mg\,ml^{-1}}$); the protein can be probed in different physical environments like the solid state, liquid state and when adsorbed to a surface; there is no background fluorescence; the sample preparation is minimal and a spectrum can be obtained in a few minutes [164].

To rapidly process and interpret the aSyn FTIR spectra, and to remove operator assisted errors, a script was developed in Matlab. The script is described in detail below, but briefly it imported the raw spectra, subtracted the background water and buffer contributions, then corrected the baseline for scatter. Resolution enhancement was implemented by taking the second derivative, and the secondary structure was estimated from this.

7.3.1 Background subtraction

The final processed spectrum should only contain absorbance peaks from the protein under investigation. To achieve this, peaks from other molecules present in the chamber were removed using a linear subtraction protocol. A peak was identified at a wavenumber, $\tilde{\nu}$, where a band from the species to be subtracted was clearly distinguishable from the protein spectrum. From the height of this peak above a baseline, a scaling factor, x_i, was calculated as:

$$x_i = A_1(\tilde{\nu}_1) - \frac{A_2(\tilde{\nu}_2) + A_3(\tilde{\nu}_3)}{2} \quad \text{where} \quad i = J, B \tag{7.1}$$

where $A_1(\tilde{\nu}_1)$ is the absorbance at wavenumber $\tilde{\nu}_1$ corresponding to the top of the subtraction peak, $A_2(\tilde{\nu}_2)$ and $A_3(\tilde{\nu}_3)$ are the absorbance values at $\tilde{\nu}_2$ and $\tilde{\nu}_3$ respectively, which form a linear baseline at the bottom of the peak. The corrected protein spectrum, J_C, was a scaled

linear subtraction of the background peak, B, from the original protein peak, J, as:

$$J_C = \frac{J}{x_J} - \frac{B}{x_B} \tag{7.2}$$

where x_J and x_B are the scaling factors for the protein and background spectra respectively. A successful background subtraction removes all the bands related to the background spectrum but does not over-subtract and create negative side lobes [211].

7.3.2 Background water subtraction

There are always traces of liquid water, atmospheric water vapour and CO_2 in the sample or chamber, which give absorbance bands in the FTIR spectrum. The water infrared absorbance is approximately an order of magnitude larger than the protein absorbance. Molecular water has three main peaks at $\sim 3400\,\mathrm{cm}^{-1}$ (O–H stretch), $\sim 2125\,\mathrm{cm}^{-1}$ (water association) and $\sim 1645\,\mathrm{cm}^{-1}$ (H–O–H bend). Water vapour creates small sharp peaks at 1684, 1670, 1662, 1653, 1646 and $1617\,\mathrm{cm}^{-1}$ [211]. Since the water vapour peaks overlap with and distort the amide I band, it is very important to subtract these peaks. The water vapour peaks are also amplified by resolution enhancing techniques [259], which can lead to the incorrect assignment of secondary structure [211]. The CO_2 bands are less problematic for secondary structure calculation, since the asymmetric stretch falls outside the range of interest at $\sim 2350\,\mathrm{cm}^{-1}$ [260] and were therefore not considered.

Physical methods were implemented to remove water from the sample and chamber. Water was removed from the protein by lyophilisation and from the KBr by heating to 100 °C for 2 h. After adding the samples into the spectrometer, the chamber was purged with dry air for 5 min to remove water vapour [261]. However, despite this, water vapour bands were observed, so mathematical spectral subtraction was also performed [211].

The FTIR spectrum of a plain KBr pellet was taken under identical conditions to the protein spectrum. An unscaled linear subtraction of the KBr pellet spectrum does not remove the water vapour peaks. This could be due to local fluctuations in temperature, pressure and air currents within the instrument which change number of water vapour molecules probed by the infrared beam [262], or it could be due to non-linear effects in the spectrometer detector which can distort the band shapes and the relative intensities of the absorption [204].

A scaled linear subtraction of the plain KBr spectrum successfully removed water vapour peaks. In previous works, the water scaling factor has been based on peaks at $2125\,\mathrm{cm}^{-1}$ [207], 1717 or $1772\,\mathrm{cm}^{-1}$ [263]. In this work the absorbance at $1635\,\mathrm{cm}^{-1}$ was compared to a baseline between 1637 and $1634\,\mathrm{cm}^{-1}$. The water corrected spectrum, J', was found by

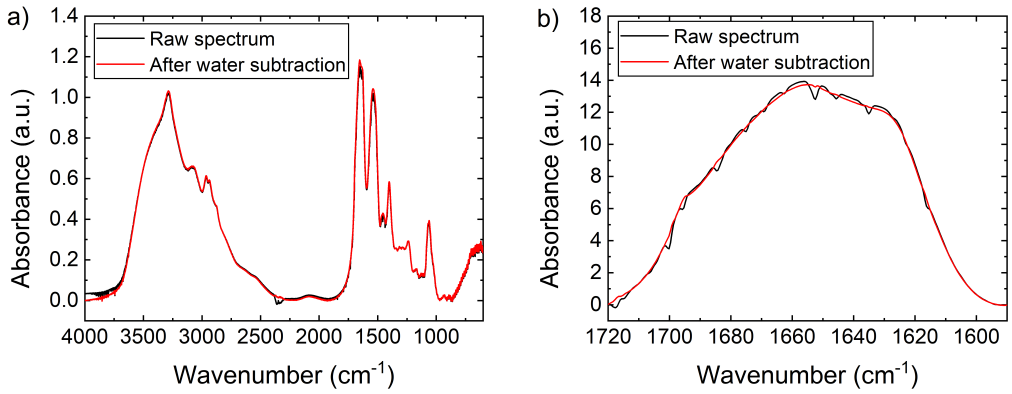

Fig. 7.1 a) FTIR spectrum and b) amide I region of WT aSyn in ammonium acetate buffer. The raw spectrum, and the spectrum after the successful application of the water vapour subtraction algorithm are shown. ASyn was prepared and lyophilised by AS and MZ.

subtracting the KBr spectrum with water peaks, B_w, from the raw protein spectrum, J, as:

$$J' = \frac{J}{x_w^J} - \frac{B_w}{x_w^{B_w}} \tag{7.3}$$

where x_w^J and $x_w^{B_w}$ are the water scaling factors for spectrum J and B_w respectively.

The successful subtraction of water vapour from the protein WT aSyn in ammonium acetate buffer is shown in Figure 7.1. This is successful since there are no water vapour bands in the region 1800–1500 cm^{-1}, and there is a straight baseline between 2000–1750 cm^{-1} [211]. Using these two criteria ensures the experimental error in the amide I band maxima is less than 3% [202].

7.3.3 Buffer subtraction

All the proteins analysed were prepared in a buffer. In addition to subtracting the water, the effects of the buffer must also be subtracted. Four different buffers were used in this work, ammonium acetate, a tris(hydroxymethyl) aminomethane (tris) based buffer, a 4-(2-hydroxyethyl)-1-piperazineethanesulfonic acid (HEPES) based buffer and a histidine sucrose buffer. Each buffer has a distinct FTIR spectrum (Figure 7.2). The ammonium acetate buffer completely evaporates when lyophilised, so does not absorb in the FTIR spectrum. The tris, HEPES and histidine-sucrose buffers however, all show absorption peaks in the amide I band. In the amide I region, the tris buffer has a narrow peak centred at 1630 cm^{-1}, the HEPES buffer has a broad peak centred at 1644 cm^{-1} and the histidine sucrose buffer has a broad peak centred at 1640 cm^{-1}.

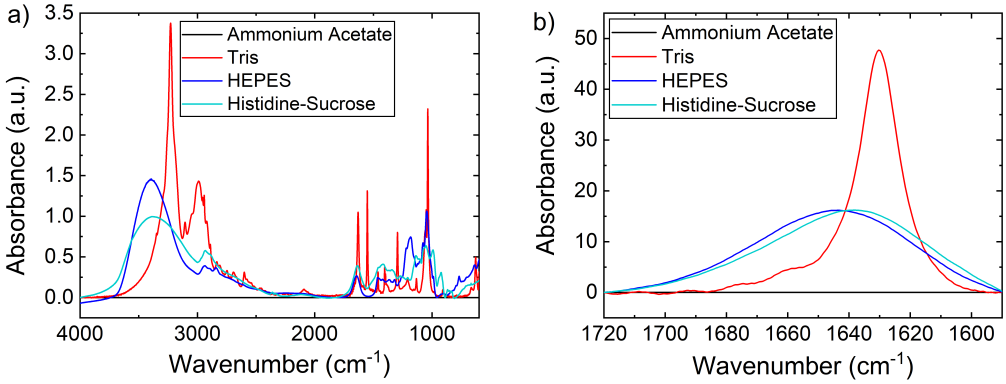

Fig. 7.2 a) Representative FTIR spectra and b) the amide I region of the lyophilised pure buffers. The ammonium acetate buffer completely evaporates when lyophilised, so does not absorb in the FTIR spectrum. The tris, HEPES and histidine-sucrose buffers however, all show absorption peaks in the amide I band. Buffers were prepared by AS.

The successful subtraction of the buffer was determined similarly to the water vapour subtraction [211]. The peaks assigned to the buffer bands must be completely removed, and over-subtraction can be identified by negative lobes [264].

7.3.4 Scatter correction and normalisation

Scatter correction and normalisation were applied after the water and buffer subtraction [265]. Variations between the baselines of the FTIR spectra can be caused by light scattering, differences in the effective path length, the temperature, sample concentration, sample reflection or instrument anomalies [266]. One of the larger effects is Lorentz-Mie scattering, which occurs when the infrared wavelength is smaller than the scattering particles and encodes information about the underlying microstructure and shape of the scattering particles in the baseline shifts [265].

To reduce the scatter related spectrum variability, techniques such as multiplicative scatter correction, standard normal variate and baseline fitting can be used. Multiplicative scatter correction [267] removes artefacts by comparing the measured spectrum to a reference spectrum, fitting a line to this, then subtracting this baseline. The standard normal variate scales the data based on the average absorbance and standard deviation [265]. A baseline can also be fitted to the data and subtracted, either using a linear baseline between two specified points [204], or a polynomial passing through points of the baseline [266].

In this work baselines were subtracted. For the full spectrum a cubic spine polynomial was subtracted [266] which passed through the minimum values in the regions 4000–3700 cm^{-1},

2020–1840 cm^{-1} and 1000–500 cm^{-1}. For the amide I region, a linear baseline was subtracted between the absorbance values at 1720 and 1600 cm^{-1} [209].

To compare different spectra, they should be normalised. Normalisation based on the maximum absorbance value or the absorbance at a chosen wavelength, is extremely simple to implement but could be problematic for noisy data. More robust methods include scaling to the total sum of the all elements or the square root of the sum of squared elements [265]. In this work, all spectra were normalised to the total area under the curve.

7.3.5 Resolution enhancement using the second derivative

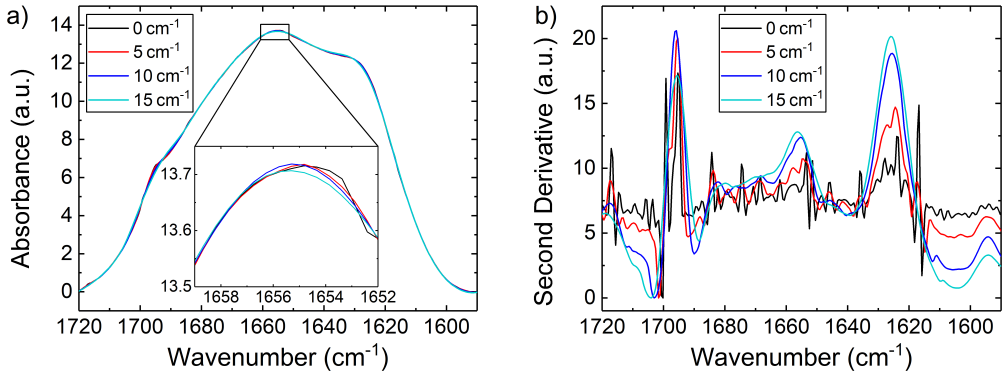

Fig. 7.3 Smoothing of the amide I region of an FTIR spectrum of WT aSyn in ammonium acetate buffer using a Savitsky-Golag (SG) filter across frame lengths of 0–15 cm^{-1}. The a) absorbance and b) second derivative spectra of the smoothed amide I region is shown. The signal is masked by noise in the unsmoothed data. As the smoothing window increases, the second derivative peaks become clear. A smoothing window of 10 cm^{-1} resolves the second derivative peaks, but does not shift the peak positions. ASyn was prepared and lyophilised by AS and MZ.

The amide I band splits into sub-bands with characteristic frequencies for each protein secondary structure. Since the width of each sub-band is larger than the distance between them, the amide I band is typically broad and featureless. Resolution enhancement (or band narrowing) enables the overlapping bands to be resolved [204], however greatly decreases the signal to noise ratio (SNR) [210]. Common resolution enhancement techniques are the Fourier self-deconvolution (FSD) or second derivative methods. FSD considers each peak as the convolution of a delta function which has position but no width, with a Gaussian or Lorentzian function of finite width [204]. The broadening effects can be removed by deconvolving the measured spectrum with a function describing the line broadening effects [205]. To perform FSD, the full-width at half maximum and a resolution enhancement factor

must be chosen by the operator [206]. Second derivative methods on the other hand do not require any operator dependant parameters and were therefore used in this work.

The second derivative was calculated using a Savitsky-Golag (SG) derivation. A SG derivation fits a polynomial of a given order to a symmetric region around the point of interest and calculates the derivative of the polynomial at each individual point [265]. The SG filter can also be used to smooth the data, acting like a moving average, fitting a polynomial of a given order across a given wavenumber range [268]. A second order SG smoothing filter was applied to the spectra in this work with windows of $5\,\mathrm{cm}^{-1}$, $10\,\mathrm{cm}^{-1}$ and $15\,\mathrm{cm}^{-1}$ (Figure 7.3). With the unsmoothed data, the signal is masked by noise. As the smoothing window increases, the second derivative peaks become clear. A smoothing window of $10\,\mathrm{cm}^{-1}$ was chosen, which resolved the second derivative peaks, but did not shift the peak positions. This smoothing width has the additional benefit of removing the effects of residual water vapour peaks which have a full width at half maximum, $\Gamma \sim 2\,\mathrm{cm}^{-1}$ without affecting the amide I sub-bands with Γ =10–30 cm^{-1}.

Taking the second derivative removes any linear baseline components, therefore a horizontal line drawn under the lowest point in the second derivative spectrum is generally subtracted to remove baseline effects. This is works well for proteins with a low α-helical content, however the second derivative spectrum of proteins with a high α-helical content have strong lobes which can go below the conventional baseline [211]. Fortunately, small deviations in the baseline position above or below the true baseline only have a small effect on the calculated secondary structure composition [266].

7.3.6 Secondary structure determination by peak fitting

The absorbance in the amide I region is related to the protein secondary structure. From the absorbance data, the protein secondary structure can be determined by principal component analysis (PCA), fitting peaks to the absorbance spectrum or fitting peaks to the resolution enhanced spectrum. PCA requires the use of a large training set of proteins with a known secondary structure. When fitting to the absorbance spectrum it is difficult to find a unique solution, since it is generally broad and featureless. Therefore, the secondary structure was determined by fitting peaks to the second derivative of the amide I region.

From the Beer-Lambert law it can be seen that the second derivative of the absorbance with respect to wavenumber is still proportional to the concentration of the species responsible for the vibration. Therefore, quantitative information about the protein secondary structure content can be found by peak fitting the second derivative of the amide I band. Each secondary structure type was shown to exhibit absorption at characteristic wavenumbers shown in Table 3.2 as follows: α-helix at 1654–1658 cm^{-1}; 3_{10}-helix at 1660–1666 cm^{-1},

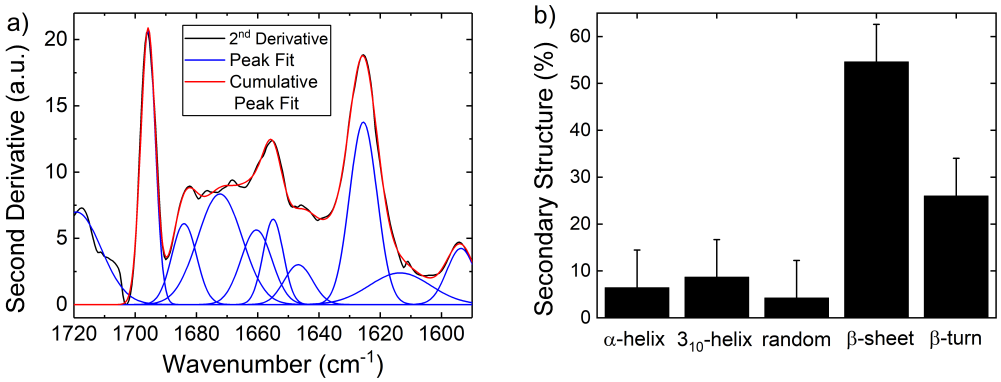

Fig. 7.4 a) Automated fitting of Gaussian curves under the second derivative spectrum for WT α-synuclein in ammonium acetate buffer. b) Secondary structure assignment based on the fit. This fitting should determine the secondary structure prediction to within 4–10% of the structure determined by XRD, although is less accurate for structures with $>$ 60% α-helical content [211, 266]. ASyn was prepared and lyophilised by AS and MZ.

parallel or antiparallel β-sheet with multiple peaks at 1623–1643 and 1689–1698 cm^{-1}; turn structures at 1666–1687 cm^{-1} and the random coil structure at 1646–1650 cm^{-1} [201, 202]. Each individual protein shows absorbance at a subset of these wavenumbers corresponding to its secondary structure [209].

Using this knowledge, an automatic peak fitting method was implemented [269] where a least square fitting procedure was applied to fit Gaussian functions to the second derivative data [208]. The starting position and limits for each peak are shown in Table 7.1. The initial fitting amplitude was $2/3$ of the absorbance at the initial wavenumber. The amplitude was contrained to be $\geqslant 0$ a.u. [208]. The initial peak width was 15 cm^{-1} and freely varied between 3.5–47 cm^{-1}, the lower width limit prevented high frequency noise being fitted and the higher width limit prevented the baseline being fitted. After the first fitting, any peaks with an amplitude less than 3.5 a.u. (approximately 10% of the maximum height of the second derivative amide I band) were rejected. The data were then refitted with the reduced number of peaks, starting from the output parameters from the first fitting, and using the same constraints.

The automatic peak fit under the second derivative is shown for WT aSyn (Figure 7.4). Each fitted sub-band was assigned to a corresponding secondary structure type. The proportion of each secondary structure type in the protein, was calculated as the area of the assigned bands relative to the area of all the bands with maxima between 1689–1623 cm^{-1}. This fitting should determine the secondary structure prediction to within 4–10% of the structure determined by x-ray diffraction (XRD), although is less accurate for structures with $>$ 60% α-helical content [211].

Table 7.1 Table showing the bounds for each peak fitted in the automatic fitting procedure, and their correlation to the secondary structure types.

Fit start (cm^{-1})	Fit limits (cm^{-1})	Assignment
1710	1720–1705	side chain
1680	1698–1688	β-sheet
1677	1687–1676	β-turn
1670	1677–1666	β-turn
1663	1666–1659	3_{10}-helix
1653	1657–1651	α-helix
1648	1651–1644	random coil
1630	1643–1623	β-sheet
1615	1620–1620	side chain
1600	1610–1590	side chain

7.3.7 Final protocol for acquiring and processing spectra

A summary of the final FTIR fitting protocol is described here. For FTIR analysis, the lyophilised protein sample was mixed with KBr using an agate mortar, and pressed into self-supporting disks. FTIR spectra were acquired with 60 scans and a resolution of $1\,cm^{-1}$. The chamber was purged for 5 min with CO_2 free dry air before recording each spectrum. A background spectrum containing pure KBr was obtained under identical conditions.

To remove the water vapour peaks, a linear subtraction of the KBr spectrum was performed, scaled to the absorbance of the water vapour peak at $1635\,cm^{-1}$ compared to a baseline at $1637–1634\,cm^{-1}$. A successful background water subtraction was determined by the complete subtraction of water vapour bands in the region $1800–1500\,cm^{-1}$, and a straight baseline between $2000–1750\,cm^{-1}$. The additional buffer peaks were subtracted similarly, with the position of the scaling factor being unique for each buffer-protein system.

The baseline shift caused by Mie-Lorentz scattering was corrected for by subtracting a baseline. For the full spectrum, a polynomial spline was subtracted which passed through the minimum values in the regions $4000–3700\,cm^{-1}$, $2020–1840\,cm^{-1}$ and $1000–500\,cm^{-1}$. Spectra were then normalised to the total area under the curve.

The second derivative of the amide I band was calculated to resolve overlapping bands. The amide I band was first smoothed using a second order SG filter with a window of $10\,cm^{-1}$. From this the second derivative was calculated and multiplied by a factor of -1. Both the absorbance and second derivative spectra were truncated to $1720–1590\,cm^{-1}$. A linear baseline for the absorbance data between $1720–1590\,cm^{-1}$ was subtracted. The baseline for the second derivative spectrum was a horizontal line through the minimum value.

A least square fitting procedure was used to fit Gaussian peaks at the wavenumbers of 1710, 1680, 1677, 1670, 1663, 1653, 1648, 1630, 1615 and 1600 cm^{-1}. The initial fitting amplitude was $2/3$ of the absorbance at this wavenumber and was $\geqslant 0$ a.u. The initial peak width was 15 cm^{-1} and was freely varied between 3.5–47 cm^{-1}. After the first fitting, peaks with amplitudes of less than 3.5 a.u. were rejected and the data was the refitted with the reduced number of peaks. From this data, the sub-bands were assigned to their corresponding secondary structure types. The proportion of each secondary structure type, was calculated as the area of each band relative to the area of all bands between 1689–1623 cm^{-1}.

The developed protocol was used throughout this work to investigate the secondary structure of monomeric aSyn in different physiologically relevant conditions.

7.4 Protein preparation conditions

The storage conditions and buffer used to prepare aSyn can significantly interfere with its structure and affect its aggregation kinetics [270]. Therefore, it is important to consider the preparation conditions of aSyn for FTIR.

In FTIR measurements, there is a compromise between the physiological relevance of the protein environment and the number of additional species with measurable FTIR bands. FTIR can be performed in live cells [271] or aqueous environments, however water has strong absorbance bands in the mid-infrared region. The water bands overlap with, and can distort the amide I band [204]. H_2O free environments are less physiologically relevant [204] and include D_2O based media [272], or drying the protein by lyophilisation [203, 273], heating [274], spray drying [275] or supercritical drying [276]. Lyophilisation was used in this work since it gives the lowest water content and is used commonly in the pharmaceutical industry [276]. During lyophilisation, the aqueous solution containing the protein is frozen, following this the pressure is lowered resulting in sublimation of the ice and bound water, leaving a dry protein powder [277].

7.4.1 Lyophilised protein formulations

The lyophilisation can induce an irreversible change in the biological activity of the proteins and can induce protein aggregation [278]. This is true of aSyn where differences in the structure and activity of the monomeric protein are seen between lyophilised and frozen samples [270]. To provide stability to the proteins and maintain their native conformation during lyophilisation, stabilisers can be added. Common stabilising agents used include

sugars like sucrose and trehalose, or surfactants like polyoxyethylene sorbitan monooleate (polysorbate 80) [277].

To examine if stabilisation additives should be used with aSyn, the effect of the additives was investigated on the structure of the widely available protein bovine serum albumin (BSA) [279]. Serum albumin is the most abundant plasma protein in mammals. It has many physiological functions relating to ligand binding [280]. BSA is also the largest component of fetal bovine serum (FBS) which is used during the cell culture of primary neurons in Chapter 6.

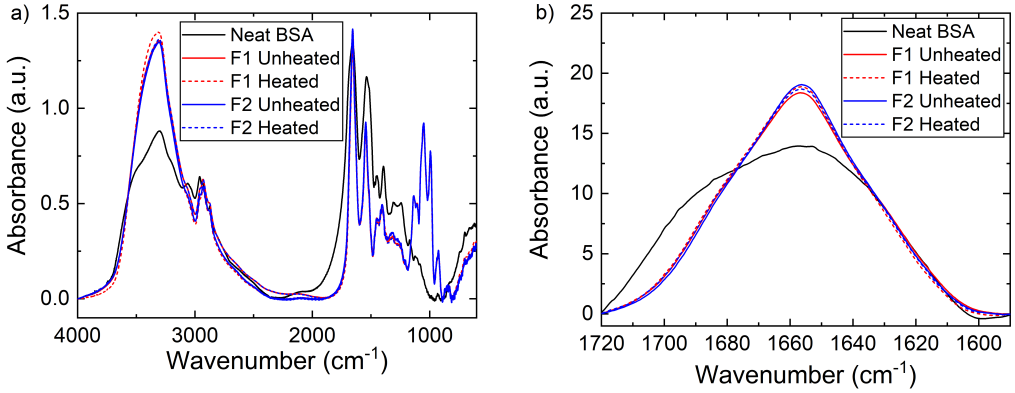

Fig. 7.5 a) Representative FTIR spectra and b) amide I region of lyophilised neat BSA, and BSA with additives. F1 is BSA with histidine and sucrose (at 278 K and heated to 410 K). F2 is BSA in with histidine, sucrose and polysorbate 80 (at 278 K and heated to 330 K). The FTIR spectrum of the neat protein is in agreement with previous FTIR studies. Significant differences were seen between neat BSA and BSA lyophilised with sugar (F1 and F2), most notably the additional peaks at 900–1200 cm^{-1} were attributed to sucrose in the lyophilised formulations. No significant differences were observed when any of the formulations were heated, or when polysorbate was added. Formulations were prepared and lyophilised by TS.

Three formulations were examined: neat lyophilised BSA (at 278 K); BSA with histidine and sucrose (F1, at 278 K and heated to 410 K) and BSA with histidine, sucrose and polysorbate 80 (F2, at 278 K and heated to 330 K) (Figure 7.5). The FTIR spectrum of the neat protein is in agreement with previous FTIR studies [281]. Significant differences were seen between the neat BSA and the samples lyophilised with sugar (F1 and F2). Most significantly, the lyophilised formulations included additional peaks in the region 900–1200 cm^{-1} which were attributed to sucrose [282]. The presence of these peaks is interesting, since a linear subtraction of the histidine sucrose buffer spectrum was applied. The fact that sucrose peaks remain in the spectrum, suggests the sugars interacted with the protein, resulting in a shift in the positions or intensities of some peaks [283]. This is in agreement with the studies which showed a difference between the NMR spectra of a physical mixture of the components and

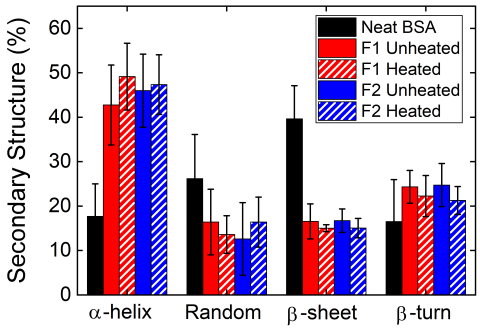

Fig. 7.6 Secondary structure composition of BSA of lyophilised neat BSA, and BSA with additives. F1 is BSA with histidine and sucrose (at 278 K and heated to 410 K). F2 is BSA with histidine sucrose and polysorbate 80 (at 278 K and heated to 330 K). Secondary structure composition was obtained by fitting Gaussian curves under the second derivative of the amide I region of the FTIR spectrum. Significant differences in the secondary structure were seen between neat BSA and BSA lyophilised with sugar (F1 and F2), most notably the increase in α-helical content and decrease in β-sheet content. No significant differences were observed when any of the formulations were heated, or when polysorbate was added. Formulations were prepared and lyophilised by TS.

a lyophilised sample. The NMR peaks from the lyophilised showed a broadening effect explained by the homogenisation of the sample [279].

Additionally, a change in the secondary structure can be observed by examining the amide I peak. The increase in the absorbance of the peak at $\sim$1655 cm^{-1} is attributed to an increase in α-helical content from $\sim 16 \pm 4\%$ for neat BSA, to $\sim 37 \pm 8\%$ for unheated BSA with the addition of histidine and sucrose (Figure 7.6).

No significant differences were observed when any formulation was heated, or when polysorbate was added, in agreement with the NMR studies performed on the same formulations [279].

Since the addition of histidine and sucrose interacted with the protein, it was deemed unnecessary to use these stabilising additives in the aSyn work.

7.4.2 Choice of α-synuclein buffer

The choice of buffer affects the aSyn structure [270]. Monomeric aSyn was prepared in three different buffers, ammonium acetate, a tris based buffer and a HEPES based buffer to fins an appropriate buffer for the FTIR work. The buffer subtraction protocol was applied using (Equation 7.2). The tris buffer scaling factor was the absorbance of the peak centred at 2992 cm^{-1} compared to a baseline between 2933–3033 cm^{-1}. The HEPES buffer scaling

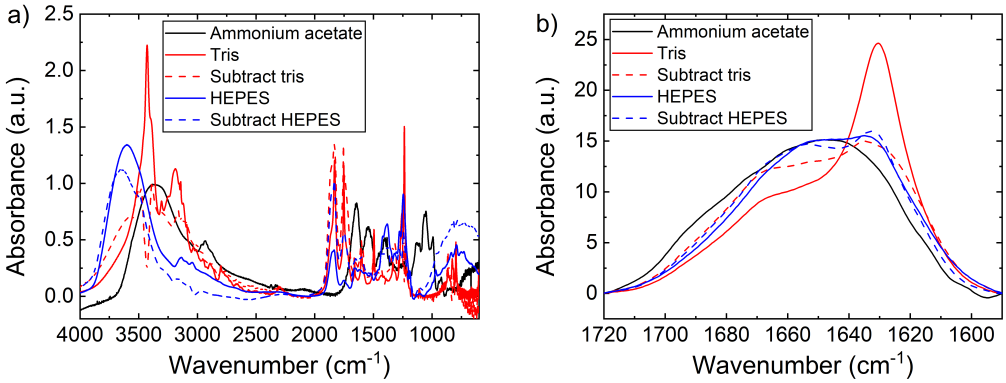

Fig. 7.7 a) Representative FTIR spectra and b) amide I region of monomeric aSyn spectra at pH 7 without additional calcium, prepared in ammonium acetate, tris and HEPES buffer. The spectra are shown before and after linear buffer subtraction. The FTIR spectrum of aSyn is different in each buffer, even after buffer subtraction. It is unclear if these differences are due to variations in the monomeric protein structure, or because of an incomplete buffer subtraction. ASyn was prepared and lyophilised by AS and MZ.

factor was the absorbance of the peak centred at 2600 cm^{-1} compared to a baseline point at 3700 cm^{-1}.

The FTIR spectrum of aSyn in different buffers before and after linear buffer subtraction (Figure 7.7), can be compared with the pure buffer spectra (Figure 7.2). The FTIR spectrum of aSyn is different in each buffer, even after buffer subtraction. It is unclear if these differences are due to variations in the monomeric protein structure, or because of an incomplete buffer subtraction. An incomplete buffer subtraction would arise if the protein interacted with the buffer, causing shifts in the absorbance bands and preventing all buffer effects being removed by a linear subtraction [283]. Ammonium acetate was chosen as the most suitable buffer since it completely evaporated when lyophilised leaving no residual peaks in the FTIR spectrum.

7.5 Structure of α-synuclein *in vitro*

Having chosen ammonium acetate as a suitable buffer, FTIR was used to examine how the local environment of aSyn affects its monomeric structure. A neutral pH with no additional calcium was chosen to mimic intracellular conditions, a low pH with no additional calcium mimicked lysosomal conditions, and a neutral pH with a high calcium concentration was chosen to mimic the extracellular conditions. FTIR was used to resolve differences in the protein secondary structure of the conformational ensemble in each environment.

7.5.1 Wild type α-synuclein

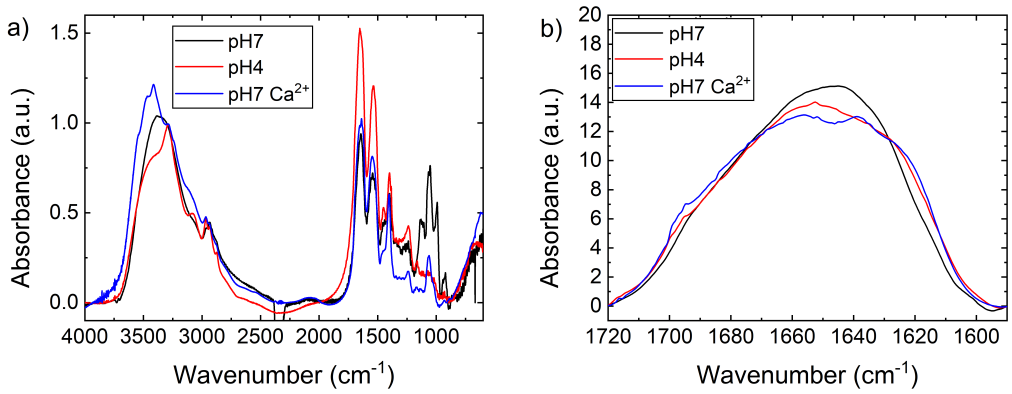

Fig. 7.8 Representative FTIR spectra of monomeric WT aSyn for a) the 4000–600 cm^{-1} region and b) the amide I region. The condition at pH 7 with no additional calcium mimicked intracellular conditions, the amide I band shows a broad asymmetric peak centred at 1645 cm^{-1} characteristic of a random coil conformation. The condition at pH 4 with no additional calcium mimicked the conditions inside a lysosome. The amide I maximum is at ~1556 cm^{-1} corresponding to an increased α-helical content compared to pH 7, and sub-bands at ~1638 cm^{-1} and ~1695 cm^{-1} also appear, corresponding to increased β-sheet content. The condition of pH 7 with a high calcium concentration mimicked the extracellular space. The amide I band has two maxima at ~1656 cm^{-1} (α-helix), and ~1637 cm^{-1} (β-sheet). ASyn was prepared and lyophilised by AS and MZ.

At neutral pH with no additional calcium represents the intracellular conditions in a neuron. Under these conditions the amide I band shows a broad asymmetric peak centred at 1645 cm^{-1} (Figure 7.8), characteristic of a random coil conformation. This agrees with other FTIR work performed on WT monomeric aSyn at neutral pH [22, 284, 285], and with the understanding that aSyn is intrinsically unstructured [286].

7.5.2 Effect of low pH on α-synuclein structure

ASyn proteins may be found in low pH environments in endosomes or lysosomes [287] (with a pH of 4.6–5.5 [288]) or if the cell pH is perturbed [289]. The FTIR spectrum of aSyn at pH 4 shows a marked change from pH 7 buffer conditions (Figure 7.8). The maximum of the amide I peak shifts from ~1645cm^{-1} to ~1556 cm^{-1} corresponding to an increased α-helical content. Sub-bands at ~1638 cm^{-1} and ~1695 cm^{-1} also appear, corresponding to increased β-sheet content.

The change in structure is likely due to the environmental pH affecting the protein charge. At pH 7, aSyn has a charge of -9 and each aSyn regions has a distinct charge: the N-terminus

is +4, the NAC region is -1 and the C-terminus is -12. When the pH is lowered, the overall charge on the protein decreases, becoming positive below the isoelectric point of pH 4.67 [290] . At low pH, the N-terminus has the greatest charge density of any aSyn region [291]. It is likely that the increase in α-helical and β-sheet content is linked to the reduction in C-terminus charge, reducing the electrostatic interaction and causing the extended conformation to become more compact and partially folded [292, 22].

7.5.3 Effect of calcium on α-synuclein structure

A high calcium concentration, and neutral pH mimicks the extracellular space around neurons in the brain. A high calcium concentration is also of interest since PD patients experience deterioration of dopaminergic neurons in the substantia nigra pars compacta [249]. This in an area of the midbrain with large calcium fluctuations, and low concentrations of calcium buffering proteins [293].

FTIR studies of monomeric aSyn at pH 7 with 2.5 mM $CaCl_2$ added, confirmed a structural change, and increased order in aSyn on addition of calcium (Figure 7.8). The band had two maxima at $\sim$1656 cm^{-1} (α-helix), and $\sim$1637 cm^{-1} (β-sheet). Calcium acts like any general salt shielding the charges on a protein, which would reduce the electrostatic interaction and explain the increase in α-helical and β-sheet content. In addition, aSyn has a calcium specific response, binding up to 6 calcium ions at the C-terminus [294], it is likely this that causes the monomeric aSyn to adopt a more ordered [295], and extended [296] structure. The increased α-helical content arises from a change in the monomeric structure, but it is unclear if the increased β-sheet content is due to the partial fibrilisation of the lyophilised sample (which occurs faster in the presence of calcium [296]), or if it is due to changes in the monomeric structure.

7.6 Conclusion

ASyn is an amyloidogenic protein implicated in PD, and can exist in many conformations which depend on its local environment. By uncovering the range of structures of monomeric aSyn in different environments it may be possible to link the different monomeric protein structures to different diseases associated with misfolding aSyn. To this aim, the structure of monomeric aSyn was investigated using FTIR, a complimentary technique to the electrophysiology and fluorescence imaging used in previous chapters.

A script was written to batch process protein FTIR spectra, and calculate their secondary structure composition. Pre-processing of the spectra was performed by a linear subtraction

to remove any water or buffer peaks, and flattening the baseline. The secondary structure composition was then estimated by fitting Gaussian curves to the second derivative of the amide I region, and relating this to the individual secondary structure components.

The aSyn was prepared for FTIR by lyophilisation in ammonium acetate buffer, which evaporates when lyophilised. Stabilising additives like histidine and sucrose were deemed unnecessary to stabilise the aSyn. The FTIR spectrum of WT aSyn at neutral pH shows a disordered protein, in agreement with previous studies. At pH 4 or with the addition of a high calcium concentration, the monomeric aSyn becomes a more ordered showing a significant increase in α-helical and β-sheet structure, likely due to the decreased charge on the protein and shielding of the protein charge enabling a more folded conformation.

To further this work in more physiological conditions, ATR-FTIR (Attenuated total reflectance FTIR) could be used, which allows samples in a liquid state and therefore proteins in a buffer before lyophilisation to be examined. Interpreting the secondary structure from ATR-FTIR measurements however is more difficult than from solid state measurements. To obtain more information about the aSyn, NMR is one of the best techniques to use, as the full structure atomic structure of the protein can be obtained as either a solid or in a liquid.

Chapter 8

Conclusion

Alzheimer's disease (AD) and Parkinson's diseases (PD) are two neurodegenerative diseases that affect $\sim$60 million people worldwide. Both diseases are linked to the misfolding of proteins from their native conformational state into β-sheeted amyloid fibrils. In AD the misfolded proteins are amyloid-β and tau, in senile plaques and neurofibrillary tangles, for PD the implicated misfolded protein is α-synuclein (aSyn), in Lewy body intracellular inclusions.

The motivation for this work was to develop and use physical techniques to better understand the role of amyloid proteins in neurodegenerative diseases. To achieve this, transparent graphene microelectrode arrays (MEAs) were designed and fabricated for use on inverted microscopes. The fabricated devices were characterised by electrochemical impedance spectroscopy (EIS) to probe the saline-electrode interface. The graphene MEAs enabled voltage trace recordings from cultured neurons to be combined with widefield, confocal fluorescence and fluorescence lifetime imaging microscopy (FLIM) on inverted microscopes. Combining these techniques will allow the location and aggregation state of amyloids to be correlated with neuronal firing patterns. Complimentary to this, Fourier transform infrared microscopy (FTIR) was used to examine the secondary structure of amyloid proteins. To achieve this, a script for estimating the secondary structure content of proteins was written and used to investigate the monomeric form of aSyn in physiologically relevant conditions.

MEAs are grids of external planar electrodes on a substrate. The MEAs measure the external action potentials generated by firing neurons, which are recorded as voltage traces. Transparent graphene MEAs were designed and fabricated to combine the MEA recordings with fluorescence imaging. This placed many constraints on the design, namely on the material processability, biocompatibility, transparency, device geometry, electrode impedance, electrode geometry and the encapsulation layer. The final device was fabricated on #1.5

coverslip substrates suitable for advanced fluorescence imaging. The electrode used was graphene since it can be grown, transferred and patterned using conventional microfabrication processes, is biocompatible with primary neurons, and is transparent. The graphene electrode diameter and spacing mirrored commercial devices purchasable from Multichannel Systems. Connecting leads bridged between the graphene electrodes and the amplifier pins and were made of indium tin oxide (ITO) and gold. Finally, Al_2O_3 and poly methylmethacrylate (PMMA) were identified as suitable encapsulation layers which can be deposited over the device, with holes etched at the electrodes.

The electrical and electrochemical properties of the graphene MEAs were probed using EIS. The graphene electrode predominantly reports on the neuronal activity via capacitive coupling with the electrode through the electrical double layer and graphene quantum capacitance. This is advantageous since it reduces the likelihood of toxic Faradaic reactions occurring at the electrode. The equivalent circuit models used to describe the EIS spectra of graphene electrodes in previous studies were compared. The simplest model which made physical sense and fitted the data was $R1 + C2/(R2 + W)$. It was shown that $R1$ is the series resistance of the leads and electrolyte, $C2$ combines the double layer capacitance and quantum capacitance at the electrode-electrolyte interface, $R2$ describes the kinetic and W the diffusive limit of the Faradaic charge transfer reactions.

Voltage traces were recorded from mouse neuronal cultures on the graphene MEAs. These were compared to recordings from commercially available TiN electrodes. Spike detection was performed on the voltage traces to identify the action potentials on both devices. The identified action potentials had a peak height of $\sim 20\,\mu V$ and a duration of $\sim 2\,ms$ as expected for extracellular recordings. The mean noise on the graphene MEA was $2.5 \pm 0.7\,\mu V$, similar to the noise levels previously observed with graphene electrodes. The maximum SNR observed on the graphene MEA was 23, which is high enough to clearly identify the action potentials, and is similar to the SNR previously recorded from embryonic rat neurons.

After recording the voltage traces, the graphene MEA was mounted on an inverted microscope. The imaging modalities shown are widefield, confocal fluorescence and FLIM. In each modality, the graphene electrodes did not obstruct or perturb the image. FLIM was shown for the first time to be compatible with electrophysiological recordings from graphene MEAs, which adds to the range of microscopy techniques compatible with a graphene MEA.

The combination of electrophysiological recordings and advanced fluorescence imaging enabled by the graphene MEA, opens up a wealth of possible experiments. The combination utilises the high temporal resolution of the MEA recordings with the high spatial resolution of the microscopes. This can be applied for example, to investigate the role of amyloid

proteins in neurodegenerative diseases. This can be done by combining work previously performed understanding the location and aggregation state of proteins in live cells using imaging techniques like FLIM, with the MEA recordings to correlate with the effect on neuronal firing patterns. One challenge of this is how to stimulate the neurons since electrical stimulation using the graphene electrodes is likely to be challenging, so instead a route involving optogenetic stimulation could be used here.

The complimentary technique FTIR spectroscopy was used to study the structure of monomeric aSyn. A script was written to batch process the FTIR spectra of proteins, and calculate their secondary structure composition. ASyn samples were prepared in ammonium acetate buffer, which evaporates under lyophilisation. Wild type (WT) aSyn at pH 7 is an intrinsically unstructured protein, but develops a more ordered structure with an increase in both α-helical and β-sheet content at pH 4 and with the addition of $CaCl_2$. This is likely due to the decreased charge on the protein and shielding of the protein charge enabling a more folded conformation.

In summary, in this work, physical techniques were developed to better understand the role of protein misfolding in neurodegenerative diseases. An optically transparent, graphene MEA was designed, fabricated and characterised. It was shown that the voltage traces could be recorded by the graphene MEA, with a similar signal to noise ratio as conventional TiN based MEAs. The advanced imaging modality FLIM was shown to be suitable for imaging neurons on the graphene MEAs. FTIR was also used to better understand the structure of monomeric aSyn which is implicated in PD.

8.1 Future work

For the graphene MEA to become commercially viable, it should be possible to reproducibly mass fabricate the device, and for it to be re-usable. Working towards this, to increase the ease of fabrication, the coverslip substrate should be supported to reduce the chance of breakage during device fabrication or use. A replacement encapsulation layer for PMMA could be found which would make the fabrication faster, and reduce charge leakage through the device. This could potentially be a biocompatible photoresist like OrmoComp® the polyimide based HD-8820 [297], or biocompatible SU8.

The equivalent circuit model $R1 + C2/(R2 + W)$ was suggested in this work as the simplest model that made physical sense and fitted the EIS data of the graphene electrode. To check this conclusion, the frequency range over which the impedance is recorded should be increased to reach the frequencies at which the impedance magnitude plateaus. The EIS spectrum of a range of different sized electrodes should also be used. In addition to this, the

EIS spectrum for each electrode could be compared to the SNR of the recorded voltage trace, to find a non-destructive EIS based measure of a good graphene electrode.

A proof of concept that voltage traces from a graphene MEA can be combined with the advanced imaging FLIM technique was shown. One interesting experiment that has been enabled relates to the amyloid protein tau which is implicated in AD. It can be investigated how the aggregation state of tau affects its propagation between neurons and the electrophysiology of the neurons. If fluorescently labelled tau is added to a neuronal cell culture, a spatial map of the location and aggregation state of tau can be obtained using FLIM. In combination with this, the effect of tau on neuronal signalling can be measured for 10s of neurons using a MEA. Combining these data with stimulation capabilities will enable the testing of the hypothesis that neuronal stimulation increases the transfer of tau and enhances tau pathology [8, 33], whereas blocking neuronal stimulation decreases the tau transfer [9].

The graphene MEAs could also possibly be combined with other advanced imaging techniques that are used in amyloid research. Other possible imaging techniques include the super-resolution techniques direct stochastical optical reconstruction microscopy (*d*STORM) [298], structured illumination microscopy (SIM) [19] and stimulated emission depletion (STED) [299]. These techniques can be applied to investigations concerning the amyloid proteins amyloid β [298], tau [6] and aSyn [300].

References

[1] World Health Organisation. Dementia a public health priority. Technical report, World Health Organisation, Geneva, Switzerland, 2012.

[2] Ole Bjørn Tysnes and Anette Storstein. Epidemiology of Parkinson's disease. *J. Neural Transm.*, 124(8):901–905, 2017.

[3] Fabrizio Chiti and Christopher M. Dobson. Protein misfolding, functional amyloid, and human disease. *Annu. Rev. Biochem.*, 75(1):333–366, 2006.

[4] Melanie R. Nilsson. Techniques to study amyloid fibril formation in vitro. *Methods*, 34(1):151–160, 2004.

[5] Don W. Cleveland, Shu Ying Hwo, and Marc W. Kirschner. Purification of tau, a microtubule-associated protein that induces assembly of microtubules from purified tubulin. *J. Mol. Biol.*, 116(2):207–225, 1977.

[6] Claire H. Michel, Satish Kumar, Dorothea Pinotsi, Alan Tunnacliffe, Peter St George-Hyslop, Eckhard Mandelkow, Eva Maria Mandelkow, Clemens F. Kaminski, and Gabriele S Kaminski Schierle. Extracellular monomeric tau protein is sufficient to initiate the spread of tau protein pathology. *J. Biol. Chem.*, 289(2):956–967, 2014.

[7] Li Liu, Valerie Drouet, Jessica W. Wu, Menno P. Witter, Scott A. Small, Catherine Clelland, and Karen Duff. Trans-synaptic spread of tau pathology in vivo. *PLoS One*, 7(2):1–9, 2012.

[8] Amy M. Pooler, Emma C. Phillips, Dawn H W Lau, Wendy Noble, and Diane P. Hanger. Physiological release of endogenous tau is stimulated by neuronal activity. *EMBO Rep.*, 14(4):389–394, 2013.

[9] Sara Calafate, Arjan Buist, Katarzyna Miskiewicz, Vinoy Vijayan, Guy Daneels, Bart de Strooper, Joris de Wit, Patrik Verstreken, and Diederik Moechars. Synaptic contacts enhance cell-to-cell tau pathology propagation. *Cell Rep.*, 11(8):1176–1183, 2015.

[10] Meryem Tardivel, Séverine Bégard, Luc Bousset, Simon Dujardin, Audrey Coens, Ronald Melki, Luc Buée, and Morvane Colin. Tunneling nanotube (TNT)-mediated neuron-to neuron transfer of pathological Tau protein assemblies. *Acta Neuropathol. Commun.*, 4(1):117, 2016.

[11] Hirohide Asai, Seiko Ikezu, Satoshi Tsunoda, Maria Medalla, Jennifer Luebke, Tarik Haydar, Benjamin Wolozin, Oleg Butovsky, Sebastian Kügler, and Tsuneya Ikezu. Depletion of microglia and inhibition of exosome synthesis halt tau propagation. *Nat. Neurosci.*, 18(11):1584–1593, 2015.

[12] Tuomas P.J. Knowles, Michele Vendruscolo, and Christopher M. Dobson. The amyloid state and its association with protein misfolding diseases. *Nat. Rev. Mol. Cell Biol.*, 15(6):384–396, 2014.

[13] Akihiko Iwai, Eliezer Masliah, Makoto Yoshimoto, Nianfeng Ge, Lisa Flanagan, H. A. Rohan de Silva, Agnes Kittel, and Tsunao Saitoh. The precursor protein of non-Aβ component of Alzheimer's disease amyloid is a presynaptic protein of the central nervous system. *Neuron*, 14(2):467–475, 1995.

[14] Fatemeh Nouri Emamzadeh. Alpha-synuclein structure, functions, and interactions. *J. Res. Med. Sci.*, 21(2), 2016.

[15] Walter J. Schulz-Schaeffer. The synaptic pathology of α-synuclein aggregation in dementia with Lewy bodies, Parkinson's disease and Parkinson's disease dementia. *Acta Neuropathol.*, 120(2):131–143, 2010.

[16] Maria Grazia Spillantini, Marie Luise Schmidt, Virginia M.-Y. Lee, John Q. Trojanowski, Ross Jakes, and Michel Goedert. Alpha Synuclein in Lewy bodies. *Nature*, 388:839–840, 1997.

[17] Hamid Charkhkar, Susheela Meyyappan, Evgenia Matveeva, Jonathan R. Moll, Daniel G. McHail, Nathalia Peixoto, Richard O. Cliff, and Joseph J. Pancrazio. Amyloid beta modulation of neuronal network activity in vitro. *Brain Res.*, 1629:1–9, 2015.

[18] Inna Kuperstein, Kerensa Broersen, Iryna Benilova, Jef Rozenski, Wim Jonckheere, Maja Debulpaep, Annelies Vandersteen, Ine Segers-Nolten, Kees Van Der Werf, Vinod Subramaniam, Dries Braeken, Geert Callewaert, Carmen Bartic, Rudi D'Hooge, Ivo Cristiano Martins, Frederic Rousseau, Joost Schymkowitz, and Bart De Strooper. Neurotoxicity of Alzheimer's disease Aβ peptides is induced by small changes in the Aβ42 to Aβ40 ratio. *EMBO J.*, 29(19):3408–3420, 2010.

[19] Clemens F. Kaminski and Gabriele S. Kaminski Schierle. Probing amyloid protein aggregation with optical superresolution methods: from the test tube to models of disease. *Neurophotonics*, 3(4):041807, 2016.

[20] Romain F. Laine, Gabriele S. Kaminksi Schierle, Sebastian Van De Linde, and Clemens F. Kaminski. From single-molecule spectroscopy to super-resolution imaging of the neuron: A review. *Methods Appl. Fluoresc.*, 4(2), 2016.

[21] Ellen Hubin, Stéphanie Deroo, Gabriele Kaminksi Schierle, Clemens F. Kaminski, Louise Serpell, Vinod Subramaniam, Nico Van Nuland, Kerensa Broersen, Vincent Raussens, and Rabia Sarroukh. Two distinct β-sheet structures in Italian-mutant amyloid-beta fibrils: A potential link to different clinical phenotypes. *Cell. Mol. Life Sci.*, 72(24):4899–4913, 2015.

[22] Vladimir N. Uversky. A protein-chameleon: Conformational plasticity of α-synuclein, a disordered protein involved in neurodegenerative disorders. *J. Biomol. Struct. Dyn.*, 21(2):211–234, 2003.

[23] Guenter W Gross. Simultaneous single unit recording in vitro with a photoetched laser deinsulated gold multimicroelectrode surface. *IEEE Trans. Biomed. Eng.*, BME-26(5):273–279, 1979.

[24] Kucku Varghese, Peter Molnar, Mainak Das, Neelima Bhargava, Stephen Lambert, Mark S. Kindy, and James J. Hickman. A new target for amyloid beta toxicity validated by standard and high-throughput electrophysiology. *PLoS One*, 5(1):1–8, 2010.

[25] Seon-ah Chong, Iryna Benilova, Hamdy Shaban, Bart De Strooper, Herman Devijver, Dieder Moechars, Wolfgang Eberle, Carmen Bartic, Fred Van Leuven, and Geert Callewaert. Neurobiology of disease synaptic dysfunction in hippocampus of transgenic mouse models of Alzheimer ' s disease : A multi-electrode array study. *Neurobiol. Dis.*, 44(3):284–291, 2011.

[26] Juliana Bender, Marcus Haag, Benjamin Jason, Christianne Gazzana, and Helena Cimarosti. Curcumin protects organotypic hippocampal slice cultures from Aβ 1 – 42 -induced synaptic toxicity. *Toxicol. Vitr.*, 27(8):2325–2330, 2013.

[27] Philipp Görtz, Mario Siebler, Ralf Ihl, Uwe Henning, Christian Luckhaus, Tillmann Supprian, and Christian Lange-Asschenfeldt. Multielectrode array analysis of cerebrospinal fluid in Alzheimer's disease versus mild cognitive impairment: A potential diagnostic and treatment biomarker. *Biochem. Biophys. Res. Commun.*, 434(2):293–297, 2013.

[28] Masafumi Shimojo, Makoto Higuchi, Tetsuya Suhara, and Naruhiko Sahara. Imaging multimodalities for dissecting Alzheimer's disease: Advanced technologies of positron emission tomography and fluorescence imaging. *Front. Neurosci.*, 9(DEC), 2015.

[29] Joseph R Lakowicz, Henryk Szmacinski, Kazmierz Nowaczyk, and Michael L. Johnson. Fluorescence lifetime imaging of free and protein-bound NADH. *Proc. Natl. Acad. Sci. U. S. A.*, 89:1271–1275, 1992.

[30] Gabriele S. Kaminski Schierle, Carlos W. Bertoncini, Fiona T S Chan, Annemieke T. Van Der Goot, Stefanie Schwedler, Jeremy Skepper, Simon Schlachter, Tjakko Van Ham, Alessandro Esposito, Janet R. Kumita, Ellen a a Nollen, Christopher M. Dobson, and Clemens F. Kaminski. A FRET sensor for non-invasive imaging of amyloid formation in vivo. *ChemPhysChem*, 12(3):673–680, 2011.

[31] Massimo Scanziani and Michael Häusser. Electrophysiology in the age of light. *Nature*, 461(7266):930–939, 2009.

[32] Duygu Kuzum, Hajime Takano, Euijae Shim, Jason C. Reed, Halvor Juul, Andrew G. Richardson, Julius de Vries, Hank Bink, Marc A. Dichter, Timothy H. Lucas, Douglas A. Coulter, Ertugrul Cubukcu, and Brian Litt. Transparent and flexible low noise graphene electrodes for simultaneous electrophysiology and neuroimaging. *Nat. Commun.*, 5:5259, 2014.

[33] Jessica W. Wu, S. Abid Hussaini, Isle M. Bastille, Gustavo A. Rodriguez, Ana Mrejeru, Kelly Rilett, David W. Sanders, Casey Cook, Hongjun Fu, Rick A.C.M. Boonen, Mathieu Herman, Eden Nahmani, Sheina Emrani, Y. Helen Figueroa, Marc I. Diamond, Catherine L. Clelland, Selina Wray, and Karen E. Duff. Neuronal activity

enhances tau propagation and tau pathology in vivo. *Nat. Neurosci.*, 19(8):1085–1092, 2016.

[34] Dong-Wook Park, Amelia A. Schendel, Solomon Mikael, Sarah K. Brodnick, Thomas J. Richner, Jared P. Ness, Mohammed R. Hayat, Farid Atry, Seth T. Frye, Ramin Pashaie, Sanitta Thongpang, Zhenqiang Ma, and Justin C. Williams. Graphene-based carbon-layered electrode array technology for neural imaging and optogenetic applications. *Nat. Commun.*, 5:5258, 2014.

[35] Dong Wook Park, Sarah K. Brodnick, Jared P. Ness, Farid Atry, Lisa Krugner-Higby, Amelia Sandberg, Solomon Mikael, Thomas J. Richner, Joseph Novello, Hyungsoo Kim, Dong Hyun Baek, Jihye Bong, Seth T. Frye, Sanitta Thongpang, Kyle I. Swanson, Wendell Lake, Ramin Pashaie, Justin C. Williams, and Zhenqiang Ma. Fabrication and utility of a transparent graphene neural electrode array for electrophysiology, in vivo imaging, and optogenetics. *Nat. Protoc.*, 11(11):2201–2222, 2016.

[36] Giorgia Zandomeneghi, Mark R.H. Krebs, Margaret G. McCammon, and Marcus Fändrich. FTIR reveals structural differences between native β-sheet proteins and amyloid fibrils. *Protein Sci.*, 13(12):3314–3321, 2004.

[37] Rabia Sarroukh, Erik Goormaghtigh, Jean Marie Ruysschaert, and Vincent Raussens. ATR-FTIR: A "rejuvenated" tool to investigate amyloid proteins. *Biochim. Biophys. Acta - Biomembr.*, 1828(10):2328–2338, 2013.

[38] Martin Von Bergen, Stefan Barghorn, Jacek Biernat, Eva Maria Mandelkow, and Eckhard Mandelkow. Tau aggregation is driven by a transition from random coil to beta sheet structure. *Biochim. Biophys. Acta - Mol. Basis Dis.*, 1739(2):158–166, 2005.

[39] Steven J. Roeters, Aditya Iyer, Galja Pletikapiä, Vladimir Kogan, Vinod Subramaniam, and Sander Woutersen. Evidence for Intramolecular Antiparallel Beta-Sheet Structure in Alpha-Synuclein Fibrils from a Combination of Two-Dimensional Infrared Spectroscopy and Atomic Force Microscopy. *Sci. Rep.*, 7:1–11, 2017.

[40] Wim L C Rutten. Selective electrical interfaces with the nervous system. *Annu. Rev. Biomed. Eng.*, 4:407–452, 2002.

[41] L J Gentet, G J Stuart, and J D Clements. Direct measurement of specific membrane capacitance in neurons. *Biophys. J.*, 79(1):314–20, 2000.

[42] Mark F. Bear, Barry W Connors, and Paradiso Michael A. *Neuroscience exploring the brain*. Lippincott Williams & Wilkins, Baltimore, USA, third edition, 2007.

[43] Micha E Spira and Aviad Hai. Multi-electrode array technologies for neuroscience and cardiology. *Nat. Nanotechnol.*, 8(2):83–94, feb 2013.

[44] A. L. Hodgkin and A. F. Huxley. Action potentials recorded from inside a nerve cell. *Nature*, 144:710–711, 1939.

[45] O. P. Hamill, A. Marty, E. Neher, B. Sakmann, and F. J. Sigworth. Improved patch-clamp techniques for high-resolution current recording from cells and cell-free membrane patches. *Pflugers Arch. Eur. J. Physiol.*, 391(2):85–100, 1981.

[46] Peter B. Kruskal, Zhe Jiang, Teng Gao, and Charles M. Lieber. Beyond the patch clamp: Nanotechnologies for intracellular recording. *Neuron*, 86:21–24, 2015.

[47] L. J. Breckenridge, R. J A Wilson, P. Connolly, A. S G Curtis, J. A T Dow, S. E. Blackshaw, and C. D W Wilkinson. Advantages of using microfabricated extracellular electrodes for in vitro neuronal recording. *J. Neurosci. Res.*, 42(2):266–276, 1995.

[48] M. Bove, S. Martinoia, G. Verreschi, M. Giugliano, and M. Grattarola. Analysis of the signals generated by networks of neurons coupled to planar arrays of microtransducers in simulated experiments. *Biosens. Bioelectron.*, 13(6):601–612, 1998.

[49] György Buzsáki, Costas A. Anastassiou, and Christof Koch. The origin of extracellular fields and currents-EEG, ECoG, LFP and spikes. *Nat. Rev. Neurosci.*, 13(6):407–420, 2012.

[50] Christine Grienberger and Arthur Konnerth. Imaging calcium in neurons. *Neuron*, 73(5):862–885, 2012.

[51] Laure Caruso, Thomas Wunderle, Christopher Murphy Lewis, Joao Valadeiro, Vincent Trauchessec, Josué Trejo Rosillo, José Pedro Amaral, Jianguang Ni, Patrick Jendritza, Claude Fermon, Susana Cardoso, Paulo Peixeiro Freitas, Pascal Fries, and Myriam Pannetier-Lecoeur. In Vivo Magnetic Recording of Neuronal Activity. *Neuron*, 95(6):1283–1291.e4, 2017.

[52] John F Barry, Matthew J Turner, Jennifer M Schloss, David R Glenn, Yuyu Song, Mikhail D Lukin, Hongkun Park, and Ronald L. Walsworth. Optical magnetic detection of single-neuron action potentials using quantum defects in diamond. *Proc. Natl. Acad. Sci.*, 113(49):14133–14138, 2016.

[53] Michael P. Maher, Jerome Pine, John Wright, and Yu Chong Tai. The neurochip: A new multielectrode device for stimulating and recording from cultured neurons. *J. Neurosci. Methods*, 87(1):45–56, 1999.

[54] S Nakanishi. Molecular diversity of glutamate receptors and implications for brain function. *Science (80-.).*, 258(5082):597–603, 1992.

[55] M. Estacion, B. P. S Vohra, S. Liu, J. Hoeijmakers, C. G. Faber, I. S. J. Merkies, G. Lauria, J. A. Black, and S. G. Waxman. Ca2+ toxicity due to reverse Na /Ca2+ exchange contributes to degeneration of neurites of DRG neurons induced by a neuropathy-associated Nav1.7 mutation. *J. Neurophysiol.*, 114(3):1554–1564, 2015.

[56] Graham Robertson, Trevor J. Bushell, and Michele Zagnoni. Chemically induced synaptic activity between mixed primary hippocampal co-cultures in a microfluidic system. *Integr. Biol. (United Kingdom)*, 6(6):636–644, 2014.

[57] Robert C. Froemke, Mu Ming Poo, and Yang Dan. Spike-timing-dependent synaptic plasticity depends on dendritic location. *Nature*, 434(7030):221–225, 2005.

[58] Y Jimbo and A Kawana. Electrical stimulation and recording from cultured neurons using a planar electrode array. *Bioelectrochem. Bioenerg.*, 29:193–204, 1992.

[59] E. M. Callaway and L. C. Katz. Photostimulation using caged glutamate reveals functional circuitry in living brain slices. *Proc. Natl. Acad. Sci.*, 90(16):7661–7665, 1993.

[60] Jerome Pine. Recording action potentials from cultured neurons with extracellular microcircuit electrodes. *J. Neurosci. Methods*, 2(1):19–31, 1980.

[61] Andrew F M Johnstone, Guenter W. Gross, Dieter G. Weiss, Olaf H U Schroeder, Alexandra Gramowski, and Timothy J. Shafer. Microelectrode arrays: A physiologically based neurotoxicity testing platform for the 21st century. *Neurotoxicology*, 31(4):331–350, 2010.

[62] Nadine Crouzin, Kevin Baranger, Mélanie Cavalier, Yannick Marchalant, Catherine Cohen-solal, François S Roman, Michel Khrestchatisky, Santiago Rivera, François Féron, and Michel Vignes. Area-specific alterations of synaptic plasticity in the 5XFAD mouse model of Alzheimer's disease: dissociation between somatosensory cortex and hippocampus. *PLoS One*, 8(9):4–12, 2013.

[63] Stuart F. Cogan. Neural stimulation and recording electrodes. *Annu. Rev. Biomed. Eng.*, 10(1):275–309, 2008.

[64] Leigh R Hochberg, Mijail D Serruya, Gerhard M Friehs, Jon A Mukand, Maryam Saleh, Abraham H Caplan, Almut Branner, David Chen, Richard D Penn, and John P Donoghue. Neuronal ensemble control of prosthetic devices by a human with tetraplegia. *Nature*, 442(7099):164–71, 2006.

[65] Alfred Stett, Ulrich Egert, Elke Guenther, Frank Hofmann, Thomas Meyer, Wilfried Nisch, and Hugo Haemmerle. Biological application of microelectrode arrays in drug discovery and basic research. *Anal. Bioanal. Chem.*, 377(3):486–495, 2003.

[66] Douglas J Bakkum, Urs Frey, Milos Radivojevic, Thomas L Russell, Jan Müller, Michele Fiscella, Hirokazu Takahashi, and Andreas Hierlemann. Tracking axonal action potential propagation on a high-density microelectrode array across hundreds of sites. *Nat. Commun.*, 4:2181, 2013.

[67] Michela Chiappalone, Alessandro Vato, Luca Berdondini, Milena Koudelka-Hep, and Sergio Martinoia. Network dynamics and synchronous activity in cultured cortical neurons. *Int. J. Neural Syst.*, 17(2):87–103, 2007.

[68] H Braak, E Braak, and J Bohl. Staging of Alzheimer-related cortical destruction. *Eur. Neurol.*, 33(6):403–408, 1993.

[69] A. L. Hodgkin and A. F. Huxley. A quantitative description of membrane current and its application to conduction and excitation in nerve. *J. Physiol.*, 117:500–544, 1952.

[70] Frauke Greve, Susanne Frerker, Anne Greet Bittermann, Claus Burkhardt, Andreas Hierlemann, and Heike Hall. Molecular design and characterization of the neuron-microelectrode array interface. *Biomaterials*, 28(35):5246–5258, 2007.

[71] Marco Bove, Massimo Grattarola, Sergio Martinoia, and Giovanni Verreschi. Interfacing cultured neurons to planar substrate microelectrodes: characterization of the neuron-to-microelectrode junction. *Bioelectrochemistry Bioenerg.*, 38(2):255–265, 1995.

[72] Jan Reinoud Buitenweg, W. L C Rutten, W. P A Willems, and J. W. Van Nieuwkasteele. Measurement of sealing resistance of cell-electrode interfaces in neuronal cultures using impedance spectroscopy. *Med. Biol. Eng. Comput.*, 36(5):630–637, 1998.

[73] John Newman. Resistance for flow of current to a disk. *J. Electrochem. Soc.*, 113(5):501–502, 1966.

[74] J. E. B. Randles. Kinetics of rapid electrode reactions. *Discuss. Faraday Soc.*, 1:11–19, 1947.

[75] D A Robinson. The electrical properties of metal microelectrodes. *Proc. IEEE*, 56(6):1065–1071, 1968.

[76] Neil Joye, Alexandre Schmid, and Yusuf Leblebici. Electrical modeling of the cell-electrode interface for recording neural activity from high-density microelectrode arrays. *Neurocomputing*, 73(1-3):250–259, 2009.

[77] Lilach Bareket-Keren and Yael Hanein. Carbon nanotube-based multi electrode arrays for neuronal interfacing: progress and prospects. *Front. Neural Circuits*, 6:122, 2013.

[78] Gytis Baranauskas, Emma Maggiolini, Elisa Castagnola, Alberto Ansaldo, Alberto Mazzoni, Gian Nicola Angotzi, Alessandro Vato, Davide Ricci, Stefano Panzeri, and Luciano Fadiga. Carbon nanotube composite coating of neural microelectrodes preferentially improves the multiunit signal-to-noise ratio. *J. Neural Eng.*, 8(6):066013, 2011.

[79] Paul Horowitz and Winfield Hill. *The art of electronics*. Cambridge University Press, second edition, 1989.

[80] Chang Hsiao Chen, Cheng Te Lin, Wei Lun Hsu, Yen Chung Chang, Shih Rung Yeh, Lain Jong Li, and Da Jeng Yao. A flexible hydrophilic-modified graphene microprobe for neural and cardiac recording. *Nanomedicine Nanotechnology, Biol. Med.*, 9(5):600–604, 2013.

[81] Dmitry Kireev, Silke Seyock, Johannes Lewen, Vanessa Maybeck, Bernhard Wolfrum, and Andreas Offenhäusser. Graphene multielectrode arrays as a versatile tool for extracellular measurements. *Adv. Healthc. Mater.*, 6(12):1601433, 2017.

[82] Rodrigo Quian Quiroga. Unsupervised spike detection and sorting problem: Detect and separate spikes. *Neural Comput.*, 16:1661–1687, 2004.

[83] Marie Engelene J. Obien, Kosmas Deligkaris, Torsten Bullmann, Douglas J. Bakkum, and Urs Frey. Revealing neuronal function through microelectrode array recordings. *Front. Neurosci.*, 8(123):1–30, 2015.

[84] Michael S Lewicki. A review of methods for spike sorting: the detection and classification of neural action potentials. *Comput. Neural Syst.*, pages 53–78, 1998.

[85] R O Wong. Calcium imaging and multielectrode recordings of global patterns of activity in the developing nervous system. *Histochem. J.*, 30(3):217–229, 1998.

[86] Ke Wang, Harvey A. Fishman, Hongjie Dai, and James S. Harris. Neural stimulation with a carbon nanotube microelectrode array. *Nano Lett.*, 6(9):2043–2048, 2006.

[87] Dion Khodagholy, Thomas Doublet, Moshe Gurfinkel, Pascale Quilichini, Esma Ismailova, Pierre Leleux, Thierry Herve, Sébastien Sanaur, Christophe Bernard, and George G. Malliaras. Highly conformable conducting polymer electrodes for in vivo recordings. *Adv. Mater.*, 23(36):268–272, 2011.

[88] Edwin M. Maynard, Craig T. Nordhausen, and Richard A. Normann. The Utah Intracortical Electrode Array: A recording structure for potential brain-computer interfaces. *Electroencephalogr. Clin. Neurophysiol.*, 102(3):228–239, 1997.

[89] Fernando Patolsky, Brian P. Timko, Guihua Yu, Ying Fang, Andrew B. Greytak, Gengfeng Zheng, and Charles M. Lieber. Detection, stimulation and inhibition of neuronal signals with high density nanowire transistor arrays. *Science (80-.).*, 313(5790):1100–1104, 2006.

[90] M. Hutzler. High-Resolution Multitransistor Array Recording of Electrical Field Potentials in Cultured Brain Slices. *J. Neurophysiol.*, 96(3):1638–1645, 2006.

[91] Peter Fromherz, Andreas Offenhauser, Thomas Vetter, and Jurgen Weis. A neuron-silicon junciton: A retzius cell of the leech on an insulated-gate field-effect transistor. *J. Chem. Inf. Model.*, 252:1290–1293, 1991.

[92] Multichannel Systems. Multichannel Systems User Manual, 2014.

[93] Xin Liu, Yichen Lu, Ege Iseri, Chi Ren, Haixin Liu, Takaki Komiyama, and Duygu Kuzum. Transparent artifact-free graphene electrodes for compact closed-loop optogenetics systems. In *2017 IEEE Int. Electron Devices Meet.*, pages 26.1.1–26.1.4, 2017.

[94] Xiaowei Du, Lei Wu, Ji Cheng, Shanluo Huang, Qi Cai, Qinghui Jin, and Jianlong Zhao. Graphene microelectrode arrays for neural activity detection. *J. Biol. Phys.*, 41(4):339–347, 2015.

[95] G W Gross, W Y Wen, and J W Lin. Transparent indium-tin oxide electrode patterns for extracellular, multisite recording in neuronal cultures. *J. Neurosci. Methods*, 15(3):243–252, 1985.

[96] Guenter W. Gross, Barry K. Rhoades, Daryl L. Reust, and Fritz U. Schwalm. Stimulation of monolayer networks in culture through thin-film indium-tin oxide recording electrodes. *J. Neurosci. Methods*, 50(2):131–143, 1993.

[97] Ki Yong Kwon, Brenton Sirowatka, Arthur Weber, and Wen Li. Opto-μ ECoG array: A hybrid neural interface with transparent μ ECoG electrode array and integrated LEDs for optogenetics. *IEEE Trans. Biomed. Circuits Syst.*, 7(5):593–600, 2013.

[98] Hiroaki Oka, Ken Shimono, Ryuta Ogawa, Hirokazu Sugihara, and Makoto Taketani. A new planar multielectrode array for extracellular recording: Application to hippocampal acute slice. *J. Neurosci. Methods*, 93(1):61–67, 1999.

[99] Jeong Soon Lee, Alexey Lipatov, Ligyeom Ha, Mikhail Shekhirev, Mohammad Nahid Andalib, Alexander Sinitskii, and Jung Yul Lim. Graphene substrate for inducing neurite outgrowth. *Biochem. Biophys. Res. Commun.*, 460(2):267–273, 2015.

[100] Jun Suzurikawa, Hirokazu Takahashi, Yuzo Takayama, Mamoru Mitsuishi, Masayuki Nakao, and Yasuhiko Jimbo. Light-addressable electrode with hydrogenated amorphous silicon and low- conductive passivation layer for stimulation of cultured neurons Light-addressable electrode with hydrogenated amorphous silicon and low- conductive passivation layer for stimulation. In *Proc. if 28th IEEE EMBS Anu. Int. Conf.*, volume 093901, pages 648–651, 2006.

[101] Pranoti Kshirsagar, Manuel Martina, Peter D. Jones, Sandra Buckenmaier, Udo Kraushaar, Thomas Chassé, Monika Fleischer, and Claus J. Burkhardt. Semitransparent carbon microelectrodes for opto- and electrophysiology. *J. Micromechanics Microengineering*, 28(7), 2018.

[102] Brian P. Timko, Tzahi Cohen-Karni, Guihua Yu, Quan Qing, Bozhi Tian, and Charles M. Lieber. Electrical recording from hearts with flexible nanowire device arrays. *Nano Lett.*, 9(2):914–918, 2009.

[103] Valentina Benfenati, Stefano Toffanin, Simone Bonetti, Guido Turatti, Assunta Pistone, Michela Chiappalone, Anna Sagnella, Andrea Stefani, Gianluca Generali, Giampiero Ruani, Davide Saguatti, Roberto Zamboni, and Michele Muccini. A transparent organic transistor structure for bidirectional stimulation and recording of primary neurons. *Nat. Mater.*, 12(7):672–80, 2013.

[104] A Spanu, S Lai, P Cosseddu, M Tedesco, S Martinoia, and A Bonfiglio. An organic transistor-based system for reference-less electrophysiological monitoring of excitable cells. *Sci. Rep.*, 5:8807, 2015.

[105] Martin Thunemann, Yichen Lu, Xin Liu, Klvllclm Klllç, Michèle Desjardins, Matthieu Vandenberghe, Sanaz Sadegh, Payam A. Saisan, Qun Cheng, Kimberly L. Weldy, Hongming Lyu, Srdjan Djurovic, Ole A. Andreassen, Anders M. Dale, Anna Devor, and Duygu Kuzum. Deep 2-photon imaging and artifact-free optogenetics through transparent graphene microelectrode arrays. *Nat. Commun.*, 9(1):1–12, 2018.

[106] R. R. Nair, P.V Blake, K. S. Grigorenko, T. J. Booth, T. Stauber, N. M R Peres, and A. K. Geim. Fine structure constant defines visual transparency of graphene. *Science (80-.).*, 320(5881):1308, 2008.

[107] Ji Cheng, Lei Wu, Xiao Wei Du, Qing Hui Jin, Jian Long Zhao, and Yuan Sen Xu. Flexible solution-gated graphene field effect transistor for electrophysiological recording. *J. Microelectromechanical Syst.*, 23(6):1311–1317, 2014.

[108] Kostas Kostarelos, Melissa Vincent, Clement Hebert, and Jose A. Garrido. Graphene in the design and engineering of next-generation neural interfaces. *Adv. Mater.*, 29(42):1–7, 2017.

[109] Yichen Lu, Hongming Lyu, Andrew G. Richardson, Timothy H. Lucas, and Duygu Kuzum. Flexible neural electrode array based-on porous graphene for cortical microstimulation and sensing. *Sci. Rep.*, 6(August):1–9, 2016.

[110] Dong Wook Park, Jared P. Ness, Sarah K. Brodnick, Corinne Esquibel, Joseph Novello, Farid Atry, Dong Hyun Baek, Hyungsoo Kim, Jihye Bong, Kyle I. Swanson, Aaron J. Suminski, Kevin J. Otto, Ramin Pashaie, Justin C. Williams, and Zhenqiang Ma. Electrical Neural Stimulation and Simultaneous in Vivo Monitoring with Transparent Graphene Electrode Arrays Implanted in GCaMP6f Mice. *ACS Nano*, 12(1):148–157, 2018.

[111] Berit Koerbitzer, Peter Krauss, Christoph Nick, Sandeep Yadav, Joerg J. Schneider, and Christiane Thielemann. Graphene electrodes for stimulation of neuronal cells. *2D Mater.*, 3:024004, 2016.

[112] Jong Bo Park, Yong-Jin Kim, Seong-Min Kim, Je Min Yoo, Youngsoo Kim, Roman Gorbachev, I I Barbolina, Sang Jin Kim, Sangmin Kang, Myung-Han Yoon, Sung-Pyo Cho, Konstantin S Novoselov, and Byung Hee Hong. Non-destructive electron microscopy imaging and analysis of biological samples with graphene coating. *2D Mater.*, 3(4):045004, 2016.

[113] C. H. Chen, C. T. Lin, J. J. Chen, W. L. Hsu, Y. C. Chang, S. R. Yeh, L. J. Li, and D. J. Yao. A graphene-based microelectrode for recording neural signals. In *16th Int. Solid-State Sensors, Actuators Microsystems Conf.*, pages 1883–1886, 2011.

[114] Sandeep Keshavan, Shovan Naskar, Alberto Diaspro, Laura Cancedda, and Silvia Dante. Developmental refinement of synaptic transmission on micropatterned single layer graphene. *Acta Biomater.*, 65:363–375, 2018.

[115] Hiroshi Makino, Chi Ren, Haixin Liu, An Na Kim, Neehar Kondapaneni, Xin Liu, Duygu Kuzum, and Takaki Komiyama. Transformation of cortex-wide emergent properties during motor learning. *Neuron*, 94(4):880–890.e8, 2017.

[116] Michael Grätzel. Photoelectrochemical cells. *Nature*, 414(November):338–344, 2001.

[117] K S Novoselov, A K Geim, S V Morozov, D Jiang, Y Zhang, S V Dubonos, I V Grigorieva, and a a Firsov. Electric field effect in atomically thin carbon films. *Science (80-.).*, 306:666–669, oct 2004.

[118] Andrea C Ferrari, Mikhail I. Katsnelson, Lieven Vandersypen, Annick Loiseau, Vittorio Morandi, Alessandro Tredicucci, Gareth M Williams, and Hee Hong. Science and technology roadmap for graphene, related two-dimensional crystals, and hybrid systems. *Nanoscale*, 7(11):4598–4810, 2015.

[119] A K Geim and K S Novoselov. The rise of graphene. *Nat. Mater.*, 6:183–191, 2007.

[120] Ivan V. Vlassiouk, Yijing Stehle, Pushpa Raj Pudasaini, Raymond R. Unocic, Philip D. Rack, Arthur P. Baddorf, Ilia N. Ivanov, Nickolay V. Lavrik, Frederick List, Nitant Gupta, Ksenia V. Bets, Boris I. Yakobson, and Sergei N. Smirnov. Evolutionary selection growth of two-dimensional materials on polycrystalline substrates. *Nat. Mater.*, 17(4):318–322, 2018.

[121] Peter W Sutter, Jan-Ingo Flege, and Eli a Sutter. Epitaxial graphene on ruthenium. *Nat. Mater.*, 7(May):406–411, 2008.

[122] Long Yang, Yuanchang Li, and Ying Fang. Nanodevices for cellular interfaces and electrophysiological recording. *Adv. Mater.*, 25(28):3881–3887, 2013.

[123] I Vlassioukiv, Murari Regmi, Pasquale Fulvio, Sheng Dai, Panos Datkos, Gyula Eres, and Sergei Smimov. Role of hydrogen in chemical vapor deposition growth of large single-crystal graphene. *ACS Nano*, 5(7):6069–6076, 2011.

[124] Xuesong Li, Weiwei Cai, Luigi Colombo, and Rodney S. Ruoff. Evolution of graphene growth on Ni and Cu by carbon isotope labeling. *Nano Lett.*, 9(1):4268–4272, 2009.

[125] Alfonso Reina, Xiaoting Jia, Daniel Nezich, Hyungbin Son, Vladimir Bulovic, Mildred S. Dresselhaus, and Jing Kong. Large area, few-layer graphene films on arbitrary substrates by chemical vapor deposition. *Nano Lett.*, 9(1):30–35, 2009.

[126] S. C. Xu, B. Y. Man, S. Z. Jiang, C. S. Chen, C. Yang, M. Liu, X. G. Gao, Z. C. Sun, and C. Zhang. Direct synthesis of graphene on SiO2 substrates by chemical vapor deposition. *CrystEngComm*, 15(10):1840, 2013.

[127] Jingyu Sun, Yubin Chen, Manish Kr Priydarshi, Teng Gao, Xiuju Song, Yanfeng Zhang, and Zhongfan Liu. Graphene Glass from Direct CVD Routes: Production and Applications. *Adv. Mater.*, 28(46):10333–10339, 2016.

[128] Keun Soo Kim, Yue Zhao, Houk Jang, Sang Yoon Lee, Jong Min Kim, Kwang S Kim, Jong-Hyun Ahn, Philip Kim, Jae-Young Choi, and Byung Hee Hong. Large-scale pattern growth of graphene films for stretchable transparent electrodes. *Nature*, 457(7230):706–710, 2009.

[129] Mingguang Chen, Robert C. Haddon, Ruoxue Yan, and Elena Bekyarova. Advances in transferring chemical vapour deposition graphene: A review. *Mater. Horizons*, 4(6):1054–1063, 2017.

[130] Jooho Lee, Yongsung Kim, Hyeon Jin Shin, Changseung Lee, Dongwook Lee, Chang Yul Moon, Juhwan Lim, and Seong Chan Jun. Clean transfer of graphene and its effect on contact resistance. *Appl. Phys. Lett.*, 103(10), 2013.

[131] Wei Hsiang Lin, Ting Hui Chen, Jan Kai Chang, Jieh I. Taur, Yuan Yen Lo, Wei Li Lee, Chia Seng Chang, Wei Bin Su, and Chih I. Wu. A direct and polymer-free method for transferring graphene grown by chemical vapor deposition to any substrate. *ACS Nano*, 8(2):1784–1791, 2014.

[132] P. R. Wallace. The band theory of graphite. *Phys. Rev.*, 71(9):622–634, 1947.

[133] D. G. Purdie, N. M. Pugno, T. Taniguchi, K. Watanabe, A. C. Ferrari, and A. Lombardo. Cleaning interfaces in layered materials heterostructures. *arXiv*, pages 1–14, 2018.

[134] Changgu Lee, Xiaoding Wei, Jeffrey W Kysar, and James Hone. Measurement of the elastic properties and intrinsic strength of monolayer graphene. *Science (80-.).*, 321:385–388, 2008.

[135] Alexander A. Balandin. Thermal properties of graphene and nanostructured carbon materials. *Nat. Mater.*, 10(8):569–581, 2011.

[136] B. Partoens and F. M. Peeters. From graphene to graphite: Electronic structure around the K point. *Phys. Rev. B*, 74(7):1–11, 2006.

[137] F. Schedin, A. K. Geim, S. V. Morozov, E. W. Hill, P. Blake, M. I. Katsnelson, and K. S. Novoselov. Detection of individual gas molecules adsorbed on graphene. *Nat. Mater.*, 6(9):652–655, 2007.

[138] Jian Hao Chen, W. G. Cullen, C. Jang, M. S. Fuhrer, and E. D. Williams. Defect scattering in graphene. *Phys. Rev. Lett.*, 102(23):1–4, 2009.

[139] Jilin Xia, Fang Chen, Jinghong Li, and Nongjian Tao. Measurement of the quantum capacitance of graphene. *Nat. Nanotechnol.*, 4(8):505–509, 2009.

[140] Serge Luryi. Quantum capacitance devices. *Appl. Phys. Lett.*, 52(6):501–503, 1988.

[141] Tian Fang, Aniruddha Konar, Huili Xing, and Debdeep Jena. Carrier statistics and quantum capacitance of graphene sheets and ribbons. *Appl. Phys. Lett.*, 91(9), 2007.

[142] Zhihong Chen and Joerg Appenzeller. Mobility extraction and quantum capacitance impact in high performance graphene field-effect transistor devices. *arXiv*, 0812.3927:1–4, 2008.

[143] Suck Won Hong, Jong Ho Lee, Seok Hee Kang, Eun Young Hwang, Yu Shik Hwang, Mi Hee Lee, Dong Wook Han, and Jong Chul Park. Enhanced neural cell adhesion and neurite outgrowth on graphene-based biomimetic substrates. *Biomed Res. Int.*, 2014:1–8, 2014.

[144] Benjamin Woodhams, Laura Ansel-Bollepalli, Jakub Surmacki, Helena Knowles, Laura Maggini, Michael De Volder, Mete Atatüre, and Sarah Bohndiek. Graphitic and oxidised high pressure high temperature (HPHT) nanodiamonds induce differential biological responses in breast cancer cell lines. *Nanoscale*, 10(25):12169–12179, 2018.

[145] Yongbin Zhang, Syed F Ali, Enkeleda Dervishi, Yang Xu, Zhongrui Li, Daniel Casciano, and Alexandru S Biris. Cytotoxicity effects of graphene and single-wall carbon nanotubes in neural phaeochromocytoma-derived PC12 cells. *ACS Nano*, 4(6):3181–3186, 2010.

[146] Hye-Bin Park, Hyo-Geun Nam, Hong-Gi Oh, Jung-Hyun Kim, Chang-Man Kim, Kwang-Soup Song, and Kwang-Hwan Jhee. Effect of graphene on growth of neuroblastoma cells. *J. Microbiol. Biotechnol.*, 23(2):274–7, 2013.

[147] Sahil Kumar Rastogi, Guruprasad Raghavan, Ge Yang, and Tzahi Cohen-Karni. Effect of graphene on non-neuronal and neuronal cell viability and stress. *Nano Lett.*, 17(5):3297–3301, 2017.

[148] Alessandra Fabbro, Denis Scaini, Veronica Leon, Ester Vázquez, Giada Cellot, Giulia Privitera, Lucia Lombardi, Felice Torrisi, Flavia Tomarchio, Francesco Bonaccorso, Susanna Bosi, Andrea C. Ferrari, Laura Ballerini, and Maurizio Prato. Graphene-based interfaces do not alter target nerve cells. *ACS Nano*, 10(1):615–623, 2016.

[149] Sung Young Park, Jaesung Park, Sung Hyun Sim, Moon Gyu Sung, Kwang S. Kim, Byung Hee Hong, and Seunghun Hong. Enhanced differentiation of human neural stem cells into neurons on graphene. *Adv. Mater.*, 23(36):263–267, 2011.

[150] Ning Li, Xuemin Zhang, Qin Song, Ruigong Su, Qi Zhang, Tao Kong, Liwei Liu, Gang Jin, Mingliang Tang, and Guosheng Cheng. The promotion of neurite sprouting and outgrowth of mouse hippocampal cells in culture by graphene substrates. *Biomaterials*, 32(35):9374–9382, 2011.

[151] Farida Veliev, Anne Briançon-Marjollet, Vincent Bouchiat, and Cécile Delacour. Impact of crystalline quality on neuronal affinity of pristine graphene. *Biomaterials*, 86:33–41, 2016.

[152] C. V. Raman and K. S. Krishnan. A new type of secondary radiation. *Nature*, 121(3048):501–502, 1928.

[153] Peter Atkins and Julio de Paula. *Atkins' physical chemistry*. Oxford University Press, 2010.

[154] A. C. Ferrari and J. Robertson. Resonant Raman spectroscopy of disordered, amorphous, and diamondlike carbon. *Phys. Rev. B*, 64(7):075414, 2001.

[155] Andrea C. Ferrari, J. C. Meyer, V. Scardaci, C. Casiraghi, M. Lazzeri, F. Mauri, S. Piscanec, D. Jiang, K. S. Novoselov, S. Roth, and A. K. Geim. Raman spectrum of graphene and graphene layers. *Phys. Rev. Lett.*, 97(18):187401–187404, oct 2006.

[156] F. Tuinstra and J. L. Koenig. Raman spectrum of Graphite. *J. Chem. Phys.*, 53(3):1126–1130, 1970.

[157] A Das, S Pisana, B Chakraborty, S Piscanec, S K Saha, U V Waghmare, K S Novoselov, H R Krishnamurthy, Andre K. Geim, Andrea C. Ferrari, and A K Sood. Monitoring dopants by Raman scattering in an electrochemically top-gated graphene transistor. *Nat. Nanotechnol.*, 3(4):210–215, apr 2008.

[158] D. M. Basko, S. Piscanec, and A. C. Ferrari. Electron-electron interactions and doping dependence of the two-phonon Raman intensity in graphene. *Phys. Rev. B*, 80(16):165413, 2009.

[159] L G Cançado, A Jorio, E H Martins Ferreira, F Stavale, C A Achete, R B Capaz, M V O Moutinho, A Lombardo, T S Kulmala, and A C Ferrari. Quantifying defects in graphene via Raman spectroscopy at different excitation energies. *Nano Lett.*, 11(8):3190–3196, aug 2011.

[160] Matteo Bruna, Anna K. Ott, Mari Ijäs, Duhee Yoon, Ugo Sassi, and Andrea C. Ferrari. Doping dependence of the Raman spectrum of defected graphene. *ACS Nano*, 8(7):7432–7441, 2014.

[161] Jakob Zabel, Rahul R. Nair, Anna Ott, Thanasis Georgiou, Andre K. Geim, Kostya S. Novoselov, and Cinzia Casiraghi. Raman spectroscopy of graphene and bilayer under biaxial strain: Bubbles and balloons. *Nano Lett.*, 12(2):617–621, 2012.

[162] Ji Eun Lee, Gwanghyun Ahn, Jihye Shim, Young Sik Lee, and Sunmin Ryu. Optical separation of mechanical strain from charge doping in graphene. *Nat. Commun.*, 3(May):1024–1028, 2012.

[163] Dieter K. Schroder. *Semiconductor analysis and device characterisation*. Wiley-VCH, 3rd editio edition, 2006.

[164] Patrick Garidel and Heidrun Schott. Fourier-transform midinfrared spectroscopy for analysis and screening of liquid protein formulations part 1: Understanding infrared spectroscopy of proteins. *Bioprocess Int.*, pages 40–46, 2006.

[165] R A Hazelwood. Derivation of optical constants from transmission measurements alone - applied to MoSe2. *Thin Solid Films*, 6:329–341, 1970.

[166] Dirk Poelman and Philippe Frederic Smet. Methods for the determination of the optical constants of thin films from single transmission measurements: a critical review. *J. Phys. D Appl. Phys*, 36(03):1850–1857, 2003.

[167] Digby D Macdonald. Reflections on the history of electrochemical impedance spectroscopy. *Electrochim. Acta*, 51:1376–1388, 2006.

[168] Mark E. Orazem and Bernard Tribollet. *Electrochemical impedance spectroscopy*. John Wiley & Sons, Hoboken, New Jersey, first edit edition, 2008.

[169] Yue Lin, Fei Liu, Gabriel Casano, Rupesh Bhavsar, Ian A. Kinloch, and Brian Derby. Pristine graphene aerogels by room-temperature freeze gelation. *Adv. Mater.*, 28(36):7993–8000, 2016.

[170] Adrian C Fisher. *Electrode dynamics*. Oxford University Press, Oxford, second edition, 1996.

[171] E. Warburg. Uber das Verhalten sogenannter unpolarisirbarer Elektroden gegen Wechselstrom. *Ann. Phys.*, 303(3):793–499, 1899.

[172] L A Geddes. Historical evolution of circuit models for the electrode-electrolyte interface. *Ann. Biomed. Eng.*, 25:1–14, 1997.

[173] BioLogic. EC-lab Software User's Manual, 2015.

[174] T Jacobsen and K West. Diffusion impedance in planar, cylindrical and spherical symmetry. *Electrochim. Acta*, 40(2):255–262, 1995.

[175] Martin Fleischmann, Stanley Pons, and John Daschbach. The ac impedance of spherical, cylindrical, disk, and ring microelectrodes. *J. Electroanal. Chem.*, 317(1-2):1–26, 1991.

[176] Z. A. Rotenberg, A. V. Dribinskii, V. P. Lukovtsev, and N. S. Khozyainova. Electrochemical impedance of microelectrodes. *Russ. J. Electrochem.*, 36(8):879–882, 2000.

[177] J. Navarro-Laboulais, J. J. Garcia-Jareno, and F. Vicente. Kramers-Kronig transformation, dc behaviour and steady state response of the Warburg impedance for a disk electrode inlaid in an insulating surface. *J. Electroanal. Chem.*, 536(1-2):11–18, 2002.

[178] Kenneth S. Cole and Robert H. Cole. Dispersion and absorption in dielectrics I. Alternating current characteristics. *J. Chem. Phys.*, 9(4):341–351, 1941.

[179] Jean-Baptiste Jorcin, Mark E. Orazem, Nadine Pebere, and Bernard Tribollet. CPE analysis by local electrochemical impedance. *Electrochim. Acta*, 51:1473–1479, 2006.

[180] Jan Reinoud Buitenweg, W L Rutten, E Marani, S K Polman, and J Ursum. Extracellular detection of active membrane currents in the neuron- electrode interface. *J Neurosci. Methods*, 115(2):211–21, 2002.

[181] Justin C. Williams, Joseph A. Hippensteel, John Dilgen, William Shain, and Daryl R. Kipke. Complex impedance spectroscopy for monitoring tissue responses to inserted neural implants. *J. Neural Eng.*, 4(4):410–423, 2007.

[182] Hengxing Ji, Xin Zhao, Zhenhua Qiao, Jeil Jung, Yanwu Zhu, Yalin Lu, Li Li Zhang, Allan H. MacDonald, and Rodney S. Ruoff. Capacitance of carbon-based electrical double-layer capacitors. *Nat. Commun.*, 5(Cmcm):1–7, 2014.

[183] G. Binnig and C. F. Quate. Atomic force microscope. *Phys. Rev. Lett.*, 56(9):930–933, 1986.

[184] Hans-Juergen Butt, Brunero Cappella, and Michael Kappl. Force measurements with the atomic force microscope: Technique, interpretation and applications. *Surf. Sci. Rep.*, 59:1–152, 2005.

[185] V L Mirnov. *Fundamentals of scanning probe microscopy*. The Russian Academy of Sciences Institute for Physics of Microstructures, Nizhniy Novgorod, 2004.

[186] N. A. Burnham, O. P. Behrend, F. Oulevey, G. Gremaud, P. J. Gallo, D. Gourdon, E. Dupas, A. J. Kulik, H. M. Pollock, and G. A.D. Briggs. How does a tip tap? *Nanotechnology*, 8(2):67–75, 1997.

[187] T R Albrecht, P Grütter, D Horne, and D Rugar. Frequency modulation detection using high-Q cantilevers microscope sensitivity for enhanced force. *J. Appl. Phys.*, 69(2):668–674, 1991.

[188] Yan Hu, Shuiqing Hu, Chanmin Su, Jian Shi, and Ji Ma. Method and apparatus of operating a scanning probe micoscope, 2014.

[189] Christian D. Wilms, Hartmut Schmidt, and Jens Eilers. Quantitative two-photon Ca2+imaging via fluorescence lifetime analysis. *Cell Calcium*, 40(1):73–79, 2006.

[190] C Lattarulo, D Thyssen, K V Kuchibholta, Hyman B T, and Bacskaiq B J. Microscopic imaging of intracellular calcium in live cells using lifetime-based ratiometric measurements of Oregon green BAPTA-1. In G Manfredi and H Kawmata, editors, *Neuro-degeneration Methods Protoc.*, chapter 25, pages 374–389. Springer, New York, first edition, 2011.

[191] J. Vangindertael, R. Camacho, W. Sempels, H. Mizuno, P. Dedecker, and K. P. F. F Janssen. An introduction to optical super-resolution microscopy for the adventurous biologist. *Methods Appl. Fluoresc.*, 6(2):022003, 2018.

[192] M Minsky. Microscopy apparatus, 1961.

[193] José Angel Conchello and Jeff W. Lichtman. Optical sectioning microscopy. *Nat. Methods*, 2(12):920–931, 2005.

[194] K Suhling, P M W French, and D Phillips. Time-resolved fluorescence microscopy. *Photochem. Photobiol. Sci.*, 4(1):13–22, 2005.

[195] Wolfgang Becker, A. Bergmann, M. A. Hink, K. König, K. Benndorf, and C. Biskup. Fluorescence lifetime imaging by time-correlated single-photon counting. *Microsc. Res. Tech.*, 63(1):58–66, 2004.

[196] Andreas Barth and Christian Zscherp. What vibrations tell about proteins. *Q. Rev. Biophys.*, 35(4):369–430, 2002.

[197] Wolfgang Kabsch and Chris Sander. Dictionary of protein secondary structure: pattern recognition of hydrogen bonded and geometrical features. *Biopolymers*, 22(12):2577–2637, 1983.

[198] Aurélie Bornot and Alexandre G de Brevern. Protein beta-turn assignments. *Bioinformation*, 1(5):153–155, 2006.

[199] Joji M. Otaki, Motosuke Tsutsumi, Tomonori Gotoh, and Haruhiko Yamamoto. Secondary structure characterization based on amino acid composition and availability in proteins. *J. Chem. Inf. Model.*, 50(4):690–700, 2010.

[200] Motosuke Tsutsumi and Joji M. Otaki. Parallel and antiparallel b-strands differ in amino acid composition and availability of short constituent sequences. *J. Chem. Inf. Model.*, 51(6):1457–1464, 2011.

[201] Aichun Dong, Ping Huang, and Winslow S. Caughey. Redox-dependent changes in β-extended chain and turn structures of cytochrome C in water solution determined by second derivative amide I infrared spectra. *Biochemistry*, 31:182–189, 1992.

[202] Jilie Kong and Shaoning Yu. Fourier transform infrared spectroscopic analysis of protein secondary structures. *Acta Biochim. Biophys. Sin. (Shanghai).*, 39(8):549–559, 2007.

[203] Andreas Barth. Infrared spectroscopy of proteins. *Biochim. Biophys. Acta*, 1767(9):1073–1101, 2007.

[204] Micheal Jackson and Henry H Mantsch. The use and misuse of FTIR spectroscopy in the determination of protein structure. *Crit. Rev. Biochem. Mol. Biol.*, 30(2):95–120, 1995.

[205] K.S. Seshadri and R Norman Jones. The shapes and intensities of infrared absorption bands - A review. *Spectrochim. Acta*, 10(7341):1013–1085, 1963.

[206] WK Surewicz and HH Mantsch. New insight into protein secondary structure from resolution-enhanced infrared spectra. *Biochim. Biophys. Acta*, 952(2):115–130, 1988.

[207] Françoise Dousseau and Michel Pézolet. Determination of the secondary structure content of proteins in aqueous solutions from their Amide I and Amide II infrared bands. Comparison between classical and partial least-squares methods. *Biochemistry*, 29(37):8771–8779, 1990.

[208] Jose Luis Arrondo, Arturo Muga, Jose Castresana, and Felix M Goñi. Quantitative studies of the structure of proteins in solution by Fourier-transform infrared spectroscopy. *Prog. Biophys. Mol. Biol.*, 59(1):23–56, 1993.

[209] D. Michael Byler and Heino Susi. Examination of the secondary structure of proteins by deconvolved FTIR spectra. *Biopolymers*, 25(3):469–487, 1986.

[210] L. Rieppo, S. Saarakkala, T. Närhi, H. J. Helminen, J. S. Jurvelin, and J. Rieppo. Application of second derivative spectroscopy for increasing molecular specificity of fourier transform infrared spectroscopic imaging of articular cartilage. *Osteoarthr. Cartil.*, 20(5):451–459, 2012.

[211] Aichun Dong, Ping Huang, and Winslow S. Caughey. Protein secondary structures in water from second-derivative amide I infrared spectra. *Biochemistry*, 29(13):3303–3308, 1990.

[212] Alison J. North and Henry Baker. Seeing is believing? A beginners' guide to practical pitfalls in image acquisition. *J. Cell Biol.*, 172(1):9–18, 2006.

[213] Nuan Chen, Lingling Tian, Anoop C. Patil, Shengjie Peng, In Hong Yang, Nitish V. Thakor, and Seeram Ramakrishna. Neural interfaces engineered via micro- and nanostructured coatings. *Nano Today*, 14:59–83, 2017.

[214] Zengguang Cheng, Qiaoyu Zhou, Chenxuan Wang, Qiang Li, Chen Wang, and Ying Fang. Toward intrinsic graphene surfaces: A systematic study on thermal annealing and wet-chemical treatment of SiO2-supported graphene devices. *Nano Lett.*, 11(2):767–771, 2011.

[215] Linm Yung-Chang, Chun-Chieh Lu, Chao-Huei Yeh, Chuanhong Jin, Suenaga Kazu, and Po-Wen Chiu. Graphene Annealing : How Clean Can It Be ? *Nano Lett.*, 12:414–419, 2012.

[216] G. Giovannetti, P. A. Khomyakov, G. Brocks, V. M. Karpan, J. Van Den Brink, and P. J. Kelly. Doping graphene with metal contacts. *Phys. Rev. Lett.*, 101(2):4–7, 2008.

[217] Kishan Thodkar, Damien Thompson, Felix Lüönd, Lucas Moser, Frédéric Overney, Laurent Marot, Christian Schönenberger, Blaise Jeanneret, and Michel Calame. Restoring the Electrical Properties of CVD Graphene via Physisorption of Molecular Adsorbates. *ACS Appl. Mater. Interfaces*, 9(29):25014–25022, 2017.

[218] Matthew J. Nelson, Silvana Valtcheva, and Laurent Venance. Magnitude and behavior of cross-talk effects in multichannel electrophysiology experiments. *J. Neurophysiol.*, 118(1):574–594, 2017.

[219] Deepak Ropireddy, Ruggero Scorcioni, Bonnie Lasher, Gyorgy Buzsáki, and Giorgio A. Ascoli. Axonal morphometry of hippocampal pyramidal neurons semi-automatically reconstructed after in vivo labeling in different CA3 locations. *Brain Struct. Funct.*, 216(1):1–15, 2011.

[220] Peter Ledochowitsch, Elisa Olivero, Tim Blanche, and Michel M. Maharbiz. A transparent ECoG array for simultaneous recording and optogenetic stimulation. *Proc. Annu. Int. Conf. IEEE Eng. Med. Biol. Soc. EMBS*, pages 2937–2940, 2011.

[221] H Al-Mumen, F Rao, W Li, and L Dong. Singular sheet etching of graphene with oxygen plasma. *Nano-Micro Lett.*, 6(2):116–124, 2014.

[222] W. van Gelder and V. E. Hauser. The etching of silicon nitride in phosphoric acid with silicon dioxide as a mask. *J. Electrochem. Soc.*, 114(8):869, 1967.

[223] Kee Scholten and Ellis Meng. Materials for microfabricated implantable devices: A review. *Lab Chip*, 15(22):4256–4272, 2015.

[224] Nathan Jackson and Jit Muthuswamy. Artificial dural sealant that allows multiple penetrations of implantable brain probes. *J. Neurosci. Methods*, 171(1):147–152, 2008.

[225] By R Fabian Pease and Stephen Y Chou. Lithography and other patterning techniques for future electronics. *Procedings IEEE*, 96(2):248–270, 2008.

[226] Ansgar Waldbaur, Holger Rapp, Kerstin Länge, and Bastian E. Rapp. Let there be chip - Towards rapid prototyping of microfluidic devices: One-step manufacturing processes. *Anal. Methods*, 3(12):2681–2716, 2011.

[227] Norio Saitou, Chusuke Munakata, and Akiji Maekawa. Analysis of trapezoid distortion due to charge-Up in electron beam recording. *Jpn. J. Appl. Phys.*, 10(3):351–356, 1971.

[228] M. Salerno and R. Cingolani. High throughput electron beam lithography on insulating substrates for photonic devices. *J. Micromechanics Microengineering*, 17(12):2414–2419, 2007.

[229] Thermo Fisher Scientific. Laboratory Reagents Handbook, 2012.

[230] J.-P. Diard, B. Le Gorrec, and C. Montella. Deviation from the polarization resistance due to non-linearity .1. Theoretical formulation. *J. Electroanal. Chem.*, 432:27–39, 1997.

[231] Xiaoxin Zou and Yu Zhang. Noble metal-free hydrogen evolution catalysts for water splitting. *Chem. Soc. Rev.*, 44(15):5148–5180, 2015.

[232] Xiang Ren, Dan Wu, Ruixiang Ge, Hongmin Ma, Tao Yan, Yong Zhang, Bin Du, Qin Wei, and Liang Chen. Self-supported CoMoS4 nanosheet array as an efficient catalyst for hydrogen evolution reaction at neutral pH. *Nano Res.*, 11(2):2024–2033, 2018.

[233] Dmitry Kireev, Max Brambach, Silke Seyock, Vanessa Maybeck, Wangyang Fu, Bernhard Wolfrum, and Andreas Offenhaüsser. Graphene transistors for interfacing with cells: Towards a deeper understanding of liquid gating and sensitivity. *Sci. Rep.*, 7(1):1–12, 2017.

[234] Gaëlle Piret, Clément Hébert, Jean Paul Mazellier, Lionel Rousseau, Emmanuel Scorsone, Myline Cottance, Gaelle Lissorgues, Marc O. Heuschkel, Serge Picaud, Philippe Bergonzo, and Blaise Yvert. 3D-nanostructured boron-doped diamond for microelectrode array neural interfacing. *Biomaterials*, 53:173–183, 2015.

[235] Dimitrios A. Koutsouras, Paschalis Gkoupidenis, Clemens Stolz, Vivek Subramanian, George G. Malliaras, and David C. Martin. Impedance spectroscopy of spin-cast and electrochemically deposited PEDOT:PSS films on microfabricated electrodes with various areas. *ChemElectroChem*, 4(9):2321–2327, 2017.

[236] Liangti Qu, Yong Liu, Jong-Beom Baek, and Liming Dai. Nitrogen-Doped Graphene as Efficient Metal-Free Electrocatalyst for Oxygen Reduction in Fuel Cells. *ACS Nano*, 4(3):1321–1326, 2010.

[237] O. Devos, C. Gabrielli, and B. Tribollet. Nucleation-growth process of scale electrodeposition-Influence of the mass transport. *Electrochim. Acta*, 52(1):285–291, 2006.

[238] Chadwick M Hales, John D Rolston, and Steve M Potter. How to culture, record and stimulate neuronal networks on micro-electrode arrays (MEAs). *J. Vis. Exp.*, 30(39):1–7, 2010.

[239] Fredrik Johansson, Patrick Carlberg, Nils Danielsen, Lars Montelius, and Martin Kanje. Axonal outgrowth on nano-imprinted patterns. *Biomaterials*, 27(8):1251–1258, 2006.

[240] Manuel S. Schroeter, Paul Charlesworth, Manfred G. Kitzbichler, Ole Paulsen, and Edward T. Bullmore. Emergence ofRich-Club Topology and Coordinated Dynamics in Development ofHippocampal Functional Networks In Vitro. *J. Neurosci.*, 35(14):5459–5470, 2015.

[241] J. H. Frank, A. D. Elder, J. Swartling, A. R. Venkitaraman, A. D. Jeyasekharan, and Clemens F. Kaminski. A white light confocal microscope for spectrally resolved. *J. Microsc.*, 227(3):203–215, 2007.

[242] K. A. Selanger, J. Falnes, and T. Sikkeland. Fluorescence lifetime studies of rhodamine 6G in methanol. *J. Phys. Chem.*, 81(20):1960–1963, 1977.

[243] Douglas Magde, Roger Wong, and Paul G. Seybold. Fluorescence Quantum Yields and Their Relation to Lifetimes of Rhodamine 6G and Fluorescein in Nine Solvents: Improved Absolute Standards for Quantum Yields¶. *Photochem. Photobiol.*, 75(4):327, 2002.

[244] I. Kaminska, J. Bohlen, S. Rocchetti, F. Selbach, G. P. Acuna, and P. Tinnefeld. Distance Dependence of Single-Molecule Energy Transfer to Graphene Measured with DNA Origami Nanopositioners. *Nano Lett.*, 19(7):4257–4262, 2019.

[245] Weiyue Chen, Laurence J. Young, Meng Lu, Alessio Zaccone, Florian Strohl, Na Yu, Gabriele S. Kaminski Schierle, and Clemens F. Kaminski. Fluorescence self-quenching from reporter dyes informs on the structural properties of amyloid clusters formed in vitro and in cells. *Nano Lett.*, 17(1):143–149, 2017.

[246] Sergey Larionov, Przemyslaw Wielgat, Yiner Wang, Dietmar Rudolf Thal, and Harald Neumann. Spatially pathogenic forms of tau detected in Alzheimer's disease brain tissue by fluorescence lifetime-based Förster resonance energy transfer. *J. Neurosci. Methods*, 192(1):127–137, 2010.

[247] Julia Gath, Luc Bousset, Birgit Habenstein, Ronald Melki, Anja Böckmann, and Beat H. Meier. Unlike twins: An NMR comparison of two α-synuclein polymorphs featuring different toxicity. *PLoS One*, 9(3):1–11, 2014.

[248] Amberley D. Stephens, Maria Zacharopoulou, and Gabriele S. Kaminski Schierle. The Cellular Environment Affects Monomeric α-Synuclein Structure. *Trends Biochem. Sci.*, pages 1–14, 2018.

[249] Filip Simunovic, Ming Yi, Yulei Wang, Laurel Macey, Lauren T. Brown, Anna M. Krichevsky, Susan L. Andersen, Robert M. Stephens, Francine M. Benes, and Kai C. Sonntag. Gene expression profiling of substantia nigra dopamine neurons: further insights into Parkinson's disease pathology. *Brain*, 132(7):1795–1809, 2009.

[250] M. C.J. Dekker, V. Bonifati, and C. M. Van Duijn. Parkinson's disease: Piecing together a genetic jigsaw. *Brain*, 126(8):1722–1733, 2003.

[251] Anna Raffaello, Cristina Mammucari, Gaia Gherardi, and Rosario Rizzuto. Calcium at the Center of Cell Signaling: Interplay between Endoplasmic Reticulum, Mitochondria, and Lysosomes. *Trends Biochem. Sci.*, 41(12):1035–1049, 2016.

[252] Giuliana Fusco, Alfonso De Simone, Tata Gopinath, Vitaly Vostrikov, Michele Vendruscolo, Christopher M. Dobson, and Gianluigi Veglia. Direct observation of the three regions in α-synuclein that determine its membrane-bound behaviour. *Nat. Commun.*, 5(May):1–8, 2014.

[253] Elizabeth R. Middleton and Elizabeth Rhoades. Effects of curvature and composition on α-synuclein binding to lipid vesicles. *Biophys. J.*, 99(7):2279–2288, 2010.

[254] Benoit I. Giasson, Ian V.J. Murray, John Q. Trojanowski, and Virginia M.Y. Lee. A hydrophobic stretch of 12 amino acid residues in the middle of α-Synuclein is essential for filament assembly. *J. Biol. Chem.*, 276(4):2380–2386, 2001.

[255] C. Del Mar, E. A. Greenbaum, L. Mayne, S. W. Englander, and V. L. Woods. Structure and properties of α-synuclein and other amyloids determined at the amino acid level. *Proc. Natl. Acad. Sci.*, 102(43):15477–15482, 2005.

[256] VV Krishnan and B Rupp. Macromolecular structure determination: comparison of X-ray crystallography and NMR spectroscopy. *eLS*, 2012.

[257] Norma J. Greenfield. Using circular dichroism spectra to estimate protein secondary structure. *Nat. Protoc.*, 1(6):2876–2890, 2007.

[258] Xiao Chen Bai, Greg McMullan, and Sjors H.W. Scheres. How cryo-EM is revolutionizing structural biology. *Trends Biochem. Sci.*, 40(1):49–57, 2015.

[259] Patrick Garidel and Heidrun Schott. Fourier-transform midinfrared spectroscopy for analysis and screening of liquid protein formulations part 2: Details analysis and applications. *Bioprocess Int.*, pages 48–55, 2006.

[260] Erik Goormaghtigh, Vincent Raussens, and Jean-Marie Ruysschaert. Attenuated total reflection infrared spectroscopy of proteins and lipids in biological membranes. *Biochim. Biophys. Acta*, 1422(2):105–185, 1999.

[261] Jennifer D'Antonio, Brian M. Murphy, Mark Cornell Manning, and Wasfi A. Al-Azzam. Comparability of protein therapeutics: Quantitative comparison of second-derivative amide I infrared spectra. *J. Pharm. Sci.*, 101(6):2025–2033, 2012.

[262] Maurizio Baldassarre, Chenge Li, Nadejda Eremina, Erik Goormaghtigh, and Andreas Barth. Simultaneous fitting of absorption spectra and their second derivatives for an improved analysis of protein infrared spectra. *Molecules*, 20(7):12599–12622, 2015.

[263] Erik Goormaghtigh, Jean Marie Ruysschaert, and Vincent Raussens. Evaluation of the information content in infrared spectra for protein secondary structure determination. *Biophys. J.*, 90(8):2946–2957, 2006.

[264] J M Valpuesta, F M Goñi, A Alonso, J L R Arrondo, and Macarulla J M. Lipid-protein interactions. The mitochondrial complex lll-phosphatidylcholine-water system. *Biochim. Biophys. Acta*, 942:341–352, 1988.

[265] Asmund Rinnan, Frans van der Berg, and Søren Balling Engelsen. Review of the most common pre-processing techniques for near-infrared spectra. *TrAC - Trends Anal. Chem.*, 28(10):1201–1222, 2009.

[266] Huayan Yang, Shouning Yang, Jilie Kong, Aichun Dong, and Shaoning Yu. Obtaining information about protein secondary structures in aqueous solution using Fourier transform IR spectroscopy. *Nat. Protoc.*, 10(3):382–396, 2015.

[267] P. Geladi, D. MacDougall, and H. Martens. Linearization and Scatter-Correction for Near-Infrared Reflectance Spectra of Meat. *Appl. Spectrosc.*, 39(3):491–500, 1985.

[268] Abraham Savitzky and Marcel J.E. Golay. Smoothing and differentiation of data by simplified least squares procedures. *Anal. Chem.*, 36(8):1627–1639, 1964.

[269] Erik Goormaghtigh, Veronique Cabiaux, and Jean-Marie Ruysschaert. Secondary structure and dosage of soluble and membrane proteins by attenuated total reflection Fourier transform infrared spectroscopy on hydrated films. *Eur. Jounal Biochem.*, 193:409–420, 1990.

[270] Amberley D. Stephens, Nadezhda Nespovitaya, Maria Zacharopoulou, Clemens F. Kaminski, Jonathan J. Phillips, and Gabriele S. Kaminski Schierle. Different structural conformers of monomeric α-synuclein identified after lyophilizing and freezing. *Anal. Chem.*, 90(11):6975–6983, 2018.

[271] Lisa M. Miller, Megan W. Bourassa, and Randy J. Smith. FTIR spectroscopic imaging of protein aggregation in living cells. *Biochim. Biophys. Acta - Biomembr.*, 1828(10):2339–2346, 2013.

[272] Luc Bousset, Laura Pieri, Gemma Ruiz-Arlandis, Julia Gath, Poul Henning Jensen, Birgit Habenstein, Karine Madiona, Vincent Olieric, Anja Böckmann, Beat H. Meier, and Ronald Melki. Structural and functional characterization of two alpha-synuclein strains. *Nat. Commun.*, 4, 2013.

[273] Marco van de Weert, Parvez I. Haris, Wim E. Hennink, and Daan J.A. Crommelin. Fourier transform infrared spectrometric analysis of protein conformation: Effect of sampling method and stress factors. *Anal. Biochem.*, 297(2):160–169, 2001.

[274] Dhiman Ghosh, Pradeep K. Singh, Shruti Sahay, Narendra Nath Jha, Reeba S. Jacob, Shamik Sen, Ashutosh Kumar, Roland Riek, and Samir K. Maji. Structure based aggregation studies reveal the presence of helix-rich intermediate during α-Synuclein aggregation. *Sci. Rep.*, 5:1–15, 2015.

[275] Ashwini Kher, Punsandani Udabage, Ian McKinnon, Don McNaughton, and Mary Ann Augustin. FTIR investigation of spray-dried milk protein concentrate powders. *Vib. Spectrosc.*, 44(2):375–381, 2007.

[276] Morten Jonas Maltesen and Marco van de Weert. Drying methods for protein pharmaceuticals. *Drug Discov. Today Technol.*, 5(2-3):81–88, 2009.

[277] Maarten A. Mensink, Henderik W. Frijlink, Kees van der Voort Maarschalk, and Wouter L.J. Hinrichs. How sugars protect proteins in the solid state and during drying (review): Mechanisms of stabilization in relation to stress conditions. *Eur. J. Pharm. Biopharm.*, 114:288–295, 2017.

[278] Massimo Stefani. Protein misfolding and aggregation: New examples in medicine and biology of the dark side of the protein world. *Biochim. Biophys. Acta - Mol. Basis Dis.*, 1739(1):5–25, 2004.

[279] Talia A. Shmool, Philippa J. Hooper, Markus Leutzsch, Amberley D. Stephens, Mario U. Gaimann, Michael D. Mantle, Gabriele S. Kaminski Schierle, Christopher F. van der Walle, and J. Axel Zeitler. Observation of high-temperature macromolecular confinement in lyophilised protein formulations using terahertz spectroscopy. *Int. J. Pharm. X*, 1:100022, 2019.

[280] Karolina A. Majorek, Przemyslaw J. Porebski, Arjun Dayal, Matthew D. Zimmerman, Kamila Jablonska, Alan J. Stewart, Maksymilian Chruszcz, and Wladek Minor. Structural and immunologic characterization of bovine, horse, and rabbit serum albumins. *Mol. Immunol.*, 52(3-4):174–182, 2012.

[281] Huai Qing, He Yanlin, Sheng Fenlin, and Tao Zuyi. Effects of pH and metal ions on the conformation of bovine serum albumin in aqueous solution An attenuated total reflection (ATR) FTIR spectroscopic study. *Spectrochim. Acta Part A Mol. Biomol. Spectrosc.*, 52(13):1795–1800, 1996.

[282] Sijin Huang, Jialei Wang, and Qing Shang. Development and evaluation of a novel polymeric hydrogel of sucrose acrylate-co-polymethylacrylic acid for oral curcumin delivery. *J. Biomater. Sci. Polym. Ed.*, 28(2):194–206, 2017.

[283] Marco Van De Weert, Ron Van 'T Hof, Jaap Van Der Weerd, Ron M.A. Heeren, George Posthuma, Wim E. Hennink, and Daan J.A. Crommelin. Lysozyme distribution and conformation in a biodegradable polymer matrix as determined by FTIR techniques. *J. Control. Release*, 68(1):31–40, 2000.

[284] Dong Pyo Hong, Anthony L. Fink, and Vladimir N. Uversky. Structural characteristics of α-synuclein oligomers stabilized by the flavonoid baicalein. *J. Mol. Biol.*, 383(1):214–223, 2008.

[285] María Soledad Celej, Rabia Sarroukh, Erik Goormaghtigh, Gerardo D. Fidelio, Jean-Marie Ruysschaert, and Vincent Raussens. Toxic prefibrillar α-synuclein amyloid oligomers adopt a distinctive antiparallel β-sheet structure. *Biochem. J.*, 443(3):719–726, 2012.

[286] Vladimir N. Uversky, Jie Li, and Anthony L. Fink. Evidence for a Partially Folded Intermediate in α-Synuclein Fibril Formation. *J. Biol. Chem.*, 276(14):10737–10744, 2001.

[287] Jakob Domert, Christopher Sackmann, Lotta Agholme, Joakim Bergström, Martin Ingelsson, Martin Hallbeck, and Emelie Severinsson. Aggregated alpha-synuclein transfer efficiently between cultured human neuron- like cells and localize to lysosomes. *PLoS One*, 11(12), 2016.

[288] Amir K. Varkouhi, Marije Scholte, Gert Storm, and Hidde J. Haisma. Endosomal escape pathways for delivery of biologicals. *J. Control. Release*, 151:220–228, 2011.

[289] Xiang-Ping Chu and Zhi-Gang Xiong. Physiological and pathological functions of acid-sensing ion channels in the central nervous system. *Curr Drug Targets*, 13(2):263–271, 2012.

[290] Vasanthy Vigneswara, Simon Cass, Declan Wayne, Edward L. Bolt, David E. Ray, and Wayne G. Carter. Molecular Ageing of Alpha- and Beta-Synucleins: Protein Damage and Repair Mechanisms. *PLoS One*, 8(4):1–12, 2013.

[291] Kuen Phon Wu, Daniel S. Weinstock, Chitra Narayanan, Ronald M. Levy, and Jean Baum. Structural Reorganization of α-Synuclein at Low pH Observed by NMR and REMD Simulations. *J. Mol. Biol.*, 391(4):784–796, 2009.

[292] Sebastian McClendon, Carla C. Rospigliosi, and David Eliezer. Charge neutralization and collapse of the C-terminal tail of α-synuclein at low pH. *Protein Sci.*, 18(7):1531–1540, 2009.

[293] D. James Surmeier and P. T. Schumacker. Calcium, bioenergetics, and neuronal vulnerability in Parkinson's disease. *J. Biol. Chem.*, 288(15):10736–10741, 2013.

[294] Janin Lautenschläger, Amberley D. Stephens, Giuliana Fusco, Florian Ströhl, Nathan Curry, Maria Zacharopoulou, Claire H. Michel, Romain Laine, Nadezhda Nespovitaya, Marcus Fantham, Dorothea Pinotsi, Wagner Zago, Paul Fraser, Anurag Tandon, Peter St George-Hyslop, Eric Rees, Jonathan J. Phillips, Alfonso De Simone, Clemens F. Kaminski, and Gabriele S. Kaminksi Schierle. C-terminal calcium binding of α-synuclein modulates synaptic vesicle interaction. *Nat. Commun.*, 9(1), 2018.

[295] Larissa A. Munishkina, Jeremy Henriques, Vladimir N. Uversky, and Anthony L. Fink. Role of Protein-Water Interactions and Electrostatics in α-Synuclein Fibril Formation. *Biochemistry*, 43(11):3289–3300, 2004.

[296] Jong Yoon Han, Tae Su Choi, and Hugh I. Kim. Molecular Role of Ca2+and Hard Divalent Metal Cations on Accelerated Fibrillation and Interfibrillar Aggregation of α-Synuclein. *Sci. Rep.*, 8(1):1–11, 2018.

[297] Dmitry Kireev, Silke Seyock, Mathis Ernst, Vanessa Maybeck, Bernhard Wolfrum, and Andreas Offenhäusser. Versatile flexible graphene multielectrode arrays. *Biosensors*, 7(1):1–9, 2016.

[298] Gabriele S. Kaminski Schierle, Sebastian Van De Linde, Miklos Erdelyi, Elin K. Esbjörner, Teresa Klein, Eric Rees, Carlos W. Bertoncini, Christopher M. Dobson, Markus Sauer, and Clemens F. Kaminski. In situ measurements of the formation and morphology of intracellular β-amyloid fibrils by super-resolution fluorescence imaging. *J. Am. Chem. Soc.*, 133(33):12902–12905, 2011.

[299] Pierre Mahou, Nathan Curry, Dorothea Pinotsi, Kaminski Schierle, Clemens Kaminski, Pierre Mahou, Nathan Curry, Dorothea Pinotsi, and Gabriele Kaminski Schierle. Stimulated emission depletion microscopy to study amyloid fibril formation. In *Proc. SPIE*, 2015.

[300] Eileen Nugent, F Kaminski, and Gabriele S Kaminski. Super-resolution imaging of alpha-synuclein polymorphisms and their potential role in neurodegeneration. *Integr. Biol.*, 9(3):206–210, 2017.

[301] T. Sit. mecp2, 2018.

[302] T. A. Nick. Matlab_MEA, 2013.

[303] Sean C. Warren, Anca Margineanu, Dominic Alibhai, Douglas J. Kelly, Clifford Talbot, Yuriy Alexandrov, Ian Munro, Matilda Katan, Chris Dunsby, and Paul M.W. French. Rapid global fitting of large fluorescence lifetime imaging microscopy datasets. *PLoS One*, 8(8), 2013.

Appendix A

Materials and methods

A.1 Device fabrication

A.1.1 Purchased microelectrode arrays

TiN microelectrode arrays (MEA, 60ThinMEA200/30iR-ITO) were purchased from Multi-channel Systems. These MEAs were fabricated on a coverslip with opaque TiN electrodes, transparent indium tin oxide (ITO) leads and SiN encapsulation layer.

A.1.2 Material deposition

All materials were deposited on # 1.5 borosilicate glass coverslips.

A.1.2.1 Conductive materials

ITO was deposited by sputter deposition (Metallifier sputter coater, Precision Atomics). A base pressure of 2×10^{-6} mbar was achieved, and argon sputtering used to deposit 100 nm from an ITO target.

Chromium/Gold was deposited by thermal evaporation (M-Braun or MiniLab 60, Moorfield Nanotechnology Ltd.) at a base pressure of $<1\times10^{-5}$ mbar. First chromium was deposited (5 nm, 0.4 Å s^{-1}) followed by gold (50 nm, 1 Å s^{-1}).

A.1.2.2 Graphene

Chemical vapour deposition (CVD) Graphene was grown by Oliver Burton. The graphene was grown in a cold walled CVD reactor (AIXTRON BM Pro 4") using copper foil (25 µm thick) as a catalyst. The copper was cleaned in acetone and isopropyl alcohol (IPA), and

partially oxidised. To synthesis graphene the copper was annealed in 50 mbar of argon (1070°C, 30 min), the exposed to 50 mbar of 4000:1000:1 Ar:H2:CH4 gas mixture (90 min) resulting in full coverage of the copper foil by graphene ($>$ 97% monolayer, grain size $>$ 100 µm).

Graphene was transferred from the copper growth substrate. Poly(methyl methacrylate) (PMMA, A8, molecular weight 495,000) was spin coated (4000 rpm, 40 s) on the copper/graphene. The copper substrate was etched in ammonium persulphate solution (1.8 g in 150 mL water). The remaining PMMA/graphene was transferred onto the desired substrate and dried (room temperature, 12 h). The device was baked (110°C, 5 min) and soaked in acetone to remove the PMMA support (1 h).

A.1.2.3 Materials for the encapsulation layer

The polymer resists were spin coated on the substrate and baked. PMMA A8 (molecular weight 495,000) was spin coated (4000 rpm, 40 s) and baked on a hotplate (120°C, 5 min). AZ5214E was spin coated (500 rpm, 5 s, then 4000 rpm, 40 s) and baked (100°C, 1 min). SU-8 2005 was spin coated deposited (4000 rpm, 40 s) and baked on a hotplate (65°C, 1 min then 95°C, 2 min).

Si_3N_4 was deposited by electron beam evaporation (K J Lesker) at a base pressure of $< 10^{-5}$ mbar from a Si_3N_4 source at a rate of 0.8 Å s^{-1}.

Al_2O_3 was deposited using atomic layer deposition (ALD, TFS200 Beneq). The chamber was pumped to a pressure of 9 mbar, and the stage heated to 125°C. Trimethylaluminum was pulsed into the chamber (200 ms) followed by a purge (2.5 s), then water was pulsed in (400 ms) followed by a purge (2.5s), this was repeated for 600 cycles to deposit 100 nm of Al_2O_3.

A.1.3 Graphene microelectrode array

Materials deposition for the graphene MEA fabrication, was performed using the methods described above. Custom built MEAs were fabricated on 48 mm^2 # 1.5 borosilicate glass coverslip (Soham Scientific).

The lithographic patterns were designed using AutoCAD® (Autodesk).To create the wire patterns, AZ5214E was used as an image reversal photoresist. AZ5214E was spin coated (500 rpm 5 s, then 4000 rpm 40 s) and baked (100°C 1 min). Photolithography was performed using a laser writer (LW-405B+, Microtech Srl) with 405 nm light (55 mJ cm^2.) The device was baked (100°C 2 min) followed by a flood exposure (289mJ cm^2). The pattern was developed in 1:4 AZ351B:water.

Chromium/gold connecting wires (5/50 nm) were deposited by thermal evaporation. The pattern for the deposited wires was defined using AZ5214E as an image reversal photoresist, and patterning using a laser writer. Lift-off was performed in acetone.

Graphene was grown by Oliver Burton by CVD on a copper catalyst. The graphene was transferred over the prefabricated electrode region by wet etching the copper in ammonium persulphate, transferring the PMMA/graphene layer and removing the PMMA in acetone. A pattern for etching the graphene was made by photolithography using a laser writer with the AZ5214E resist. Graphene was etched using an O_2 reactive ion etcher (NanoEtch, Moorfield Nanotechnology Ltd) at 6 W (40 s).

A PMMA encapsulation layer was spin coated over the entire device. 30 µm holes were opened up using electron beam lithography (Nanobeam NB1). To provide a conductive charge dissipation layer, gold was deposited by thermal evaporation (15 nm, rate 0.5 $\text{Å}\,\text{s}^{-1}$) over the resist. The electron beam had an exposure dose of $6\,\text{C}\,\text{m}^{-2}$. Following the lithography, gold was removed using 1:3 gold etchant:water (30 s). The PMMA resist was developed in 3:7 IPA:water.

To enable cell culture, cylindrical glass wells (24 mm outer diameter, 19 mm inner diameter, 6 mm high) were purchased from Soham Scientific and attached to the device using multipurpose silicone-elastomer based sealant (Dow Corning, 732). A removable ALA MEA-MEM lid with a semi-permeable fluorinated ethylene-propylene membrane was placed over the well during cell culturing.

A.2 Cell culture

A.2.1 Embryonic rat primary hippocampal cell culture

Primary cultures were prepared by Miranda Robbins. Neurons from the hippocampi of E18 Sprague-Dawley rats were dissected in Hanks Buffered Salts Solution (HBSS) and stored in Dulbecco's Modified Eagle's Medium (DMEM) on ice before trypsinisation. To separate cells, hippocampi were incubated in 0.25% trypsin with 0.1% DNAse in 2 mL DMEM at (37°C, 20 min). The cells were then washed 4 times in 0.1% DNAse in DMEM. The cells were washed in 10% fetal bovine serum (FBS) in DMEM and triturated in a p200 pipette in 10% FBS in DMEM 80–100 times. Neurons were then plated at $5\times10^4\,\text{ml}^{-1}$ on 0.01% poly-L-lysine treated devices. The cells were maintained in media consisting of neurobasal medium with 2% B27 and 0.25% Glutamax incubated at 37°C, 5% CO_2, 95% humidity.

A.2.2 Mouse hippocampal neuron cell culture

Mouse hippocampal cell cultures were prepared by Susanna Mierau, Ricardo Conci and Timothy Sit. C57BL/6 mice were kept at the Physiology Department, University of Cambridge. Postnatal day 0–1 mice were produced by breeding female mice heterozygous for deletion *Mecp2* depletion with male mice that were wild-type for *Mecp2*. With respect to *Mecp2*, the male mice were wild-type, hemizygous or knockout, and female mice were wild-type or heterozygous.

Before cell plating, MEAs were rinsed with water, proteinase K (0.5 mg/mL, left overnight) and then water. The TiN-MEAs were exposed to O_2 plasma to increase their hydrophilicity and promote cell adhesion, then autoclaved. The graphene MEAs were sterilised by submersion in ethanol, then ultraviolet (UV) light exposure. After cleaning, poly-L-lysine (PLL, 0.1%, P8920) was added to the MEA central region, and rinsed off via exchange of PBS. Diluted laminin was added (4 µl, 1 mg/mL to the MEA central region and a ring of Neurobasal medium (30 µl) was added. The MEAs were stored in the incubator for 24–48 h.

Hippocampal cultures from mice obtained on the day of birth (post natal day 0–1) were used. Following dissection, the cortecies or hippocampi were dissociated in papain (0.125 mg/mL) and warmed in a 37°C water bath (25 min). Papain reaction was stopped by adding FBS (4%, 1 mL) and debris separated through centrifugation (0.4 relative centrifugal force, 10 min). The supernatant was removed, and the pellet was resuspended in NB/B27 media (1 mL, 37°C). Cells were plated at a concentration of 2×10^5 ml^{-1} in drops of 20–40 µL. The laminin on the prepared MEAs was aspirated before plating, and after plating, 600 µL of NB-B27 medium with 0.5 mM of L-glutamine was added to the MEAs. Cultures were kept at 37°C and 5% CO_2 / 95% air. Cultures were fed through exchanging one third of the medium three times per week. The exchange medium was prepared by adding L-glutamine (0.5 mM) to NB-B27 medium [240].

A.3 Protein lyophilisation

A.3.1 Bovine serum albumin

The bovine serum albumin (BSA) based protein formulations were prepared by Talia Shmool. The formulations examined were: neat BSA; F1 is 2.3 mM BSA, 25 mM histidine-HCl and 265 mM sucrose; F2 is 1.1 mM BSA, 25 mM histidine-HCl, 265 mM sucrose, 0.04% polysorbate 80.

All the formulations were lyophilised using a lyophiliser (VirTis, BenchTop). The formulations were frozen by cooling to 233 K (30 min), then raising the temperature to

253 K. Primary drying was performed at 253 K for 650 min under 133 mbar; followed by a secondary drying step at 313 K for 360 min, 133 mbar. The vials were subsequently closed under reduced pressure (850 mbar), at 298 K using a rubber stopper, and were crimped with aluminium seals. Vials were stored at 278 K until measurement and analysis. The water content for each lyophilised formulation was determined using Karl Fischer coulometric titration, ensuring the residual moisture was less than 2.5%.

A.3.2 α-synuclein

α-synuclein (aSyn) was prepared and purified by Amberley Stephens and Maria Zacharopoulou. The buffers used for FTIR analysis of aSyn were ammonium acetate, a tris(hydroxymethyl) aminomethane (tris) based buffer and a 4-(2-hydroxyethyl)-1-piperazineethanesulfonic acid (HEPES) based buffer. The tris buffer contains 20 mM Tris-HCl in $H_2O$and is kept at pH 8. The HEPES buffer contains 20 mM NaCl, 2.5 mM KCl, 25 mM HEPES, 30 mM Glucose, pH 7.4 in H_2O with NaOH.

Human wild-type (aSyn) was expressed using plasmid pT7-7. The plasmids were heat shocked into Escherichia coli One Shot® BL21 STAR™ (DE3) and purified as previously described [270]. Briefly, expressed aSyn was purified using ion exchange chromatography on a HiPrep Q FF 16/10 anion exchange column (GE Healthcare). aSyn was then further purified on a HiPrep Phenyl FF 16/10 (High Sub) hydrophobic interaction chromatography column (GE Healthcare). aSyn was extensively dialysed against 20 mM Tris pH 7.2 and concentrated using 10 k MWCO amicon centrifugal filtration devices (Merck KGaA) and stored at -80°C until use. Before experiments 1 mL of aSyn was further purified using a Superdex 75 pg 10/300 GL size exclusion chromatography (SEC) column (GE Healthcare) to obtain monomeric protein. Purification was performed on an AKA Pure (GE Healthcare).

To prepare samples for FTIR analysis, aSyn monomer was buffer exchanged into 20 mM ammonium acetate pH 7 or pH 4 with or without 2.5 mM $CaCl_2$ using PD10 Desalting columns (GE Healthcare). The samples were snap frozen in liquid nitrogen and lyophilised in a LyoQuest 85 freeze-dryer (Telstar).

A.4 Characterisation techniques

A.4.1 Ultraviolet-visible spectroscopy

Ultraviolet-visible (UV-vis) spectroscopy was performed using a Cary 7000 UV-VIS-NIR Spectrometer (Agilent Technologies). Scans of transmittance were performed at 300–1500 nm and a background air spectrum was subtracted.

A.4.2 Raman spectroscopy

Raman spectra were acquired using a Renishaw inVia spectrometer equipped with a 50× objective at 514.5 nm and a laser power of 2.08 mW. Spectra were acquired from 1000–3500 cm^{-1}. The intensity of the 2D peak at 2694 cm^{-1} was used for the mapping with 20 µm spacing between points.

A script to batch process the graphene spectra was written in Matlab (based on Section 7.3). Firstly, cosmic rays, observed as sharp intense peaks in the Raman spectrum, were removed. Secondly, the glass background was subtracted using a linear background subtraction scaled to the peak at $\sim 1202\,cm^{-1}$. Thirdly, the baseline was flattened, removing the broad fluorescence peaks. Fourthly, the spectrum was normalised the area under the curve. Finally, each peak was fitted to a single Lorentzian and the parameters of the curves were extracted for further analysis. Peaks were fitted at the wavenumbers where graphene absorbs in the Raman spectrum: the D peak at $\sim 1350\,cm^{-1}$; the G peak at $\sim 1580\,cm^{-1}$; the D' peak at $\sim 1600\,cm^{-1}$; the D+D' peak at $\sim 2450\,cm^{-1}$; the 2D peak at $\sim 2680\,cm^{-1}$ the D+D" peak at $\sim 2680\,cm^{-1}$ and the 2D' peak at $\sim 3200\,cm^{-1}$ [155, 156].

A.4.3 Electrochemical Impedance spectroscopy

Electrochemical impedance spectra were acquired in phosphate buffered saline solution (PBS). The PBS was pH 7.4 comprising 1.06 mM potassium phosphate monobasic (KH_2PO_4), 155 mM sodium chloride and 2.97 mM sodium phosphate dibasic ($Na_2HPO_4 - 7\,H_2O$).

Impedance was measured in a two probe setup between a gold planar reference electrode (area 26.3 mm^2) and the graphene electrode (area 30 µm) under investigation. The impedance of the reference electrode was measured against a tungsten probe (DCP 100 Series, FormFactor). Electrodes were contacted using tungsten probes (DCP 100 Series, FormFactor) positioned with a probe station (CascadeMicrotech, Summit 12000). Impedance measurements were performed using an impedance analyser (Agilent Technologies, 4294A) with a perturbation amplitude of 500 mV in Chapter 4, and 10 mV in Chapter 5.

All data were analysed using EC-lab (Bio-Logic). Data were fitted to an equivalent circuit model using Zfit. The fit method was randomise (5000 iterations) plus simplex (5000 iterations), with a weighting to the impedance magnitude $|Z|$ applied. The level of fitting was evaluated using $\chi^2/|Z|$, where χ^2 is as the sum of the squares of residuals. Spectra were simulated using Zsim from 10^2–10^6 Hz.

A.4.4 Direct current measurements

Contact resistance was measured using a graphene strip 5 µm wide and a transmission line with 2, 10, 19, 29, 45, 65, 90, 125, 180, 285 µm spacing's. Pads were contacted using tungsten probes (DCP 100 Series, FormFactor) positioned with a probe station (CascadeMicrotech, Summit 12000). Current-voltage sweeps were measured with a semiconductor device analyser (Agilent Technologies, B1500A).

A.4.5 Atomic force microscopy

The thickness of the deposited encapsulation materials were found with atomic force microscopy (AFM, Bruker Dimension Icon) or stylus profilometry (Bruker DektakXT Stylus Profilometer). The AFM was used in PeakForce Tapping mode with ScanAsyst.

A.4.6 Fourier transform infrared spectroscopy

For FTIR analysis of lyophilised proteins, KBr was heated (100°C, 2 h) to remove any water. 300 µg of lyophilised protein was mixed with potassium bromide (KBr) using an agate mortar, and pressed into 7 mm self-supporting disks using a load of 10 tons. FTIR spectra were acquired using a Cary 680 FTIR spectrometer (Agilent Technologies, CA, USA) with 60 scans and a resolution of 1 cm^{-1}.

A.4.6.1 Data analysis

All data were analysed using Matlab. A background spectrum of pure KBr was taken under identical conditions. Water vapour and buffer contributions were removed by a scaled linear subtraction. The water vapour scaling factor was the absorbance at 1635 cm^{-1} compared to a baseline at 1637–1634 cm^{-1}. The tris buffer scaling factor was the absorbance at 2992 cm^{-1}, compared to a linear baseline between 2933–3033 cm^{-1}. The HEPES buffer scaling factor was the absorbance at 2600 cm^{-1} compared to a baseline point at 3700 cm^{-1}. The histidine-sucrose buffer scaling factor was the absorbance at 851 cm^{-1} compared to a linear baseline at 882–818 cm^{-1}.

Baseline shift was removed by subtracting a convex line which passed through the minimum values in the regions 4000–3700 cm^{-1}, 2020–1840 cm^{-1} and 1000–500 cm^{-1}. Spectra were normalised to the area under the curve.

The amide I band was first smoothed using a second order SG filter with a window of 10 cm^{-1} before calculating the second derivative. The absorbance and second derivative spectra were truncated to 1720–1590 cm^{-1}. A linear baseline for the absorbance data was

between 1720–1590 cm^{-1} was subtracted. The baseline for the second derivative spectrum was a horizontal line through the minimum value.

Gaussian peaks were fitted at 1710, 1680, 1677, 1670, 1663, 1653, 1648, 1640, 1630, 1615 and 1600 cm^{-1}. The initial fitting amplitude was $2/3$ of the absorbance at this wavenumber and was constrained to be greater than 0 a.u. The initial peak width was 15 cm^{-1} and was freely varied between 3.5–47 cm^{-1}. After the first fitting, peaks with amplitudes of less than 3.5 a.u. were rejected and the data was the refitted with the reduced number of peaks.

From this data, the sub-bands were assigned to their corresponding secondary structure types. The proportion of each secondary structure type, was calculated as the area of each band relative to the area of all bands at 1689–1623 cm^{-1}.

A.4.7 Voltage trace recordings

MEA recordings were made by Susanna Mierau, Timothy Sit and Riccardo Conci. Recordings were made at DIV 14, using the MEA-1200 amplifier (MultiChannel Systems) with a sampling rate of 25 kHz. Data were acquired using the MC Rack software (MultiChannel Systems). During the recording, the temperature was maintained at 37°C using the TC01 temperature controller and TCX-Control software (MultiChannel Systems). Photos of cultures on MEAs were taken using a microscope set up and the Wasabi software (Hamamatsu software).

The code for processing and analysing the voltage traces was written by Prez Jarzebowski and Timothy Sit in Matlab [301]. All data were processed and analysed by the author.

Data were converted to a binary file (.raw) format using MC DataTool (Multichannel Systems) and to a Matlab readable format (.mat) using *Matlab_ MEA* [302]. Or converted to (.h5) file using Multichannel DataManager (Multichannel DataManager), and opened in Matlab using *McsHDF5.McsData* (Multichannel Systems).

Voltage traces from sixty electrodes were plotted with *gridTrace*. Spikes were detected using *detectSpikes*, with an order 3 butterworth filter from 600–8000 Hz. The threshold was the root mean square of the data multiplied by 5.5 and subtracted from the sample mean. A refractory period of 2 ms prevented multiple detections of a single firing event. Raster plots showing the firing events were plotted using *singleRastPlot*, and the shape of the detected spikes were extracted using *spikeAlignment*, which extracts data points from 2 ms either side of the detected spike time.

A.5 Microscopy techniques

A.5.1 Brightfield, widefield microscopy

Images of cell cultures on MEAs were taken using a microscope set up and the Wasabi software (Hamamatsu software).

A.5.2 Confocal and fluorescence lifetime imaging microscopy

Images were taken on a fluorescence lifetime imaging microscopy (FLIM) microscope by Chetan Poudel. The microscope was built around a confocal platform (Olympus FV300, Olympus, Japan) and utilised a supercontinuum source (Fianium Whitelase, NKT Photonics, Denmark) with 40 MHz repetition rate. The microscope was integrated with a time-correlated single photon counting (TCSPC) FLIM module (B& H GmBH, Berlin, Germany). The equipment is a modified version of a previously published multi-parametric imaging system [241].

The fluorescent dye Rhodamine 6G was pipetted onto an uncoated glass coverslip control, and coverslips coated in PMMA, or graphene. The calcium indicator Oregon Green BAPTA-1 (OGB-1, where BAPTA is 1,2-bio(o-aminophenoxy) ethane-N,N,N',N-tetraacetic acid) was added to the extracellular space.

The fluorescent dye was excited (at 510 nm for Rhodamine 6G and 485 nm for OGB-1) using an acousto-optic tunable filter (AA Optoelectronic AOTFnC-VIS) after the supercontinuum source. This excitation light was further filtered for excitation (with FF01-525/39 for Rhodamine 6G and FF01-474/27 for OGB-1) and fluorescence emission (with FF01-624/40 for Rhodamine 6G and FF01-525/39 for OGB-1) (all bandpass filters from Semrock, New York, USA). Each image was acquired for two minutes to collect enough photons for accurate measurement of fluorescence lifetimes in each pixel. The fluorescence decays were processed using FLIMfit [303]. The lifetime curves were fitted with a mono exponential decay function for Rhodamine 6G and known double exponential decay functions for OGB-1 [190].